A Heavy Graphene Analogue amongst the Bismuth Subiodides as Host for Unusual Physical Phenomena

DISSERTATION

zur Erlangung des akademischen Grades

Doctor rerum naturalium
(Dr. rer. nat.)

vorgelegt

der Fakultät Mathematik und Naturwissenschaften
der Technischen Universität Dresden

von

M. Sc. Bertold Rasche

geboren am 2. März 1988 in Weimar

Eingereicht am 26. September 2016

Die Dissertation wurde in der Zeit vom Mai 2012 bis September 2016
an der Professur für Anorganische Chemie II angefertigt.

Gutachter:	Prof. Dr. rer. nat. habil. Michael Ruck (TU Dresden) Prof. Dr. rer. nat. habil. Dirk Johrendt (LMU München)
Datum der Verteidigung:	22.12.2016

Mitleid mit Perspektive
oder *Die Ansichten eines Baumes*

Hier, wo ich stehe, sind wir Bäume,
die Straße und die Zwischenräume
so unvergleichlich groß und breit.
Mein Gott, mir tun die kleinen Bäume
am Ende der Allee entsetzlich leid!

Erich Kästner

Contents

Abbreviations

0D	zero-dimensional
1D	one-dimensional
2D	two-dimensional
2D-TI	two-dimensional topological insulator
3D	three-dimensional
3D-TI	three-dimensional topological insulator
ARPES	angle-resolved photoelectron spectroscopy
BZ	Brillouin zone
CCD	charge-coupled device
DFT	density functional theory
DOS	density of states
DSC	differential scanning calorimetry
EDX	energy-dispersive X-ray analysis
ELI-D	electron localisability indicator
FPLO	full-potential local-orbital
FWHM	full-width half-maximum
GGA	generalised gradient approximation
HAADF	high-angle annular dark field
HRTEM	high-resolution transmission electron microscopy

ILS	isolated layer structure
LCAO	linear combination of atomic orbitals
LDA	local density approximation
LDOS	local density of states
MO	molecular orbital
PXRD	powder X-ray diffraction
QHE	quantum hall effect
QSH	quantum spin hall
QSHE	quantum spin hall effect
RT	room temperature
SAED	selected-area electron diffraction
SCXRD	single-crystal X-ray diffraction
SEM	scanning electron microscopy
SHE	spin hall effect
SOC	spin-orbit coupling
SQUID	superconducting quantum interference device
STEM	scanning transmission electron microscopy
STM	scanning tunnelling microscopy
STS	scanning tunnelling spectroscopy
TB	tight-binding
TCI	topological crystalline insulator
TEM	transmission electron microscopy
TG	thermogravimetric analysis
TI	topological insulator
VCA	virtual crystal approximation

1. Introduction

1.1. Beginning of the Information Age

After J.C. Maxwell's theoretical prediction in 1865[1] and H.F. Hertz' discovery of the electromagnetic waves in 1888[2] the vacuum tube had been the first widely used active electronic element during the beginning of the 20th century, which allowed to benefit from these discoveries. It was possible to rectify and amplify the oscillating, weak electromagnetic waves and therefore, one was able to send information wireless over huge distances. Radios became the first possibility to broadcast information easily and quickly amongst a giant audience and therefore started the age of information.[3]

But soon the vacuum tube revealed its first limitations. During World War II the development of the radar required high oscillation frequencies, which were needed to identify aeroplanes with high precision. These high frequencies could not be handled by vacuum tubes, why the search for a substitute began.[4–6]

A first solution to this problem was developed based on a much older solid-state device. This older device, the "cat's whisker", was an invention of J.C. Bose in 1904,[7] following an even older observation by F. Braun in 1874 using a thin metal wire touching the surface of a lead sulfide crystal.[8] But although the radar worked, the technique had not been understood and the big technical revolution led by solid-state science was still to come.

When in 1947/48 the transistor was invented by J. Bardeen, W.H. Brattain and W. Shokley at Bell Labs (and a bit later independently by H.F. Mataré and H. Welker in France) no one actually expected *it* to be the start of this revolution.[4–6, 9] The New York times only mentioned the discovery on page 46, between the announcement of new radio shows.[10] Nevertheless, it turned out, that the transistor as foundation of the modern microprocessor was one of the most important inventions of the century. And only in a joint effort of solid-state chemists and physicists this achievement had been possible. First, chemists, such as J.H. Scaff, H.C. Theuerer and H. Welker made the high quality material available, which was needed to work out the different contributing effects. At that time, silicon and germanium were the materials in the focus of research. Germanium had the advantage of an almost 500 °C lower melting point, making the purification process easier. Therefore, the first transistor was based on germanium. Nevertheless, due to its bigger band gap, today's microelectronic industry is almost exclusively build on silicon. Second, physicists, such as the theoreticians W. Schottky or N.F. Mott, developed the theory concerning the interfaces of semiconductors (and metals). And finally, experimentalists, as the inventors mentioned above, brought together the material and the theoretical ideas.[4–6] From that moment on, the transistor was going to be the measure of economic, scientific and maybe also social progress for the next 60 years.

Silicon at its Limits

The transistor as measure of progress was and is closely related to the famous "Moore's law", a prediction by G.E. Moore, which he made in 1965[13] (slightly adapted in 1975[14]) and has become a (self-fulfilling) prophecy. It says that the number of transistors on a microprocessor chip will double every 24 month, what has been true for the last 60 years (Figure 1.1). But now it might have come the time, where this rule of thumb breaks down,[15, 16] which is illustrated by the stagnating frequencies (and therefore the clock speed) at which the transistors work, although the number of transistors still increases (Figure 1.1).

The problem of today's silicon based microprocessors is in general the ongoing shrinking of the devices. Meanwhile, the nominal size of structures on a microelectronic

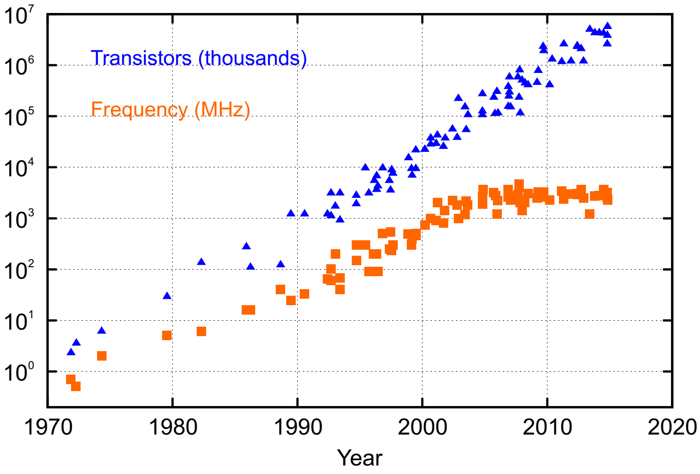

Figure 1.1.: Development of the number of transistors (in thousand) per microprocessor chip and of the central processing unit clock speed (in MHz) during the past 50 years (Selected data from K. Rupp[11] adapted under the creative commons licence[12]).

chip is only about 14 nm [15, 17] and this introduces great problems. The first one is also the reason why the frequencies have stagnated. Due to the resistance that the moving electrons experience, heat is produced. The smaller the devices become, the more heat per volume is accumulated and has to be lead off. In the early 2000s, features first became smaller than 90 nm [15] and due to the heat density within the microchips it was impossible to cool the processor, if the speed was increased further. The solution at that stage was the parallelisation of processing, which led to today's multicore microprocessors. [15] But the parallelisation has its limitations, as the programs have to be able to make use of it and at a certain stage, more parallelisation does not lead to higher performance. And again, just as it was the case with the vacuum tube in the 20th century, the need for higher frequencies could be the trigger of a new technological revolution.

But there is an even more fundamental limitation than the heat problem. With decreasing size of the transistors, we approach the length scale of the electron mean free path and therefore the world of quantum phenomena. For example, the devices are going to suffer from leakage due to tunnel effects. Simultaneously, the production process, which has been based on lithography for decades, becomes much more difficult. [15, 16, 18]

Envisioning the Next Revolution

Several approaches have been developed to overcome the problems connected to the ongoing shrinking of the devices. Mainly, it has been aimed at a higher efficiency and therefore less heat production. This includes the simplest idea to use other (semiconductor) materials with higher charge carrier mobilities than silicon, such as germanium or InAs, although at the price of a smaller band gap. [16] Similarly, graphene and carbon nanotubes have been discussed as future materials. [19–22] Another solution are so called single-electron devices, where a single electron encodes one bit, instead of several thousands of electrons which are currently needed to switch a transistor. [18, 23]

More fundamental is the idea of encoding a bit not by charge as today, but by the spin of an electron. Electronics based on this idea, the so called "spintronics", would need a completely new system of entering, handling and reading of spins, but finally leading to very high efficiencies. [24]

Even more fundamental is the idea of quantum computing. This would be more than a new technical solution, but rather a completely new concept how to compute. Information storage and handling in terms of bits, with a bit being either 0 or 1, would be similar in a quantum computer, although the bits are then called qubits.

Nevertheless, the requirements for these qubits are very much different due to the different way tasks are processed. Currently, computation means connecting bits by logical operations, with any connection of different bits being a separate process. For a quantum computer, computation means to entangle the coherent wave functions of qubits, processing in parallel any possible connection of all qubits in all states. In principle, an initial state is constructed with the qubits, the system is "left alone" for some while and afterwards a final state can be read out.[25] Therefore, qubits have to be connected to a (long-time coherent) wave function and altering as well as reading of the state of this wave function should be easily possible.

For all these concepts, several technical solutions are being developed. Especially in the case of the more fundamental approaches, the "spintronics" and the quantum computer, various ideas how to handle the spin or how to encode a qubit, respectively are being discussed.[24, 25] Amongst others, a relatively new class of materials could provide a basis: the topological insulators. With respect to the spintronics, they allow for a dissipationless transport of spins. With respect to quantum computing they could host Majorana fermions, which is one way to represent a qubit and will be further discussed at the end of this chapter.[26–29] But what are topological insulators?

1.2. Topological Insulators

A "New" Insulating State

Topological insulators are a fundamentally new state of matter, which makes it necessary to split the class of insulators (including semiconductors, which are essentially small-gap insulators[1]) into two subcategories: the "normal" insulators and the topological insulators.[26, 27, 32, 33] Or in other words, into the topologically trivial and into the topologically non-trivial insulators, respectively. Their difference manifests itself in the nature (topology) of their electronic band structure with respect to each other, or, more generally, with respect to the vacuum, which is defined as "the" normal insulator.

If one considers the band structure of an insulator, meaning an electronic band structure of a periodic, infinite system, with a band gap at the Fermi energy. Then, any electronic band structure can be either adiabatically (and therefore continuously) transformed into the vacuum band structure, *or not*. That these two options exist is

---

[1] One could even add semimetals, as the theoretical basis on which this classification builds up only requires, that at any given k-point the two bands in the vicinity of the Fermi energy are separated by a finite energy.[30–32]

due to the different topologies of the electronic band structures, which only become obvious in the higher dimensional Hilbert space.[27, 32]

Topology in Physics

To illustrate the idea of topology an example from geometry is very helpful. One can consider two-dimensional (2D) surfaces in three-dimensional (3D) space, e.g. the surface of a sphere compared to the surface of a doughnut (Figure 1.2). In geometry both are characterised by the number of holes penetrating the surface in 3D space, their so called genus g. In case of the sphere g is 0, in case of the doughnut g is 1. Both are therefore not homeomorph, meaning they cannot be continuously transformed into each other.

Similarly, this also holds for electronic band structures. The electronic band structure of the periodic infinite system within the first Brillouin zone is the "surface" from the geometry example. As the topology of the 2D surface is revealed by drawing it in 3D space, the topology of the electronic band structure is "revealed" by analysing the band structure in the Hilbert space, the "space" of all possible quantum states of the system. A number used to categorise the electronic band structures due to their topology is called a Chern number, similar to the genus in geometry. Again, this number originates from mathematics[34] (the theory of fibre bundles) and was first used and explained in the context of electronic structures by D.J. Thouless, M. Kohmoto, M.P. Nightingale and M. den Nijs in 1982.[35]

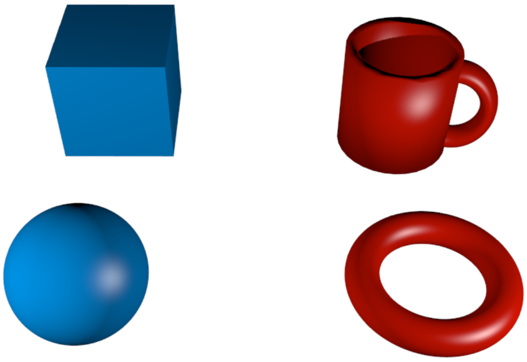

Figure 1.2.: Surfaces of geometric objects can be categorised according to their topology. On one hand, the surface of a sphere and a cube are homeomorph to each other and belong to the genus $g = 0$ class (left, blue). On the other hand, the surface of a doughnut and a cup are also homeomorph to each other, but belong to the genus $g = 1$ class (right, red) and are therefore *not* homeomorph to the surface of a sphere or a cube.

By introducing the concept of topology and Chern numbers in the electronic band theory, THOULESS *et.al.* were able to explain the quantisation of the Hall resistivity in an external magnetic field, as it was observed for the quantum Hall effect (QHE) in 1980.[36] This effect appears for 2D electron systems at very low temperatures and high magnetic fields. It goes hand in hand with an electronic band gap in the interior of the 2D electron system and dissipationless charge transport along the edges in so-called chiral edge states (Figure 1.3a). The quantum Hall state was actually the first "topological insulator"[32] and the chiral edge states (and therefore the dissipationless charge transport) are protected by the non-trivial topology of the bulk electronic band structure. As this protection at the boundary of the system is a direct consequence of the bulk properties, this is referred to as the bulk-boundary correspondence. These edge states are different from many other (unprotected) edge or surface states found for insulators, which can be localised by small local perturbations (which exist in any real system) and therefore do not allow for any transport. A Chern number, in this specific case the so-called TKNN-invariant, encodes this non-trivial topology of the bulk band structure.[32,37]

Different Flavours of Topological Insulators

That a topologically protected electronic state can also exist without an external magnetic field was discovered later and led in 2005 first to the formulation of the two-dimensional topological insulators (2D-TIs),[38–40] then of the three-dimensional TIs (3D-TIs)[30,41,42] and finally of the topological crystalline insulators (TCIs).[43,44] Meanwhile the field of topologically protected phases is expanding rapidly and it is realised that many known problems can be explained from the viewpoint of topological protection. Besides further electronic states,[45] topological phases of sound and light[46] and the superfluid phase of helium are examples.[47] What is common to all the classifications based on topology is the fact, that a certain symmetry protects, or better, guarantees the non-trivial topology and that, if this symmetry is broken, the formerly protected phase can be adiabatically transformed into a topologically trivial phase.[44,45,48] In the case of the QHE it is the gauge symmetry,[49] for TIs this symmetry was originally the time-reversal symmetry,[38,40] but in the case of the TCIs also crystal symmetries have been discovered to protect the topology of the electronic band structure.[43,44]

The original idea leading to the formulation of the TI theory was brought up by HALDANE. Having established the non-trivial topology of the electronic structure of the QHE, he asked whether an electronic system similar to the one of the QHE could

(a) QHE (b) SHE

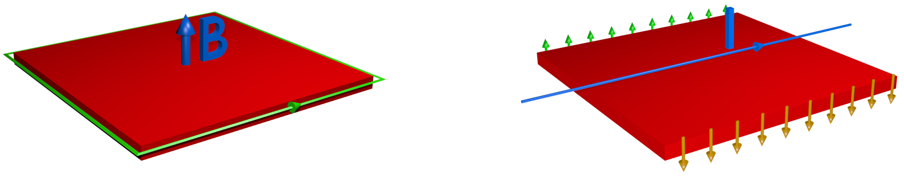

(c) QSHE / 2D-TI (d) "weak" 3D-TI (e) strong 3D-TI

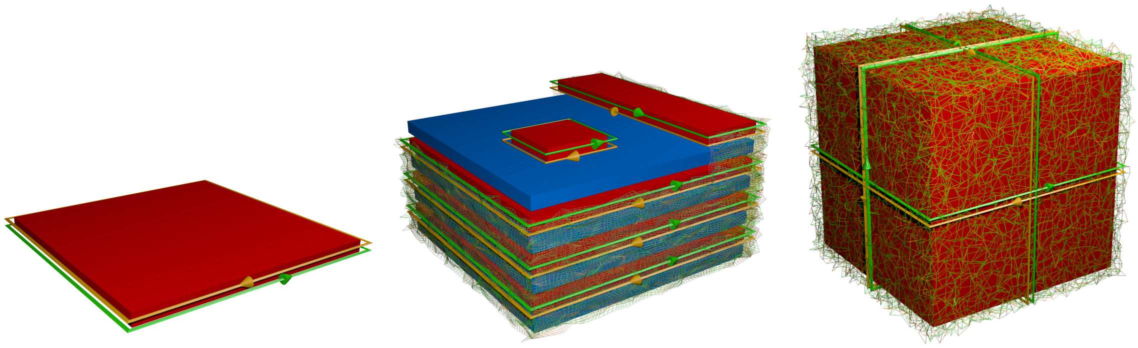

Figure 1.3.: Illustrations for (a) the quantum Hall effect (QHE) with magnetic field $\vec{B}$, (b) the spin Hall effect (SHE) with current I and (c) the quantum spin Hall effect (QSHE). The latter is the foundation of the class of 2D-TIs. The two other TI-classes based on time-reversal symmetry, which result from the expansion to three dimensions, are (d) the “weak” 3D-TIs (with an isolated edge and island on top of the “dark surface”, which does not exhibit protected surface states) and (e) the strong 3D-TIs

.

exist, but without an external magnetic field driving the system into a topologically protected insulating state.[50] Without an external magnetic field, the system could allow for time-reversal symmetry, which is otherwise always broken.[38–40, 51] While the model suggested by Haldane still broke time-reversal symmetry, a long known effect helped to resolve this issue: the spin Hall effect (SHE). The SHE describes the phenomenon that a separation of electrons with opposite spin occurs intrinsically, perpendicular to a current, due to spin-orbit coupling (Figure 1.3b). This is very similar to the classic Hall effect, where *charge* is separated perpendicular to a current due to a *magnetic field*.[51–54]

Examining the essential ingredients of the (intrinsic) SHE, it was realised that spin-orbit coupling (SOC) not only led to a separation of spins, but that in a similar way to the external magnetic field in the QHE, SOC could drive an electronic system

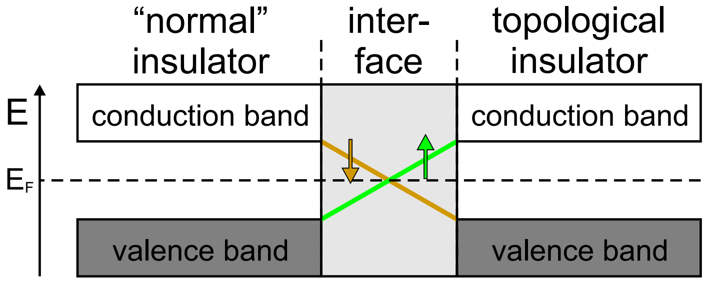

Figure 1.4.: At the interface of a "normal" insulator (e.g. vacuum) and a topological insulator metallic (helical) surface states with locked momentum and spin arise from the different topologies of the electronic band structures.

into a topologically non-trivial insulating state. This effect was consequently called quantum spin Hall effect (QSHE) as it can be viewed as two copies of the QHE. Consequently, one has two instead of one edge states that host counter-propagating electrons with opposite spin, which is necessary if one wants to retain the time-reversal symmetry (Figure 1.3c). Again, as in the QHE, the topology of the bulk electronic band structure guarantees the existence of edge states at the edge to a topologically trivial system (bulk-boundary correspondence), as long as the underlying symmetry, in this case the time-reversal symmetry, is unbroken. The Chern number encoding the non-trivial topology for the QSHE is the Z_2-invariant, similar to the TKNN-invariant for the QHE. The electronic systems showing the QSHE was later-on also named a 2D-TI.

The unique edge (2D-TI) or surface (3D-TI, see below) states arising from the non-trivial topological properties of the respective bulk electronic band structures could also be seen as a crossing of the bands at the Fermi energy to connect the non-trivial with the trivial topology, e.g. of the vacuum (Figure 1.4). Consequently, these edge or surface states are metallic, but with the very unique property that for an electron within such a state, its spin and momentum are locked due to time-reversal symmetry. Therefore, backscattering of these electrons is suppressed as long as time-reversal symmetry remains unbroken (e.g. magnetic impurities would break time-reversal symmetry).[27, 32, 44] These so called helical edge states allow for dissipationless *spin* transport, similar to the dissipationless *charge* transport for the QHE.

If, besides time-reversal symmetry, the system preserves inversion symmetry, this concept becomes a bit more illustrative. Then the topology of the electronic band structure is encoded by the parity eigenvalues of the bands below the Fermi energy and the Z_2-invariant can be calculated as a product of these eigenvalues at the time-reversal invariant momenta (which are four or eight specific points in the first Brillouin zone in 2D or 3D, respectively). The topology becomes non-trivial if the product is

-1.[27,30,32] From a chemists perspective, this means that within an odd number of occupied bands, atomic orbitals with different parities have to contribute. As only p-orbitals have a negative parity eigenvalue (they are *ungerade*), one has to focus on their properties. Two aspects favour a situation, where in different directions different orbital contributions dominate and therefore one band can have different parity eigenvalues at different time-reversal invariant momenta. One aspect is the anisotropy of the structure itself and the second is strong SOC. The latter splits the three degenerate p-orbitals with odd parity (p_x, p_y, p_z) into one $p_{1/2}$-orbital with even parity and two $p_{3/2}$-orbitals with odd parity. Consequently, this can lead to a mixture of orbitals of different parities within one band. The discussed edge/surface states then connect states of the same parity. This is actually always the case, but if the number of these connections is even, the edge states are not protected (the topology is trivial) and they become localised at the edge/surface. For an odd number of connections, the states are protected by topology and can cross the Fermi level without being gapped.

The expansion of the QSHE (2D-TI) to three dimensions was possible by stacking weakly interacting QSHE layers to a 3D structure and thereby forming a surface state out of the former edge states (Figure 1.3d).[30,41,42] This stack was ineptly named a weak 3D-TI, as it was first believed that due to the coupling of the edge states of the QSHE layers the formed surface state parallel to the stacking direction would be no longer protected and therefore not show the unique properties discussed above. But it has been shown, that this is not the case.[55–59] Furthermore, edges or islands on the surface of such a "weak" 3D-TI behave as a 2D-TI.[60] Besides the "weak" 3D-TIs also strong 3D-TIs were derived, for which any surface exhibits topologically protected states (Figure 1.3e).

As mentioned, for the 2D-TI (QSHE) one Z_2-invariant encodes the topological properties. In three dimensions the topology of the electronic band structure is encoded by four Z_2-invariants $\nu_0; (\nu_1, \nu_2, \nu_3)$, with the first one indicating "weak" ($\nu_0 = 0$) or strong ($\nu_0 = 1$) properties and the other three being a representation of the (pseudo 2D) properties in each spatial direction.

Experimental Evidence

Experimental verification of this new state of matter has so far focused on two aspects.[30,32] One is the direct observation of the edge or surface states itself, including the attempt to resolve the spin polarisation of these states. The second is more indirect and concerns the transport properties, which should be very unique due to the low-dimensionality of the edge (1D) or surface (2D) states as well as the forbidden backscattering due to the spin-momentum locking. The transport approaches include also predictions for Hall and magneto resistance (e.g. quantised Hall resistance or negative magneto resistance due to weak anti-localisation).[32, 61]

The quantised conductance was then actually the first experimental verification of a (2D-)TI state and it was observed in transport measurements on HgTe sandwiched between two layers of CdTe in 2007.[62] Only in 2008 and 2009 also the direct observation of the surface states (of a strong 3D-TI) via angle-resolved photo-electron spectroscopy (ARPES) was successful on the surface of the strong 3D-TI $Bi_{1-x}Sb_x$.[63, 64] As the electronic structure of the surface of $Bi_{1-x}Sb_x$ is very complicated ($Z_2 = 1; (1, 1, 1)$), another prediction for the long known thermoelectric materials Bi_2Te_3, Bi_2Se_3 and Sb_2Te_3 to be strong 3D-TIs laid the foundation on which most of today's TI research is based.[65] Especially, Bi_2Te_3 and Bi_2Se_3, which were confirmed to be strong 3D-TIs by ARPES,[31, 66, 67] have been dominating the field as they have a single Dirac cone on their surface ($Z_2 = 1; (0, 0, 0)$). Since then, many more transport experiments and direct observations have been conducted to prove the unique properties of TIs of all kinds.[32] Several difficulties, especially with transport experiments (e.g. non-insulating bulk due to impurities[32, 68]) or with resolving the spin polarisation (e.g. unknown correlation of polarisation of the incident photons in ARPES and spin polarisation[32, 69]) appeared.

Nevertheless, until the discovery of the herein presented "weak" 3D-TI $Bi_{14}Rh_3I_9$, research was almost exclusively concerned with strong 3D-TIs, although, as mentioned, the notation "weak" is misleading, as the surface states are protected anyway. Besides missing materials, one reason is, that ARPES as the most established tool to check for topologically protected states is difficult to realise on "weak" 3D-TIs. Their natural cleaving plane, which is exploited to create sufficiently clean samples for ARPES, is usually the "dark surface", meaning the surface on which no protected states exist and which is defined by the weak topological invariants (ν_1, ν_2, ν_3) (Figure 1.3c). In contrast to that, this dark surface also holds the great potential of the "weak" 3D-TIs, the 1D edge states at edges or islands on such a dark surface. This handicap of ARPES was overcome with scanning tunnelling microscopy (STM) and spectroscopy (STS). It was realised that they are powerful tools to examine the surface of a material with respect to the topologically protected states, especially at edges on these surfaces.[60, 70, 71] This was shown e.g in the case of bismuth,[72] and will be demonstrated within this work.

TIs' Prospects

How can TIs contribute to the discussion about spintronics and quantum computing? And can they help to pave the way into a new era of computation? The profit in case of spintronics is very direct, as a dissipationless transport of spins would be a useful tool to move and inject spins in any spintronic circuit. The relation to quantum computing with Majorana fermions as qubits needs a further ingredient: superconductivity. The combination of a superconducting and a 1D topologically protected state should host a pair of Majorana fermions as quasi-particles at the ends of the 1D channel. Majorana fermions are uncharged fermions and, most importantly, their own anti-particles. Since their theoretical prediction in 1937 by Ettore Majorana[73] they have not been undoubtedly observed as free particles.[28,74] As a 1D topologically protected state is required to host such a pair of Majorana fermions, besides nanoribbons of strong 3D-TIs, especially 2D-TIs and the surfaces of weak 3D-TIs are promising in the search for these states. If one is able to create these quasi-particles in solid-state, it is still a long way to use them as qubits in a quantum computer and to entangle their wave functions in order to actually perform calculations.[26–29,44,74]

Whether or whether not one expects a new revolution in microelectronics led by TIs, the new physical effects associated with this new class of materials leaves us with the question how and where to find corresponding compounds. Especially, concerning the necessity of protected 1D edge states for quantum computing the search for the so far under-represented 2D-TIs and "weak" 3D-TIs should be intensified. But this task may be even expanded to a much more general quest: to understand low-dimensional electronic systems from a chemists perspective. If we gain this understanding, e.g. in the case of TIs, one could judge from the structure and bonding (the "chemistry") whether a material exhibits certain physical effects. It includes the task to join the mainly physical point of view, starting from the free electron, with the mainly chemical point of view, starting from the maximum localised electron in an atom. Although the latter is also famous in physics as tight-binding approach, especially solid-state physicists prefer the first, also known as plane-wave approach. Interestingly, Pearson and Brattain pointed out that also during the discovery of the transistor the consideration of both viewpoints was necessary to yield a complete picture and to explain the observed effects.[4] A good way to begin this task, is to explain what a low-dimensional electron system is from a physicists and from a chemists perspective.

1.3. Realisations of Low-Dimensional Electron Systems

Restricting Electrons

Generally, when speaking about low-dimensional systems, it is meant, that the mobility of the electrons is restricted to certain spatial directions, or in other words to certain areas, in contrast to a free electron. The latter is described in physics by the Fermi gas theory. Essentially, this is an ideal gas of non-interacting electrons.[75, 76] Such electrons are known to any chemist as metallic electrons e.g. in sodium. The type of bonding which belongs to such electrons is consequently the metallic bonding.

From a physicists perspective, such an electron can be restricted by any kind of potential barrier. Therefore, the electron would then only be allowed to move e.g. in a plane, which would be a 2D electron system, or in a channel, which would be a 1D electron system. These restrictions have a strong influence on the formerly non-interacting electrons and the physical description has to be altered from the Fermi gas to the two-dimensional electron gas (2DEG), which is still very similar to the Fermi gas, or in one dimension to the Luttinger liquid.[75, 76] It turns out, that the fewer degrees of freedom exist for the electrons, the stronger the system behaves as a correlated system and the more the all-electron wave function is different from just a superposition of many single-electron wave functions.[75, 76]

Structure chemistry offers various ways to create such potential barriers. The most obvious barrier is the surface of a material. For a TI or, coming back to the beginning, for a transistor, already the existence of such an interface generates restricted electrons. But usually, to yield a restriction of the electron mobility by the surface, the size of the structure has to be reduced to the order of the length of the electron mean free path. Such a restriction, which shall be called *size confinement*,[77] is the basis of nanotechnology and can occur in one, two or three directions.[78–80] The resulting systems are called 2D (nanosheets and -flakes), 1D (nanotubes and -wires) or 0D (nanoparticles) structures, respectively with the dimensionality being identical with the "degrees of freedom" for the electrons.

The effects connected to this *size confinement* have been known (although not understood) since the antique, when red gold nanoparticles were used to colour glass.[81] Today, nanotechnology has forged its way into many areas of science, technology and everyday live due to the extraordinary physics.[78, 81] Concerning the electronic properties, depending on their dimensionality several applications are being discussed. For instance nanoparticles could improve solar-cell materials[82], while nanowires, nanotubes[19, 20, 83] as well as nanosheets[84, 85] might be just the more efficient materials for microelectronics mentioned earlier.

But there are other barriers for electron movement well known to chemists, connected to two basic types of chemical bonding. These two basic types are the ionic and the covalent bonding and at least in their extreme, they yield localised and therefore restricted electrons. Such a restriction of the electron mobility shall be called *chemical confinement.*[77] To explain, how electrons become localised in these cases it is worth to have a look at chemical bonding in general.

Classically, any chemical bond is formed as all atoms try to attain a fully filled shell. Quantum-mechanically, a bond means that the electronic wave functions of the bond-forming atoms (atomic orbitals) overlap. Thereby, a new electronic wave function is formed (molecular or, for solids, crystal orbital), which in a good approximation can be described as a linear combination of the atomic orbitals (LCAO theory[86, 87]). These combination are either lower, higher or similar in energy compared to the original atomic orbitals and are therefore called bonding, anti-bonding or non-bonding states, respectively. The type of bond that is formed depends on the energy difference of the original atomic orbitals and the strength of their overlap. Both influences the energy difference of the bonding and anti-bonding state, e.g. does a stronger overlap of atomic orbitals with similar energy lead to a higher energy difference of the bonding and anti-bonding state. Classically, this compares mainly to the question of electronegativity.[86, 87]

Interestingly, for metallic and covalent bonds the scenario is in principle the same. In both cases the energies of the partaking atomic orbitals are very similar. Classically, the corresponding atoms have a similar electronegativity (which usually implies a similar number of valence electrons). The major difference is the strength of the overlap and therefore the gain of energy with each formed bond. While for a covalent bond this overlap is very strong and with a few bonds usually the shell of the atom is filled, the overlap in case of a metallic bond is weak and the coordination number increases therefore to its geometrically allowed maximum. This quantitative difference on a local scale becomes a qualitative difference in the bulk. As explained by the electronic band theory, the discrete states of molecular orbitals become continuous bands in crystalline solids and the bonding and anti-bonding states expand in energy and become valence and conduction bands, respectively.[86, 87] In case of the strong splitting for a covalent bond, this results in an energy gap between the fully filled valence bands and the empty conduction bands. On the contrary, due to the weak splitting in metals the valence and conduction bands overlap and no energy gap remains. Concerning the localisation of electrons the existence or non-existence of an energy gap is crucial, as for electron

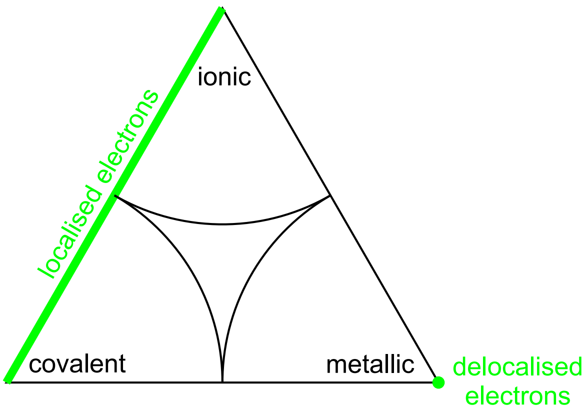

Figure 1.5.: The Arkel-Ketelaar triangle emphasising the smooth transition between the metallic, covalent and ionic bond. Bonds considered something in between metallic and covalent/ionic allow for selective restriction of electron mobility within a structure.

movement the electrons have to be able to continuously pick up kinetic energy. But only in a metal the necessary free states are available, while in the covalent case the electrons would first have to overcome the energy gap. Classically, one could think of electrons being localised in two-electron-two-centre ($2e2c$) bonds for the covalent case and electrons jumping from one bond to the next in the metallic case. Nevertheless, the transition from a metallic bond to a covalent bond is very smooth. Starting from a metal with weakly overlapping atomic orbitals, electrons become more and more localised due to an increasing orbital overlap, first restricting the movement to certain directions in space, then locally in multi-centre bonds and finally in $2e2c$ bonds.

The situation for an ionic bond distinguishes itself from that of the metallic and covalent bond, as the atomic orbitals forming the bond are very different in energy. Classically, this refers to atoms which have very different electronegativities (which usually implies very different numbers of valence electrons). The huge energy difference of the atomic orbitals means that the newly formed bonding state is very similar to the atomic orbital of the more electronegative element (valence-electron-rich), while the formed anti-bonding state is very similar to the atomic orbital of the less electronegative element (valence-electron-poor). Classically, this can be viewed as a transfer of electrons from the atom with less valence electrons to the valence-electron-rich atom and both atoms becoming charged ions. Interestingly, in solid-state the resulting arrangement of the atoms is very similar to the one in metals, with high coordination numbers, as due to the electrostatic interactions the ions are packed together as spherical charged particles. On the contrary, the electronic band structure is similar to the one of a covalent structure, as the high difference in energy of the original atomic orbitals directly transfers to the splitting of the bonding and anti-bonding states which results in an energy gap between valence and conduction bands. Therefore, similarly to the situation of a covalent bond, no electron movement is possible as long as the electrons cannot overcome the energy gap. Again, as the difference of the energy of the original atomic orbitals (classically, the electronegativity) can be smoothly increased or decreased, also the character of a bond can be smoothly varied from ionic to covalent and metallic.

A traditional way to emphasise the smooth transitions between metallic, covalent and ionic bond, at least in solid-state, is the Arkel-Ketelaar triangle (Figure 1.5).[88–90]

Structures Hosting Restricted Electrons

If the chemical bonding is something in between these three extremes, and/or if metallic parts are held together by ionic interactions, it offers the opportunity to host low-dimensional electronic systems, as then conducting and insulating parts coexist within one structure. For example, if a metallic strand is embedded in an ionic matrix, for a sufficient distance between adjacent strands the delocalised electrons of the metallic bond will be restricted to the strand and therefore behave as electrons in a 1D channel. Such a restriction could be called *structural confinement*,[77] although it might be also considered a consequence of the *chemical confinement*. Such systems are well known, e.g. in structures belonging to the metallic Zintl phases, an expansion of the classical Zintl phases.[77, 91, 92] While the latter combine ionic and covalent interactions and can be understood within the $(8-N)$-rule,[92, 93] metallic Zintl phases belong to a class where the covalent interactions become more and more delocalised due to an insufficient number of valence electrons or very diffusive orbitals. For example the diffusive valence orbitals of antimony form metallic $^1_\infty\mathrm{Sb}^-$-strands in $\mathrm{Li_2Sb}$ or metallic $^2_\infty\mathrm{Sb}^-$-meshes in $\mathrm{YbSb_2}$.[93]

But also the so called subiodides of bismuth, which have been investigated within this thesis, are such systems. Furthermore, bismuth has the strongest SOC of all stable elements[2]. As mentioned in Section 1.2, this makes it very suited for the creation of topologically non-trivial phases, as the splitting of the p-orbitals due to SOC becomes as big as 1.95 eV for a single bismuth atom[95] (although this becomes much smaller in a condensed structure) and therefore makes it more probable to get mixed parities within bands formed by the atomic p-states.

Already the binary phase system of bismuth and iodine exhibits an unusual man-

---

[2] Formally the naturally occurring $^{209}\mathrm{Bi}$ isotope is metastable with respect to α-decay. But with a half-life of $1.9(2)\times10^{19}$ yr it can be practically regarded as stable.[94]

ifold of phases, which cannot be understood in terms of pure ionic bonding, as it is expected from structures with halides. Besides the BiI_3, which meets the expectations of an ionic compound of a group 15 and a group 17 element with Bi^{3+} and I^-, compounds as Bi_4I_4, $Bi_{14}I_4$, $Bi_{16}I_4$ and $Bi_{18}I_4$ are known.[96–101] Virtually, in all of these compounds, smaller or bigger pieces of the elemental bismuth structure are "cut out" by iodine. While the structures mainly follow a covalent pattern, the latter three are metallic (semimetals).[101, 102] Furthermore, with respect to the search for TI materials, Bi_4I_4 was discovered to be a strong 3D-TI.[103] Introducing transition elements as a third component expands this class to a versatile playground to study low-dimensional systems. By varying the composition within the phase systems, it is possible to tune the fraction of ionic, covalent and metallic interaction and thereby to create 0D (homoatomic or transition-metal-centred bismuth clusters), 1D (strands, channels and tubes) and 2D or 3D networks.[77, 104, 105] Within these different structures the restricted electron mobility has already proven to provoke unusual physical phenomena, such as ferromagnetism and superconductivity within the same structure.[106]

Therefore, and due to the mentioned strong SOC, the discovery of the first "weak" 3D-TI, the layered structure of $Bi_{14}Rh_3I_9$, fits very well into this class of materials. It inspired this thesis, which presents a systematic search for similar layered (pseudo-2D) structures based on a comprehensive experimental and theoretical investigation of the bismuth–platinum-metal–iodine systems. This includes the investigation of different phase systems in Chapter 3, the structural and physical characterisation of the identified phases and comparison with quantum-chemical calculations in Chapter 4 and 5. Thereby, Chapter 4 deals with compounds sharing a 2D hexagonal arrangement of platinum-metal-centred bismuth-cubes as structural fragment, amongst others the mentioned $Bi_{14}Rh_3I_9$, but also the long known $Bi_{13}Pt_3I_7$.[107] This 2D hexagonal arrangement, which will be referred to as honeycomb network throughout the text and for which the phrase "heavy graphene analogue" will be established, was identified to play the essential role for the topologically non-trivial properties. The resemblance to graphene is drawn, as a (hypothetical) graphene with strong SOC (a "heavy graphene") was the first TI ever put forward by theoreticians. Nevertheless, in each of the similar structures, the honeycomb network is found in a different environment, which drastically changes the topology of the electronic band structure. Therefore, these compounds hosting the"heavy graphene analogue" in different surroundings might be the key to understand the topological non-trivial insulating state of matter and its "chemistry". Chapter 5 discusses compounds which do not comprise the honeycomb network, but were discovered during the systematic investigation of the bismuth–platinum-metal–iodine phase systems.

Finally, if one finds a correlation of the chemical bonding and the structure on one side and the electronic properties on the other side, it would enable us to interpret electronic properties in terms of chemistry and vice versa. For instance in the case of TIs, the surface states might have an analogy in chemical bonding, which could help to exploit their unusual properties or to find similar effects in other structures. The herein presented research shall be a small piece in the big puzzle of resolving this relation and therefore give a perspective for the far future on how to overcome today's limitations for the microprocessor.

2. Experimental

2.1. Synthesis

Starting Materials

All starting materials were handled in an argon-filled glovebox (MBraun UNIlab; $p_{O_2}/p^\ominus < 1\,\text{ppm}; p_{H_2O}/p^\ominus < 1\,\text{ppm}$) and before proceeding further sealed in silica ampoules under vacuum ($p < 0.1\,\text{Pa}$).

Bismuth (Merck) was treated with streaming H_2 at 220 °C before being used. Tin (Chempur; > 99.90 % metal base), Platinum (ChemPur, > 99.95 % metal base), Rhodium (Merck, > 99.90 % metal base), Palladium (Degussa; > 99.99 % metal base), Ruthenium (Riedel-de Haen, > 99.00 % metal base) and Iridium (Alfa Aesar, > 99.90 % metal base) were used without further purification. BiI_3 was synthesised from the elements and sublimed twice.[108]

$Bi_{14}Rh_3I_9$

Bismuth, rhodium, and BiI_3 in the molar ratio Bi : Rh : I = 14 : 3 : 9 were ground in an argon-filled glovebox and sealed in a silica ampoule (0.1 ml for DSC measurements and 3.5 ml for further synthesis). The total mass of the batch was adjusted such that the mass concentration of BiI_3 corresponded to $72\,\text{mg}\,\text{ml}^{-1}$. Annealing at 365 °C for at least three days yielded almost phase-pure $Bi_{14}Rh_3I_9$ powders with a small impurity of 2 % to 3 % bismuth.

For the growth of larger crystals the described mixture of Bi, Rh, and BiI_3 was heated to 700 °C in a tubular furnace at a rate of approximately $350\,\text{K}\,\text{h}^{-1}$. Fast cooling to 420 °C at $-2\,\text{K}\,\text{min}^{-1}$ and then slowly cooling to 365 °C at $-1\,\text{K}\,\text{h}^{-1}$ followed instantaneously. After three days the ampoule was cooled to room temperature (RT).

$Bi_{38}Pt_9I_{14}$

Bismuth, platinum, and BiI_3 in a molar ratio Bi : Pt : I = 38 : 9 : 14 were ground in an argon-filled glovebox and sealed in a silica ampoule (0.1 ml for DSC measurements and 3.5 ml for further synthesis). Powders were obtained by annealing the mixture at 290 °C for 5 d, followed by quenching to RT.

Single crystals were grown by heating ($2\,\mathrm{K\,min^{-1}}$) $Bi_{38}Pt_9I_{14}$ powder to 430 °C and subsequent slow cooling ($-1\,\mathrm{K\,h^{-1}}$) to 290 °C. After being held at 290 °C for 5 d, the ampoule was quenched to RT.

$Bi_{13}Pt_3I_7$

Bismuth, platinum, and BiI_3 in a molar ratio Bi : Pt : I = 13 : 3 : 7 were ground in an argon-filled glovebox and sealed in a silica ampoule. Powders were obtained by annealing the mixture at 380 °C for 5 d, followed by quenching to RT.

Single crystals were grown by heating the mixture to 700 °C, followed by cooling with $-4\,\mathrm{K\,min^{-1}}$ to 450 °C and further cooling with $-1\,\mathrm{K\,h^{-1}}$ to 380 °C and keeping this temperature for 6 d, followed by quenching to RT.

$Bi_{13}Pd_3I_7$

Bismuth, palladium, and BiI_3 in a molar ratio Bi : Pt : I = 13 : 3 : 7 were ground in an argon-filled glovebox and sealed in a silica ampoule. Powders were obtained by annealing the mixture at 310 °C for 5 d, followed by quenching to RT.

Single crystals were grown by heating the mixture to 700 °C, cooling as quickly as possible to 310 °C and holding the temperature for 3 months. After quenching to RT, besides $Bi_{13}Pd_3I_7$ single crystals also large $\beta-$BiI crystals were yielded from this procedure.

$Bi_8Pt_5I_3$

Bismuth, platinum, and BiI_3 in the molar ratio Bi : Pt : I = 8 : 5 : 3 were ground in an argon-filled glove-box and sealed in a silica ampoule (0.1 ml), with a total mass load of approx. $1000\,\mathrm{mg\,ml^{-1}}$. Powders were obtained by annealing the mixture at 600 °C for 5 d, followed by quenching to RT.

Single crystals were grown by heating the mixture quickly to 750 °C and slowly cooling ($-1\,\mathrm{K\,h^{-1}}$) it to 600 °C. After 5 d, the ampoule was quenched to RT.

$Bi_{16}Pt_{11}I_6$

Bismuth, platinum, and BiI_3 in the molar ratio Bi : Pt : I = 8 : 5 : 3 were ground in an argon-filled glove-box and sealed in a silica ampoule (3 ml), with a total mass load of approx. 60 mg ml^{-1}. Powders were obtained by annealing the mixture at 400 °C for 5 d, followed by quenching to RT.

Single crystals were grown by fast heating of the mixture to 630 °C, followed by cooling with -2 K min^{-1} to 620 °C and slower cooling (-1 K min^{-1}) to 550 °C. After 5 d, the ampoule was quenched to RT.

Bi_4RhI_2

Bismuth, rhodium, and BiI_3 in the molar ratio Bi : Rh : I = 4 : 1 : 2 were ground in an argon-filled glovebox and sealed in a silica ampoule. Powders were obtained by annealing the mixture at 458 °C for 5 d, followed by quenching to RT in water (as Bi_4RhI_2 is metastable at RT fast quenching is essential).

Single crystals were grown by heating the mixture to 700 °C at 350 K h^{-1}, followed by cooling to 500 °C at -2 K min^{-1} and then slowly cooling to 458 °C at -1 K h^{-1} and holding the temperature for 5 d, subsequently followed by fast quenching to RT in water. If we introduced further steps in the slow (-1 K h^{-1}) cooling process from 500 °C to 458 °C, e.g. at 470 °C and at 465 °C for 3 d, respectively, the size of the grown needles could be increased up to several mm (Section 3.1.1).

2.2. Methods

Powder X-ray Diffraction (PXRD)

Powder X-ray diffraction (PXRD) was performed on a PANalytical X'Pert Pro Powder diffractometer in Bragg-Brentano geometry equipped with a Ge(1 1 1)-monochromator, a rotating sample stage, and a PIXcel detector, using Cu-$K_{\alpha 1}$ radiation (λ = 154.056 pm). The data were collected using a divergence slit that kept the illuminated sample area constant with a silicon single crystal sample holder to reduce the diffusive X-ray scattering.

Single-Crystal X-ray Diffraction (SCXRD)

Single crystals were measured on a four-circle diffractometer Bruker-Nonius Kappa APEX II CCD, with a Mo-tube (λ(Mo-$K_{\alpha 1}$) = 71.073 pm), a graphite(0 0 2)-monochromator, and a CCD detector. Integration as well as polarisation, and Lorentz factor corrections of the data were conducted within the APEX2 suite.[109] Optimisation of the observed crystal shape based on equivalent reflections in the corresponding Laue class and the numerical absorption corrections were performed with X-Red and

X-Shape.[110,111] For the structure solution with charge flipping methods, Jana2006 was employed.[112,113] The refinement was conducted in the SHELX2014 program suite.[114] Graphical representations of the structures were developed with Diamond.[115]

Thermal Analysis

Thermal analysis for closed systems was performed in sealed silica ampoules (0.1 ml) via differential scanning calorimetry (DSC) using a Setaram Labsys ATD-DSC device with a K-probe sensor (NiCr/NiAl) and Al_2O_3 as reference. Thermal analysis for open systems was performed in an open Al_2O_3 crucible under Ar-flow ($100\,\mathrm{ml\,min^{-1}}$) via DSC combined with thermogravimetric analysis (TG) using a Netzsch STA 409 PC/PG with a S-probe sensor ($Pt_{10}Rh/Pt$).

In addition to these in situ experiments, various samples were tempered at predefined temperatures (Chapter 3) to analyse ex situ the transitions indicated by the signals in DSC measurements.

Scanning Electron Microscopy (SEM) and Energy Dispersive X-ray (EDX) Analysis

Scanning electron microscopy (SEM) was performed with a SU8020 (Hitachi) with a triple detector system for secondary and low-energy backscattered electrons ($U_a =$ 1 kV to 5 kV).

The compositions of selected crystals were determined by semi-quantitative energy dispersive X-ray analysis (EDX) ($U_a = 30\,\mathrm{kV}$) using a SU8020 SEM (Hitachi) equipped with a Silicon Drift Detector X-Max^N (Oxford Instruments). The data were processed (Integration, Puls-Pileup correction) within the AZtec software package.[109]

Transmission Electron Microscopy (TEM)

Measurements and data analysis as well as preparation of the figures were performed by Dr. Isaeva (TU Dresden). The facilities were provided by Prof. Koch and Prof. Kaiser at the University of Ulm.

Samples were prepared by grating single crystals over a lacey carbon grid, thus depositing fragments. In addition, thin lamella were cut from a single crystal perpendicular to the largest facet, i.e. along the stacking direction, with an ultra-microtome (Ultracut, Leica Microsystems) equipped with a diamond knife. Prior to it, the crystal was embedded in the epoxy resin Epon (Fluka) that was then polymerized at 60 °C.

The nominal lamella thickness was approximately 50 nm while locally crystalline flakes with a thickness between 5 and 15 nm were observed. High resolution transmission electron microscopy (HRTEM) and selected area electron diffraction (SAED) studies were performed on a FEI Titan F20 microscope with C_s-correction operating at 80 kV and on a CM20 microscope (Philips) operating at 200 kV. For image acquisition, a $2k \times 2k$ Slow-Scan CCD-Camera (Gatan) was used. Image simulations were done with the JEMS software.[116]

Scanning Transmission Electron Microscopy (STEM)

Measurements and data analysis were performed by Dr. Van den Broek (HU Berlin). The facilities were provided by Prof. Koch and Prof. Kaiser at the University of Ulm.

The single crystal was embedded in the epoxy resin Epon (Fluka) that was then polymerized at 60 °C. Subsequently, thin lamella were cut perpendicular to the largest facet, i.e. along the stacking direction, with an ultramicrotome (Ultracut, Leica Microsystems) equipped with a diamond knife. The nominal lamella thickness was approximately 50 nm, while locally, crystalline flakes with a thickness of approximately 10 nm were observed. High-angle annular dark-field scanning transmission electron microscopy (HAADF-STEM) studies were performed at a FEI Titan F20 microscope with image correction, operating at 300 kV.

Scanning Tunneling Microscopy (STM) and Scanning Tunneling Spectroscopy (STS)

Measurements and data analysis as well as preparation of most of the figures were performed by Dr. Pauly under supervision of Prof. Morgenstern at the RWTH Aachen.

The microscopic measurements have been performed in a home-built scanning tunnelling microscope in ultra-high vacuum (UHV: $p = 1 \times 10^{-11}$ mbar) at $T = 6$ K.[117] Topographic STM images and ${}^{dI}/_{dU}$ (STS) images are recorded in constant-current mode with voltage U applied to the sample. The ${}^{dI}/_{dU}(U)$ spectra are recorded after stabilising the tip at a sample voltage U_{stab} and current I_{stab} before opening the feedback loop. All spectroscopic measurements are carried out using a lock-in technique with a modulation frequency $\nu = 1.4$ kHz and amplitude $U_{mod} = 4$ mV (8 mV), resulting in an energy resolution $\delta E = \sqrt{(3.3 k_B T)^2 + (1.8 e U_{mod})^2} \approx 7$ meV (14 meV) (e, electron charge and k_B, Boltzmann constant).[118] To first order, ${}^{dI}/_{dU}(U)$ is proportional to the local density of states (LDOS) at the measured sample position at energy E with respect to the Fermi level of the sample $E_F(\text{sample})$ ($E = E_F(\text{sample}) + eU$) and to the LDOS of the tip at the Fermi level of the tip $E_F(\text{tip})$. However, if the tip LDOS at $E_F(\text{sample})$ does not vanish, one gets an additional contribution from the LDOS of the tip at energy E according to $E = E_F(\text{tip}) - eU$ multiplied by the LDOS of the sample at $E_F(\text{sample})$.[118] Therefore, if the LDOS of the sample at $E_F(\text{sample})$ is not zero, but the LDOS at an energy E is zero, ${}^{dI}/_{dU}(U)$ will not become zero at E due to the LDOS of the tip. This explains the remaining ${}^{dI}/_{dU}$ intensity at voltages corresponding to the band gap of a single intermetallic honeycomb layer as presented in Section 4.2.4.[1]

Angle-resolved photoelectron spectroscopy (ARPES)

Measurements have been carried out at the 1^3-ARPES facility[119, 120] at Helmholtz centre Berlin using the synchrotron radiation from the BESSY storage ring and were supervised by Dr. Borisenko from the IFW Dresden.

The samples have been cleaved in situ resulting in atomically clean shiny surfaces. Photon energies in the range of 30 eV to 150 eV have been used to excite photo electrons. The sample temperature has been kept below 1 K during the measurements, except for the data from Figure 4.13a (15 K). Energy and momentum resolution have been chosen to be sufficiently small not to modify the natural width of the spectral features.

Electrical Resistivity

Measurements on powders were performed by Mr. Koban and Dr. Schnelle at the Max Planck Institute for Chemical Physics of Solids Dresden. Measurements on single crystals were conducted by Dr. Skrotzki, M.Sc. Naumann, Dr. Schönemann and Dr. Kampert at the Helmholtz Centre Dresden Rossendorf. Measurements on single crystals of $Bi_{14}Rh_3I_9$ were also performed by Dr. Vakaliuk under the supervision of Dr. Heß at the IFW Dresden.

Powders were cold-pressed to cylindrical pellets in a sapphire die cell. The electrical resistivity was measured between 4 K to 320 K using four platinum contacts in the Van-der-Pauw setup.

---

[1] The apparent pseudo-gap at $E_F(\text{sample})$ does not remove this contribution due to the finite energy resolution of the experiment.[118]

Single-crystals were contacted with four gold wires (50 µm) glued to the crystal with graphite paste (Dupont 7105 + diluter 8260) which dries on air at RT. Magnetoresistance (MR) and Hall resistivity (or Hall voltage) were extracted as the symmetrical and asymmetrical part of the resistivity as a function of the magnetic field applied in opposite directions, respectively.

Magnetisation Measurements

Most measurements were performed by Mr. Koban and Dr. Schnelle at the Max Planck Institute for Chemical Physics of Solids Dresden. Measurements on $Bi_{13}Pt_3I_7$ were conducted by Dr. Skrotzki, M.Sc. Naumann, Dr. Schönemann and Dr. Kampert at the Helmholtz Centre Dresden Rossendorf.

The samples were filled in pre-calibrated silica tubes. The magnetisation was measured in fields of $\nu_0 H = 2\,\mathrm{mT}$, 0.1 T, 3.5 T and 7 T in a SQUID magnetometer (MPMS-XL7, Quantum Design). A Honda-Owen type correction[121, 122] to the susceptibility for ferromagnetic traces was applied in case the magnetic susceptibility for fields, where saturation of the magnetisation of the ferromagnetic phase is assumed (3.5 T and 7 T), differed significantly. Some samples were measured at several other magnetic fields up to 14 T.

Quantum Chemical Calculations

Dr. Koepernik (IFW Dresden) developed the tight-binding model for the isolated layer model (Section 4.2.2) and calculated the unfolded electronic band structure of $Bi_{14}Rh_3I_9$. Dr. Richter calculated finite slabs of $Bi_{14}Rh_3I_9$ and the dispersion of the Dirac cone. Facilities were provided by Prof. van den Brink at the IFW Dresden.
Facilities for all other calculations performed by myself were provided by the ZIH of the TU Dresden.

All scalar- and full-relativistic calculations were performed with the Full-Potential Local-Orbital (FPLO) code,[123] version 14.00, within the local density approximation (LDA) using the parametrisation PW92[124] or the generalised gradient approximation (GGA) using the parametrisation PBE.[125] The Blöchl corrected linear tetrahedron method with a 12 × 7 × 7 k-mesh for $Bi_{14}Rh_3I_9$, 12 × 6 × 4 k-mesh for $Bi_{13}Pt_3I_7$ and for $Bi_{13}Pd_3I_7$, a 12 × 12 × 4 k-mesh for $Bi_{38}Pt_9I_{14}$, a 17 × 17 × 14 k-mesh for $Bi_8Pt_5I_3$ (for the primitive, not the C-centred cell), a 10 × 10 × 15 k-mesh for $Bi_{16}Pt_{11}I_6$,

Table 2.1.: The basis states (adjusted atomic wave functions) that were treated as valence states for the used elements

Atom	Valence States								
Ru		4s	4p	4d	5s	5p	5d	6s	
Rh		4s	4p	4d	5s	5p	5d	6s	
Pd		4s	4p	4d	5s	5p	5d	6s	
I		4s	4p	4d	5s	5p	5d	6s	6p
Os	4f	5s	5p	5d	6s	6p	6d	7s	
Ir	4f	5s	5p	5d	6s	6p	6d	7s	
Pt		5s	5p	5d	6s	6p	6d	7s	
Bi		5s	5p	5d	6s	6p	6d	7s	7p

$15 \times 6 \times 7$ k-mesh for Bi_4RhI_2 (cell choice according to $P2_1/c$, not $P2_1/n$, as FPLO cannot handle the latter) and a $12 \times 12 \times 1$ k-mesh for the isolated two-dimensional honeycomb-layers $[Bi_{12}M_3I]^{x+}[I_8]^{x-}$ was employed, after checking for convergence with respect to the number of k-points (min. 9000 k-points pm). Spin–orbit coupling (SOC) was implemented on the level of the four-component Dirac equation. Topological invariants were calculated according to the supplement of Reference 126. The basis states that were treated as valence states are listed in Table 2.1.

Mulliken population analysis[127] was directly provided by FPLO. Charges according to the quantum theory of atoms in molecules (QTAIM) developed by Bader[128] were calculated with the DGrid program package[129] via a topological analysis of the electron density, which was provided by an FPLO module.[130]

Chemical bonding was characterised via the electron localisability indicator (ELI-D, Υ_D^{σ}).[131, 132] The ELI-D field was computed from the converged SCF calculations using the ELI-D module[130] for the FPLO program package.[123] The field maxima (attractors) can mark out various bonding features such as atomic shells, lone pairs and chemical bonds. Topological analysis of ELI-D was performed in the DGrid 4.6 program[129] by a procedure similar to that of the Quantum Theory of Atoms in Molecules by Bader.[128] The integration of electron density within the resultant basins yielded the electron count for all bonding features. The atomic contributions into the bonding basins were computed via integration of the intersection between the bonding ELI-D basin and the respective QTAIM basins for atomic constituents. The ELI-D localisation domains were visualised in real space with the Paraview program package.[133]

3. Synthesis and Thermodynamic Properties of the new Subiodides in the Bismuth–Platinum-metal–Iodine Systems

Prior to the start of the investigations, two compounds featuring the honeycomb network, which is described in Section 4.1, were known: $Bi_{14}Rh_3I_9$ and $Bi_{13}Pt_3I_7$. Besides exploring the corresponding phase systems $Bi-Rh-I$ and $Bi-Pt-I$, the results of which are presented in Sections 3.1 and 3.2, respectively, it was also of interest, whether in similar phase systems the same structural fragment could be found. As both, rhodium and platinum belong to the group of the platinum-metals, we additionally considered the phase systems $Bi-M-I$ with M being ruthenium, osmium, iridium and palladium. Support for this idea came from quantum-chemical calculations, which are presented in Section 4.2 and which predicted possible topological insulators amongst the palladium and the iridium containing systems. Results within these phase systems are shown in Section 3.3.

In general, mixtures of bismuth, platinum-metal M and BiI_3 were prepared and sealed in small silica ampoules. This reactive mixture was heated with $2\,\mathrm{K\,min^{-1}}$ in a DSC-experiment (“reaction DSC”) up to 800 °C, subsequently followed by cooling with $-2\,\mathrm{K\,min^{-1}}$ and two further cycles of heating and cooling and characterisation of the final product by PXRD.

During the initial heating usually several exothermic signals indicated temperatures where formations of stable phases took place. Separate ampoules with the same mixture were prepared and annealed at these temperatures. After subsequent quenching these samples were analysed by PXRD and again by DSC to identify possible new phases and their decomposition temperatures. The subsequent two heating and cooling cycles were necessary because of two reasons: (a) investigate whether a possible new phase would also form on cooling from the melt (which is often kinetically hindered, as most of the ternary bismuth-subhalides decompose peritectically) and (b) if the new phase would form on cooling, to identify the decomposition temperature and compare it to the results of the separately annealed samples. In case a phase did not form on cooling with $-2\,\mathrm{K\,min^{-1}}$ the rate was decreased to a minimum of $-0.1\,\mathrm{K\,min^{-1}}$. If the composition of a new phase was identified (e.g. via EDX or SCXRD) the DSC experiments were repeated with the exact composition.

3.1. The Bi–Rh–I System

3.1.1. $Bi_{14}Rh_3I_9$ and Bi_4RhI_2[134]

After the serendipitous discovery of $Bi_{14}Rh_3I_9$ and the recognition of the topological non-trivial properties of its electronic structure (Section 4.2), great effort has been devoted to the rationalisation of the synthesis and the optimisation of the crystal growth. The combination of DSC and TG experiments and complementary annealing experiments at derived temperatures made it possible to gain insight into the complex

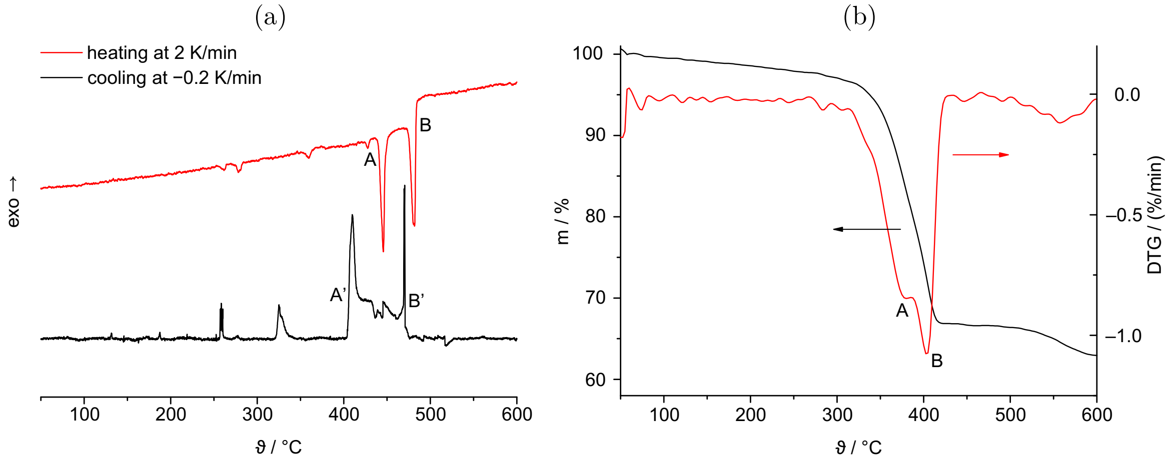

Figure 3.1.: (a) DSC experiment: Heating of $Bi_{14}Rh_3I_9$ and subsequent cooling of the formed melt in a closed system. **A**: first decomposition step. **B**: second decomposition step. **A'**: crystallisation of $Bi_{14}Rh_3I_9$. **B'**: crystallisation of the Bi_4RhI_2. Additional peaks on the cooling curve correspond to crystallisation of $Bi_{43}Rh_3I_{36}$ (≈ 330 °C) and Bi (≈ 269 °C).
(b) Mass loss and differentiated mass loss of $Bi_{14}Rh_3I_9$ upon heating in a stream of argon (open system: $p = 1\,\mathrm{bar}$). **A**: first decomposition step. **B**: second decomposition step.

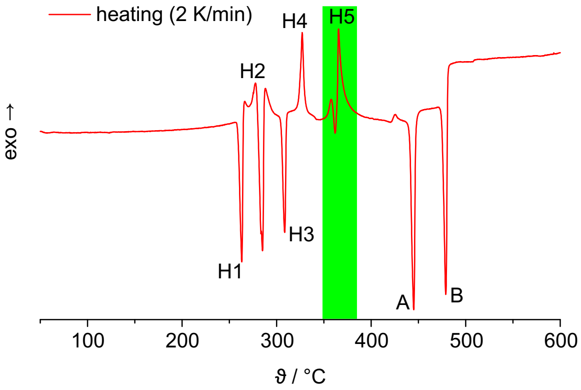

Figure 3.2.: DSC experiment: Heating of a stoichiometric mixture Bi, Rh and BiI_3 (molar ratio: Bi : Rh : I = 14 : 3 : 9) in a closed system. Highlighted region: formation of $Bi_{14}Rh_3I_9$. Signals are assigned in Table A.1.

phase relations in the ternary Bi–Rh–I system. This investigation also yielded the new ternary phase Bi_4RhI_2 formerly named phase X.[134] The temperature stability range of $Bi_{14}Rh_3I_9$ has been experimentally evaluated in a closed system under equilibrium conditions as well as in an open system under standard conditions: At first, it has been established that in a closed system, e.g. a sealed silica ampoule, $Bi_{14}Rh_3I_9$ decomposes peritectically at 441 °C (signal A in Figure 3.1a) into the new ternary phase Bi_4RhI_2 plus $BiI_{3(l,g)}$ and $Bi_{(l)}$. Consequently, the PXRD pattern of a sample that had been annealed at 458 °C and subsequently quenched shows no reflections of $Bi_{14}Rh_3I_9$ but predominantly of Bi_4RhI_2, crystalline BiI_3 and BiOI (presumably from BiI_3 hydrolysis in air) (Appendix: Figure A.2). Bi_4RhI_2 then decomposes at 475 °C (signal B in Figure 3.1a) into $BiI_{3(l,g)}$, the high-temperature modification $Bi_2Rh(aP12)$[135] and $Bi_{(l)}$, as can be expected from the binary phase diagrams.[136]

Second, it was found that in an open system, e.g. an open alumina crucible under a flow of argon ($p = 1$ bar), $Bi_{14}Rh_3I_9$ decomposes already at 380 °C, as seen from the TG experiment (Figure 3.1b). The differential TG (DTG) curve shows that the two-step decomposition process is similar to the one in the closed system. On the first step at 380 °C, a mixture of $BiI_{3(l,g)}$, $Bi_{(l)}$, and Bi_4RhI_2 is formed (peak A in Figure 3.1b). The latter compound decomposes on the second step at 400 °C into $BiI_{3(s,g)}$, $Bi_4Rh_{(s)}$, and $Bi_3Rh_{(s)}$ (peak B) in accordance with the binary phase diagrams.[136] At these temperatures the vapour pressure of BiI_3 is in between 0.04 and 0.08 bar, which leads to the observed mass loss in the TG experiment.

The formation of $Bi_{14}Rh_3I_9$ has been studied in a DSC experiment by heating a stoichiometric mixture of Bi, Rh, and BiI_3 (molar ratio: Bi : Rh : I = 14 : 3 : 9) in a closed system and has been attributed to the exothermic signal at 355 °C (green

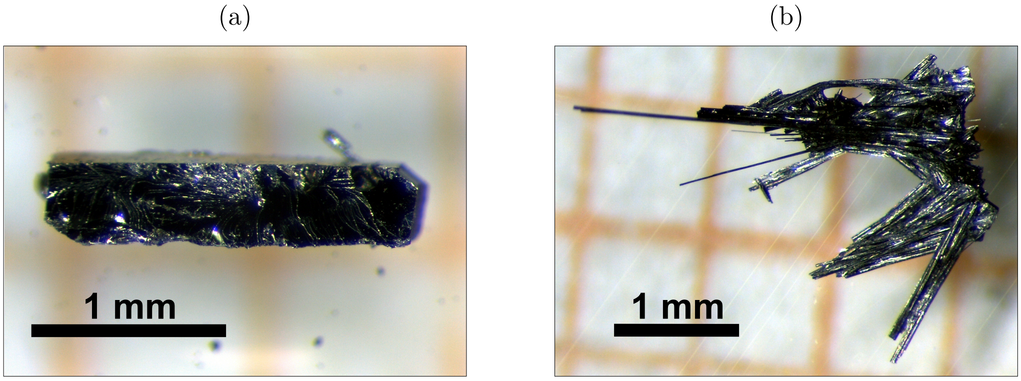

Figure 3.3.: Crystals of (a) $Bi_{14}Rh_3I_9$ and (b) Bi_4RhI_2.

region in Figure 3.2, all assigned signals see Appendix: Table A.1). This conclusion is supported by the following findings: Samples annealed at 300 or 330 °C for 1 h (Appendix: Figures A.4 and A.5) contained a mixture of $Bi_9Rh_2I_3$,[137] $Bi_{43}Rh_3I_{36}$[1], $Bi_{14}Rh_3I_9$ and binary compounds (see Table A.1). Samples annealed at 370 °C for 1 h contained almost exclusively $Bi_{14}Rh_3I_9$ (Appendix: Figure A.1) and minor admixtures of elemental bismuth. Differences between the product spectra of dynamic DSC measurements ($\Delta T/\Delta t = 2\,\mathrm{K\,min^{-1}}$) and isothermal annealing experiments (1 h) could be rationalised by varying reaction kinetics.

In order to find the optimal crystal-growth parameters, several DSC experiments in a closed system (silica ampoule) were performed starting from a homogeneous melt at 600 °C with different cooling rates (from $-0.2\,\mathrm{K\,min^{-1}}$ up to $-10\,\mathrm{K\,min^{-1}}$). Recrystallisation of $Bi_{14}Rh_3I_9$ at 410 °C was observed only for the slowest cooling rate of $\Delta T/\Delta t = -0.2\,\mathrm{K\,min^{-1}}$ (signal A′ in Figure 3.1a), leading to the conclusion that crystallisation from the melt is strongly hindered by kinetics. An independent experiment, in which a melt was cooled from 600 to 365 °C at $-0.1\,\mathrm{K\,min^{-1}}$ and subsequently quenched (Appendix: Figure A.3), also confirmed that $Bi_{14}Rh_3I_9$ crystallises on slow cooling.

The recrystallisation of Bi_4RhI_2 was observed at 468 °C at any cooling rate (signal B′ in Figure 3.1a). The remaining signals could be attributed to the (pseudo-)binary Bi–Rh and Bi–I systems.[136]

The optimised synthetic technique, based on the given data, is described in detail in Section 2.2. For $Bi_{14}Rh_3I_9$ big platelets could be grown with surfaces of approximately 1 mm² and up to 0.5 mm thickness (Figure 3.3a). The crystals cleave easily, e.g. with a sticky tape. To separate the cleaved pieces, the sticky tape can be dissolved

---

[1] The phase was previously described as $Bi_{14}Si_2RhI_{12}$.[138] But further investigations suggest that the actual composition is $Bi_{43}Rh_3I_{36}$, which will be used in this work.[139]

with acetone. The surface was characterised on atomic scale via scanning tunnelling microscopy (STM), which is discussed in Section 4.1.1. For Bi_4RhI_2 thin needles of several millimetres in length could be grown. They occur as bundles as shown in Figure 3.3b and tend to fan out on slight mechanical pressure.

3.1.2. Phase Width of $Bi_{14}Rh_3I_9$ and Substitution Experiments

In angle resolved photo-electron spectroscopy (ARPES) and STM experiments the Fermi level was found above the energy gap in agreement with the observed metallic behaviour in the resistivity measurements, while it should reside within the gap according to the calculations (Section 4.2). The first idea was, that this could be a result of a phase width of $Bi_{14}Rh_3I_9$ with respect to the bismuth content. Structurally this could be imagined, as within the iodido-bismuthate layer only every second iodide octahedra is occupied by bismuth (see structure in Section 4.1.1). Therefore, on one hand it was checked whether such a phase width existed and whether a certain composition would lead to insulating crystals with the Fermi level within the energy gap. On the other hand, it was also aimed on curing the problem via substitution of ruthenium for rhodium, as this would also reduce the electron count. A similar substitution of ruthenium with rhodium had been conducted successfully for a similar compound.[140]

Substitution Experiments

For substitution experiments the following nominal compositions were analysed: "$Bi_{14}Rh_{2.97}Ru_{0.03}I_9$", "$Bi_{14}Rh_{2.85}Ru_{0.15}I_9$", "$Bi_{14}Rh_{2.7}Ru_{0.3}I_9$", "$Bi_{14}Rh_{2.25}Ru_{0.75}I_9$" and "$Bi_{14}Rh_{1.5}Ru_{1.5}I_9$". The samples were prepared according to the optimised synthetic protocol given in Section 2.2. PXRD patterns of the final products showed phase mixtures of $Bi_{14}Rh_3I_9$, $Bi_4Ru_{1-x}Rh_xI_2$[140] and bismuth. With increasing ruthenium content the intensities of the PXRD pattern of $Bi_{14}Rh_3I_9$ decreased and almost vanished for the composition "$Bi_{14}Rh_{1.5}Ru_{1.5}I_9$", while pattern intensities for $Bi_4Ru_{1-x}Rh_xI_2$ increased (Figure 3.4a). The composition of crystals of these samples determined via EDX experiments varies almost independently of the nominal composition of the sample (Figure 3.4b). Both experiments suggest that the substitution of rhodium by ruthenium in $Bi_{14}Rh_3I_9$ was not successful, but that the ruthenium is included in Bi_4RuI_2. Within the latter one, ruthenium can actually be substituted with rhodium.[140] The originally reported increasing cell parameters with increasing rhodium content accompanying this substitution (and therefore smaller 2θ values of the reflections in the PXRD pattern) were also observed in the herein presented

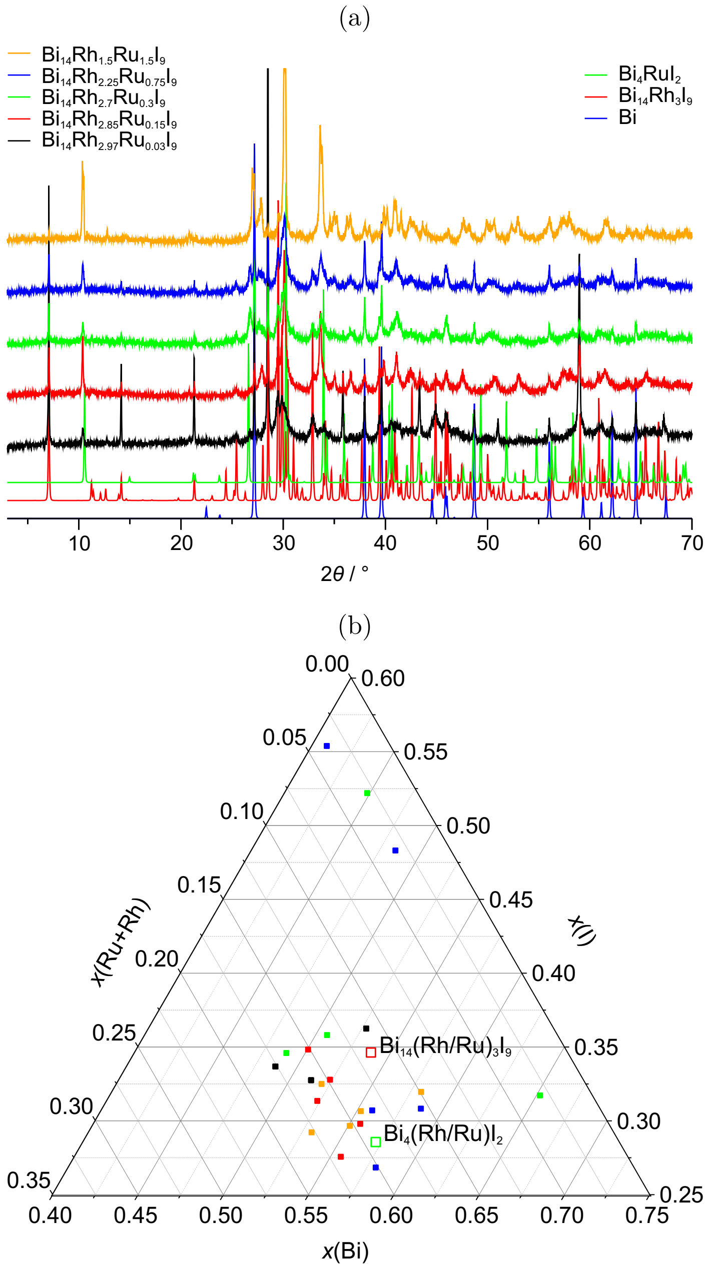

Figure 3.4.: (a) PXRD patterns of the products of the rhodium-ruthenium substitution experiments, for nominal compositions "$Bi_{14}Rh_{2.97}Ru_{0.03}I_9$" (black), "$Bi_{14}Rh_{2.85}Ru_{0.15}I_9$" (red), "$Bi_{14}Rh_{2.7}Ru_{0.3}I_9$" (green), "$Bi_{14}Rh_{2.25}Ru_{0.75}I_9$" (blue) and "$Bi_{14}Rh_{1.5}Ru_{1.5}I_9$" (orange). Reference patterns of $Bi_{14}Rh_3I_9$ (red), Bi_4RuI_2 (green) and Bi (blue) are shown.
(b) Compositions of selected crystals from the samples of the rhodium-ruthenium substitution experiments determined via EDX, for the nominal compositions as given in (a) (same colour code). Theoretical compositions of $Bi_{14}Rh_3I_9$ (red frame) and Bi_4RuI_2 (green frame) are given as references.

experiments (Appendix: Figure A.6). This also explains, why for the composition $Bi_{14}Rh_{1.5}Ru_{1.5}I_9$ reflections of $Bi_{14}Rh_3I_9$ almost vanish. Nevertheless, as EDX results indicate compositions close to the theoretical composition of $Bi_{14}Rh_{3-x}Ru_xI_9$, it is possible that very small amounts of ruthenium are tolerated by $Bi_{14}Rh_3I_9$. This problem could be further elucidated via SCXRD, but no suitable single crystals were found.

Phase Width

To estimate a possible phase width of $Bi_{14}Rh_3I_9$, crystals were grown according to the optimised synthetic protocol in Section 2.2, with four different nominal compositions: "$Bi_{10}Rh_3I_9$", "$Bi_{12}Rh_3I_9$", "$Bi_{14}Rh_3I_9$" and "$Bi_{16}Rh_3I_9$". The respective PXRD patterns (Appendix: Figure A.7) indicate that besides varying amounts of bismuth, $Bi_{14}Rh_3I_9$ was formed as the majority phase. From each sample several crystals were selected and characterised with EDX to determine the composition (Figure 3.5). The results indicate, that no deficiency of bismuth is tolerated by $Bi_{14}Rh_3I_9$, as the compositions of selected crystals taken from the bismuth-poor samples still agree with $Bi_{14}Rh_3I_9$. For the bismuth-rich sample "$Bi_{16}Rh_3I_9$", the result is ambiguous. On one hand, the mean values deviate from the theoretical value of $Bi_{14}Rh_3I_9$ and tend to the composition "$Bi_{16}Rh_3I_9$". On the other hand, the much bigger error bars, especially for the bismuth fraction, might indicate traces of elemental bismuth. This would also agree with the increased reflection intensities of elemental bismuth in the PXRD patterns (Appendix: Figure A.7). Furthermore, the theoretical composition

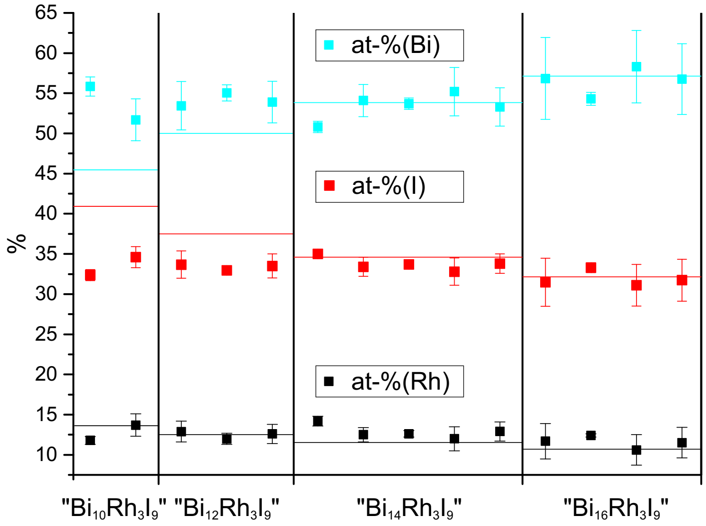

Figure 3.5.: Via EDX measured compositions of crystals from samples with the nominal compositions "$Bi_{10}Rh_3I_9$", "$Bi_{12}Rh_3I_9$", "$Bi_{14}Rh_3I_9$" and "$Bi_{16}Rh_3I_9$". The lines represent the theoretical values.

$Bi_{14}Rh_3I_9$ lies still within the error margin. All in all, a bismuth deficiency can be almost excluded and bismuth excess is unlikely.

Finally, from the analysis of the surface with STM combined with quantum chemical calculations discussed in Section 4.2 another, much more probable interpretation for the observed Fermi level shift was found: It seems as if only the surface is affected by the shift due to the salt-like character in the stacking direction.

3.2. The Bi–Pt–I System

Within this phase system the compound $Bi_{13}Pt_3I_7$ has been known since 1997.[107] Its thermodynamic properties and synthesis was intensively investigated in a Master thesis and a publication[141] and are therefore only briefly presented here.

3.2.1. $Bi_{13}Pt_3I_7$[142]

According to a previous report, annealing of a mixture of Bi, BiI, and PtI_2 (or Bi, Pt and I_2) at 630 K for several weeks is required to obtain $Bi_{13}Pt_3I_7$.[107] By-products such as BiPt, Bi_2Pt and BiI_3 form during the synthesis. Here, the phase formation and decomposition of $Bi_{13}Pt_3I_7$ was investigated by DSC. Upon heating of a stoichiometric

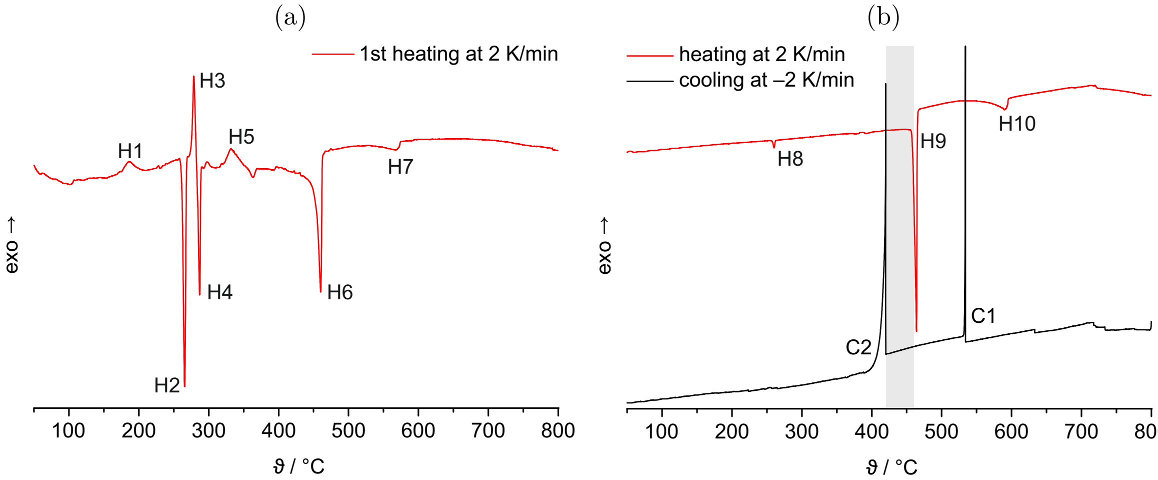

Figure 3.6.: DSC experiments: (a) Heating of a mixture of Bi, BiI_3, and Pt (molar ratio: Bi : Pt : I = 13 : 3 : 7) in a closed system (Signals see Appendix: Table A.3a).
(b) Heating (red) and subsequent cooling (black) of $Bi_{13}Pt_3I_7$, with minor bismuth contaminations in a closed system. **H9** indicates the decomposition of $Bi_{13}Pt_3I_7$. **C2** indicates the crystallisation of $Bi_{13}Pt_3I_7$. The shaded area marks the Ostwald-Miers region (Signals see Appendix: Table A.3b).

mixture of Bi, PtI_2 and BiI_3 (Bi : Pt : I = 13 : 3 : 7) with $2\,K\,min^{-1}$ to 800 °C, several thermal signals are registered (Figure 3.6a). To attribute the signals, mixtures of the starting materials were annealed for 1 h at the respective temperatures and then the sample compositions were identified by PXRD. The exothermic signal at 176 °C (H1) corresponds to the formation of $Bi_{20}Pt_3I_{36}$,[143] while the exothermic signal at 321 °C (H5) indicates the formation of $Bi_{13}Pt_3I_7$, which decomposes at 452 °C (H6). Further exo- or endothermic signals H2, H3, H4, and H7 are associated with the binary system Bi-Pt (Appendix: Table A.3a).

In a further DSC experiment, the peritectic decomposition and formation of $Bi_{13}Pt_3I_7$ was investigated (Figure 3.6b and Appendix: Table A.3b). $Bi_{13}Pt_3I_7$ decomposes according to the following equation:

$$Bi_{13}Pt_3I_7 \rightleftarrows 3Bi_2Pt(hP9) + {}^{14}\!/\!{}_3Bi_{(l)} + {}^{7}\!/\!{}_3BiI_{3\,(l,g)} \qquad \text{at } 459\,°C.$$

Subsequent cooling of the homogeneous melt results in two exothermic signals. The signal at 534 °C (C1) can be attributed to the crystallisation of $Bi_2Pt(hP9)$; the signal at 420 °C (C2) to the recrystallisation of $Bi_{13}Pt_3I_7$.[136] Remarkably, this DSC experiment yields almost phase pure $Bi_{13}Pt_3I_7$ (Appendix: Figure A.8), suggesting a reaction of Bi_2Pt with the remaining melt.

Based on the data above, an optimised temperature program was employed for the synthesis of $Bi_{13}Pt_3I_7$. A mixture of Bi, PtI_2, and BiI_3 according to the composition of the target compound was heated up to 700 °C. The resulting melt was rapidly cooled ($-240\,K\,h^{-1}$) down to 450 °C to obtain only small and highly reactive crystallites of $Bi_2Pt(hP9)$. Subsequently, $Bi_{13}Pt_3I_7$ crystals were grown in the estimated Ostwald-Miers region (420 °C to 459 °C; Figure 3.6b) by slow cooling ($-1\,K\,h^{-1}$) down to 380 °C. After a further six days at this temperature, the furnace was turned off and allowed to cool down to room temperature. The product was single-phase $Bi_{13}Pt_3I_7$ consisting of black platelets of up to $1\,mm^2$ in surface.

3.2.2. $Bi_{38}Pt_9I_{14}$[144]

Starting from a mixture of bismuth, platinum, and BiI_3, we recorded for the nominal composition "Bi_3PtI" an exothermic signal superimposed with endothermic signals that indicate formation reactions (Figure 3.7a). Another sample of the mentioned composition annealed at 290 °C, i.e. above the temperature of the formation reaction, gave unindexed reflections in the PXRD experiment, that could later be assigned to the new ternary phase $Bi_{38}Pt_9I_{14}$. Although only few, very small crystals could

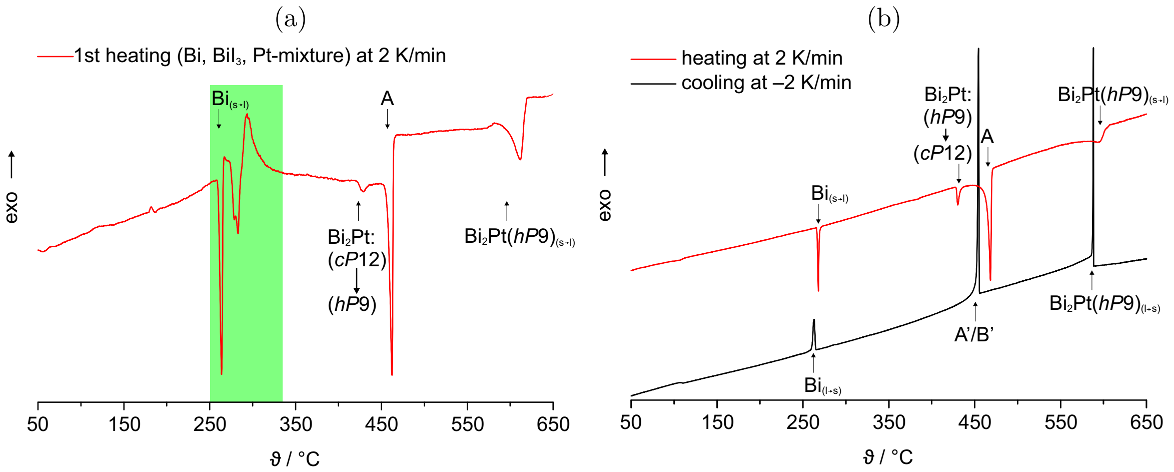

Figure 3.7.: DSC experiments: (a) Heating of a mixture of Bi, BiI$_3$, and Pt in a closed system. The green area indicates the region where formation of the new compound takes place. **A** indicates the decomposition of $Bi_{38}Pt_9I_{14}$.
(b) Heating (red) and subsequent cooling (black) of $Bi_{38}Pt_9I_{14}$, with bismuth and Bi$_2$Pt contaminations in a closed system. **A** indicates the decomposition of $Bi_{38}Pt_9I_{14}$. **A′/B′** indicates the simultaneous crystallisation of $Bi_{38}Pt_9I_{14}$ and $Bi_{13}Pt_3I_7$, as the latter was identified in the final product via PXRD (Figure A.10).

be extracted manually, it was possible to determine the approximate composition by EDX.

Annealing a mixture of bismuth, platinum, and BiI$_3$ with this composition for 1 week at 290 °C yielded $Bi_{38}Pt_9I_{14}$ as the majority phase and bismuth together with Bi$_2$Pt(*cP*12) as minority phases (Appendix: Figure A.9). Using this sample, we determined $Bi_{38}Pt_9I_{14}$ to be stable up to about 465 °C in a closed system (Figure 3.7b). It decomposes peritectically into Bi$_2$Pt(*hP*9), $BiI_{3(l)}$ and liquid bismuth following the equation:

$$Bi_{38}Pt_9I_{14(s)} \rightarrow 9Bi_2Pt_{(s)} + 4\,{}^2\!/_3 BiI_{3(l)} + 15\,{}^1\!/_3 Bi_{(l)} \qquad \text{at } 465\,^\circ\text{C}.$$

This might explain the minority phases in the product. Cooling ($-2\,\text{K}\,\text{min}^{-1}$) the respective homogeneous melt from 650 °C initially led to the crystallisation of Bi$_2$Pt(*hP*9) at approximately 590 °C (depending on the precise Bi:Pt ratio), then the crystallisation of $Bi_{38}Pt_9I_{14}$ at 454 °C and finally the crystallisation of the bismuth eutectic (Figure 3.7b). In the PXRD pattern of the final mixture, besides the expected phases $Bi_{38}Pt_9I_{14}$, Bi$_2$Pt(*cP*12) and bismuth also $Bi_{13}Pt_3I_7$ showed up (Appendix: Figure A.10). $Bi_{13}Pt_3I_7$ itself decomposes at 459 °C into Bi$_2$Pt(*hP*9) and a melt of bismuth and BiI_3.[141, 142] Therefore, the exothermic signal at 454 °C seems to include the crystallisation of $Bi_{38}Pt_9I_{14}$ *and* $Bi_{13}Pt_3I_7$. In general, a strong competition between $Bi_{38}Pt_9I_{14}$ and $Bi_{13}Pt_3I_7$ was observed.

A repetition of the experiment with a cooling rate of $-1\,K\,h^{-1}$ and holding at 290 °C for 5 d yielded mainly crystals of $Bi_{38}Pt_9I_{14}$. All further experiments were performed on these. The composition was confirmed via EDX spectroscopy on several crystals (Appendix: Figure A.11 and Table A.11c). For a SEM picture of such a crystal, see Appendix: Figure A.12.

3.2.3. $Bi_8Pt_5I_3$ and $Bi_{16}Pt_{11}I_6$[145]

Phase formation in the metal-rich part of the ternary system Bi–Pt–I was explored using DSC. Tiny ampoules ($V \approx 0.1\,mL$) with mixtures of bismuth, platinum, and BiI_3 were heated up to 800 °C and cooled down to room temperature with rates of $-2\,K\,min^{-1}$. The procedure was instantly repeated in a second cycle. The typical load was $1000\,mg\,mL^{-1}$.

For a sample with the molar ratio Bi : Pt : I = 3 : 2 : 1 three unidentified endothermic signals at 592 °C, 610 °C and 618 °C emerged in the course of the second heating cycle (Figure 3.8, all assigned signals see Appendix: Table A.4a). The subsequent cooling curve showed no unambiguously related recrystallisation signal

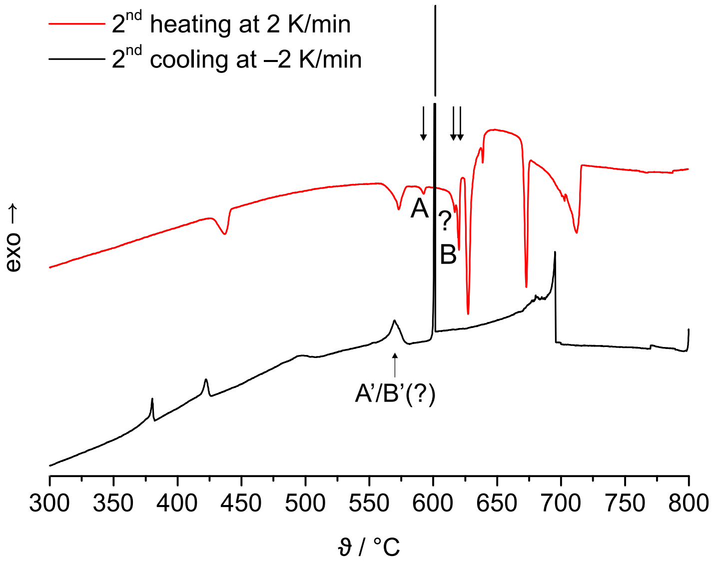

Figure 3.8.: DSC experiment: A pre-reacted mixture of bismuth, platinum and BiI_3 (molar ratio Bi : Pt : I = 3 : 2 : 1) in an closed ampoule loaded with $1000\,mg\,mL^{-1}$. After the first cycle (not shown here), two signals in the course of heating (**A**, **B**) indicate the decomposition of $Bi_{16}Pt_{11}I_6$ and $Bi_8Pt_5I_3$.

with respect to these three signals (Figure 3.8, all assigned signals see Appendix: Table A.4b). This did not change when lowering the cooling rate to $-0.1\,\mathrm{K\,min^{-1}}$. Nevertheless, in the PXRD pattern of the final product unindexed reflections, later assigned to the new phases, were observed (Appendix: Figure A.13). Therefore, at several temperatures (410 °C, 550 °C, 600 °C, 620 °C and 650 °C) powders in the composition Bi : Pt : I = 3 : 2 : 1 were annealed for 3 d, quenched and analysed via PXRD (Appendix: Figure A.14). Two unknown phases, later identified as $\mathrm{Bi_{16}Pt_{11}I_6}$ and $\mathrm{Bi_8Pt_5I_3}$, were found, each synthesised as majority phases. $\mathrm{Bi_{16}Pt_{11}I_6}$ was yielded at 410 °C and $\mathrm{Bi_8Pt_5I_3}$ at all other temperatures except for 650 °C. With the almost phase pure powders of $\mathrm{Bi_{16}Pt_{11}I_6}$ and $\mathrm{Bi_8Pt_5I_3}$ one was able to identify the decomposition temperatures via DSC to be $\vartheta_{Peak} = 587\,°\mathrm{C}$ for $\mathrm{Bi_{16}Pt_{11}I_6}$ and $\vartheta_{Peak} = 619\,°\mathrm{C}$ for $\mathrm{Bi_8Pt_5I_3}$ (Appendix: Figure A.15), which is in good agreement with the originally observed, unknown endothermic effects in the first DSC experiment. Nevertheless, in the case of $\mathrm{Bi_{16}Pt_{11}I_6}$ the temperatures already differ by 5 °C, which hints at a dependency of the decomposition temperature on the load of the ampoules.

For this reason, the synthesis of single crystals was heavily hampered, as in the relevant temperature regime the composition of the condensed phase is changed by considerable evaporation of bismuth iodides.[146] Therefore, samples of the mentioned composition were sealed in ampoules varying the mass to volume ratio. Cooling samples down from 700 °C to room temperature with $-2\,\mathrm{K\,min^{-1}}$ yielded exclusively crystals of $\mathrm{Bi_8Pt_5I_3}$ for a load of $128\,\mathrm{mg\,mL^{-1}}$, whereas samples with 215, 412, and $819\,\mathrm{mg\,mL^{-1}}$ resulted in mixtures with increasing $\mathrm{Bi_{16}Pt_{11}I_{16}}$ content (Appendix: Figure A.17). Starting from $\mathrm{Bi_8Pt_5I_3}$, the influence of the relative load on the compound formation could formally be described by the equation:

$$11\mathrm{Bi_8Pt_5I_{3(s)}} \rightleftarrows 5\mathrm{Bi_{16}Pt_{11}I_{6(s)}} + 7\mathrm{Bi_{(l)}} + \mathrm{BiI_{3(g)}}.$$

The equation says that the higher the mass to volume ratio in the ampoule, i.e. the smaller the relative gas-phase volume, the more the equilibrium shifts to the left site. In fact, we observe the opposite in terms of load and decomposition temperatures. This could be due to the relatively small effect, as both compositions are very close and only 1 mol $\mathrm{BiI_3}$ is formed per 11 mol $\mathrm{Bi_8Pt_5I_3}$. Thus, we propose two other equilibria:

$$\begin{aligned} \mathrm{Bi_{16}Pt_{11}I_{6(s)}} &\rightleftarrows \mathrm{Bi_8Pt_5I_{3(s)}} + 5\mathrm{BiPt_{(s)}} + \mathrm{Bi_2Pt_{(s)}} + \mathrm{BiI_{3(g)}} && \text{at } 587\,°\mathrm{C}; \\ \mathrm{Bi_8Pt_5I_{3(s)}} &\rightleftarrows 3\mathrm{BiPt_{(s)}} + 2\mathrm{Bi_2Pt_{(s)}} + \mathrm{BiI_{3(g)}} && \text{at } 619\,°\mathrm{C}. \end{aligned}$$

In accordance with this sequence, the specific heat of decomposition (from DSC) is

9 J g^{-1} for $Bi_{16}Pt_{11}I_6$ and 10 J g^{-1} for $Bi_8Pt_5I_3$. Nevertheless, the dependency of the phase formation on the partial pressure of BiI_3 could explain, why during the synthesis of powder samples (as described above) $Bi_{16}Pt_{11}I_6$ is formed at lower temperatures (410 °C) than $Bi_8Pt_5I_3$ (550 °C).

Both compounds are stable in air and form black, shiny platelets, which tend to cleave under mechanical sheer forces (see SEM images in the Appendix: Figure A.18). The composition was confirmed via an EDX analysis: EDX($Bi_8Pt_5I_3$): Bi : Pt : I = 51(1) : 31(1) : 17(1) experimental, 50 : 31 : 19 theoretical; EDX($Bi_{16}Pt_{11}I_6$): Bi : Pt : I = 49(1) : 34(1) : 17(1) experimental, 48 : 33 : 18 theoretical.

3.3. Other Bi – *M* – I Systems

3.3.1. The Bi – Ru – I and Bi – Os – I System

The experiments performed on ruthenium or osmium for nominal compositions corresponding to $Bi_{14}M_3I_9$ and $Bi_{13}M_3I_7$ did not yield any ternary or binary phases (osmium) or only the known phase Bi_4RuI_2. The latter already has been mentioned in context with the substitution experiments in Section 3.1.2, while structural details will be discussed in Section 5.2. In general, Bi_4MI_2 seems to be a strong competitor to compounds with the honeycomb layer as structural fragment, as it is also a high-temperature phase in the Bi – Rh – I phase system.

3.3.2. The Bi – Ir – I System

For the Bi – Ir – I system in Figure 3.9a the first and second heating cycle of the corresponding DSC experiment of a mixture of bismuth, BiI_3 and iridium with the overall composition Bi : Ir : I = 14 : 3 : 9 are shown. After the formation reactions in the first cycle an unassigned endothermic signal at 447 °C appeared, which was also observed in the second cycle after cooling down to RT at the rate of -2 K min^{-1}. In the corresponding PXRD pattern (Figure 3.9b) two phases, bismuth and $Bi_{43}Ir_3I_{36}$[2] could be identified, which leaves no further unindexed reflections. $Bi_{43}Ir_3I_{36}$ is already known from the Bi – Rh – I phase system as a competing phase in this composition range. The PXRD pattern agrees well with the two endothermic signals in the second heating cycle of the DSC experiment and yields a decomposition temperature of 447 °C for $Bi_{43}Ir_3I_{36}$. Interestingly, this signal seems to be split, which could mean that there is

---

[2] The phase was previously described as $Bi_{14}Si_2IrI_{12}$.[138] But further investigations suggest that the actual composition is $Bi_{43}Ir_3I_{36}$, which will be used in this work.[139]

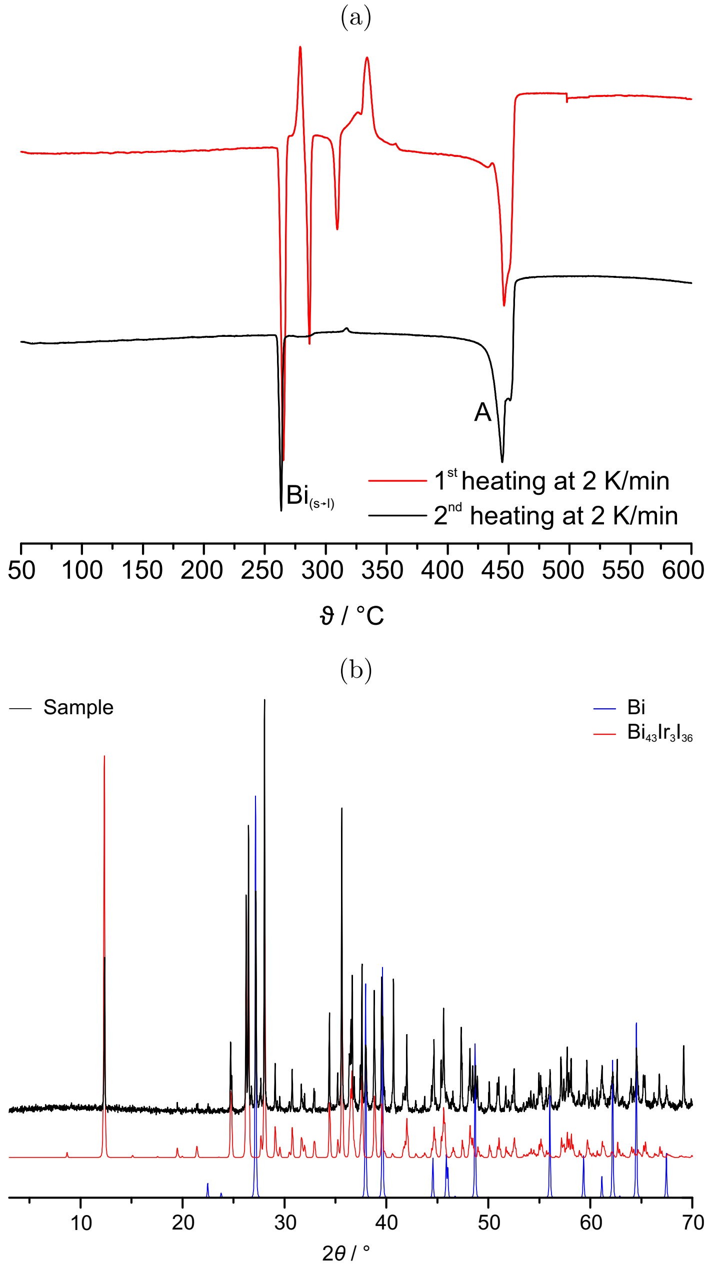

Figure 3.9.: (a) DSC experiment: First and second heating cycle (2 K min^{-1}) of a mixture of Bi, BiI_3, and Ir (molar ratio Bi : Ir : I = 14 : 3 : 9) in a closed system, with **A** indicating the decomposition of $Bi_{43}Ir_3I_{36}$.
(b) PXRD pattern of the product after the DSC experiment (two times heating from RT to 700 °C and cooling back down to RT with 2 K min^{-1} and -2 K min^{-1}, respectively). Elemental bismuth and $Bi_{43}Ir_3I_{36}$ are given as references.

another, very similar phase in the phase system with almost the same decomposition temperature. Nevertheless, no indication of a phase with the honeycomb motive could be found for the Bi–Ir–I phase system.

3.3.3. The Bi–Pd–I System – $Bi_{13}Pd_3I_7$

For the Bi–Pd–I system the DSC experiment with the composition Bi : Pd : I = 13 : 3 : 7 yielded an unassigned signal at 320 °C (Figure 3.10a). The second heating cycle is similar to the first one, with the difference, that the mentioned unknown signal became much less pronounced, even when the cooling rate was reduced from $-2\,\mathrm{K\,min^{-1}}$ to $-0.1\,\mathrm{K\,min^{-1}}$. Nevertheless, in a PXRD of the final product of such a DSC experiment some reflections could not be attributed to any known phase from the Bi–Pd–I system (Appendix: Figure A.19) but could be indexed with the reference pattern of $Bi_{13}Pt_3I_7$. Therefore, we annealed a sample of the composition Bi : Pd : I = 13 : 3 : 7 at 310 °C, directly beneath its assumed decomposition temperature, and yielded almost phase pure $Bi_{13}Pd_3I_7$ according to the PXRD pattern (Appendix: Figure A.20). A DSC experiment of the same powder confirmed the decomposition temperature of 320 °C (Figure 3.10b).

The observed severe kinetic hindrance during the cooling process can be explained by the comparably low decomposition temperature, which is even below the melting point of the BiI_3–Bi eutectic at 350 °C[136] (Figure 3.10b). Therefore, in contrast

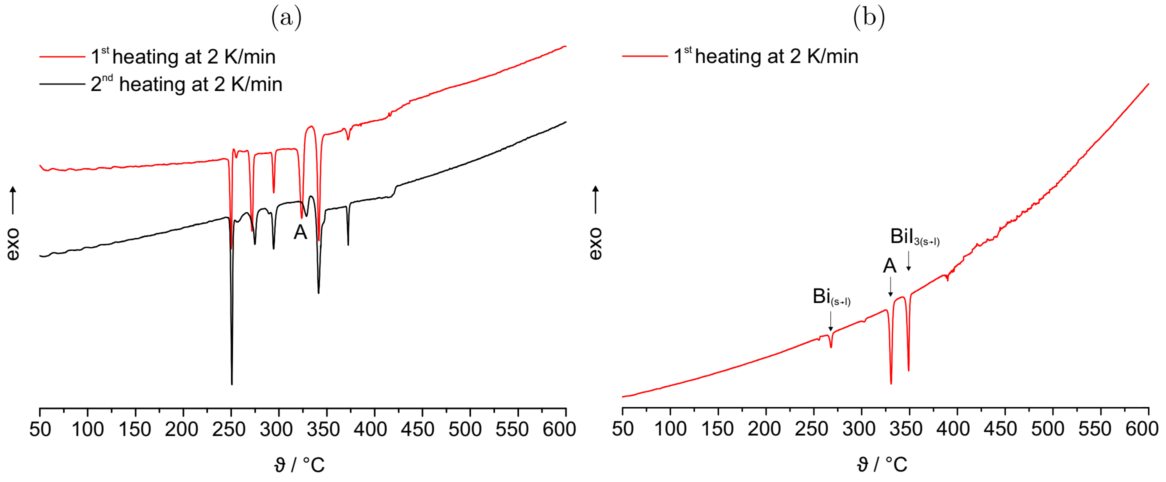

Figure 3.10.: DSC experiment: (a) First and second heating cycle ($2\,\mathrm{K\,min^{-1}}$) of a mixture of Bi, BiI_3, and Pd (molar ratio Bi : Pd : I = 13 : 3 : 7) in a closed system, with **A** indicating the decomposition of $Bi_{13}Pd_3I_7$.
(b) Heating of $Bi_{13}Pd_3I_7$ in a closed ampoule with $2\,\mathrm{K\,min^{-1}}$. **A** indicates the decomposition of $Bi_{13}Pd_3I_7$.

to most of the other ternary phases, $Bi_{13}Pd_3I_7$ cannot crystallise from a BiI_3 melt. That implies a solid-state reaction with long diffusion paths and leads to a very slow crystallisation process. Only after annealing a sample at 310 °C for 3 months, single crystals suitable for single crystal X-ray diffraction could be grown. On such crystals the composition was confirmed via EDX (Appendix: Figure A.21).

4. The Honeycomb Lattice $^{2}_{\infty}[(\mathrm{Bi}_{8/2}M)_3\mathrm{I}]$ – A Heavy Graphene Analogue

This chapter is dedicated to the honeycomb lattice $^{2}_{\infty}[(\mathrm{Bi}_{8/2}M)_3\mathrm{I}]$ and all structures sharing this two-dimensional fragment, with M being an element of the platinum-group. In Section 4.1, the experimentally synthesised structures are presented and compared, with respect to their distances, symmetry, etc., but also with respect to their chemical bonding. In the case of $\mathrm{Bi}_{14}\mathrm{Rh}_3\mathrm{I}_9$ the discussion concentrates on the characterisation of the surface and real-structure effects, i.e. stacking faults, twinning, etc., as this is the key to understand the n-doping seen in ARPES and STM/STS presented in Section 4.2.

Consequently, Section 4.2 concentrates on the topological properties of all introduced compounds and especially on the non-trivial topology of $\mathrm{Bi}_{14}\mathrm{Rh}_3\mathrm{I}_9$. Besides various experiments, such as ARPES, STM/STS and resistivity measurements, a theoretical framework connecting the different synthesised materials is introduced. This finally helps to give strong evidence for $\mathrm{Bi}_{14}\mathrm{Rh}_3\mathrm{I}_9$ having a topologically non-trivial electronic band structure and to rationalise the differences to the other, topologically trivial structures. Thereby, the phrase “heavy graphene analogue” is justified, which links the honeycomb network to graphene, the first TI ever put forward by theoreticians.[39] In addition, further physical properties are analysed and compared with the results of quantum-chemical calculations. Thereby, hints for an unusual superconductivity in the topologically trivial semimetals $\mathrm{Bi}_{13}\mathrm{Pt}_3\mathrm{I}_7$ and $\mathrm{Bi}_{13}\mathrm{Pd}_3\mathrm{I}_7$ are found.

4.1. Structure Chemistry

Within the two-dimensional network $^{2}_{\infty}[(\mathrm{Bi}_{8/2}M)_3\mathrm{I}]$ platinum-metal (M) centred bismuth-cubes are connected via their edges to form a honeycomb-like, or with respect to the platinum-metal Kagome-like, arrangement. Thereby, trigonal- and hexagonal-

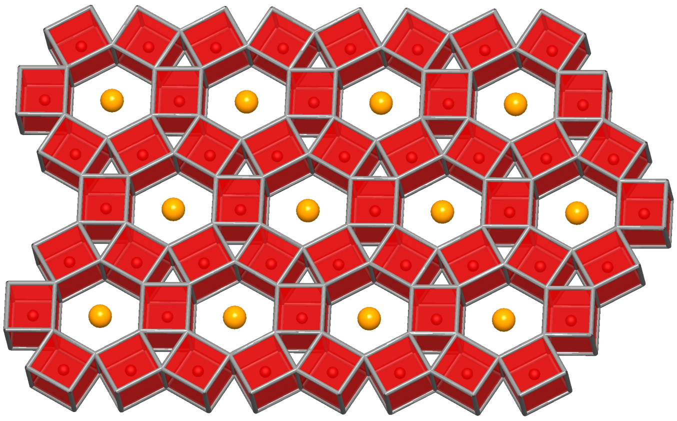

Figure 4.1.: The honeycomb layer $^{2}_{\infty}[(\mathrm{Bi}_{8/2}M)_3\mathrm{I}]$. Every corner of a M-centred cube (red) is occupied by a bismuth atom. The hexagonal-prismatic voids are filled with iodide ions (orange).

prismatic voids are emerging, of which the latter are occupied by iodide ions (Figure 4.1). To emphasise the structural similarity to graphene, which plays an important role from perspective of physical properties (Section 4.2), this fragment will be called honeycomb network or honeycomb layer. As is presented in this section, the honeycomb network occurs stacked, separated differently by two types of "spacer layers", depending on the material. Hand in hand goes a varying charge and number of valence electrons available within this structural motive.

In the first part of this section, newly discovered compounds, or compounds with improved single crystal data, will be presented and their structure discussed explicitly. In the second part, Section 4.1.4, all known structures with the mentioned honeycomb network $^{2}_{\infty}[(\mathrm{Bi}_{8/2}M)_3\mathrm{I}]$ will be compared with respect to their structural differences, e.g. distances and symmetry.

4.1.1. $\mathrm{Bi}_{14}\mathrm{Rh}_3\mathrm{I}_9$[134, 147]

Within $\mathrm{Bi}_{14}\mathrm{Rh}_3\mathrm{I}_9$ the honeycomb like layers, with rhodium in the centres of the bismuth-cubes, are separated by iodido-bismuthate(III) layers. These consist of $[\mathrm{BiI}_2\mathrm{I}_{4/2}]^-$ octahedra that share edges to form zigzag chains $^{2}_{\infty}[\mathrm{BiI}_4]^-$, which run along the b-axis (Figure 4.2). Consequently, the honeycomb network has a charge of +2 per formula unit: $[(\mathrm{Bi}_4\mathrm{Rh})_3\mathrm{I}]^{2+}$. An extensive discussion of the crystal structure and the pseudo-symmetry of the two layer types can be found in references 126, 134, 141. In this section the focus is on the surface structure and the real-structure effects of $\mathrm{Bi}_{14}\mathrm{Rh}_3\mathrm{I}_9$ crystals.

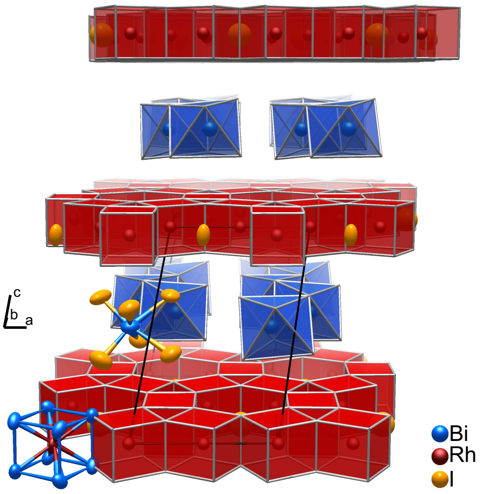

Figure 4.2.: Triclinic crystal structure of $Bi_{14}Rh_3I_9$. Insulating iodido-bismuthate layers of $[Bi_2I_8]^{2-}$ zigzag chains (blue) separate the intermetallic honeycomb layers $[(Bi_4Rh)_3I]^{2+}$ that consist of hexagonal nets of edge-sharing $Bi_{8/2}Rh$ cubes with iodide ions in its hexagonal voids.

The $Bi_{14}Rh_3I_9$ crystals cleave very easily parallel to the (0 0 1) plane and smooth surfaces, although not on an atomic scale, can be prepared using a sticky tape. STM on such a cleaved surface of $Bi_{14}Rh_3I_9$ identifies the iodido-bismuthate layer and the honeycomb layer by their different atomic scale structures and their corresponding different step heights (Figure 4.3). The regular honeycombs (Figure 4.3b) belong to the honeycomb layer with the atomic structure in agreement with the one deduced from X-ray diffraction. The hexagonally arranged spots (Figure 4.3c) fit to the iodide ions of the iodido-bismuthate layer, although the observed voids hint to a certain reconstruction, namely desorption of iodine. Combining the STM step height of both layers (1.2 nm) provides a good agreement with the respective layer thickness deduced from the unit cell as shown in Figure 4.2 (1.25 nm).

Revisiting the issue of an *n*-doping as observed by ARPES and STS (Section 4.2), the analysis of the surface provides valuable answers. As discussed in Section 3.1.2 no phase width of $Bi_{14}Rh_3I_9$ could be verified. In general, a stack of alternately charged ionic layers should undergo certain changes at the surface in order to compensate for the missing counter charge of the absent layer.

Therefore, the observed *n*-doping as well as the mentioned iodine deficiency at the surface of the iodido-bismuthate layer can be rationalised by retracing the mechanical cleavage process of the layered $Bi_{14}Rh_3I_9$ crystal. The STM investigations of surfaces generated by cleavage under ultra-high vacuum (UHV) conditions show that the honeycomb layer $[(Bi_4Rh)_3I]^{2+}$ typically remains undamaged (Figure 4.3b)

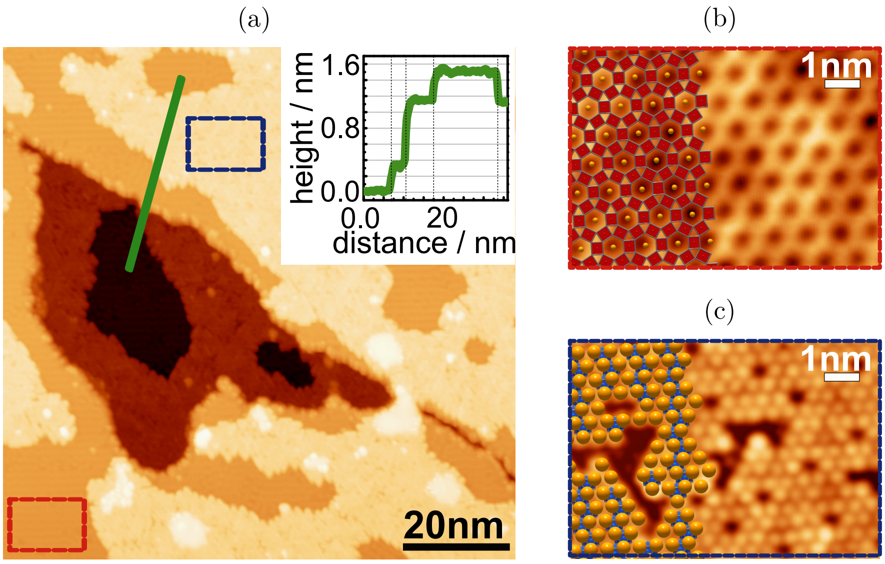

Figure 4.3.: (a) STM image of cleaved $Bi_{14}Rh_3I_9$ ($U = 1\,V$, $I = 100\,pA$). Inset: height profile along the green line.
(b) and (c) Zoomed-in view of the red (b) and blue (c) dashed boxes in (a) showing the intermetallic honeycomb layer and the iodido-bismuthate layer, respectively. The atomic model structure is overlaid (colour-coded as in Figure 4.2). In (c): $U = 1.5\,V$, $I = 100\,pA$, and in (d) $U = -1.3\,V$, $I = 100\,pA$.

while the iodido-bismuthate spacer $[Bi_2I_8]^{2-}$ is fragmented (Figure 4.3c). Presuming that the two crystal fragments bear no net charge, two borderline scenarios have to be considered.

In the case of homogeneous splitting, the spacer is bisected and two $[BiI_4]^{-}$ surfaces are generated (Scheme 1a). Here, as the electron count is not altered, electronically nothing should change, or, in other words, the Fermi level is expected to stay in the topologically non-trivial energy gap (details on the electronic structure in Section 4.2.1, Figure 4.12). Unfortunately, this variant is unlikely due to the bonding strength within the spacer layer and does not match our observations.

Alternatively, the crystal cleaves between the honeycomb layer and the spacer, which then form the new surfaces of the two fragments (heterogeneous splitting: Scheme 1b). According to our assumption of splitting into uncharged fragments, the terminating honeycomb layer will have the nominal charge of +1 instead of +2 per formula unit due to the missing anionic spacer layer on top (chemically reduced, *n*-doped surface). The additional electron is accommodated by shifting the Fermi level into the conduction band, in this way rendering the surface metallic (details on the electronic structure in Section 4.2.1, Figure 4.12).

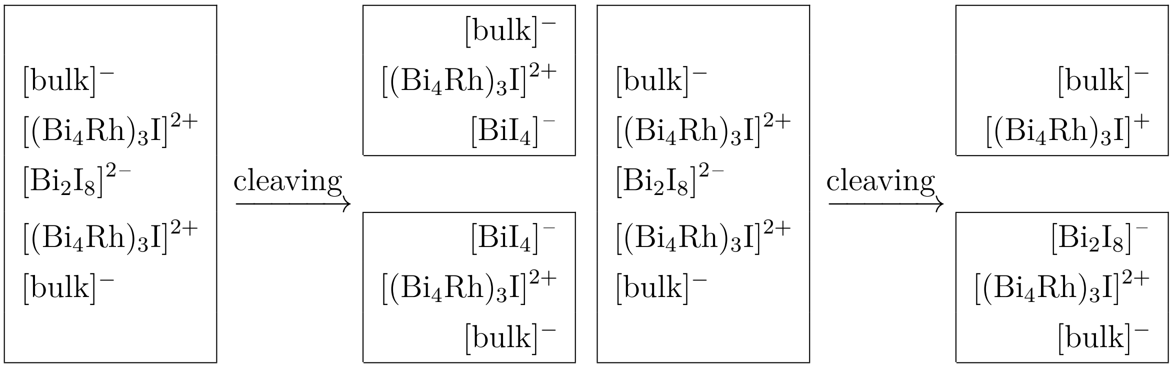

(a) homogeneous splitting (b) heterogeneous splitting

Scheme 1: Two splitting scenarios for $\mathrm{Bi_{14}Rh_3I_9}$.

The terminating spacer of the other fragment necessarily has one electron less than needed. Such an oxidised (*p*-doped) $[\mathrm{Bi_2I_8}]^-$ layer is chemically unstable and decomposes, such that nominally favourable Bi^{3+} and I^- configurations are realised:

$$[\mathrm{Bi_2I_8}]^- \rightarrow [\mathrm{Bi_2I_7}]^- + {}^{1}\!/_{2}\mathrm{I_2}.$$

Assuming, that only the top iodine layer of the surface iodido-bismuthate layer desorbs iodine, the iodine deficiency in that layer would nominally amount to a maximum of 25 %, if only heterogeneous splitting takes place. Desorption of molecular iodine is supported by the UHV conditions under which the cleavage was performed. After this chemical (redox) reaction, which removes the *p*-doping of the terminating layer, the Fermi level is situated in the band gap for this part of the surface.

Experimentally, the iodine deficiency in those areas of the new surface that are terminated by the surface spacer layer has been determined by simply counting the missing atoms in STM images. Therefore, the atomic model structure of a perfect spacer lattice was overlaid. The deficiency of iodine atoms was found to be on average 19(3) %. However, one has to keep in mind that one can only count missing iodine atoms in the interior area of the spacer layer, while iodine atoms desorbed from an edge cannot be distinguished from the edge itself. Thus, the measured deficiency is well in line with the scenario of charge compensation by 25 % iodine desorption. Alternatively, the edge of the spacer layer surface can be interpreted as a homogeneous splitting scenario, such that iodine desorption takes only place in the interior area of the spacer.

The actual cleaving process leads to a fragmented surface with alternating areas of honeycomb layer and spacer layer at the surface (Figure 4.3a) and therefore to a

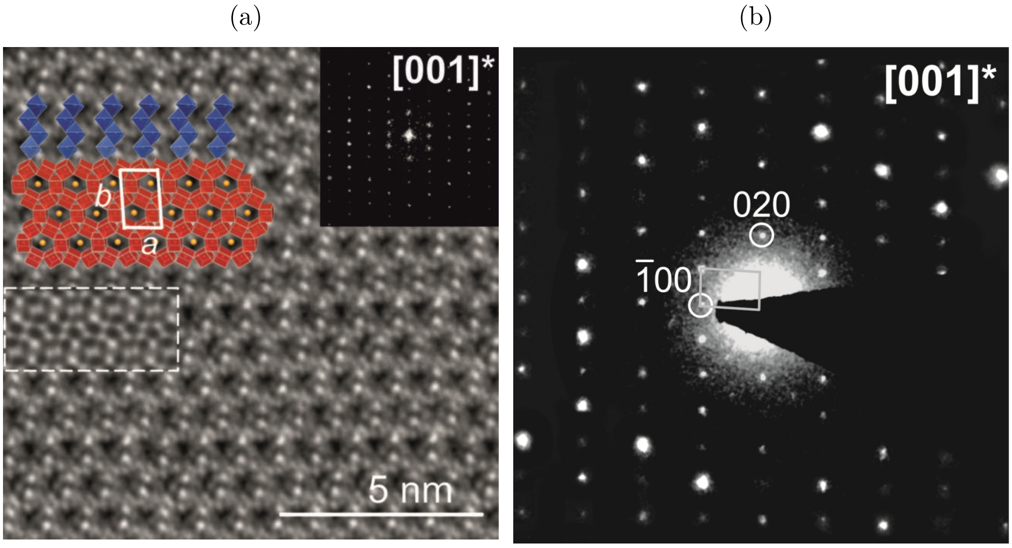

Figure 4.4.: (a) A HRTEM image of the $[0\,0\,1]^*$ zone with an inserted Fourier transform, simulated HRTEM (d = 8 nm, t = 10 nm), and an overlay with a single honeycomb layer and a single layer of iodido-bismuthate chains. The bright spots correspond to iodine atoms, and grey regions correspond to bismuth and rhodium atoms, while the black spots represent cavities, according to simulations.
(b) An experimental electron diffraction pattern of the $[0\,0\,1]^*$ zone. The unit cell is outlined by a solid white line.

cleaving scenario, which is in between the two introduced extreme. Nevertheless, only the p-doping of the spacer layer at the surface can be resolved by iodine desorption, while the n-doping of the honeycomb layer at the surface remains. Therefore, any surface will remain n-doped.

It seems very probable, that the resulting shift of the Fermi level for the honeycomb layer is the explanation concerning the observed n-doping in ARPES and STS as well as the metallic resistivity for $Bi_{14}Rh_3I_9$.

To analyse real-structure effects in the bulk, HRTEM was employed. The SAED pattern of the $[0\,0\,1]^*$ zone is in accordance with the triclinic unit cell (Figure 4.4b). The HRTEM image of the $[0\,0\,1]^*$ zone shows perfect ordering in the layer plane. It exhibits a predominantly hexagonal pattern with reduced symmetry, created by the inclined stack of honeycomb layers and the overlying iodido-bismuthate chains (Figure 4.4a). The observed atomic ordering fully corresponds to the crystal structure model derived from the X-ray diffraction experiment.

As dictated by the six-fold symmetry, a honeycomb layer offers multiple equal placements for the adjacent iodido-bismuthate layer including rotations in multiples

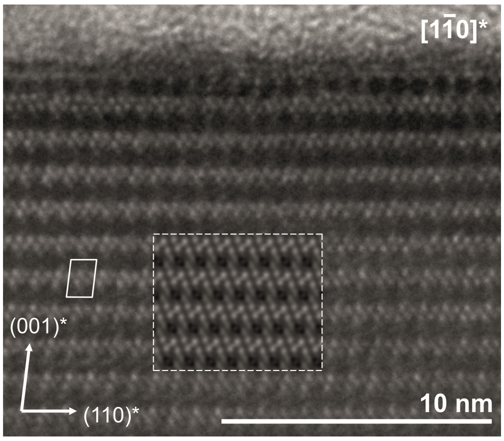

Figure 4.5.: A HRTEM image of the $[1\,\bar{1}\,0]^*$ zone with an inserted simulated HRTEM ($d = 20\,\mathrm{nm}$, $t = 5\,\mathrm{nm}$). The bright spots correspond to iodine atoms, grey regions correspond to bismuth and rhodium atoms, while the black spots represent cavities, according to simulations. The unit cell is outlined by a solid white line.

of 60° around the normal of the honeycomb layer, i.e. c^*. Fortunately, the propagation of the iodido-bismuthate chains can be easily imaged by HRTEM since they contribute prominently to the image contrast in broad ranges of thicknesses and defoci values. Both the X-ray and the TEM investigations confirm that all iodido-bismuthate chains run in parallel along the b-axis. This can be seen for example in the HRTEM image of the $[1\,\bar{1}\,0]^*$ zone, which also demonstrates a high degree of ordering at the unit-cell level (Figure 4.5). Parallel orientation of the chains can be associated with the slight deviation of the honeycomb layer from hexagonal metrics (Section 4.1.4). In the underlying case this is apparently sufficient to ensure transmission of the information on chain alignment in the course of crystal growth.

The twofold axes, present in the layer groups of both fragments, trigger the formation of polysynthetically twinned crystals (T1 and T2, Figure 4.6c). Thereby, the inclination of the stacking vector changes in neighbouring domains as has been observed in the X-ray diffraction and the TEM experiments (Figure 4.6a and Appendix: Figure A.22). Furthermore, deviations from the regular stacking occur if a honeycomb layer is shifted by $b/2$. This can easily happen, since the translation period of the iodido-bismuthate chains is only half of the one of the honeycomb layer. According to the C-centring of the ortho-hexagonal setting (centring vector $a/2 + b/2$), this shift is equivalent to $a/2$. Such shifts create anti-phase boundaries (A, Figure 4.6c), as seen in the HRTEM images (Figure 4.6b and Appendix: Figure A.22). With reference to a possible coupling between the topologically non-trivial honeycomb layers, it is noteworthy that at the domain boundaries of both observed defect types the rela-

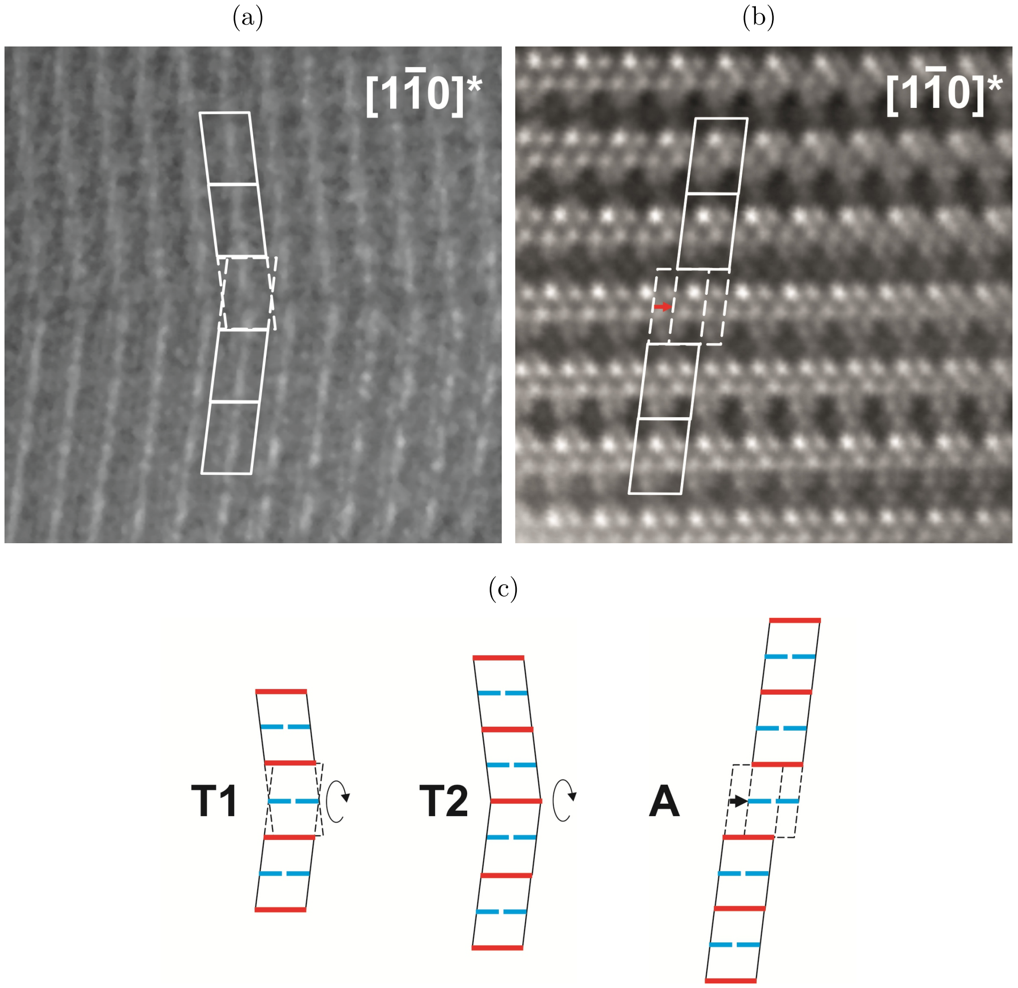
(a) (b) (c)

Figure 4.6.: (a) A twin domain and (b) an anti-phase domain observed in the HRTEM image of the $[1\,\bar{1}\,0]^*$-zone. Solid white lines show a row of adjacent unit cells, and dashed lines indicate the hypothetical regular stacking at the domain boundary. The twin boundary appears to lie in an iodido-bismuthate layer. For a twin boundary in the honeycomb layer see appendix: Figure A.22.
(c) Sketch of twin domain boundaries at either an iodido-bismuthate layer (T1) or a honeycomb layer (T2) as well as of an anti-phase boundary (A). Propagation of the iodido-bismuthate layer and the honeycomb layer is indicated by blue and red lines, respectively.

tive position of subsequent honeycomb layers is equivalent to the situation inside the domains.

In crystals with a high density of such stacking faults, twin and/or anti-phase boundaries, the ordered domains are small and diffuse scattering in the rows of reflections parallel to c^* (Appendix: Figure A.23) jeopardizes the crystal structure determination. So far it had been possible to produce crystals with less diffuse scattering, nevertheless, tending to be twinned and feign a monoclinic cell with $a = 1588\,\mathrm{pm}$, $b = 914\,\mathrm{pm}$, $c = 1284\,\mathrm{pm}$, and $\beta = 102.4°$ ($\alpha \approx \gamma \approx 90.0(4)°$). Therefore, in the original structure solution, the crystal was described as a twin with a mirror plane perpendicular to a being the twin element.[126, 141]

Thanks to the optimised crystal growth parameters as described in Section 2.2 it was possible to grow single crystals with (almost) no defects according to the single crystal X-ray diffraction experiment (Appendix: Tables A.4 to A.10). The original structure was confirmed and it can be shown, that no phase transition occurs down to 150 K. The thermal expansion parameters were determined to be ${}^{\Delta a}/_{(a\Delta T)} = 3.8 \times 10^{-5}\,\mathrm{K}^{-1}$, ${}^{\Delta b}/_{(b\Delta T)} = 3.7 \times 10^{-5}\,\mathrm{K}^{-1}$ and ${}^{\Delta c}/_{(c\Delta T)} = 4.5 \times 10^{-5}\,\mathrm{K}^{-1}$. The thermal expansion in a and b direction only differs by 4 %, meaning that the influence of the iodido-bismuthate chains running along the b-axis is only minor and the thermal expansion is dictated by the honeycomb network. The much stronger thermal expansion in c direction (17 % stronger than in the a and 22 % stronger than in the b direction) is expected for such a layered compound. Nevertheless, it should be considered when discussing the effect of weak coupling between two adjacent honeycomb networks, that the distances become smaller by reducing the temperature.

4.1.2. $Bi_{38}Pt_9I_{14}$[144]

SCXRD experiments revealed that $Bi_{38}Pt_9I_{14}$ crystallises in the hexagonal space group $P6/mmm$ (No. 191) with $a = 922.50(2)\,\mathrm{pm}$ and $c = 2671.09(7)\,\mathrm{pm}$ at RT and $a = 919.15(3)\,\mathrm{pm}$ and $c = 2661.79(9)\,\mathrm{pm}$ at 120 K (Appendix: Tables A.11 to A.17). The dominating structural motive in the layered structure of $Bi_{38}Pt_9I_{14}$ (Figure 4.7a) is the honeycomb layer ${}^{2}_{\infty}[(\mathrm{Bi}_{8/2}\mathrm{Pt})_3\mathrm{I}]^{+3}$. It is isomorph to the honeycomb network in $Bi_{14}Rh_3I_9$, but with a platinum instead of rhodium and a different charge. I consists of platinum-centred bismuth cubes (Pt–Bi, 288.7 pm to 289.1 pm) that again share edges (Figure 4.7b). The honeycomb network has a height of 332.8 pm (defined by the Bi–Bi distance along [0 0 1]). Within the trigonal- and hexagonal-prismatic voids of this network, Bi–Bi distances are 320.0 and 347.9 pm, respectively.

The honeycomb layers stack primitively, i.e. with the same position in the (0 0 1)

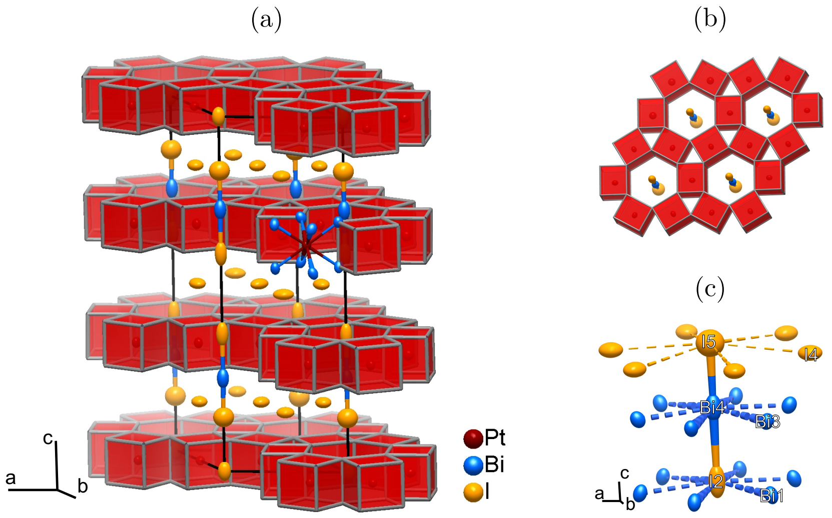

Figure 4.7.: Crystal structure of $Bi_{38}Pt_9I_{14}$. The platinum-centred bismuth cubes are coloured red. (a) Shows the whole unit cell, (b) a detailed view of the hexagonal channels hosting the $[BiI_2]^-$ anions and (c) the $[BiI_2]^-$ anion with its surroundings.

plane, and are separated by single layers of iodide ions (I–Bi, 363.6 pm to 367.2 pm). As a consequence of the eclipsed arrangement of the honeycomb layers, their hexagonal voids form channels along stacking direction [0 0 1]. These are filled with a linear sequence of iodide and double the number of $[BiI_2]^-$ anions (Bi–I, 293.1 and 333.7 pm), creating a three-fold superstructure in [0 0 1]. A refinement of the occupancies of the channel atoms resulted in almost the same figures of merit ($R_1(all) = 3.12$; $wR_2(all) = 3.23$; goodness of fit on $F^2 = 1.129$) and only marginal deviations from the nominal occupancies, with atom I2 (Figure 4.7c) showing the largest deviation (occupancy of 0.98). The chemical compositions obtained from single-crystal structure refinement as well as from EDX measurements strongly support the formula $Bi_{38}Pt_9I_{14}$.

In the diffraction pattern, the superstructure reflections are weak because only a small fraction of the total electron density contributes to them. They also fade rapidly with increasing diffraction angles, indicating some long-range disorder, probably between the channels. HAADF-STEM confirms the regular tripling of the unit cell and does not indicate any stacking faults (Figure 4.8). As in an HAADF-STEM image the intensities vary monotonously with atomic number, the difference in the occupation within the iodide layers due to the superstructure can be visualised. Every third (dark) line along the stacking direction belonging to an iodide layer becomes even darker, as it has only three instead of four iodide ions per unit cell.

The ellipsoids representing the anisotropic displacement parameters of the channel

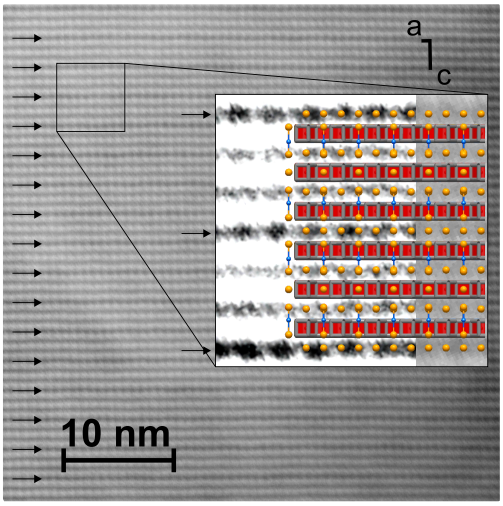

Figure 4.8.: HAADF-STEM image of the [0 1 0]* zone of $Bi_{38}Pt_9I_{14}$. Image grey shades vary monotonously with atomic number; therefore, the brighter lines belong to the honeycomb layer and the darker lines to the iodide layer. Of the latter, every third is even darker (indicated by arrows), belonging to the less occupied iodide layer of the superstructure induced by the channel occupation. The inset shows improved contrast in an overlay with the structure model.

atoms are elongated along [0 0 1] with the exception of I5. I5 is at the level of the iodide layer separating the honeycomb networks and thus also has an increased number of lateral vibrations. The linear extrapolation of all principal mean square atomic displacements to 0 K shows no remarkable differences between channel atoms and the rest of the structure (Table A.18). Hence, the elongation along [0 0 1] seems to be no artefact of positional disorder but is mainly caused by thermal vibrations. The thermal expansion coefficients are $^{\Delta a}/_{(a\Delta T)} = 2.1 \times 10^{-5}\,\mathrm{K}^{-1}$ and $^{\Delta c}/_{(c\Delta T)} = 2.0 \times 10^{-5}\,\mathrm{K}^{-1}$ and therefore almost the same, which is unusual for a layered material.

A hitherto unknown and striking structural fragment is the linear $[BiI_2]^-$ ion. The Bi−I distances are 334 and 293 pm. The latter is shorter than in BiI_3 (305.4 and 312.5 pm) and among the shortest reported.[148–150] This unusual diiodidobismuthate(I) anion seems to profit from its environment in the hexagonal channels. The bismuth(I) atom and the more remote iodide ion are close to the centres of the bismuth hexagons of the honeycomb layer (Bi$\cdots$Bi, 345.6 pm; I$\cdots$Bi, 351.3 pm), while the closer iodide ion of the dumbbell is surrounded by iodide ions separating the honeycomb layers (I$\cdots$I, 407.0 pm) and therefore not very much supported by its environment. Evidence for the charge of −1 for this three-atom anion, and consequently the bismuth +I oxidation state, will be provided in Section 4.2.5 by quantum-chemical calculations in comparison to physical experiments. Thereby, also the structured formula $[(\mathrm{Bi}_{8/2}\mathrm{Pt}^{4/3+})_3]_3[(\mathrm{I}^-)_3]_3[\mathrm{BiI_2}^-]_2[\mathrm{I}^-]$ is justified.

4.1.3. $Bi_{13}Pt_3I_7$ and $Bi_{13}Pd_3I_7$

Both structures are very similar and will therefore be discussed together, although they are not isotypic. In $Bi_{13}Pt_3I_7$ and $Bi_{13}Pd_3I_7$ (Figure 4.9) the bismuth cubes in the honeycomb layer are platinum or palladium-centred, respectively: ${}^2_\infty[(\mathrm{Bi}_{8/2}(\mathrm{Pt/Pd})_3\mathrm{I}]^{+3}$ (d(Pt−Bi) = 284.8 pm to 292.1 pm and d(Pd−Bi) = 284.9 pm to 291.7 pm). The height of the honeycomb network is 335.1(1) pm or 330.4(1) pm for the platinum or palladium compound, respectively (defined by the Bi−Bi distance along [0 0 1]). Within the trigonal- and hexagonal-prismatic voids of this network, Bi−Bi distances are 318.6(1) and 342.3(1) pm ($Bi_{13}Pt_3I_7$) or 320.5(1) and 343.3(1) pm ($Bi_{13}Pd_3I_7$), respectively. The honeycomb layers are alternately separated by an iodido-bismuthate layer (as in $Bi_{14}Rh_3I_9$) and an iodide layer (as in $Bi_{38}Pt_9I_{14}$), which yields alternately long and short distances, respectively between adjacent honeycomb layers (Figure 4.9). In $Bi_{13}Pt_3I_7$ the honeycomb layers are separated by 929(2) pm and 533(3) pm and in $Bi_{13}Pd_3I_7$ by 930(2) pm and 534(4) pm, respectively.

As recently reported $Bi_{13}Pt_3I_7$ crystallises in space group $P\bar{1}$ (No. 2), with

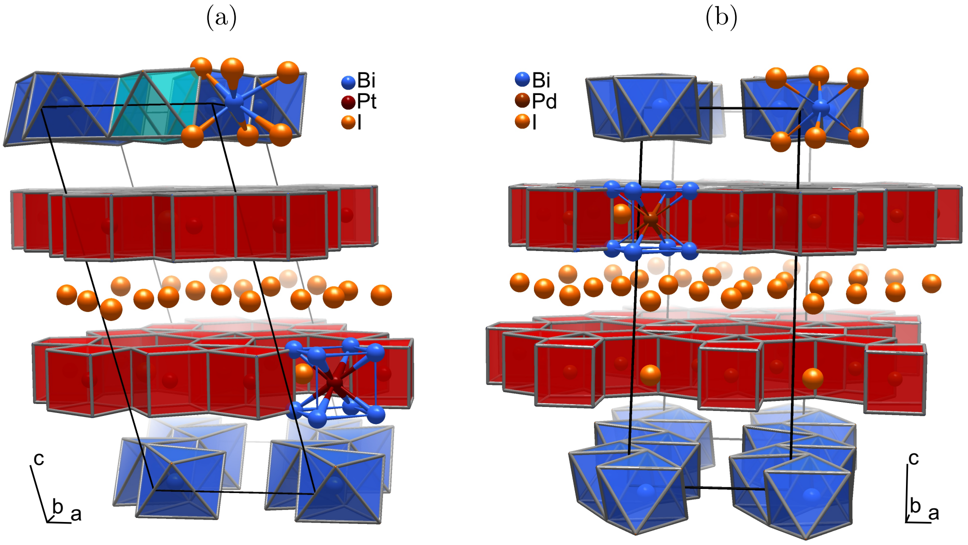

Figure 4.9.: Crystal structure of (a) $Bi_{13}Pt_3I_7$ and (b) $Bi_{13}Pd_3I_7$. The M-centred bismuth cubes are coloured in red. The bismuth-centred iodide octahedra are coloured in blue. The (empty) cyan coloured ocatahedra in the $Bi_{13}Pt_3I_7$ structure would be occupied in the $Bi_{13}Pd_3I_7$ structure. The unit cells of the ordered structures are outlined by black lines.

$a = 911.51(3)\,\mathrm{pm}$, $b = 1578.26(5)\,\mathrm{pm}$, $c = 2243.01(7)\,\mathrm{pm}$, $\alpha = 103.649(1)°$, $\beta = 101.620(1)°$, $\gamma = 90.091(1)°$ at RT.[142] Complementing these results, new single crystal data at 150 K have been acquired (details Appendix: Table A.19 to A.22), which makes it possible to deduce the thermal expansion parameters ${}^{\Delta a}/_{(a\Delta T)} = 2.5 \times 10^{-5}\,\mathrm{K}^{-1}$, ${}^{\Delta b}/_{(b\Delta T)} = 2.3 \times 10^{-5}\,\mathrm{K}^{-1}$ and ${}^{\Delta c}/_{(c\Delta T)} = 2.3 \times 10^{-5}\,\mathrm{K}^{-1}$. The structure suffers from severe stacking faults, which for certain crystals makes it impossible to resolve the iodido-bismuthate strands. In such cases, all iodide octahedra of this layer appear as partially occupied. The resulting smaller unit cell ($a = 911.9\,\mathrm{pm}$, $b = 912.6\,\mathrm{pm}$, $c = 2149.6\,\mathrm{pm}$, $\alpha = 89.969°$, $\beta = 83.955°$, $\gamma = 60.087°$) is the one that was published when the structure was first discovered.[107]

$Bi_{13}Pd_3I_7$ crystallises in the same triclinic space group $P\bar{1}$ (No. 2), with $a = 914.68(6)\,\mathrm{pm}$, $b = 1585.30(11)\,\mathrm{pm}$, $c = 2189.85(15)\,\mathrm{pm}$, $\alpha = 76.009(4)°$, $\beta = 89.828(4)°$, $\gamma = 90.085(4)°$ at RT. Unfortunately, as already in the case of $Bi_{14}Rh_3I_9$ (Section 4.1.1) and $Bi_{13}Pt_3I_7$, the crystals tend to suffer from stacking faults, namely anti-phase boundaries, which occur within the iodido-bismuthate layer and manifest themselves in disorder within these layers. By optimising the synthesis with the help of DSC experiments (Section 3.3), this problem could not be solved, while in case of the rhodium and the platinum compound it was possible to get well ordered crystals (Section 4.1.1, above and reference 142). This might be attributed to the fact, that $Bi_{13}Pd_3I_7$ has a decomposition temperature even below the melting point of BiI_3. Therefore, at RT the palladium structure was actually solved in a smaller triclinic cell ($a = 914.68(6)\,\mathrm{pm}$, $b = 914.54(5)\,\mathrm{pm}$, $c = 2187.81(16)\,\mathrm{pm}$, $\alpha = 78.067(5)°$, $\beta = 78.141(5)°$, $\gamma = 60.080(5)°$) with a 50 % occupation for all bismuth positions within the iodido-bismuthate layer (Appendix: Tables A.23 to A.26). Nevertheless, weak superstructure reflections indicate at least partial ordering and the mentioned bigger unit cell. Therefore, the case of $Bi_{13}Pd_3I_7$ is similar to the situation for $Bi_{13}Pt_3I_7$ when it was first discovered.

Only the data at 120 K were sufficient to solve and refine the structure in the bigger cell with the (partial) ordering, although still with a high R_σ value of 0.10 ($a = 910.73(8)\,\mathrm{pm}$, $b = 1577.50(13)\,\mathrm{pm}$, $c = 2182.61(18)\,\mathrm{pm}$, $\alpha = 76.035(5)°$, $\beta = 89.909(5)°$, $\gamma = 90.105(5)°$ at 120 K; Appendix: Tables A.23 and A.27 to A.29). Considering the occupation of the bismuth positions in the iodido-bismuthate layer (Bi25, Bi26, Bi27 and Bi28) as an indicator for the extent of order concerning the stacking sequence, one can estimate 90 % to be ordered. Due to the low intensity to noise (${}^{I}/_{\sigma}$) ratio for the data, the displacement parameters for Bi25 and Bi27 as well as Bi26 and Bi28 had to be set as equal. The thermal expansion coefficients are ${}^{\Delta a}/_{(a\Delta T)} = 2.5 \times 10^{-5}\,\mathrm{K}^{-1}$, ${}^{\Delta b}/_{(b\Delta T)} = 2.8 \times 10^{-5}\,\mathrm{K}^{-1}$ and ${}^{\Delta c}/_{(c\Delta T)} = 1.9 \times 10^{-5}\,\mathrm{K}^{-1}$.

That $Bi_{13}Pt_3I_7$ and $Bi_{13}Pd_3I_7$ are only similar and not isotypic can be attributed to a slightly changed stacking sequence with respect to the iodido-bismuthate chains. Projecting two adjacent chains onto the (0 0 1) plane, the position of the chains in the *a*-*b*-plane shifts in both structures by $1/3\vec{b}$, but for the platinum compound an additional shift by $1/2\vec{a}$ is observed (Figure 4.9). Therefore, within the unit cell of the palladium compound γ *and* β are close to 90°, while the latter is 101.64° for the platinum structure. That the palladium compound has still no monoclinic symmetry, although the metric conditions of a monoclinic cell are met, is due to the shift of $1/4\vec{a}$ of the honeycomb layers within the *a*-*b*-plane, which is not compatible with a twofold rotation axis nor a 2_1 screw axis along *a* (in this setting $\alpha = 76.009°$ would be the monoclinic angle).

The differing stacking sequence of the palladium compound compared to the platinum compound seems to be a result of the slight differences of these two elements, although their behaviour is in general regarded as very similar. Nevertheless, it could also be that both stacking variants are realised for both structures and the selected crystals accidentally showed the one or the other sequence. Though, it shall be noted that for both structures several crystals have been measured, all showing the described respective stacking pattern.

4.1.4. Comparison of the Honeycomb Layer Structures

Comparison of the honeycomb layer in the known compounds $Bi_{14}Rh_3I_9$, $Bi_{13}Pt_3I_7$, $Bi_{13}Pd_3I_7$, $Bi_{12}Pt_3I_5$,[142] and $Bi_{38}Pt_9I_{14}$ reveals mainly similarities (Figure 4.10). The Pt–Bi and Pd–Bi distances are almost equal, and again very similar to the Rh–Bi distance, which does not surprise, as platinum, palladium and rhodium all three belong to the platinum-group elements and their atoms all have similar sizes (Figure 4.10a). Most probable this also indicates a similar electronic state for the *M*-atom in the cube centre.

Comparing the Bi–Bi distances, one has to differentiate between the heights of the layers, the distances along the triangles and the distances along the hexagons (Figure 4.10c). All Bi–Bi distances range between the intra- and interlayer Bi–Bi distance in elemental bismuth, being 307 pm and 353 pm, respectively (Figure 4.10a). In all structures the Bi–Bi distances in the triangles are about 320 pm and the ones in the hexagons are about 345 pm. Only the layer heights differ significantly between the platinum- and palladium-compounds on one side (approx. 333 pm) and the rhodium-based compound (318 pm) on the other side. For the latter the cube height is even the shortest of all Bi–Bi distances.

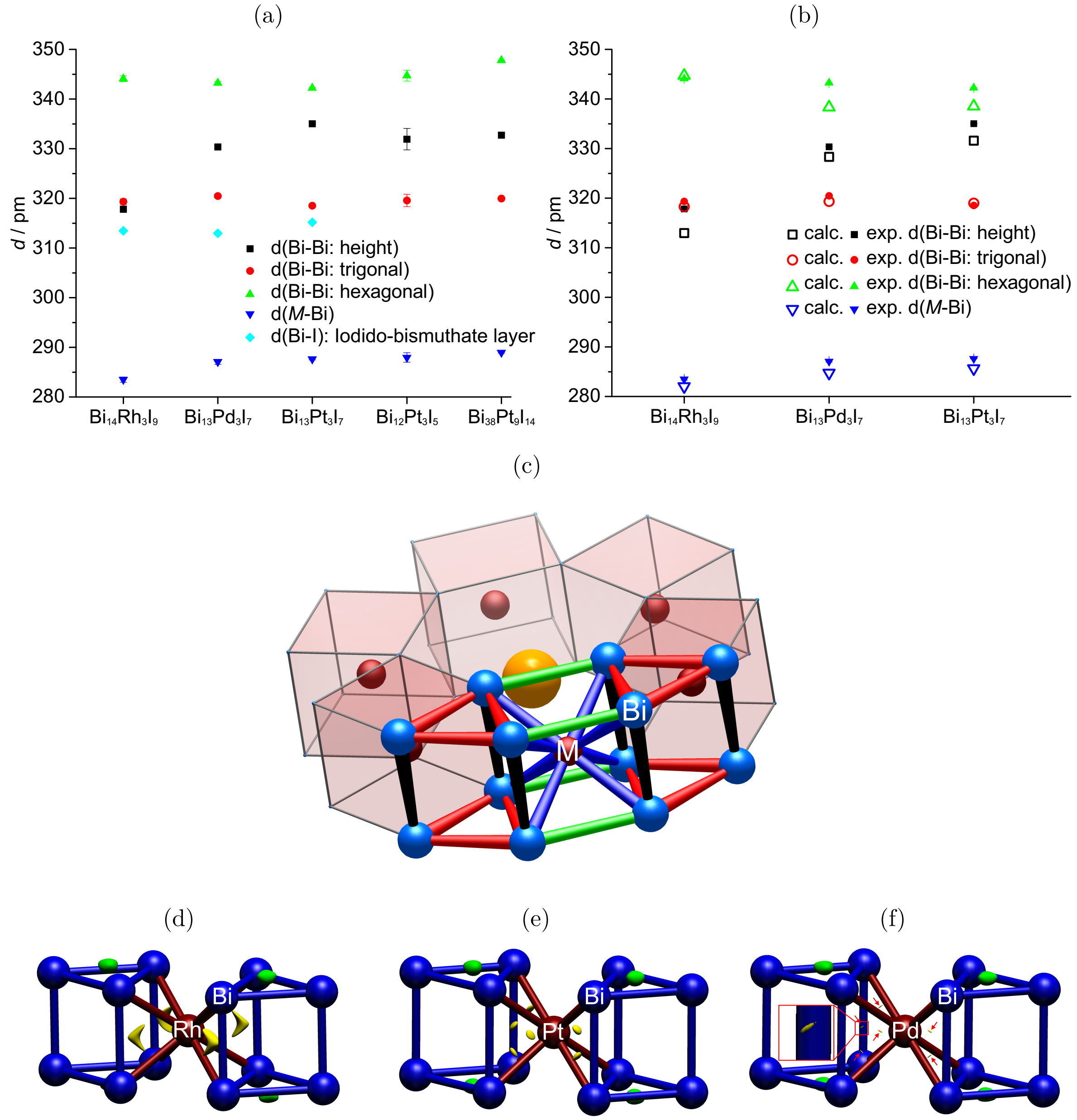

Figure 4.10.: (a) and (b) Three kinds of distances between bismuth atoms and between bismuth and the platinum-group element in the honeycomb layer $^2_\infty[(\mathrm{Bi}_{8/2}M)_3\mathrm{I}]$ (colour coding according to the sketch in (c)). The bismuth-iodine distances for the iodido-bismuthate layer are given for structures which comprise this layer type (cyan). The given error bars indicate $\pm 3\sigma$ calculated from the e.s.d.s of the atomic positions.
(d), (e), (f) Structural fragments with selected ELI-D localisation domains indicated by isosurfaces ($\Upsilon_D^\sigma = 1.0 \pm 0.03$, to optimise the graphical representation; for a quantitative discussion see Section 4.2.2) for the isolated layer structures (ILSs) of rhodium, platinum and palladium, respectively.

On the one hand, the different spacers separating the honeycomb layers could yield an explanation for this trend. Only in the platinum and palladium compounds a pure iodide layer appears as spacer, which means that the distance to at least one neighbouring honeycomb layer is short ($< 563\,\mathrm{pm}$), while the iodido-bismuthate layer as the only spacer in $\mathrm{Bi_{14}Rh_3I_9}$ results in long distances ($> 926\,\mathrm{pm}$) between the honeycomb layers. On the other hand, the number of valence electrons for the honeycomb network differs between the platinum, and palladium and the rhodium compound, respectively. In principle, each platinum (palladium) atom yields one valence electron more compared to rhodium, which increases the number of valence electrons within the honeycomb network by three per sum formula. Although, e.g. in $\mathrm{Bi_{13}Pt_3I_7}$ ($\mathrm{Bi_{13}Pd_3I_7}$) a pure iodide layer accepts four electrons per three intermetallic cubes while an iodido-bismuthate layer accepts only two electrons per three intermetallic cubes, the overall number of valence electrons is still higher in $\mathrm{Bi_{13}Pt_3I_7}$ ($\mathrm{Bi_{13}Pd_3I_7}$) compared to $\mathrm{Bi_{14}Rh_3I_9}$. This could then lead to an expansion of the honeycomb layers, as e.g. anti-bonding states become occupied. An additional effect related to the number of valence electrons is the differing charge of the honeycomb layers of $+3$ within the platinum (palladium) and $+2$ for the rhodium compound, which could also play a role.

The theory concerning the number of valence electrons and the occupation of anti-bonding states is supported by a topological analysis of the ELI-D field. Although, this analysis was in most cases conducted for a relaxed isolated honeycomb layer (subsequently referred to as isolated layer model: ILS), it will be shown that such a model represents all important features of the electronic and therefore also atomic structure (Section 4.2). At that stage the justification of the models will be restricted to a juxtaposition of the experimental distances and the ones from the relaxed models. Both agree very well, especially the discussed peculiarity of the heavily changing cube heights (Figure 4.10b).

For the experimentally realised structures with the elements Rh, Pd, Pt as M in the cube centre, two bonding features can be found in the ELI-D field for the models (Figure 4.10d to 4.10f). One corresponds to the $M{-}\mathrm{Bi}$ interaction and is more or less located directly between between these. The other relates to a three-centre bismuth interaction and can be found slightly above (and beneath) the centres of the Bi-triangles. Although, the strength of these bonds changes (details Section 4.2.2, Figure 4.22b), the distances directly related, namely the $M{-}\mathrm{Bi}$ distance and the distance of the Bi-atoms within the triangles, stay almost constant in the relaxed models as well as in experiment. In the same series, the height of the bismuth cubes changes and a detailed comparison of the $M{-}\mathrm{Bi}$ bonding basins gives evidence for the idea that this happens due to anti-bonding states that become occupied. If rhodium is in the cube centre, actually only four $M-$Bi bonding basins per cube are formed, with contributions from an upper and a lower bismuth atom, and the rhodium atom, indicating bonding interactions between the upper and the lower bismuth atoms of the cube (nevertheless, the shape of the basins also indicates a strong pairwise $M-$Bi character). On the contrary, for platinum or palladium in the cube centre these basins split into two, most likely due to anti-bonding interactions, yielding eight $M-$Bi basins per cube. This is further supported by a quantitative analysis, which reveals that the Bi$-M$ bond weakens in the series Rh, Pt, Pd (see Section 4.2.2: Figure 4.22a and 4.22b).

Considering again the whole layered structure, the only other distances of interest are the Bi$-$I distances within the iodido-bismuthate layer, which are very similar for all structures where this type of layer appears (Figure 4.10a). This is expected, as the layer itself has a strong ionic character with I^- and Bi^{3+} and therefore is more or less independent of the electronic situation within the honeycomb layer. Consequently, also the distances between two honeycomb layers separated by such an iodido-bismuthate layer are very similar (Figure 4.11a). In contrast to that, the separation height of the pure iodide layer significantly differs between the compounds comprising this layer type (Figure 4.11a). Nevertheless, the largest difference occurs comparing $Bi_{38}Pt_9I_{14}$ on one hand and all other compounds on the other hand. This can be explained by the occupation of the hexagonal channels running along [0 0 1]. Most likely the distances of adjacent honeycomb layers try to adapt to the channel occupation with $[BiI_2]^-$ ions and iodide ions. Almost the same reason leads to the threefold superstructure.

Analysis of the thermal expansion parameters yields further insight into the layer interactions. For these layered compounds besides a and b, especially the stacking direction [0 0 1] is of interest and will be discussed instead of c. Nevertheless, it shall be mentioned, that these expansion parameters were extracted from single crystal diffraction experiments and therefore have to be considered with care, as the possible error due to the fact that only one selected crystal was used can be large and was not evaluated.

The thermal expansion in [0 0 1]-direction of $Bi_{14}Rh_3I_9$ is the largest observed in these structures, while $Bi_{13}Pd_3I_7$ has the smallest thermal expansion in the same direction. $Bi_{13}Pt_3I_7$ and $Bi_{38}Pt_9I_{14}$ have expansion parameters in the [0 0 1] direction which are in the order of magnitude of the respective expansion parameters in a and b direction (Figure 4.11c). As the thermal expansion of $Bi_{38}Pt_9I_{14}$ seems to be heavily influenced by the $[BiI_2]^-$ ions in the hexagonal channels, the discussion of the different expansion parameters will be restricted to the other three compounds.

To understand the differences, a closer look onto the different parts of the struc-

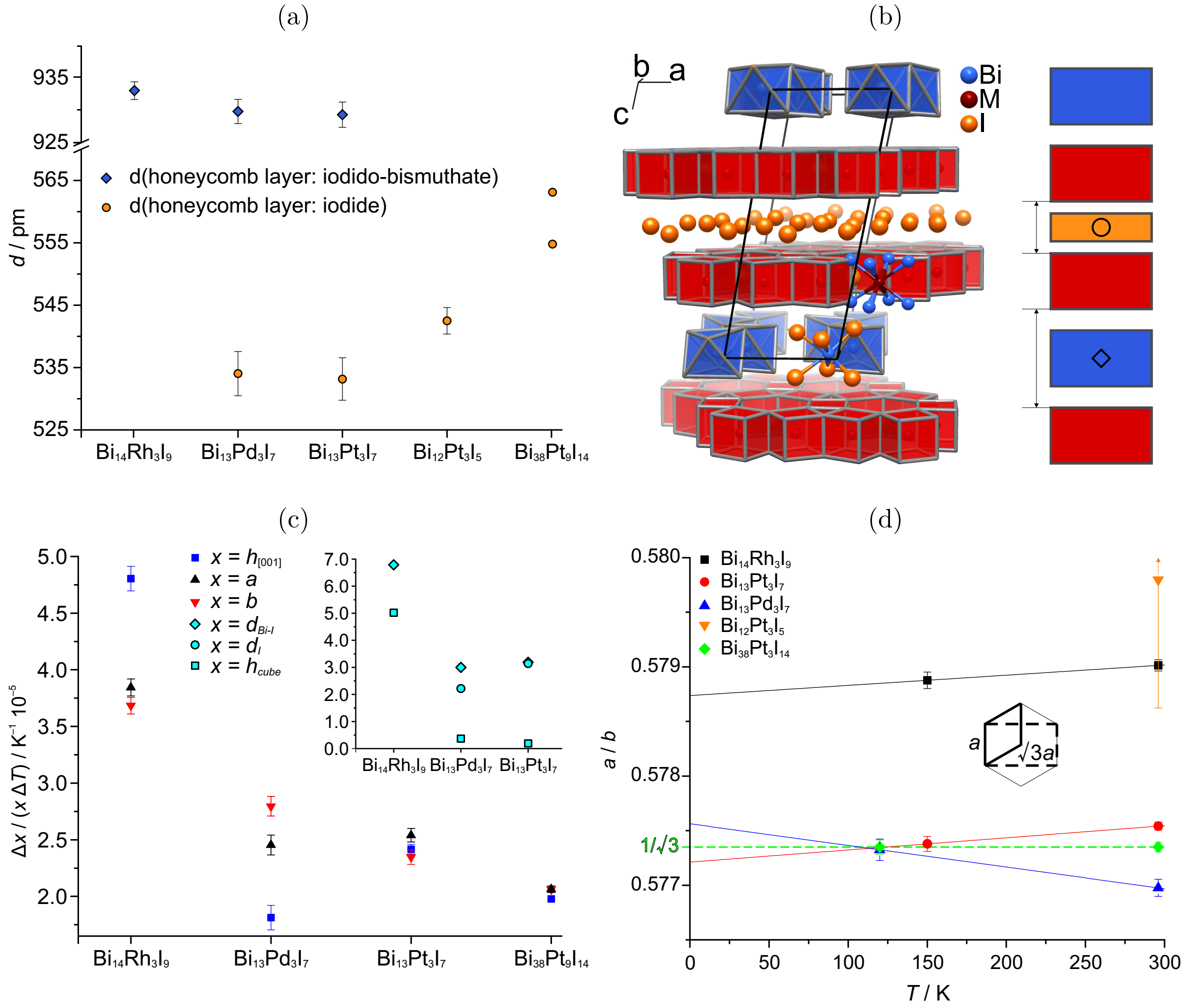

Figure 4.11.: (a) Distances between two honeycomb layers $^{2}_{\infty}[(\mathrm{Bi}_{8/2}M)_3\mathrm{I}]$ if either separated by a iodido-bismuthate layer (blue diamond) or an iodide layer (orange circle), which is exemplarily illustrated in (b) with the structure of $\mathrm{Bi_{13}Pt_3I_7}$.
(c) Thermal expansion parameters for the a and b-axis and for the height of the unit cell along the stacking direction [0 0 1] ($h_{[0\,0\,1]}$) of different structures with the honeycomb layer motive ($^{2}_{\infty}[(\mathrm{Bi}_{8/2}M)_3\mathrm{I}]$). Inset: Thermal expansion parameters for the distances between two adjacent honeycomb layers separated by an iodide layer (d_I: cyan circle) or an iodido-bismuthate layer (d_{Bi-I}: cyan diamond) and the height of the bismuth cubes within the honeycomb layer (h_{cube}: cyan square) for $\mathrm{Bi_{13}Pt_3I_7}$ and $\mathrm{Bi_{13}Pd_3I_7}$.
(d) a/b-ratio of the (pseudo-)ortho-hexagonal cell for different structures with the honeycomb layer motive ($^{2}_{\infty}[(\mathrm{Bi}_{8/2}M)_3\mathrm{I}]$) at different temperatures compared to the value of $1/\sqrt{3}$ for a hexagonal cell (see inset).

tures is necessary. Already the two layer types which are common in all three structures expand very differently with increasing temperature. In general, the height of the iodido-bismuthate layer can increase strongly, as, due to the at least partial ionic character, mainly the thermal vibrations of the atoms define the distances. Nevertheless, for the platinum and the palladium compound the expansion parameter is only half the one of the rhodium compound (Inset: Figure 4.11c). Maybe this can be attributed to the slight disorder in the iodido-bismuthate layers in the cases of the platinum and the palladium compound, which in principal could mean that different orientations of the iodido-bismuthate strands exist. Nevertheless, in all cases this part is the one that expands most on heating.

The honeycomb layer itself shows also a very different behaviour. For $Bi_{13}Pt_3I_7$ and $Bi_{13}Pd_3I_7$ the layer height is almost temperature independent, while in $Bi_{14}Rh_3I_9$ it heavily increases with temperature (Inset: Figure 4.11c). As discussed above, for the platinum and the palladium compound anti-bonding states are occupied. As this is the reason for the honeycomb layer being generally higher in these cases compared to $Bi_{14}Rh_3I_9$, it could also explain the smaller expansion parameters. Much less pronounced, the same effect can be observed for the thermal expansion parameters of the a and b axis of the respective compounds.

These differences explain why $Bi_{14}Rh_3I_9$ behaves different from $Bi_{13}Pt_3I_7$ and $Bi_{13}Pd_3I_7$. Nevertheless, it does not yield an explanation for the differences of the latter two. For the expansion along [0 0 1] one has to consider the layer of iodide ions. This type of layer expands less with increasing temperature for the palladium compound compared to the platinum compound (Inset: Figure 4.11c). As the relative position of two adjacent honeycomb layers separated by an iodide layer is the same in both compounds it is difficult to understand this behaviour.

Nevertheless, the different thermal expansion parameters in $\vec{a}$ and $\vec{b}$ direction could have a structural reason. As discussed, the iodido-bismuthate chains running along the b axis are stacked differently. Maybe the additional shift of $^1/_2\vec{a}$ in the case of $Bi_{13}Pt_3I_7$ compared to $Bi_{13}Pd_3I_9$ is decisive for the relative difference between the thermal expansion in $\vec{a}$ and $\vec{b}$ direction within both structures.

Finally, as the hexagonal honeycomb layer in three of the compounds appears as a part of a triclinic structure, the deviations of the pseudo-hexagonal symmetry of the layer from the hexagonal symmetry, as in $Bi_{38}Pt_9I_{14}$, has been analysed. As the a-b plane of the triclinic cell corresponds to the (pseudo-)ortho-hexagonal (C-centred) setting, one can calculate the $^a/_b$-ratio and compare it to the value of an actual ortho-hexagonal cell of $^1/_{\sqrt{3}}$ (Figure 4.11d).

$Bi_{13}Pt_3I_7$ and $Bi_{13}Pd_3I_7$ are closest to the hexagonal symmetry. At low temperatures they become hexagonal within the error bar, but would again deviate from the hexagonal symmetry on further cooling, if their temperature dependence can be extrapolated linearly. The latter might be actually not the case, as, notably, the kind of deviation from the hexagonal symmetry for both structures differs (for $Bi_{13}Pt_3I_7$ $^a/_b \geq {}^1/\sqrt{3}$ and for $Bi_{13}Pd_3I_7$ $^a/_b \leq {}^1/\sqrt{3}$ at RT) but nevertheless both show a tendency towards hexagonal symmetry to low temperatures.

In contrast to these compounds, $Bi_{14}Rh_3I_9$ and $Bi_{12}Pt_3I_5$ are much further off the hexagonal symmetry. The latter shows the strongest deviation, although with a large error bar due to the synthetic procedure.[142] $Bi_{14}Rh_3I_9$ on the other hand has a narrow error bar and does not cross the perfect value of $^a/_b = {}^1/\sqrt{3}$ at any temperature if extrapolated linearly. The latter can be understood again considering the different layer types separating the honeycomb networks. Most probably, the iodido-bismuthate layer with its strands, belonging to the layer group $p2/b11$,[134] introduces the essential part of the distortion from the hexagonal symmetry. As the only separating layer type in $Bi_{14}Rh_3I_9$ its influence is much more pronounced. On the contrary, in $Bi_{13}Pt_3I_7$ and $Bi_{13}Pd_3I_7$ the additional separating layer type, the iodide ions, belongs also to the hexagonal layer group $p6/mmm$, as the honeycomb layer itself, which reduces the distortion. Although $Bi_{12}Pt_3I_5$ seems to contradict this interpretation, the strong deviation from the hexagonal symmetry in this orthorhombic structure can most probably be explained by the heavily twinning of the crystals after the topochemical transformation or maybe by the fact, that the structure is metastable and its electronic structure is off the equilibrium.[142]

Conclusions

In summary, the honeycomb layer ${}^2_\infty[(Bi_{8/2}M)_3I]$ is structurally very similar in all known compounds in which it appears and very robust even against the exchange of the central atom in the bismuth cubes, namely rhodium, platinum or palladium. Nevertheless, small, but significant differences are observed, especially concerning the number of valence electrons. These differences are most obvious if the type of the separating layer differs or, as in the case of $Bi_{38}Pt_9I_{14}$, a different approach for the charge compensation is observed with the hexagonal channels hosting $[BiI_2]^-$ ions. Similarly to the structural situation, the basic physical properties of the *isolated* honeycomb layers change only marginally, what will be discussed in Section 4.2. Nevertheless, the three-dimensional arrangement of the honeycomb layers, especially the spacers separating them, has a heavy impact on the properties.

4.2. Theoretical Modelling and Physical Properties

The first part of this section is dedicated to initial calculations and experiments which gave evidence for $Bi_{14}Rh_3I_9$ being the first experimentally realised weak 3D-TI (Section 4.2.1). Its electronic structure is analysed theoretically and compared to ARPES and transport experiments.

The second part (Section 4.2.2) identifies the honeycomb lattice $^2_\infty[(Bi_{8/2}M)_3I]$ as the essential structural part of $Bi_{14}Rh_3I_9$ for its TI properties and plants a seed for a systematic investigation of all introduced structures based on this layer type. It is shown that a single layer of this kind is a 2D-TI for certain platinum-metals M, while it becomes a trivial insulator in other cases. Furthermore, a structural and electronic analogy of the $^2_\infty[(Bi_{8/2}M)_3I]$ lattice is drawn to graphene and its notion as "heavy graphene analogue" (a "graphene" with strong SOC) is justified. This is of interest, as graphene was the first TI ever put forward by theoreticians.[39]

Within the third part (Section 4.2.3) the topologically trivial semimetals $Bi_{13}Pt_3I_7$ and $Bi_{13}Pd_3I_7$ are introduced. This reveals the strong influence of the spacers and the stacking of the honeycomb layers on the topology of the electronic band structure. Additionally, the experiments performed to support the calculations indicate a superconducting transition for both compounds.

The fourth part (Section 4.2.4) joins the theoretical predictions within the introduced family of structures, to prove the non-trivial topology of $Bi_{14}Rh_3I_9$ by STM experiments on $Bi_{14}Rh_3I_9$ and $Bi_{13}Pt_3I_7$. Although, in both cases the comprising isolated honeycomb layer is calculated to be topologically non-trivial, the whole structures have very different physical properties, due to their different stacking sequence. With STM the predicted edge channels on the surface of the "weak" 3D-TI $Bi_{14}Rh_3I_9$ are revealed, while for the topologically trivial structure of $Bi_{13}Pt_3I_7$ nothing alike is observed. Furthermore, these experiments establish $Bi_{14}Rh_3I_9$ as potential material for an application in spintronics or as building part of a quantum computer.

The last part (Section 4.2.5) deals with $Bi_{38}Pt_9I_{14}$, in which the honeycomb layers couple strongly, but which is difficult to explore, as no crystals of sufficient size could be grown and no physical experiments on single crystals are available. Therefore, the focus is on the unusual linear structural fragment $[BiI_2]^-$ and the confirmation of the rare charge of +I for bismuth. Nevertheless, the results of the calculations are discussed with respect to the topological properties of the electronic structure.

4.2.1. The Weak 3D-TI $Bi_{14}Rh_3I_9$ – Stacked Topological Insulator Built from Bismuth-based Graphene Sheet Analogues[126]

The fact that the weakly coupled honeycomb layers in $Bi_{14}Rh_3I_9$ have the same structural symmetry as graphene sheets suggests similarities also in the electronic structure. Indeed, a scalar-relativistic band structure calculation for $Bi_{14}Rh_3I_9$, where the spin-orbit coupling (SOC) is effectively switched off, reveals the presence of two Dirac cones in the triclinic Brillouin zone, which are situated at the Fermi level (Figure 4.12a). Unfolding the triclinic zone to a hexagonal one, it is observed that the two inequivalent Dirac cones appear very close to the K and K'-point at the edge of the hexagonal Brillouin zone, precisely where they are in graphene (Figure 4.12c). The very weak hopping of electrons between the layers causes the Dirac cones to pick up a minor dispersion perpendicular to the plane (Appendix: Figure A.24), rendering the calculated band structure quasi-2D.

However, for a proper understanding of the electronic band structure one needs to go beyond calculations in scalar-relativistic approximation. Whereas the relativistic SOC in, for instance, graphene is very weak (it is expected to open a gap on an energy scale of approximately 1×10^{-3} meV (0.01 K)[151]) bismuth is well-known for its strong SOC that can drive and stabilise topologically non-trivial electronic states. As one is thus dealing with graphene-like Dirac cones in the presence of strong SOC, the mechanism proposed in reference 39 to stabilise a topologically non-trivial quantum spin Hall (QSH) state is applicable to the honeycomb layers of $Bi_{14}Rh_3I_9$. Indeed, a full-relativistic band structure calculation reveals a gaping out of the Dirac cones, resulting in a calculated band gap of 210 meV, corresponding to 2400 K (Figure 4.12b).

To confirm the topological non-trivial nature of the resulting insulating state the four topological Z_2 invariants[30, 41, 42, 152] ν_0; (ν_1, ν_2, ν_3) were calculated with the full-potential local-orbital (FPLO) band structure code[123] (see Supplement of reference 126 for details). This calculation is based on an analysis of the wave function parity eigenvalues at the eight time-reversal invariant points of the band structure, as illustrated in Figure 4.12f. Owing to the stacking of the quasi-2D honeycomb planes in which SOC has gapped out the Dirac cones, one expects $Bi_{14}Rh_3I_9$ to be a weak 3D-TI and indeed ν_0 is found to be 0. The other topological invariants are calculated to be $(\nu_1, \nu_2, \nu_3) = (0, 0, 1)$. The fact that $\nu_0 = 0$ and $\nu_3 = 1$ proves that $Bi_{14}Rh_3I_9$ is a weak 3D-TI and confirms that the honeycomb planes form sheets of QSH insulators that are stacked along the c-axis. It implies that in the Altland-Zirnbauer classification[153] $Bi_{14}Rh_3I_9$ belongs to the symplectic (AII) topology class. On surfaces perpendicular to the normal (0 0 1) (and therefore parallel to the honeycomb planes, which are the

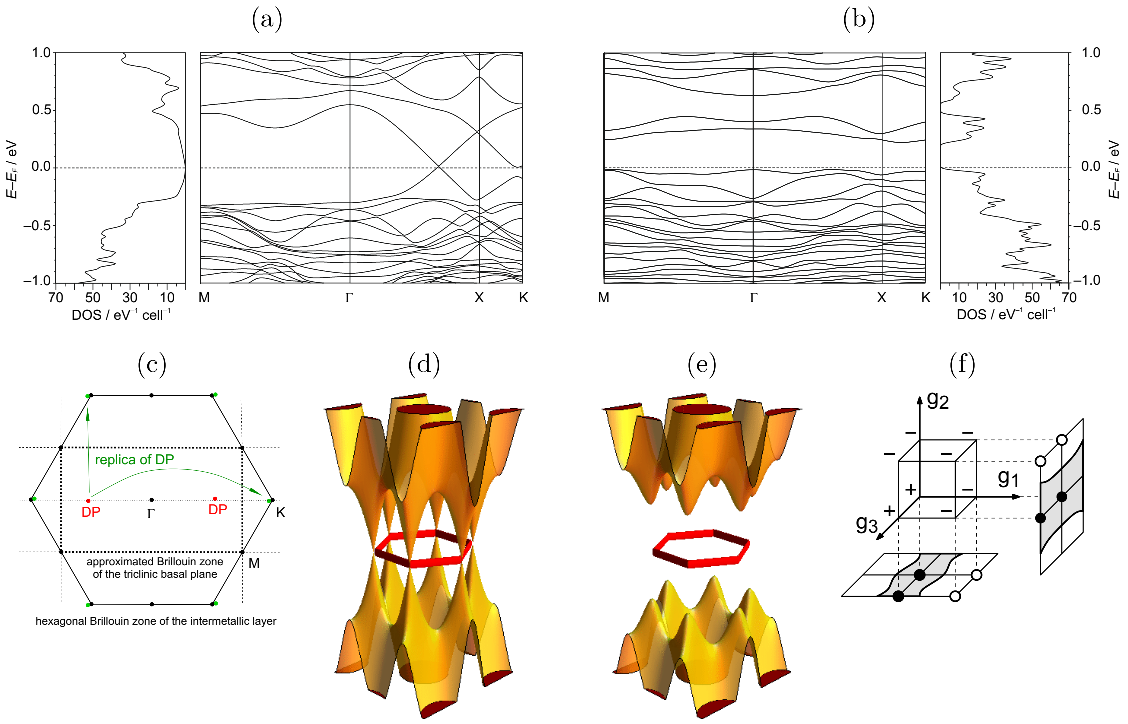

Figure 4.12.: (a) Scalar relativistic band structure of triclinic $Bi_{14}Rh_3I_9$. On the line $\overline{\Gamma X}$ a Dirac cone is present.
(b) Fully relativistic band structure of triclinic $Bi_{14}Rh_3I_9$, where the spin–orbit interaction opens up a gap of ≈ 210 meV.
(c) Projections of the Dirac points (DP, red) onto the two-dimensional Brillouin zone (dashed lines) of the triclinic basal plane. Replication of the DP (green) to the neighbouring Brillouin zones yields positions close to the K-points of the unfolded hexagonal Brillouin zone (solid lines).
(d) Illustration of the Dirac cones in the situation without spin–orbit interaction and (e) the topological gap induced by the spin–orbit interaction.
(f) Parity eigenvalues at the eight time-reversal-invariant points in the 3D Brillouin zone, where g_3 corresponds to the direction perpendicular to the Bi–Rh planes. The parity eigenvalues lead to the topological invariants $\nu_0;(\nu_1,\nu_2,\nu_3) = 0;(0,0,1)$. Projected parities on the planes perpendicular to g_1 and g_2 illustrate the presence of topological edge states on these surfaces.

natural cleaving planes of the material) topological surface states will thus be absent. At any other surface an even number of Dirac cones appears, each having a strongly anisotropic group velocity due to the quasi-2D nature of the bulk band structure. The metallicity of these surface states is stable against disorder, which, as for strong topological insulators in the symplectic class, does not act as a source of localisation.[55, 56]

The band structure obtained from the electronic structure calculations can be

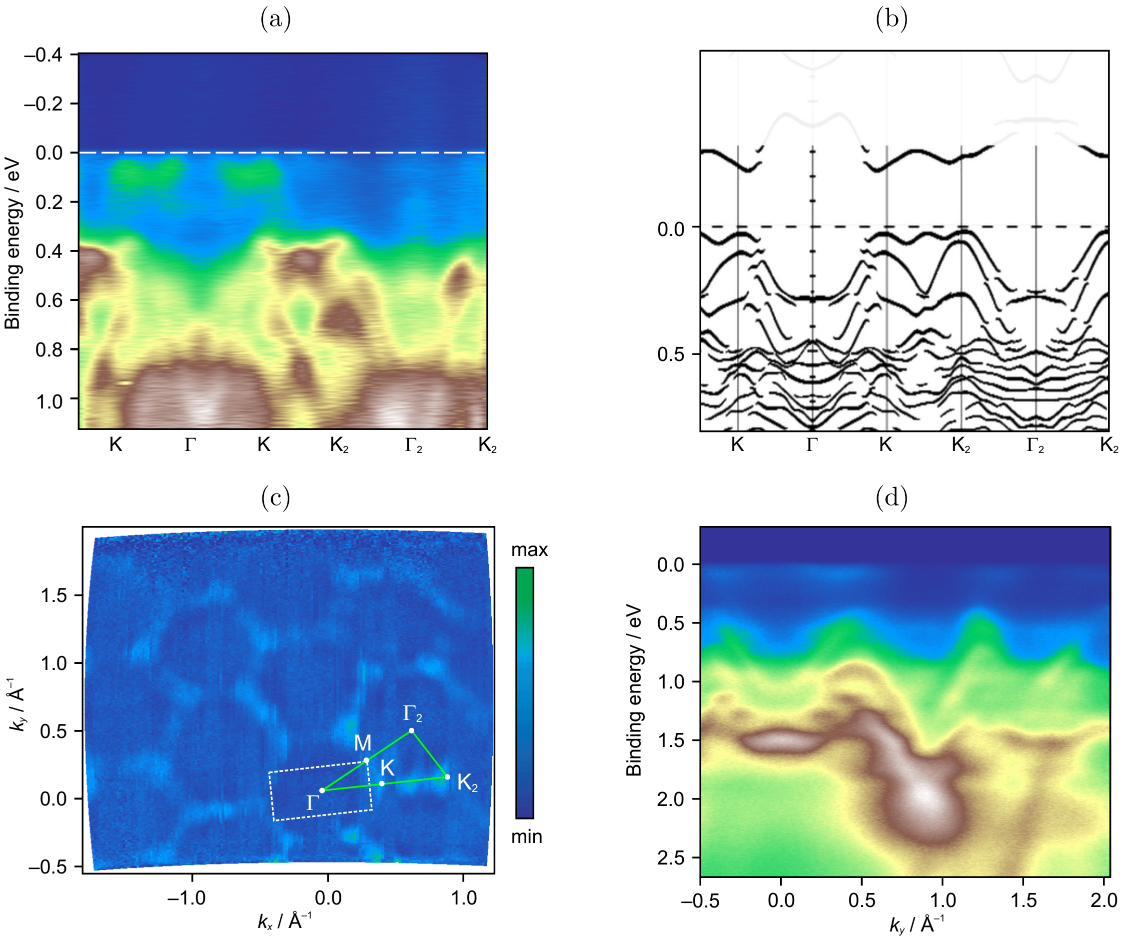

Figure 4.13.: In $Bi_{14}Rh_3I_9$ a small amount of electron doping brings the Fermi level into the conduction band, so that the topological band gap becomes clearly visible. (a) Momentum-energy intensity plot along the high-symmetry $\overline{\Gamma\mathrm{K}}$ direction of the unfolded Brillouin zone. (b) Unfolded full-relativistic band structure along the same direction.
(c) Momentum distribution at 0.4 eV binding energy integrated within a 50 meV window. White dashed lines show the trigonal, surface projected Brillouin zone.
(d) Typical momentum-energy distribution taken along the cut that corresponds to $k_x = 0$ in (c).

tested experimentally by ARPES, which in particular can provide the experimental value of the electronic band gap, if by slight electron doping the Fermi level of the material is pushed into the conduction band. The ARPES spectra in Figure 4.13a and 4.13d are consistent with the material being n-doped, which is discussed in Section 4.1.1 (and in more detail in reference 147).

One can compare the ARPES results with the full-relativistic band-structure calculations in the unfolded Brillouin zone selecting the $\overline{\Gamma\mathrm{K}}$ high-symmetry direction

(Figure 4.13a and 4.13b, for other cuts see Supplement of reference 126). This is a direction where the Dirac cones are found in the scalar-relativistic approximation. The agreement between experimental data and full-relativistic calculations is remarkable. First, the observed gap, as determined considering the distance between the features of the integrated spectral weight (over three Brillouin zones), is $\approx 270\,\mathrm{meV}$, which is consistent with the relativistic band structure. Also the number and behaviour of the dispersing features clearly seen in ARPES intensity plots are essentially captured by the bands projected to the hexagonal Brillouin zone. The prominent examples are the in-equivalence of Γ and Γ_2 and structures between K and K_2, both also present in the calculated band structure.

This agreement confirms experimentally the validity of the calculated band structure in the presence of SOC, the bands for which the topological invariants were calculated to be ν_0; $(\nu_1,\ \nu_2\ ,\ \nu_3) = 0$; (0, 0, 1). This topologically non-trivial state is understood in terms of the graphene-like structure of the intermetallic Bi−Rh planes, for which two Dirac cones are present at the Fermi level in a calculation without SOC. Experimentally the SOC is of course unavoidable and switching it on in the calculation gaps out the Dirac cones and generates the weak topological 0; (0, 0, 1) state. As a consequence spin-locked topological surface states will be present at any crystal face that is not parallel to the (0 0 1) plane[1]. Such faces, however, do not correspond to natural cuts of the crystal and the associated surface roughness has prevented the observation of these spin-polarised surface states by ARPES on, for instance, (1 0 0) surfaces. But, as will be shown in Section 4.2.4, scanning tunnelling microscopy and spectroscopy are able to directly probe these states at step edges of the natural (0 0 1) cleaving plane.

Finally, the momentum distribution of ARPES intensity at 400 meV binding energy, just below the calculated Fermi level of $Bi_{14}Rh_3I_9$, clearly shows a hexagonal pattern (Figure 4.13c), as is expected from the band structure calculations where the top of the valence band is formed by a dispersive feature that is relatively flat between the K-points. The hexagonal pattern justifies the unfolding of the Brillouin zone carried out to facilitate the comparison to ARPES. At the same time its slight irregularity reflects the overall triclinic crystal symmetry.

The hexagons observed in ARPES emphasise the structural and electronic similarities of $Bi_{14}Rh_3I_9$ to graphene, which are further elucidated in the next Section 4.2.2.

---

[1] Although, these surface states are also expected to form Dirac cones, these must not be confused with the bulk Dirac cones present in the scalar-relativistic band structure calculation. The surface states can only be calculated in finite slab calculations, which are very time-consuming and have only been conducted for a simplified tight-binding model.[154]

The compelling difference with graphene is that the large SOC drives $Bi_{14}Rh_3I_9$ electronically into a topologically insulating state, corresponding to a 3D stack of 2D QSH states, which is very different from the strong topological insulator states observed so far in bulk materials such as Bi_2Se_3 or Bi_2Te_3 and which is predicted to leave marked signatures on electronic transport through its spin-polarised, stacked quasi-1D topological surface states.[55, 56]

These unique transport properties, though, can not be probed, as the n-doping, being advantageous in case of ARPES, renders $Bi_{14}Rh_3I_9$ metallic. Although, as discussed in Section 4.1.1 (and in more detail in reference 147), the n-doping only effects the honeycomb layers directly at the surface, this nevertheless means, that $Bi_{14}Rh_3I_9$ without any modification should be a metal. And indeed, transport measurements on single crystals confirm this metallic behaviour (Figure 4.14). The strong anisotropy of the resistivity in-plane and out-of-plane, meaning within the plane of the honeycomb layers and perpendicular to it, already indicates that the metallicity is restricted to the n-doped surface honeycomb layer ($^{\rho_c}/_{\rho_{ab}} \geq 200$). Latest experiments on a sintered powder give further evidence that the bulk part of the crystals without the surfaces is actually insulating. The measurements on the powders show a semimetallic behaviour, which is in good agreement with the main part of the powder being semiconducting and only parts of the (partially oriented) surface being metallic.[155] Furthermore, the intrinsic band gap of approximately 150 meV extracted from an Arrhenius plot in the high-temperature region of the measurement[2] is in the order of magnitude of the calculated band gap of 230 meV.

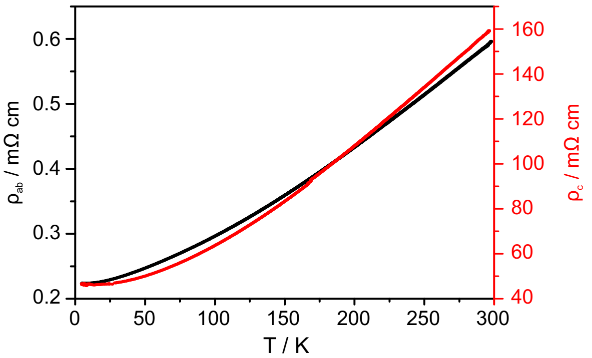

Figure 4.14.: Resistivity versus temperature behaviour for a platelet of $Bi_{14}Rh_3I_9$ parallel to the honeycomb layers (ρ_{ab}) and perpendicular to the honeycomb layers (ρ_c).

---

[2] As the authors of the article do not provide such a plot, the data were extracted with G3data[156] and then converted accordingly.

4.2.2. A Single Honeycomb Layer as a 2D-TI[157]

To establish a theoretical framework based on which the different synthesised compounds could be compared, a theoretical model based on a single, isolated honeycomb layer $^2_\infty[(\mathrm{Bi}_{8/2}M)_3\mathrm{I}]$ – already briefly introduced in Section 4.1.4 as ILS– is used. As three of the platinum-group elements (Rh, Pt, Pd) have led to compounds, the theoretical study is expanded to the whole platinum-group and the influence of this platinum-element substitution is analysed. The already introduced phrase "heavy graphene analogue" can be further justified via a combined reciprocal and real space analysis of the electronic structure.

Structural Modelling

Starting from the weak 3D-TI $\mathrm{Bi}_{14}\mathrm{Rh}_3\mathrm{I}_9$ (Figure 4.15a), the overall structural complexity can be reduced by recovering the hexagonal symmetry of the honeycomb layer $^2_\infty[(\mathrm{Bi}_{8/2}\mathrm{Rh})_3\mathrm{I}]^{2+}$. In the structure model, a single honeycomb layer is isolated together with the iodine atoms of the $[\mathrm{Bi}_2\mathrm{I}_8]^{2-}$-spacer compatible with the honeycomb layer symmetry $p6/mmm$. These iodine atoms are kept to compensate the charge. They are treated by the virtual crystal approximation (VCA) to guarantee the number of valence electrons to be as in the original compound. Therefore, the charges of the spacer iodide ions are reduced down to -0.25 by replacing the iodine atoms I with pseudo-atoms $_Z\mathrm{I}$ with a nuclear charge $Z = 53.75$. This yields the following formula: $[({}_{53.75}\mathrm{I})_4]^-[(\mathrm{Bi}_{8/2}\mathrm{Rh})_3\mathrm{I}]^{2+}[({}_{53.75}\mathrm{I})_4]^-$. The resultant model is referred to as isolated-layer

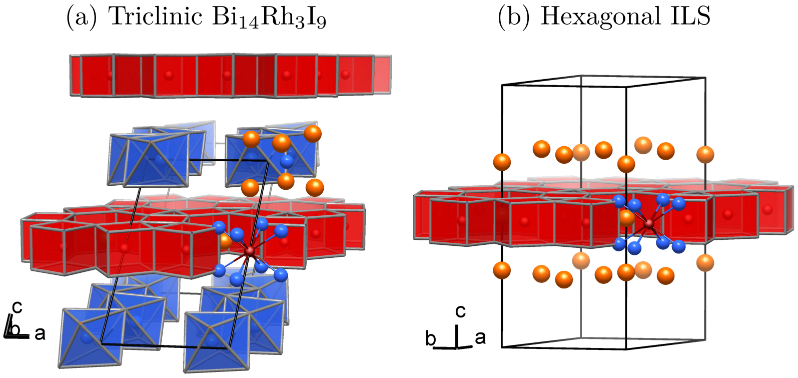
(a) Triclinic $\mathrm{Bi}_{14}\mathrm{Rh}_3\mathrm{I}_9$

(b) Hexagonal ILS

Figure 4.15.: Structure of (a) triclinic $\mathrm{Bi}_{14}\mathrm{Rh}_3\mathrm{I}_9$ (space group $P\bar{1}$) and (b) the corresponding hexagonal isolated-layer structure (ILS) (layer group $p6/mmm$). The intermetallic part of the honeycomb layer, a network of rhodium-centred bismuth-cubes, is coloured in red. Atom colours: Bi: blue; I: orange; Rh: red.

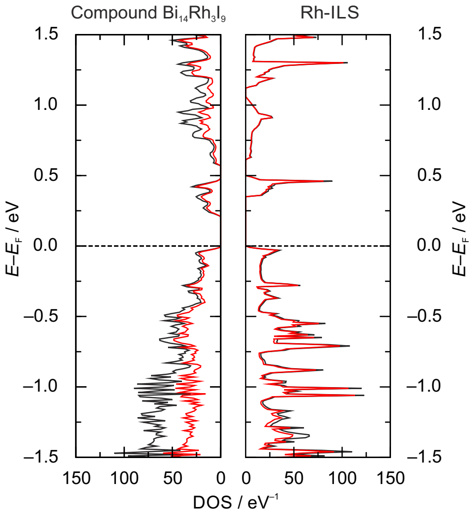

Figure 4.16.: Total density of states (DOS, black) for the original compound $Bi_{14}Rh_3I_9$ (left) and the isolated layer model (right) with the partial DOS for the honeycomb layer (red).

structure (ILS) or, in the specific case with rhodium, as Rh-ILS, throughout the text and is shown in Figure 4.15b. The Rh-ILS as well as all other ILSs were relaxed using the FPLO program package[123] under the restrictions of the $p6/mmm$ layer symmetry and by varying the cell axes with a step width of 0.1Å. All atomic positions were optimised on each step with a convergence criterion of 10^{-3}eV/Å.

Already the fact that the DOS in the original compound $Bi_{14}Rh_3I_9$ close to the Fermi level is dominated by the DOS of the honeycomb layer justifies an ILS. Furthermore, the features of the original DOS and the ILS-DOS agree very well (Figure 4.16). Direct comparison of the electronic band structure of the ILS with the one of the parent compound $Bi_{14}Rh_3I_9$ is achieved by unfolding the original triclinic Brillouin zone onto a hexagonal Brillouin zone (Figure 4.17). The unfolded bands close to the Fermi level can be identified in the band structure of the hexagonal Rh-ILS (Figure 4.17). Also the topological character of the various band gaps carries over directly to the ILS, in spite of a slight relative shift of the bands resulting in a small increase of the lower topological gap at the expense of the upper one. This confirms that the influence of the spacer as well as of the stacking of the honeycomb layers on the electronic structure is small in the case of $Bi_{14}Rh_3I_9$ and establishes the Rh-ILS as a QSH layer or, in other words, as a 2D-TI.

Metal substitutions were simulated by structural relaxation of M-ILSs with $M =$ Ru, Pd, Os, Ir, Pt. Only slight changes in the interatomic distances were observed (Section 4.1.4 and Appendix: Figure A.25). To a first approximation, the number of valence electrons in the honeycomb layer was kept the same as in the original Rh-

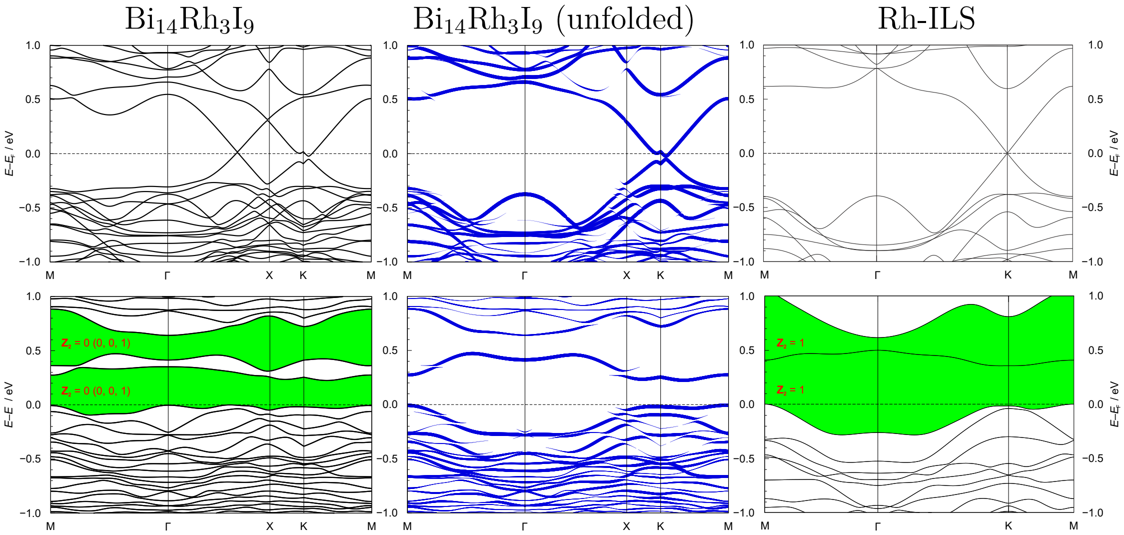

Figure 4.17.: Electronic band structure and unfolded electronic band structure for $Bi_{14}Rh_3I_9$ (left) compared to the electronic band structure of the model (right), in a scalar-relativistic (upper line) and a full-relativistic approach (lower line), respectively. For the gap at and above the Fermi energy the topological invariants are given.

ILS by VCA applied to the iodine sites. For Ru and Os this implies a lower, for Pd and Pt a higher charged M-ILS as compared to Rh and Ir, since the number of valence electrons increases with group number. Assumed charge flexibility of the M-ILS is plausible, since compounds with variously charged spacers and transition metals from different groups have already been synthesised (Section 4.1). Nevertheless, other possible electron counts for the M-ILSs were computationally addressed as well and are discussed below. Scalar- and full-relativistic band structures and the topological invariants were subsequently calculated for all M-ILSs (Figure 4.18 and Figure 4.19, Appendix: Figure A.26 and Table A.55).

Electronic Structure

For full-relativistic band structures, a topologically non-trivial “warped” gap of varying width can be found for all M-ILSs (Figure 4.19). The term “warped” refers to the fact that two bands are non-crossing and therefore have an energy separation at each k-point in the Brillouin zone. Yet, as they can have an energy overlap at *different* k-points this “warped” gap is not necessarily an actual energy gap, even if the “warped” band structure is adiabatically connected to a fully gapped electronic state (just as a semimetal and a semiconductor behave to each other).

The bands that change the Z_2-invariant from trivial to non-trivial or vice versa

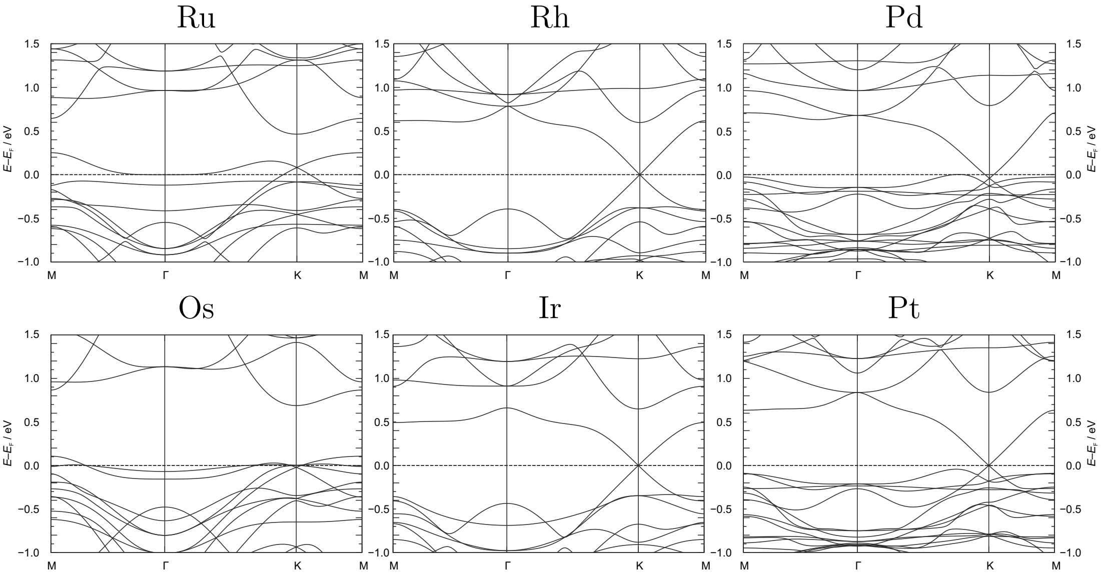

Figure 4.18.: Scalar-relativistic band structures for the ILS-series, all with a valence-electron count equal to the one in the original honeycomb layer $[(Bi_4Rh)_3I]^{2+}$, arranged as in the Periodic Table of Elements.

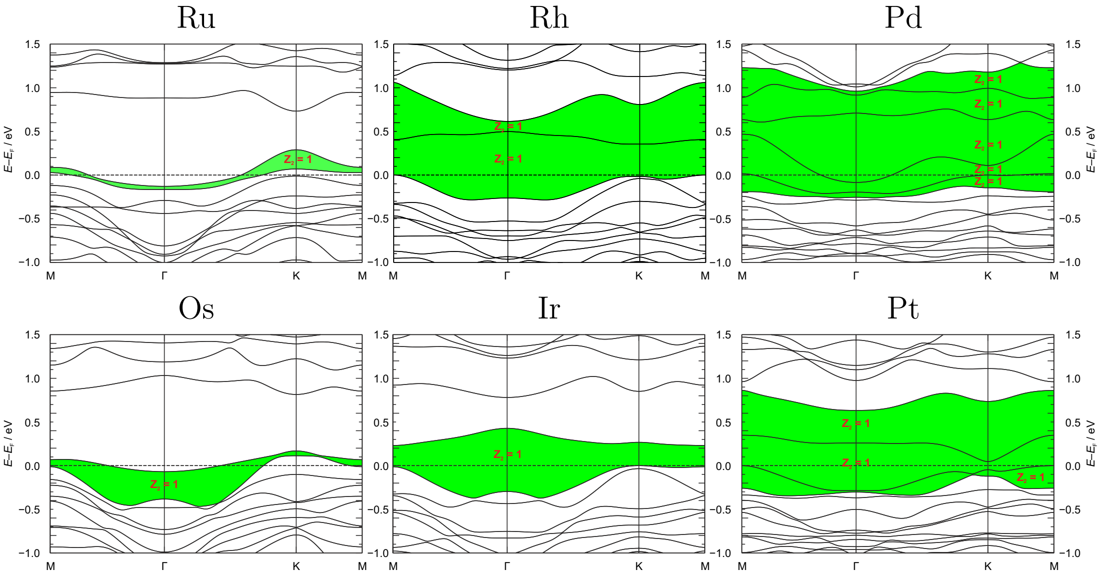

Figure 4.19.: Full-relativistic band structures for the ILS-series, all with a valence-electron count equal to the one in the original honeycomb layer $[(Bi_4Rh)_3I]^{2+}$, arranged as in the Periodic Table of Elements. The green shading depicts topologically non-trivial regions close to the Fermi energy, E_F (see explanation in the text).

shall be called “topologically active” bands, whereas the ones that do not change Z_2 shall be called “topologically in-active” bands. Formally topological activity can be calculated separately for all (even crossing) bands. The change in topological nature, however, only manifests itself in a warped or real gap above the last active band (phase continuity condition for non-crossing band complexes).

As shown in Figure 4.19, only in case of the Rh-, Ir-, Pt- and Pd-ILS an actual band gap of the material falls into the discussed topologically non-trivial region in the vicinity of the Fermi energy. Hence, these ILSs should support the QSHE given a certain number of valence-electrons. On the contrary, the Ru- and Os-ILS have only a large trivial gap, while the topologically active bands encompass a non-trivial warped gap.

The Rh-, Ir- and Pt-ILS are found to be insulating, with a valence-electron count as found in the original $Bi_{14}Rh_3I_9$ structure. On the contrary, in the cases of M = Ru, Os and Pd addition of two electrons per formula unit is necessary to achieve the insulating state. Via additional calculations it was established that the ILS band structure changes only insignificantly for such an amount of electron doping (Appendix: Figure A.26). The same number of electrons added to the Rh-, Ir- and Pt-ILS will drive these systems from one insulating state to another, the latter being topologically non-trivial for the Rh- and Pt-case.

The described differences in the electronic band structures obviously arise from the *d*-states of the transition elements: these are the valence states that vary from one M-ILS to the other. Generally, the energy position of the *d*-band within a period becomes lower with increasing group number of the M-element. Thus, in the ILS-series the energies of the populated *d*-states are also lowered with increasing group number, which means that the contribution of the *d*-states to the DOS close to the Fermi energy progressively decreases (Figure 4.20).

Origin of the Topologically Non-trivial Nature

In order to uncover the mechanism that drives the ILS systems into a topologically insulating state, the appropriate tight-binding (TB) models from the calculated band structures are extracted and the influence of M-element substitutions on the topological band character is analysed. The TB-description includes the Bi p_z- and p_{xy}-states, and the M *d*-states (details in Supplement of reference 157). Considered are nearest neighbour interactions for each pair of elements. Switching all of them on step-by-step, one arrives at a well-reproduced scalar-relativistic band structure for the Rh- or any other ILS.

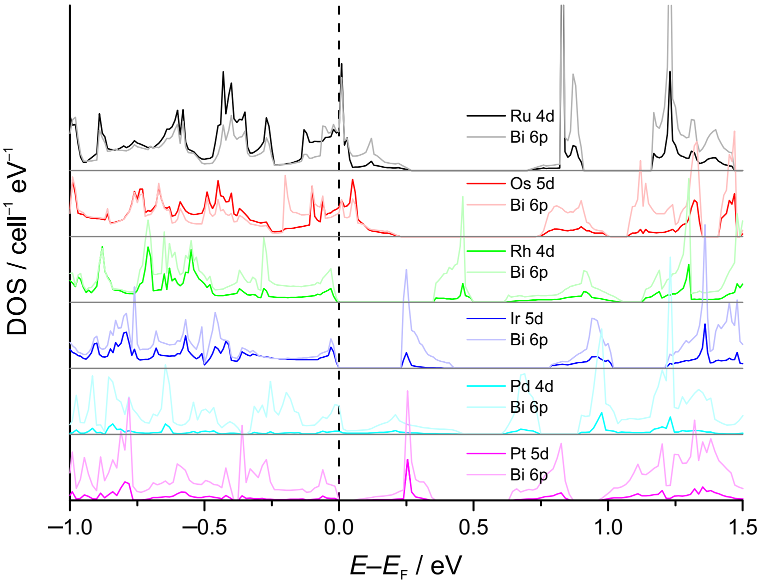

Figure 4.20.: Partial DOS of the transition element d-states and the bismuth 6p-states for the six models with a valence-electron count equal to the one in the original honeycomb layer $[(Bi_4Rh)_3I]^{2+}$.

The sets of model parameters extracted from the scalar-relativistic FPLO-based calculations were found rather similar for all ILS. The decisive differences arise from the position of the onsite energies of the M d-orbitals relative to the onsite energies of the Bi p_z and p_{xy}-orbitals (as suggested above). Moreover, the similarity of all band structures enables us to derive all other models from the Rh-ILS by simply shifting the onsite energies of the M d-states with respect to the Bi p-orbitals (details in Supplement of reference 157). As a result, the evolution of the band structure upon M-substitutions can be traced qualitatively and quantitatively by means of just one parameter, the d-state onsite energy: the lowering of the d-state energies is chiefly responsible for the changes in the ILS band structure. Ordering from the highest onsite d-energy to the lowest yields the sequence Os, Ru, Ir, Rh, Pt and Pd.

Subsequently, the emergence of the topologically non-trivial state was analysed by switching on SOC. Continuously increasing the strength of the SOC, one can trace the evolution of the scalar-relativistic bands into their full-relativistic counterparts. Figure 4.21 presents a scheme of the most discernible situations. For Os and Ru the topologically active bands that form a cone at the K-point in the scalar-relativistic band structure reside near the bottom of a large gap. When the SOC is switched on, these crossing bands gap out, thus forming a very narrow topological region warped in the k-space. However, this region is located below a larger trivial gap that determines the trivial insulating character of the Ru- and Os-based models (if charged with two

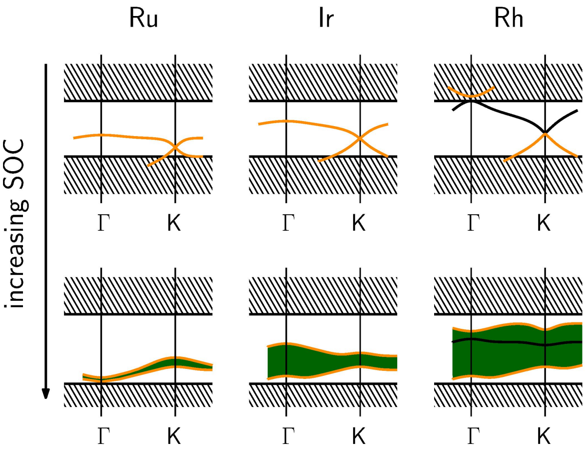

Figure 4.21.: Sketch of the evolution of the scalar- into the full-relativistic band structure by switching on the spin-orbit-coupling. The shaded areas represent the valence and conduction band continua. Orange bands are topologically active. Black bands are in-active (explanation see text). The green area is topologically non-trivial.

additional electrons). For Ir, the dispersion of the cone-forming bands is larger, so that a sizeable topologically non-trivial gap appears with SOC.

The remaining Rh-, Pt- and Pd-ILS fall into an essentially different category. Due to the wide energetic spread of the cone-forming bands a second band crossing occurs at the Γ-point. This additional crossing affects the topological activity of the adjacent bands and the upper part of the cone at the Γ-point becomes topologically active. The SOC gaps out both cones so that the topologically non-trivial region becomes even broader in energy than in the Ir-ILS and topologically in-active bands reside within this region.

From Rh to Pd more and more in-active bands are found within the topologically non-trivial region. Most likely the increasing energetic difference of the Bi p_z-p_z antibonding and bonding states allows for this trend, which can be traced by the spectral weight in the TB-model.

Complementary, this trend of decreasing onsite energies of the d-states is also reflected in real space in the chemical bonding, which was visualised and quantified via analysis of the electron localisability indicator (ELI-D) field. Previously this approach revealed two types of bonding basins for the triclinic structure of $Bi_{14}Rh_3I_9$. One was assigned to Rh–Bi interactions and the other corresponded to a three-centre bismuth interaction.[126] The first type of ELI-D basin is present in all six M-ILSs (yellow isosurface in Figure 4.22a) and accounts for the rigidity of this single honeycomb layer. Basin population, i.e. the number of electrons per bond, decreases in the same sequence in which the onsite energies lower from Os to Pd (Figure 4.22b). Ru and Os interact most strongly with bismuth, while Pt and Pd, which have their *d*-states filled, draw less electrons from the bismuth atoms and show weaker interactions.

Graphene with Strong Spin-orbit-coupling

The second type of ELI-D bonding feature is *only* present in the ILS with Rh, Ir, Pd, and Pt, i.e. in the topologically non-trivial phases. The basin attractor is located slightly off the plane formed by three bismuth atoms in both bases of each bismuth triangular prism (see green isosurface in Figure 4.22a). The evaluation of basin population shows that the strength of this bonding increases within the group and with the period number. The three-centre Bi−Bi bonding intensifies with the weakening of the M−Bi bonding, leaving more electrons on the Bi-site for homoatomic interactions. Thus, a correlation with the population of the M *d*-states can be established: Ru and Os form strong M–Bi bonds and contribute significantly to the states near the Fermi level, while Pd and Pt retreat from the Fermi level, which is then dominated by Bi−Bi bonding.

The intriguing finding is that at least one topologically non-trivial energy gap is found for all ILSs that show this three-centre bismuth bonding. The importance of this three-centre bismuth bond becomes even more striking when comparison is made between the hexagonal arrangement in the ILSs and graphene (Figure 4.22c). The position of the basin attractors matches with the positions of the carbon atoms. The topologically non-trivial M-ILSs can thus be considered as graphene analogues in a sense that three-centre bismuth bonds reside in place of the carbon atoms. As these bonding attractors are found on both sides of the honeycomb layer one might conclude that these basins can be compared to the lobes of the p_z-orbitals of the carbon atoms in graphene. Having a minimal TB-model at hand, one can evaluate whether these real-space similarities of the M-ILSs and graphene are also reflected in the electronic structure. The topological properties of the graphene lattice arise from the Dirac cone formed by p_z-orbitals, upon inclusion of SOC. The topological nature of the M-ILSs should similarly be related to a lattice arrangement of molecular orbitals (MOs) which are contributed by several bismuth atomic orbitals. An analysis of the band structure reveals that the Dirac-like cone occurring at the K-point is indeed related to an effective MO which combines six of the Bi p_z-orbitals into a single pseudo-p_z-orbital (Figure 4.22d). Therefore the cone observed at the Fermi level in the ILSs is to a notable extent analogous to the Dirac cone in graphene. Nevertheless it should be emphasised that the evolution of the topological gaps in the series cannot be solely attributed to Bi-p_z spectral weight. The situation in the ILSs

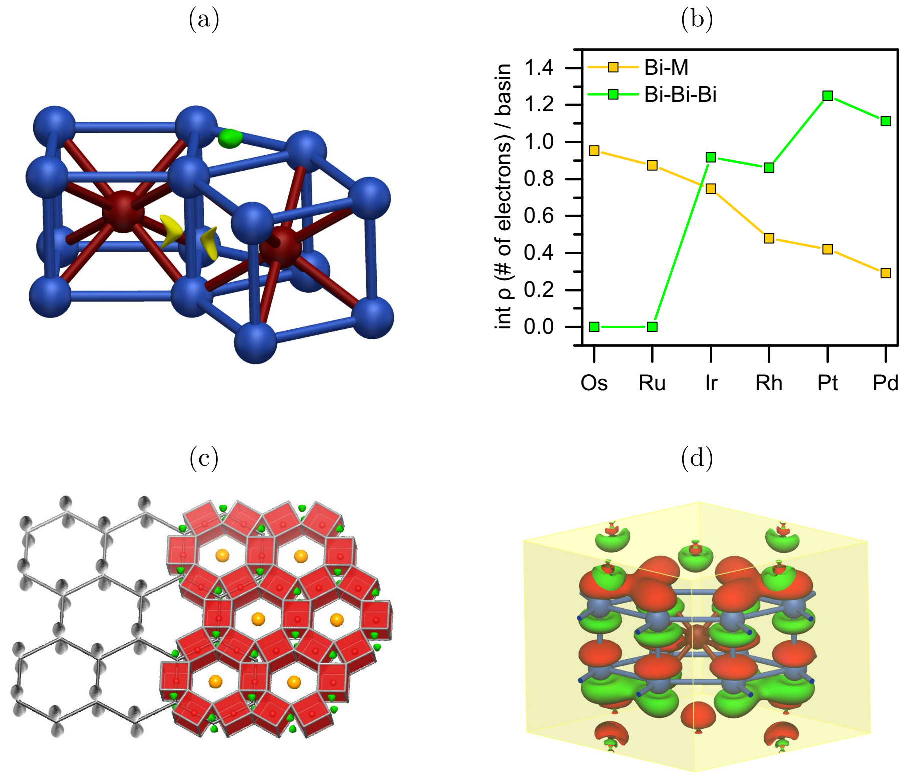

Figure 4.22.: (a) Two selected ELI-D localisation domains shown within an ILS structural fragment. One domain is depicted for each basin type: the Bi$-M$-bond (yellow) and the three-centre bismuth bond (green).
(b) Integrated electron density within these ELI-D basins for all M-ILSs (same colour code as for (a)).
(c) Overlay of structure of graphene (left, scaled by a factor of approx. 3.8) with sketches of the p_z-orbitals (grey) and the ILS (right) with the ELI-D localisation domains of the three-centre bismuth bond (green isosurface).
(d) Structural fragment with two Bi_6-prisms, indicating the spin-up component of the Γ-point wave function of a band with anti-bonding triangular MO weight. On each prism six Bi p_z-orbitals combine into a single pseudo p_z-orbital.

is more complex: although the Dirac cone in the scalar-relativistic band structure has significant Bi p_z-character, hybridisation with other states takes place, giving rise to further topologically active bands.

4.2.3. The Topologically Trivial Semimetals $Bi_{13}Pt_3I_7$ and $Bi_{13}Pd_3I_7$

Besides the honeycomb lattice with rhodium in the centres of the bismuth cubes, Section 4.2.2 has also established the platinum and palladium based nets as 2D-TIs, with two possible topologically non-trivial gaps, depending on the number of electrons. For both, two similar compounds were discovered ($Bi_{13}Pt_3I_7$ and $Bi_{13}Pd_3I_7$, see Section 4.1.3). The two different spacers, the iodido-bismuthate layer and the pure iodide layer, yield a charge of +3 for the honeycomb layer: $[(Bi_{8/2}M)_3I]^{3+}[BiI_4]^-[I^-]_2$. Compared to the rhodium compound $[(Bi_{8/2}Rh)_3I]^{2+}[(BiI_4)_2]^{2-}$ this still means two electrons more per sum formula, as each of the three platinum/palladium atoms has one valence electron more. Therefore, a single honeycomb layer within $Bi_{13}Pt_3I_7$ and $Bi_{13}Pd_3I_7$ is a 2D-TI with a band gap of 230 meV and 196 meV, respectively (Section 4.2.2 and Appendix: Figure A.26).

Nevertheless, the effect of stacking yields a completely different result for the 3D compounds compared to $Bi_{14}Rh_3I_9$, as the DOS (Figure 4.23) and the band structure (Figure 4.24) show. The palladium as well as the platinum compound become

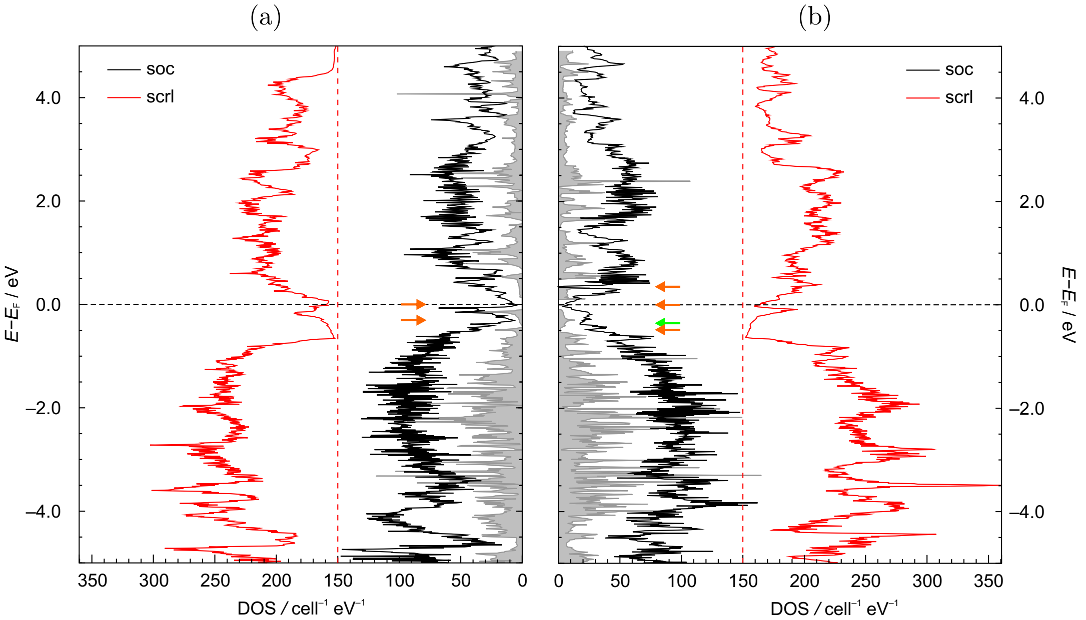

Figure 4.23.: Density of states (DOS) from scalar-relativistic (red) and full-relativistic (black) calculations for (a) $Bi_{13}Pt_3I_7$ and (b) $Bi_{13}Pd_3I_7$. The full-relativistic DOS of an isolated honeycomb layer $[Bi_{12}M_3I]^{3+}$, with M = Pt or Pd, as introduced in Section 4.2.2 is given as reference (grey). The charge of +3 corresponds to the situation as found in both compounds. Arrows mark pseudo-gaps (see also Figure 4.24).

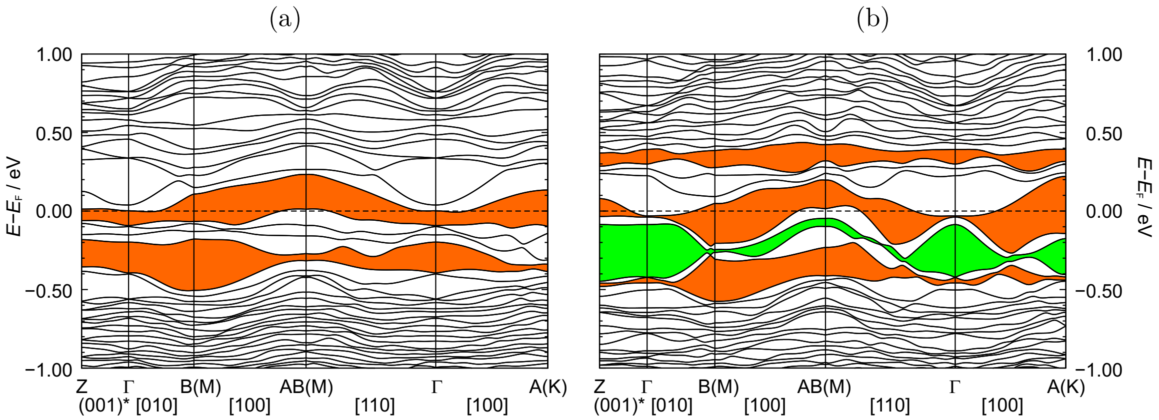

Figure 4.24.: Full-relativistic, electronic band structure of (a) $Bi_{13}Pt_3I_7$ and (b) $Bi_{13}Pd_3I_7$ along selected directions. The directions given in normal and square brackets refer to the conventional reciprocal and real space lattice, respectively. The ΓZ direction corresponds to the stacking direction of the layers. For pseudo-gaps which can be identified via the DOS (Figure 4.23) the colours for the warped gap (see Section 4.2.2) indicate whether the gap is topologically trivial (orange) or non-trivial with the strong Z_2-invariant being 1 (green).

semimetals with a typical pseudo-gap at the Fermi energy, visible in the DOS. Also the other formerly gaps of the isolated honeycomb layers become pseudo-gaps, despite the fact that the DOSs of the compounds still resemble very well the DOSs of the respective isolated honeycomb layers (Figure 4.23). At the same time, the semimetallic character is directly visible in the band structure, as no band directly connects the valence and the conduction bands. One finds a small hole pocket around the AB-point (which corresponds to the M-point of the pseudo-hexagonal Brillouin zone) and an electron pocket around the Γ-point for both structures (Figure 4.24). Furthermore, all these pseudo-gaps now correspond to *trivial* warped gaps, with one exception in the palladium case (Figure 4.24). This is in agreement with theoretical predictions for a stack of 2D-TIs, where pairwise coupling takes place.[55, 57] Compared to $Bi_{14}Rh_3I_9$ with all distances between two adjacent 2D-TIs being equally long, alternating long and short distances as in $Bi_{13}Pt_3I_7$ or $Bi_{13}Pd_3I_7$ are expected to lead to localisation of the surface states and therefore to a trivial band structure, although in this case the pairwise coupling additionally renders the former 2D-TIs semimetallic.[55, 57]

That both structures still have flat bands along the stacking direction ($\overline{\Gamma Z}$) is due to the mainly electrostatic interactions between the pairs of honeycomb layers and the good screening by the iodido-bismuthate layers. Nevertheless, although the bands along $\overline{\Gamma Z}$ are flat in both cases, the positions of the bands relative to the Fermi level differ slightly. This seems to be a result of slightly different dispersions of the bands especially along the $\overline{\Gamma\text{B}}$ direction, which is the propagation direction of the iodidobismuthate strands. In $Bi_{13}Pd_3I_7$ the last and the second-to-last fully filled band are split by approximately 350 meV at the Γ-point and almost touch each other very close to the edge of the first Brillouin zone in the direction of B. On the contrary, the same bands in $Bi_{13}Pt_3I_7$ have almost no dispersion and are separated at each k-point by less than 100 meV. The very same reason leads to the mentioned difference of a non-trivial pseudo-gap in $Bi_{13}Pd_3I_7$, while in $Bi_{13}Pt_3I_7$ at the same energy no pseudo-gap is present. Nevertheless, the similarities prevail and therefore the physical measurements will be discussed for both compounds together.

The intriguing finding, that only by changing the stacking sequence from $Bi_{14}Rh_3I_9$ with one spacer to $Bi_{13}Pt_3I_7$ and $Bi_{13}Pd_3I_7$ with two different spacers changes the topological properties, will be elaborated in a separate Section (4.2.4) after discussion of the basic physical properties of the platinum and palladium compound.

The resistivity versus temperature behaviour of $Bi_{13}Pt_3I_7$ measured for two crystals, a platelet and an elongated plank is shown in Figure 4.25. In both cases after an increase of the resistivity on cooling, the curve runs through a maximum and decreases again down to approximately 4 K, when both samples become superconducting. This behaviour is in good agreement with the calculation, as for a semimetal with a pseudo gap a low carrier concentration is expected, which means that thermally excited electrons give a significant contribution to the conduction at high temperatures. This contribution decreases on cooling (similar as in a semiconductor and in opposite to a normal metal). On the other hand, the mobility of the electrons increases on cooling and after the number of carriers stays almost constant (no significant thermal excitations, only the electrons at the Fermi level contributing) this effect gives a falling resistivity on cooling (as in a normal metal).

The exponential decrease of charge carriers down to approximately 100 K followed by a plateau can be traced with the Hall voltage (Figure 4.26a). In good approximation the Hall voltage is inverse proportional to the number of charge carriers and can be calculated with the following equation:

$$U_{Hall} = A_{Hall}\frac{B_{\perp}I}{d},$$

with

$$A_{Hall} = -\frac{1}{ne}.$$

Where U_{Hall} is the Hall voltage measured perpendicular to the applied current I and

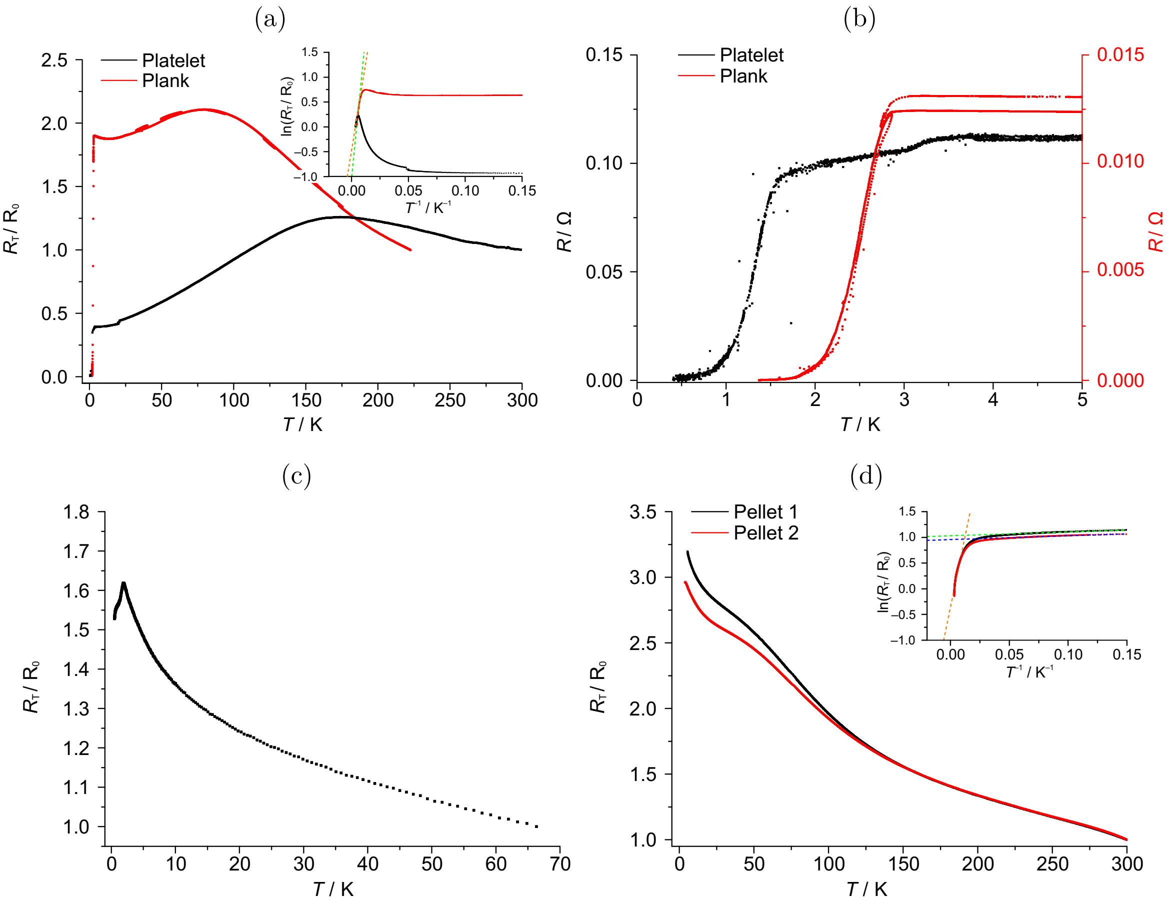

Figure 4.25.: Resistivity versus temperature behaviour for (a) a platelet and an elongated plank of $Bi_{13}Pt_3I_7$ with (b) zoom in the region of the superconducting transition; (c) a pressed powder-pellet of $Bi_{13}Pt_3I_7$; (d) two pressed powder-pellets of $Bi_{13}Pd_3I_7$.
Insets in (a) and (d): Arrhenius plots of the resistivity with a fit for the intrinsic and extrinsic (latter only palladium) dominated regions.

magnetic field $B_\perp$, A_{Hall} is the Hall coefficient, d is the thickness of the sample and n is the charge carrier density and e the elementary charge. This equation is only valid for a perfect Van-der-Pauw setup and with only one type of charge carriers. Nevertheless, for a relative comparison of the number of charge carriers the Hall voltage can still be used and nicely confirms the theory for the resistivity maximum.

Therefore, this maximum could be an indicator of the purity of the sample, as a higher number of impurities should yield an extended semiconductor-like behaviour, which means that the maximum would be shifted to lower temperatures. This is observed for the measurement on the platelet compared to the plank, with the respective maximum at 160 K versus 80 K. This interpretation also coincides with Arrhenius-fits within the semi-conducting-like regions (inset Figure 4.25a), which yield band gaps of

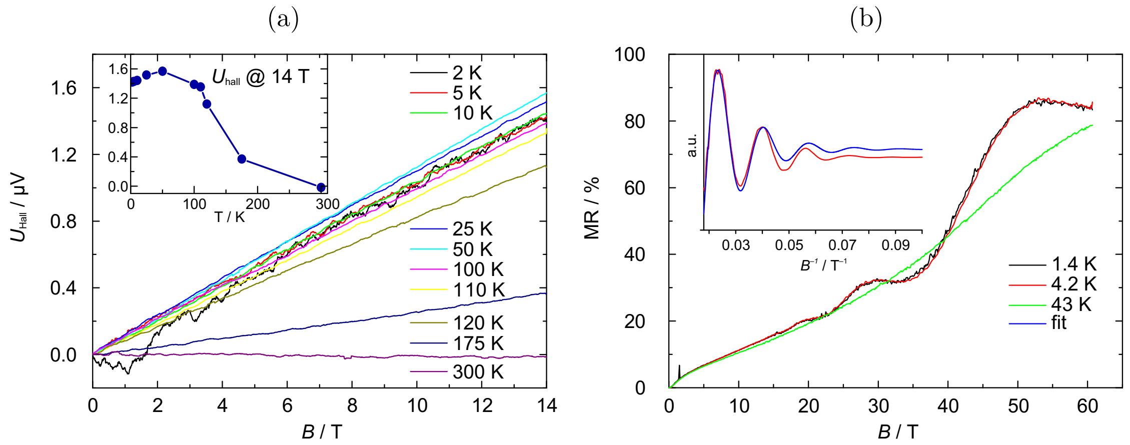

Figure 4.26.: (a) Hall voltage versus magnetic field at different temperatures. Inset: The Hall voltage at 14 T versus temperature.
(b) Magnetoresistance (MR) versus magnetic field at different temperatures.

40 meV and 24 meV, respectively, underlining the higher number of impurities for the plank.

Unfortunately, for $Bi_{13}Pd_3I_7$ no crystals of sufficient size for a four-point measurement could be grown (Section 3.3.3). Therefore, the resistivity versus temperature data were acquired on two pressed powder-pellets (Figure 4.25d). The measurement shows semi-conductive behaviour from room temperature down to approximately 2 K, which would be in contradiction to the calculated semimetal (Figure 4.23b and 4.24b). Nevertheless, the resistivity increases only by a factor of three and the intrinsic band gap from an Arrhenius plot is only 18 meV (inset Figure 4.25d), which both is relatively small (cf. Bi_4RhI_2 in Section 5.2.2) and might actually hint at a semimetal as was calculated and also found in the case of $Bi_{13}Pt_3I_7$. Even more convincing, a measurement of the resistivity on a pressed powder-pellet of the platinum compound shows the same behaviour with a constantly rising resistance and *no* maximum around 100 K (Figure 4.25c).[3] Reviewing the interpretation of the resistivity curve of the platinum crystals, a possible explanation would be that the mobility of the charge carriers for the measured powders of $Bi_{13}Pd_3I_7$ and $Bi_{13}Pt_3I_7$ does not increase as strongly as in the $Bi_{13}Pt_3I_7$ crystals. The mobility is proportional to the mean free path of the charge carriers and as the latter might become in the order of the size of the grains in the powder at low temperatures, the additional scattering at the grain boundaries would prevent a further increase of the mean free path. Therefore, the reason which

---

[3] In contrast to the palladium-pellet, the $Bi_{13}Pt_3I_7$-pellet was measured to temperatures below the superconducting transition and therefore the resistivity falls after this phase transition.

Table 4.1.: Results of the magnetic measurements for $Bi_{13}Pt_3I_7$ and $Bi_{13}Pd_3I_7$ from several fits (Figure 4.27b, Appendix: Figure A.28 and A.29). The ferromagnetic part of the magnetisation at weak fields M_g is given at 5 mT for $Bi_{13}Pt_3I_7$ and at 2 mT for $Bi_{13}Pd_3I_7$. Data for a Curie-Weiss fit were only available for $Bi_{13}Pd_3I_7$, therefore a separate dia- ($\chi_g(dia)$) and paramagnetic ($\frac{C}{T-\Theta}$) part of the susceptibility are only available in that case. C is the Curie constant and Θ the Curie temperature.

	M_g(ferro)		χ_g(dia+para) =	χ_g(dia) +	$\frac{C}{T-\Theta}$	
	saturated	weak field			C	Θ
	/10^{-4} emu g^{-1}		/10^{-7} emu g^{-1}		/10^{-6} emu g^{-1}	/K
			$Bi_{13}Pt_3I_7$			
sample 1	9	5	−2.44	–		
sample 2	12	3	−3.55	–		
			$Bi_{13}Pd_3I_7$			
sample 1	54	3	−2.23	−3.31	1.2	−8
sample 2	291	48	−2.77	−6.47	46.8	−135

leads to a decreasing resistivity at low temperatures and a maximum in the resistivity curve for the crystals of $Bi_{13}Pt_3I_7$ would not hold for the measurements conducted on powders.

A final verification of the interpretation of the resistivity curves and the band structure could be done by measuring the Fermi surface of the respective compounds. In the case of $Bi_{13}Pt_3I_7$ a first step in this direction has been taken, as crystals of sufficient quality were grown and showed strong Shubnikov-de-Haas oscillations in the resistivity versus magnetic field curve at 4.2 K (Figure 4.26b). The oscillation frequency, or better the period is inversely proportional to the (reciprocal) area enclosed by the extremal orbit of the Fermi surface S perpendicular to the magnetic field $\vec{B}$:

$$\Delta\left(\frac{1}{B}\right) = \frac{2\pi e}{\hbar S}.$$

From the inset of figure 4.26b one can extract $S = 1.4 \times 10^{13}\,\mathrm{cm}^{-2}$. In relation to the area of the first Brillouin zone in the $\vec{a^*}$-$\vec{b^*}$ plane, which is about $7.3 \times 10^{13}\,\mathrm{cm}^{-2}$, this is a very realistic value and agrees qualitatively with the calculations, judging from a visual examination (Appendix: Figure A.27). A final comparison of experiment and calculation makes measurements under various angles necessary, as well as a much finer k-mesh for the calculations of the Fermi surface, as has been used so far.

Except for the maximum in the resistivity curve, which can be explained with the calculated band structures and DOSs, in the case of $Bi_{13}Pt_3I_7$ superconductivity is

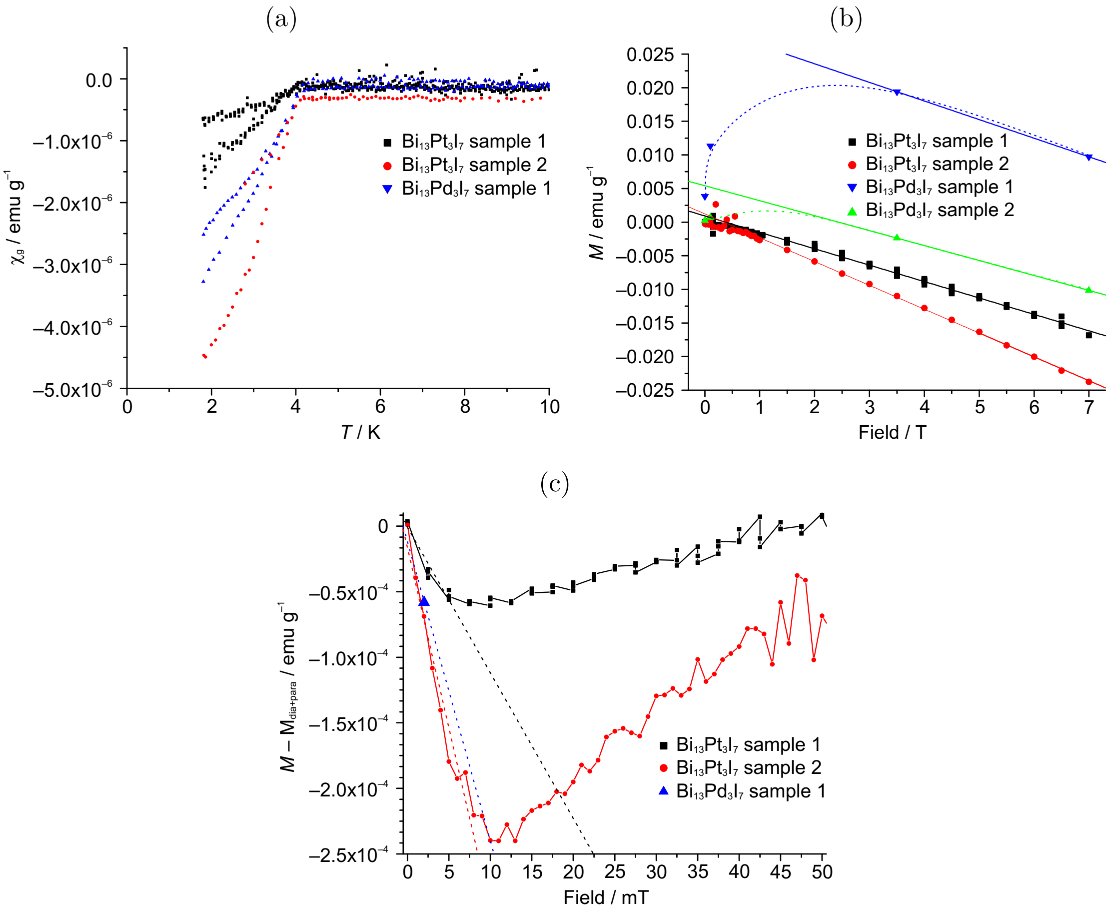

Figure 4.27.: (a) Magnetic susceptibility versus temperature at low temperatures of $Bi_{13}Pt_3I_7$ (two samples) at 5 mT and of $Bi_{13}Pd_3I_7$ (one sample) at 2 mT. (b) Magnetisation versus magnetic field at 2 K to determine the dia- (and para-) magnetic susceptibility, as well as the (saturated) ferromagnetic part of the magnetisation (linear fit at fields > 1 T) for $Bi_{13}Pt_3I_7$ and $Bi_{13}Pd_3I_7$ (two samples each).
(c) Magnetisation versus magnetic field at 2 K at small fields after correction for dia- (non-superconducting), para- and ferromagnetism to determine the volume fraction that becomes superconducting within the Meissner phase for $Bi_{13}Pt_3I_7$ (two samples) and $Bi_{13}Pd_3I_7$.

observed in (Figure 4.25b). To further elucidate the superconducting behaviour, also in the case of the palladium compound for which the resistivity was not measured to comparable low temperatures, magnetisation data were acquired. The magnetic susceptibility measured at small fields and corrected for dia- (except for the superconducting part), para- and ferromagnetism (Table 4.1 and Figure 4.27b, Appendix: Figure A.28 and A.29) shows a superconducting transition for both, the platinum and the palladium compound, at around 4 K (Figure 4.27a). This transition, with similar transition temperatures, is observed independently of the impurities present in the sample. The two $Bi_{13}Pt_3I_7$ samples have only minor ferromagnetic impurities but different paramagnetic impurities, which lead to a magnetic susceptibility at high fields which is less or more diamagnetic (sample 1 and sample 2 in Table 4.1, respectively). On the other hand, the saturated ferromagnetic magnetisation is much higher in the case of the palladium samples pointing to more ferromagnetic impurities, but the magnetic susceptibilities at high fields are very similar (Table 4.1). Comparing the derived susceptibilities at high fields for all four samples, with the ones calculated from the diamagnetic increments[158] ($-1.9 \times 10^{-7}\,\mathrm{emu\,g^{-1}}$ for $Bi_{13}Pd_3I_7$ as well as $Bi_{13}Pd_3I_7$) the results seem to agree well. Nevertheless, a Curie-Weiss fit to a susceptibility plot over the temperature for high fields in the case of $Bi_{13}Pd_3I_7$ (7 T; Appendix: Figure A.28) reveals paramagnetic impurities and a significantly different diamagnetic susceptibility for sample 1 and sample 2 of $Bi_{13}Pd_3I_7$ (Table 4.1). The latter is three times as large as the sum of the diamagnetic increments and hints to additional diamagnetic impurities. Therefore, all data have to be handled with care, as several intermetallic phases (BiPt, $Bi_2Pt(cP12)$) as well as thin films of elemental bismuth become superconducting around 4 K.[159–162]

Nevertheless, as crystals of $Bi_{13}Pt_3I_7$ become superconducting in the resistivity measurements and the onsets for the superconductivity in the magnetisation measurements are independent of the impurities in three of the four samples and for the fourth sample the impurities show up very clearly (Appendix: Figure A.29d), the volume fraction of the Meissner phase was determined for the first three samples (Figure 4.27c). From the slope of the ferro-, dia- and paramagnetically corrected data at small magnetic fields one gets with the density ρ and molar mass M of $Bi_{13}Pt_3I_7$ ($\rho = 9.17\,\mathrm{g\,cm^{-3}}$, $M = 4190\,\mathrm{g\,mol^{-1}}$) and $Bi_{13}Pd_3I_7$ ($\rho = 8.46\,\mathrm{g\,cm^{-3}}$, $M = 3924\,\mathrm{g\,mol^{-1}}$) superconducting volume fractions of 0.01 % and 0.03 % for the two $Bi_{13}Pt_3I_7$ samples, respectively and 0.03 % for the $Bi_{13}Pd_3I_7$ sample (sample 1). As these volume fractions are very small, one might actually account the observed superconductivity to certain impurities, which are still able to form a closed path in the cases of the $Bi_{13}Pt_3I_7$ crystals by accumulating at the surface. Nevertheless, two other explanations are possible. First, one has to consider the London penetration depth, which could in case of a powder, with a relatively high surface to volume ratio, lead to a very small superconducting volume fraction. As a very rough approximation, one could consider the London penetration depth of $YBa_2Cu_3O_7$, which are amongst the longest ever reported, to get an upper limit for the resulting particle size:

$$\frac{V_{superconduction}}{V_{all}} = 1 \times 10^{-4} \text{ to } 3 \times 10^{-4}$$

$$\begin{aligned} V_{superconduction} &= N_{particles} \cdot {}^{4}\!/\!{}_{3}\pi (r_{particle} - \lambda_L)^3 \\ V_{all} &= N_{particles} \cdot {}^{4}\!/\!{}_{3}\pi r_{particle}^3 \end{aligned}$$

$$\Rightarrow r_{particle} = \frac{\lambda_L}{1 - \sqrt[3]{\frac{V_{superconduction}}{V_{all}}}} = \frac{894\,\text{nm}}{1 - \sqrt[3]{1 \times 10^{-4} \text{ to } 3 \times 10^{-4}}} \approx 1\,\mu\text{m}$$

where $N_{particles}$ is the number of particles, $r_{particle}$ is the (hypothetical) radius of the spherical particles and λ_L is the London penetration depth.[76, 163] The size of 1 µm is very small for particles of a "normal" powder. Still, one could further assume that the temperatures down to which the data where measured are still very close to the critical temperature T_c, which implies a much longer penetration depth.[76] Unfortunately, 2 K is the lowest temperature at which the magnetic properties were determined. Possibly, the volume fraction of the superconducting phase will rise significantly at lower temperatures.

But one might also think of a different explanation. This second explanation aims at the structure itself and at the possibility that only the surface becomes superconducting. This idea is justified by the fact, that the former one-dimensional topologically protected states of the isolated honeycomb layers are gaped by the pairwise coupling in the three-dimensional stacks, but nevertheless, this gaping might be in the order of the superconducting gap. Therefore, these surface states, which have minor influence at high temperatures due to being gaped, might actually be the reason for the superconducting behaviour. As the penetration depth of the edge states p was determined to be approximately 1 nm (Section 4.2.4) one can estimate the radius

$r_{particle}$ of (hypothetical) spherical shaped particles:

$$\frac{V_{superconduction}}{V_{all}} = 1 \times 10^{-4} \text{ to } 3 \times 10^{-4}$$

$$\begin{aligned} V_{superconduction} &\approx A_{surface} \cdot p = N_{particles} \cdot A_{particle} \cdot p = N_{particles} \cdot 4\pi r_{particle}^2 \cdot p \\ V_{all} &= N_{particles} \cdot V_{particle} = N_{particles} \cdot {}^4\!/_3 \pi r_{particle}^3 \end{aligned}$$

$$\Rightarrow r_{particle} = \frac{3p}{\frac{V_{superconduction}}{V_{all}}} = \frac{3 \cdot 1\,\text{nm}}{1 \times 10^{-4} \text{ to } 3 \times 10^{-4}} = 10\,\mu\text{m to } 30\,\mu\text{m}$$

with $N_{particles}$ being the number of particles. In contrast to 1 µm derived from the first explanation, the range of 10 µm to 30 µm seems quite realistic for a powder. That makes this theory at least plausible.

The resistivity measurements are in good agreement with the calculated band structures and DOS and confirm the similar electronic structures of the two compounds $Bi_{13}Pt_3I_7$ and $Bi_{13}Pd_3I_7$. The differences which have been observed can be attributed to the difference of a powder compared to a crystal. The overall agreement of experiment and calculation also suggests that the predicted changes in the topological properties from the (2D) isolated layer structures to the stacked (3D) structures are true, which will be further elaborated in the following Section. The measured superconducting transition was examined by magnetic measurements and seems either to be caused by impurities or probably by an unusual intrinsic property of the electronic structure.

4.2.4. Non-trivial Edge Channels and the Influence of the Environment on the Topological Properties[164]

Having the honeycomb network in $Bi_{14}Rh_3I_9$ identified as the 2D-TI being responsible for the non-trivial properties, a characterisation of the material as weak 3D-TI should be possible on the surface of respective crystals via STM and scanning tunnelling spectroscopy (STS). One should be able to reveal the edge channels predicted for weak 3D-TIs on “dark surfaces”,[60] which is the (0 0 1) surface in this structure. Furthermore, as structures with the same 2D-TI are at hand (with other platinum-metals in the cube centre; see Section 4.2.2), an investigation of $Bi_{13}Pt_3I_7$ shows the influence of the environment, namely the spacer separating these honeycomb layers, on the non-trivial TI properties.

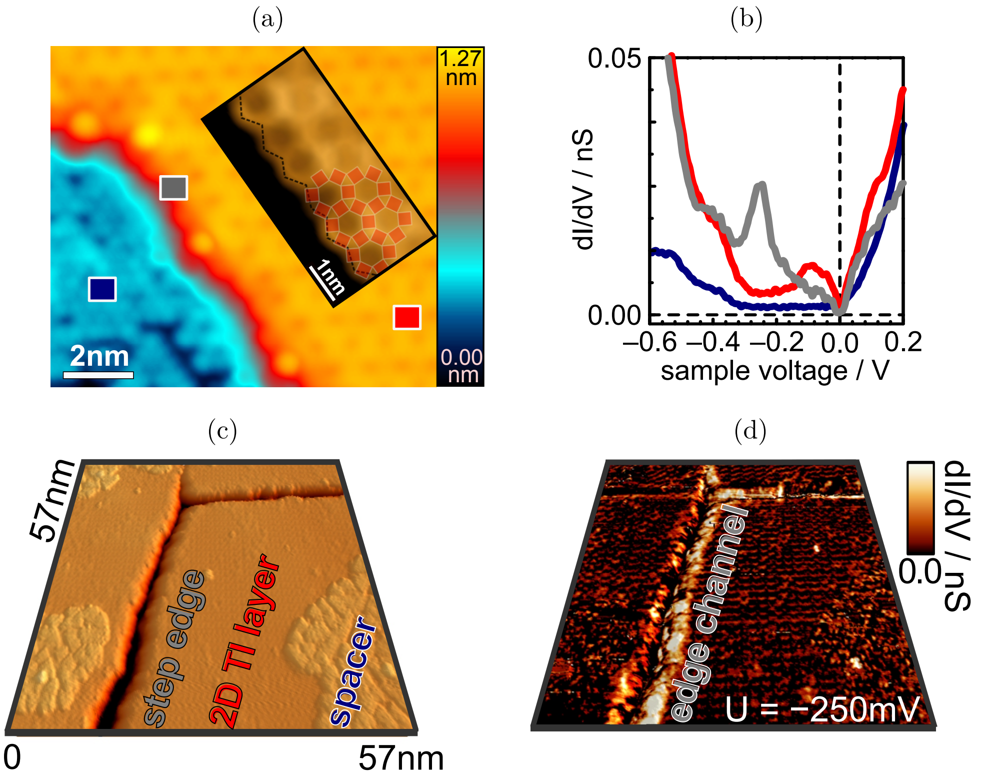

Figure 4.28.: (a) Squares mark the regions, where the correspondingly coloured ${}^{dI}/_{dU}(U)$ spectra in (b) were aquired ($U_{stab} = 0.8\,\mathrm{V}$, $I_{stab} = 100\,\mathrm{pA}$, $U_{mod} = 4\,\mathrm{mV}$). Notice the linearly vanishing ${}^{dI}/_{dU}$ intensity around E_F , which is attributed to a two-dimensional Coulomb gap of Efros-Shklovskii type.[165]
(c) and (d) STM and ${}^{dI}/_{dU}$ images, respectively, within the 2D-TI band gap of a region with step edges of the 2D-TI layer ($U = -250\,\mathrm{mV}$, $I = 100\,\mathrm{pA}$, $U_{mod} = 4\,\mathrm{mV}$). A strong ${}^{dI}/_{dU}$ intensity appears at the step edges, being on average different on the right (0.1 nS) and the left (0.07 nS), most probably due to the different stacking of the two step edges with respect to the underlying spacer layer $[\mathrm{Bi_2I_8}]^{2-}$ caused by the crystal structure.[134]

Figure 4.28b shows the locally measured differential conductivity ${}^{dI}/_{dU}(U)$, known to represent the local density of states (LDOS),[166] as recorded on the honeycomb layer (red curve), on the spacer layer (blue curve) and at the step edge of the honeycomb layer (grey curve). On the honeycomb layer, one finds a gap between $U = -180\,\mathrm{mV}$ and $U = -360\,\mathrm{mV}$.[4] This is in excellent agreement with the gap measured by ARPES at $-170\,\mathrm{mV}$ to $-370\,\mathrm{mV}$ below the Fermi level E_F (see Section 4.2.1 and reference 126). Importantly, there is a strong ${}^{dI}/_{dU}$ intensity within this 2D-TI gap if measured

---

[4] The remaining intensity within the gap is explained in Section 2.2. A comprehensive discussion can be found in the Supplement of reference 164.

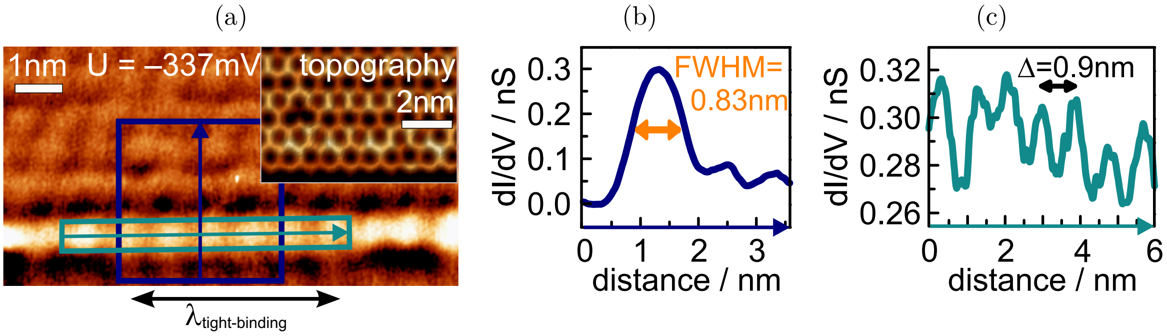

Figure 4.29.: (a) $^{dI}/_{dU}$ image within the bulk band gap ($U_{stab} = -337\,\text{mV}$, $I_{stab} = 100\,\text{pA}$, $U_{mod} = 4\,\text{mV}$) of the step edge area shown in the inset as a STM image ($U = 0.8\,\text{V}$, $I = 100\,\text{pA}$). Rectangles and arrows mark the areas and directions, respectively of the profile lines shown in (b) and (c). The $\lambda_{tight-binding}$ marks the electron wavelength of the edge state at this particular energy as deduced from tight-binding calculations.[154]
(b) Profile line perpendicular to the step edge and averaged in the parallel direction over the blue rectangle in (a) with the full-width half-maximum (FWHM) of the edge state marked.
(c) Profile line along the step edge taken from the green rectangle in (a) with the marked peak distance corresponding to the size of one unit cell.

at the step edge. This indicates the edge state. The peak maximum is in the lower part of the band gap, in accordance with the dispersion from tight-binding calculations.[154] A larger gap is revealed for the spacer layer, as expected. These properties are present on all areas of the sample with slightly different intensity distributions, which are attributed to different local chemistry or to a different density of states of the probing tip.

Figure 4.28d shows a spatially resolved $^{dI}/_{dU}$ map corresponding to the topography of Figure 4.28c and measured at a sample voltage within the band gap of the 2D-TI. Bright stripes at all step edges, mostly being about 15° off from the zigzag direction, indicate the presence of an edge mode, as also found on all other step edges of the honeycomb 2D-TI layer.

Another example of the edge state is shown in Figure 4.29a, where its Bloch-type character appears as an oscillation with unit cell periodicity along the zigzag direction (Figure 4.29c). A profile line across the edge state exhibits a full-width at half-maximum (FWHM) of only 0.83 nm (Figure 4.29b). This is an upper limit due to possible convolution effects with the tip shape. Thus, the edge state is confined to a single unit cell (width = 0.92 nm), as predicted by tight-binding calculations.[154] Such a width is much smaller than for edge states of the buried 2D-TI made of HgTe quantum wells (edge state width ≈ 200 nm[62, 167]), implying the possibility of con-

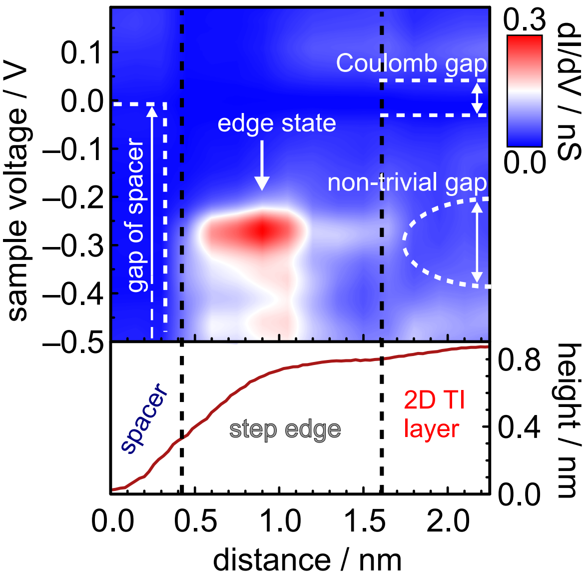

Figure 4.30.: Colour plot of $dI/dU(U)$ spectra taken across the step edge. Three different lateral regions are separated by dotted lines and labelled within the topographic profile below. Different energetic features are marked.

structing much smaller devices. Theory predicts that the helical conduction remains robust, mostly for step edge heights containing an odd number of exposed stacks, and is even stabilised by disorder,[56, 59] where it should be noted that for an even number of stacks a finite size gap can open.[60] Thus, simply scratching the surface tends to induce one-dimensional electron channels with a robust conductivity of at minimum e^2/h.[55]

Moreover, the intensity fluctuations of the edge state in Figure 4.29a along the edge are small, as expected for the prohibited backscattering. To sustain this assumption, the electron wavelength as deduced from tight-binding calculations[154] $\lambda_{\text{tight-binding}}$ was added. Obviously, there is no structure with periodicity $\lambda_{\text{tight-binding}}/2$ (that is, no standing electron waves), in remarkable contrast to conventional one-dimensional electron systems, where such oscillations exhibit LDOS intensity oscillations close to 100 %.[168]

Next, it is investigated, whether the edge state covers the whole non-trivial band gap, as predicted by topology. Figure 4.30 is a colour-coded representation of the energy-dependent LDOS across the step edge. It reveals a pronounced edge state intensity throughout the whole non-trivial band gap and slightly weaker intensity even in the energy region below, as expected from tight-binding calculations.[154] These characteristics have been found for all ten probed step edges with lengths from 6 nm to 40 nm, which is shown in detail in reference 164.

To further consolidate the topological character of the edge states in $Bi_{14}Rh_3I_9$,

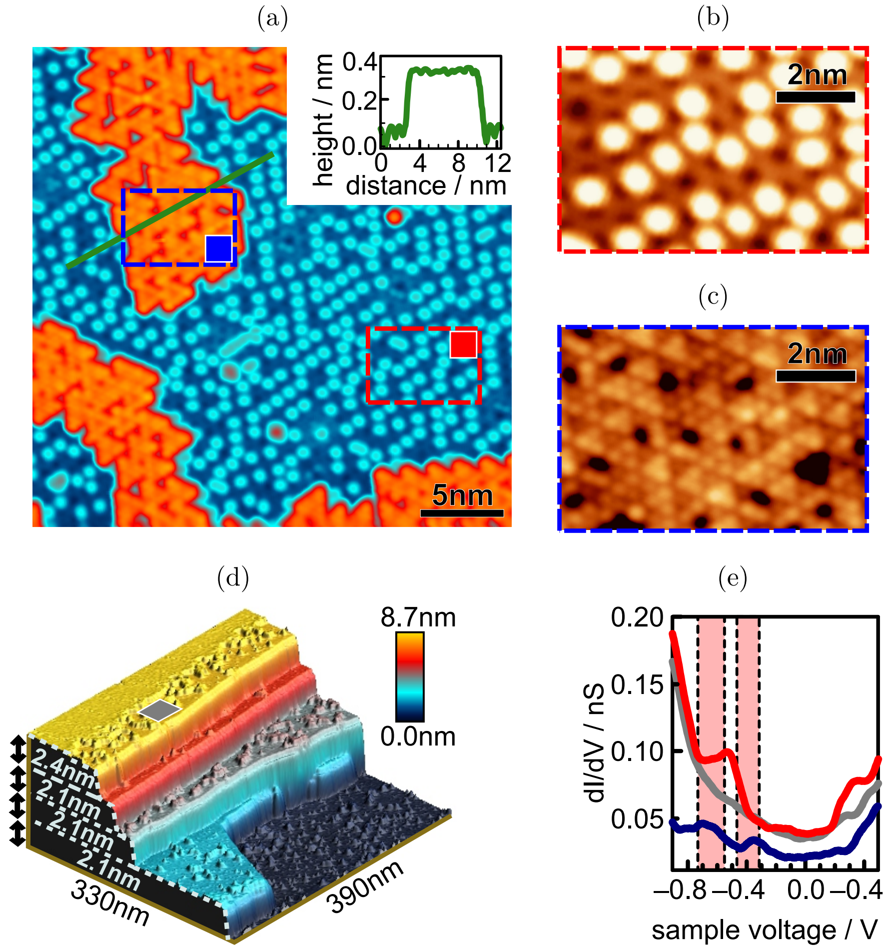

Figure 4.31.: (a) STM image ($U = 1\,\mathrm{V}$, $I = 100\,\mathrm{pA}$) of cleaved $\mathrm{Bi_{13}Pt_3I_7}$. Inset: height profile along the green line.
(b) and (c) Zoomed-in view of the red (b) and blue (c) dashed boxes in (a) showing the honeycomb (2D-TI) layer and the iodido-bismuthate layer, respectively. The honeycomb layer has adatoms (most probably iodide ions) on top. In (b) $U = 0.6\,\mathrm{V}$, $I = 100\,\mathrm{pA}$ and in (c) $U = 1\,\mathrm{V}$, $I = 100\,\mathrm{pA}$.
(d) STM image ($U = 1\,\mathrm{V}$, $I = 100\,\mathrm{pA}$) showing step heights of one unit cell (2.1 nm).
(e) Local ${}^{dI}/_{dU}(U)$ spectra ($U_{stab} = 1\,\mathrm{V}$, $I_{stab} = 100\,\mathrm{pA}$, $U_{mod} = 8\,\mathrm{mV}$) recorded at the positions exemplarily marked by the correspondingly coloured squares in (a) and (d). (Pseudo-) band gaps deduced from ARPES[164] and the density of states (DOS) (Section 4.2.3) are marked in red.

the very similar system $Bi_{13}Pt_3I_7$ was investigated, where Rh is replaced by the heavier Pt. The chemical composition is slightly different, such that every second spacer layer is replaced by a single layer of iodide ions (see Section 4.1 for details). The honeycomb layer is again a 2D-TI, as revealed by DFT (details see Section 4.2.2), whereas the compound $Bi_{13}Pt_3I_7$ itself is semimetallic and topologically trivial (see Section 4.2.3). The two different spacers in $Bi_{13}Pt_3I_7$ lead to an alternating coupling between adjacent 2D-TI layers, giving rise to a "dimerisation". Theoretically it has been shown that such a dimerisation can render a topological gap trivial.[55, 57]

STM images of the cleaved surface of $Bi_{13}Pt_3I_7$ (Figure 4.31a) again exhibit two different layers, one with hexagonally arranged spots (Figure 4.31c), triangularly reconstructed and with defects, identified as the insulating $[Bi_2I_8]^{2-}$ spacer and the other with a honeycomb structure (Figure 4.31b) rendering it the 2D-TI. The iodido-bismuthate layer as surface looks the same as in $Bi_{14}Rh_3I_9$. The 2D-TI layer on the other hand exhibits single atoms on top, most probably remaining iodide ions from the spacer, which is different compared to the 2D-TI surface on $Bi_{14}Rh_3I_9$ crystals, which had no adatoms. This could be a result of the higher charge of the honeycomb (2D-TI) layers in $Bi_{13}Pt_3I_7$, which becomes obvious when comparing the structured formulas: $[(Bi_{8/2}Pt)_3I]^{3+}[I^-]_2[BiI_4]^-$ and $[(Bi_{8/2}Rh)_3I]^{2+}[(BiI_4)_2]^{2-}$. Interestingly, such iodide ions are absent within the last two unit cells close to the zigzag step edges (Figure 4.31d and 4.32b, topography). Pure iodide layers, which are the second spacer besides the iodido-bismuthate layer, have not been observed, which hints at the strong interactions between two adjacent honeycomb layers separated by a pure iodide layer. Therefore, most step heights (Figure 4.31d) cover a complete unit cell of the dimerised layers in the stacking direction (2.1 nm). Two pseudo gaps, which were identified by ARPES[164] and in the DOS, are found to be trivial in DFT calculations, albeit originating from non-trivial gaps of the 2D-TI (Section 4.2.2 and 4.2.3: Figure 4.19, 4.23 and 4.24). In agreement, STS shows no edge states within these band gaps (Figure 4.31e and 4.32b) on any of the ten step edges probed.

In Figure 4.32 step edges of the honeycomb (2D-TI) layer on the surface of $Bi_{14}Rh_3I_9$ (Figure 4.32a) and $Bi_{13}Pt_3I_7$ (Figure 4.32b) crystals are directly compared (identical contrast). While the edge state of $Bi_{14}Rh_3I_9$ is clearly apparent, no such state is observed for $Bi_{13}Pt_3I_7$. Thus, the dimerised structure of $Bi_{13}Pt_3I_7$, where stacks are built from paired 2D-TIs, is trivial without protected edge states, in accordance with the results from the DFT calculations and general theoretical considerations.

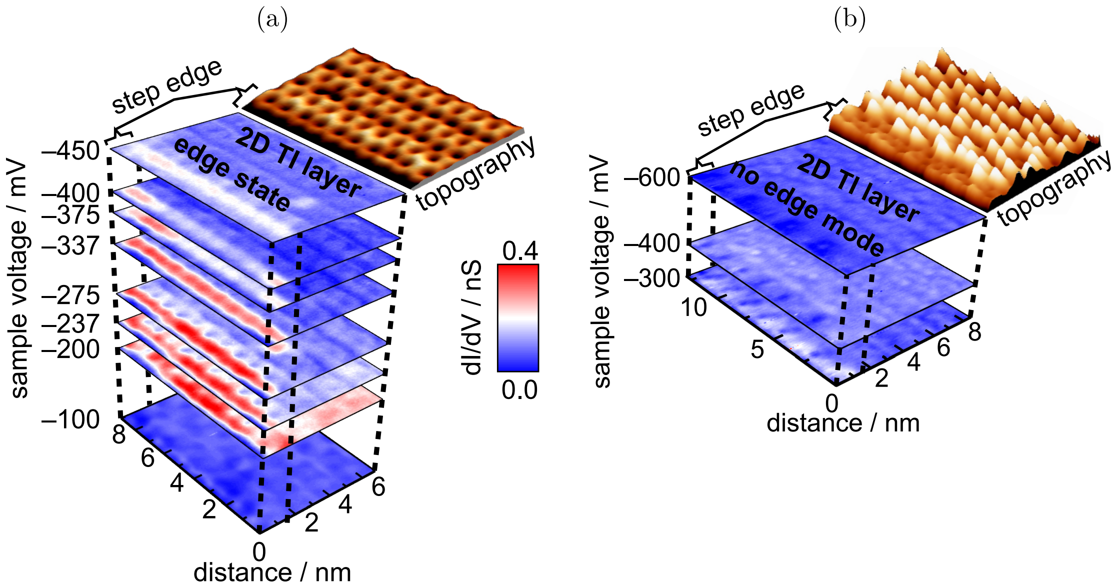

Figure 4.32.: (a) and (b) Stacked $^{dI}/_{dU}$ images ($I_{stab} = 100\,\mathrm{pA}$, $U_{mod} = 8\,\mathrm{mV}$) of the respective areas shown in the background STM image ($I = 100\,\mathrm{pA}$, $U = 0.6\,\mathrm{V}$) for (a) $\mathrm{Bi_{14}Rh_3I_9}$ and (b) $\mathrm{Bi_{13}Pt_3I_7}$. The data were recorded at voltages corresponding to the electronic (pseudo) band gaps of $\mathrm{Bi_{14}Rh_3I_9}$ (Figure 4.28b) and $\mathrm{Bi_{13}Pt_3I_7}$ (Figure 4.31e), respectively. In both cases the same contrast has been used.

4.2.5. Bismuth in the Rare +I Oxidation State within $\mathrm{Bi_{38}Pt_9I_{14}}$[144]

For $\mathrm{Bi_{38}Pt_9I_{14}}$ the unusual +I oxidation state of the bismuth atom in the $[\mathrm{BiI_2}]^-$ ion was in the focus of the investigations. Evidence of the charge of -1 for this three-atom anion, and consequently the bismuth +I oxidation state, was provided by DFT-based structure optimisations of isolated $[\mathrm{BiI_2}]$ molecules with different charges of 1, 0, -1, and -2. In all cases, symmetric molecules were obtained and the calculated $\mathrm{Bi-I}$ distances were 280.0 pm, 287.9 pm, 301.4 pm and 322.5 pm, respectively. The experimental mean value of 313.1 pm falls between the distances calculated for charges -1 and -2, excluding the oxidation state of +III for bismuth.

This was further corroborate via an analysis of the electronic structure. As absolute charges from quantum chemical calculations, whether from Mulliken population analysis or according to Bader's quantum theory of atoms in molecules (QTAIM), cannot be transcribed into oxidation states as assigned in chemistry, comparable systems with confirmed oxidation states are needed. Fortunately, with $\mathrm{Bi_{14}Rh_3I_9}$ and $\mathrm{Bi_{13}Pt_3I_7}$, such systems are known, with bismuth atoms in the iodido-bismuthate spacers having the common oxidation state of +III. The Mulliken analysis yields charges of +0.6 and

+0.5 for such bismuth atoms in $Bi_{14}Rh_3I_9$ and $Bi_{13}Pt_3I_7$, respectively. The Mulliken charge of +0.2 for the bismuth atom in the $[BiI_2]^-$ ion is much smaller, supporting the +I oxidation state. The QTAIM analysis gives similar results, as the bismuth(III) atoms in $Bi_{13}Pt_3I_7$ and $Bi_{14}Rh_3I_9$ yield a charge of +1, while the bismuth(I) atom of the $[BiI_2]^-$ ion has a QTAIM charge of +0.2. In combination with the above mentioned structure optimisation argument, this is strong evidence for bismuth in the +I oxidation state.

One might expect a magnetic moment for a bismuth(I) ion, as two degenerate 6*p*-orbitals should be occupied with unpaired electrons (triplet state). However, strong spin–orbit coupling lifts the degeneracy of the 6*p*-orbitals, resulting in an energetically lower $6p_{1/2}$ and two degenerate energetically higher $6p_{3/2}$-orbitals, i.e. a singlet state. Accordingly, the calculated magnetic moments of an isolated $[BiI_2]^-$ ion are $2\,\mu_B$ from a scalar-relativistic approach and $0\,\mu_B$ from a full-relativistic approach. In accordance with the predicted singlet state, measurements of the magnetic susceptibility of $Bi_{38}Pt_9I_{14}$ indicate diamagnetic behaviour with χ_{mol} matching the sum of diamagnetic increments of $-0.002\,\text{emu}\,\text{mol}^{-1}$.[158] At very low temperatures, impurities lead to a slightly increased magnetic susceptibility (Figure 4.33 and more detailed Appendix: Figure A.30). On the basis of this evaluation of the $[BiI_2]^-$ ion, one can assign a charge to the honeycomb layer. The structured formula of $Bi_{38}Pt_9I_{14}$ is then $[(Bi_{8/2}Pt^{4/3+})_3]_3[(I^-)_3]_3[BiI_2{}^-]_2[I^-]$. With a charge of +4/3 per $Bi_{8/2}Pt$ cube, the elec-

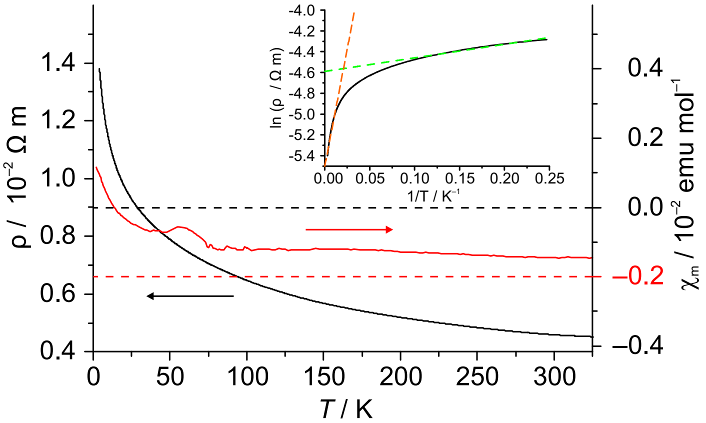

Figure 4.33.: Resistivity (black) and molar magnetic susceptibility (red) vs. temperature for $Bi_{38}Pt_9I_{14}$. A χ_{mol} of $-0.002\,\text{emu}\,\text{mol}^{-1}$ indicates the sum of the diamagnetic increments.[158] The inset is an Arrhenius plot for the resistivity behavior with linear fits for the extrinsically (green) and intrinsically (orange) dominated regimes. The feature in magnetisation near 50 K is very likely due to traces of molecular oxygen in the magnetometer.

tronic configuration in the intermetallic part of the honeycomb layer is the same as in $Bi_{13}Pt_3I_7$ or $Bi_{13}Pd_3I_7$. Moreover, this configuration means that a single honeycomb layer is a 2D-TI, as shown in Section 4.2.2.

In $Bi_{13}Pt_3I_7$, this 2D-TI state is cancelled out by the so-called "pairing" of TI layers via iodide layers. Within the structure, alternating thick iodido-bismuthate and thin iodide spacers create pairs of honeycomb layers that interact across the short distance and thereby become topologically trivial, as discussed in Section 4.2.3 and 4.2.4.[55, 56, 169] Moreover, this interaction turns the compound into a semimetal.

$Bi_{38}Pt_9I_{14}$, however, is a stack of honeycomb layers separated by only iodide spacers. The short interlayer distances provoke interactions between the TI layers. From the viewpoint of theory, different options are possible. It could mean that depending on the number of honeycomb layers the stack could be a TI (odd number of layers) or a trivial insulator (even number of layers).[55, 57, 169] Others proposed that the number of layers within the unit cell accounts for the topological character,[170] with an odd number yielding a TI. Therefore, the three-fold superstructure of $Bi_{38}Pt_9I_{14}$ is promising. The coupling strength should mainly influence the anisotropy and "shape" of the non-trivial surface state.[56, 171]

Before evaluating the question of topological behaviour, first it had to be determined whether $Bi_{38}Pt_9I_{14}$ is an insulator at all. The calculated density of states (DOS) suggests a metal, although with a significant drop of the DOS at the Fermi energy (Appendix: Figure A.31). This result is the same for a scalar-relativistic or full-relativistic approach with a local density approximation (LDA) or a generalised gradient approximation (GGA) exchange correlation potential and for calculations with one spin only or with spin polarisation. In contrast, resistivity measurements on powders indicate weakly semiconducting behaviour (Figure 4.33). From an Arrhenius plot (inset of Figure 4.33), an extrinsically dominated regime and an intrinsically dominated regime can be identified, with energy gaps of $\approx 0.2\,\mathrm{meV}$ and $8\,\mathrm{meV}$, respectively. These very narrow gaps could explain why the DFT-based calculations did not yield a gap at the Fermi energy, as this is a known issue of the method.[172]

Whether $Bi_{38}Pt_9I_{14}$ is a (narrow-gap) semiconductor or rather a semimetal, the question of topological non-trivial behaviour remains. As the calculations yield no gap, the actual character of the measured gap can potentially be identified only via ARPES, via STM, or maybe via ^{209}Bi nuclear magnetic resonance (NMR), as a correlation between topological nature and chemical shielding has been reported recently.[173] However, the very narrow gap will also hamper these experiments. At least the topological invariants for the highest fully occupied and all partially occupied bands at the

Fermi energy are non-trivial, and in three of four cases, the strong topological invariant is 1, meaning that $Bi_{38}Pt_9I_{14}$ could even be a strong 3D-TI (Appendix: Table A.56).

Conclusions

Full-relativistic calculations indicated that $Bi_{14}Rh_3I_9$ is a TI, the first experimentally realised material in the class of the weak 3D-TIs. The electronic band structure could be verified via ARPES, as the surface shows n-doping (Section 4.1.1) and hence the band structure around the Fermi energy is accessible. The drawback of the n-doped surface are the resulting metallic, instead of the expected semiconducting, transport properties. The scalar-relativistic calculations hinted at a strong similarity to graphene.

This similarity was investigated via an isolated layer model (ILS). This model retains all essentials of the electronic structure of $Bi_{14}Rh_3I_9$, confirming that the latter is a stack of 2D-TIs. Furthermore, the model allowed an investigation of the chemical bonding within the honeycomb layer and to establish a TB-model, both confirming the resemblance between the honeycomb layer and graphene beyond purely structural aspects. Additionally, a systematic substitution of Rh by the other platinum-metals within the ILS established besides the Rh-ILS the systems with Pd, Ir, and Pt as 2D-TIs.

Nevertheless, in agreement with theoretical predictions, the stacking of the 2D-TIs with two different spacers in $Bi_{13}Pt_3I_7$ and $Bi_{13}Pd_3I_7$ yields trivial semimetals. Alternating short and long distances lead to a pairwise coupling of the honeycomb layers and therefore gap out the surface states. Simultaneously, $Bi_{13}Pt_3I_7$ and $Bi_{13}Pd_3I_7$ showed signs of an unusual superconductivity.

Finally, STM and STS experiments were able to reveal the 1D edge states on the surface of the weak 3D-TI $Bi_{14}Rh_3I_9$. Strong support for the non-trivial topology of these states was found, e.g. that no edge states were observed for the structurally similar, but topologically different compound $Bi_{13}Pt_3I_7$.

In $Bi_{38}Pt_9I_{14}$ the honeycomb layers are exclusively separated by short distances, giving another interesting example of a stacking sequence of the 2D-TI. But as the compound was calculated to be metallic, an evaluation with respect to its topological properties was not possible, although transport experiments indicated a small-gap semiconductor. At the same time, strong evidence for bismuth in the rare oxidation state +I was found.

5. Further new Compounds in the Bi–Rh–I and Bi–Pt–I Phase Systems

5.1. $Bi_8Pt_5I_3$ and $Bi_{16}Pt_{11}I_6$[145]

5.1.1. Structure

$Bi_8Pt_5I_3$

X-ray diffraction on a single-crystal of $Bi_8Pt_5I_3$ revealed a monoclinic lattice with space group $C2/m$ and lattice parameters $a = 1850.7(2)\,\text{pm}$, $b = 391.46(3)\,\text{pm}$, $c = 1340.5(1)\,\text{pm}$, and $\beta = 113.28(1)^\circ$ at RT (details see Appendix: Table A.30 to A.34). All atoms reside on mirror planes. The crystal structure (Figure 5.1) is organised in layers parallel to $(2\,0\,\bar{1})$. Corrugated intermetallic layers ${}^2_\infty[Bi_8Pt_5]^{3+}$ alternate with monolayers of non-coordinating iodide ions ($\text{Bi}\cdots\text{I1} \geq 340.6\,\text{pm}$). The comparatively weak interlayer bonding facilitates mechanical cleavage and delamination (Appendix: Figure A.18). Yet, stacking faults do not occur because of the corrugation.

The platinum atoms are in square (Pt1), trigonal-prismatic (Pt2), or capped trigonal-prismatic coordination (Pt3) by bismuth atoms. Each bismuth atom is expected to be involved in largely delocalised multi-centre bonding to other bismuth

Table 5.1.: Selected interatomic distances /pm in $Bi_8Pt_5I_3$ at 298(1) K. Standard deviations are 0.1 pm.

Atoms	Distance	Atoms	Distance	Atoms	Distance
Pt 1 –Bi 1	4 × 284.4	Pt 2 –Bi 1	276.2	Pt 3 –Bi 2	2 × 289.6
–Pt 2	4 × 275.9	–Bi 1	290.6	–Bi 3	2 × 305.4
		–Bi 2	2 × 282.2	–Bi 4	2 × 276.5
Bi–Bi	≥ 330.9	–Bi 3	2 × 292.1	–Bi 4	279.2
Bi···I1	≥ 340.6	–Pt 3	275.0		

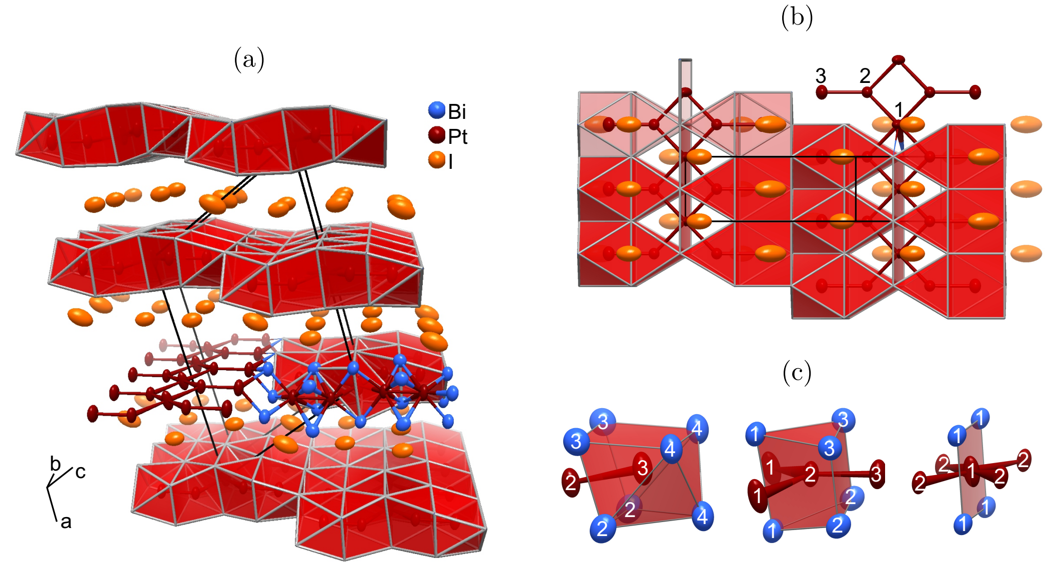

Figure 5.1.: Crystal structure of $Bi_8Pt_5I_3$: (a) view parallel to the layers, emphasising the platinum-centred bismuth polyhedra; For one stripe of connected platinum atoms the bismuth atoms were removed. (b) view perpendicular to the layers; (c) coordination of platinum atoms; ellipsoids represent 99 % probability.

atoms and three or four platinum atoms. The Bi – Bi distances ($\geq$ 330.9 pm; Table 5.1) and the number of neighbouring atoms are typical for such situations, although no bonding basins are found for the electron localisability indicator ELI-D.[131, 132] The Pt – Bi distances in the coordination polyhedra range from 276 pm to 305 pm, with an average of 287 pm. In the intermetallic compound Bi_2Pt($hP9$), which has a similar metals' ratio, the average Bi – Pt distance is 279 pm.[174] It might be noted that Bi_3Pt_2 is even closer in composition, however, only an average structure model with defect NiAs type is known. Inside the intermetallic layer, additional covalent bonding between platinum atoms defines flat stripes of five atoms width, which run parallel [0 1 0]. The number of Pt – Pt bonds is four for Pt1, three for Pt2, and one in the case of Pt3. The Pt – Pt distances fall into the narrow interval from 275.0 pm to 275.9 pm and hence are similar to the Pt – Pt distances in elemental platinum (277 pm)[175] but much shorter than in the platinum triangles in Bi_2Pt (299 pm).[174]

The largest displacement components of the platinum atoms are perpendicular to the Pt – Pt bonds. I1 has a much larger displacement parameter than I2, which corresponds to the difference of I1 $\cdots$ Bi (>363 pm) and I2 $\cdots$ Bi (>340 pm) distances. Upon cooling down to 150 K, the structure changes only marginally. The unequal thermal expansion coefficients ${}^{\Delta a}/_{(a\Delta T)} = 2.7 \times 10^{-5}\,\mathrm{K}^{-1}$, ${}^{\Delta b}/_{(b\Delta T)} = 0.7 \times 10^{-5}\,\mathrm{K}^{-1}$, and ${}^{\Delta c}/_{(c\Delta T)} = 1.5 \times 10^{-5}\,\mathrm{K}^{-1}$ reflect the strongly anisotropic character of the bonding situation.

$Bi_{16}Pt_{11}I_6$

$Bi_{16}Pt_{11}I_6$ has almost the same composition as $Bi_8Pt_5I_3$, but a rather different tetragonal layer structure with $a = 1386.6(1)$ pm and $c = 924.5(1)$ pm (details see Appendix: Table A.36 to A.40). The adopted space group $P42_12$ (no. 90) is rare; the inorganic crystal structure data base (ICSD) lists only 15 further entries with this symmetry.[176] The structure is acentric but not polar (Figure 5.2). Single layers of iodide ions separate the intermetallic layers ${}^2_\infty[Bi_{16}Pt_{11}]^{6+}$. The bismuth coordination of the platinum atoms is octahedral (Pt1), trigonal prismatic (Pt2, Pt4), or capped trigonal-prismatic (Pt3). Pt−Bi distances fall into the range between 267 pm to 306 pm (Table 5.2).

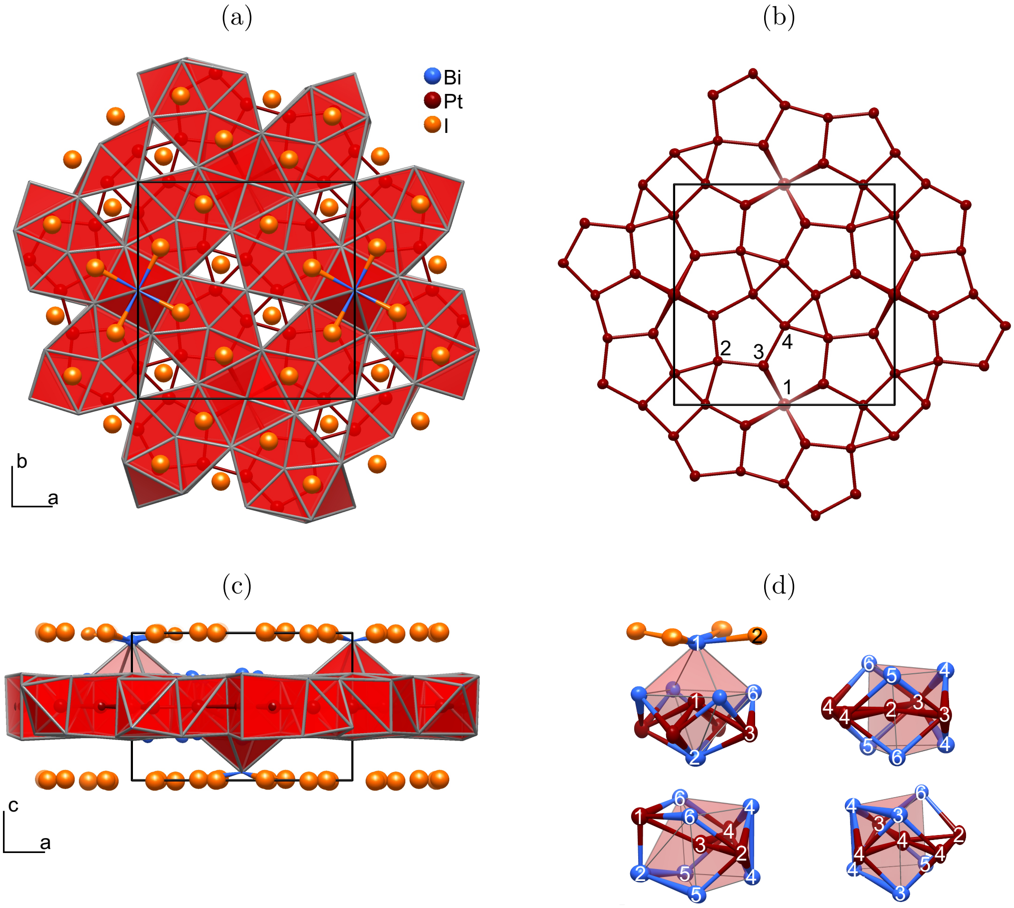

Figure 5.2.: Crystal structure of $Bi_{16}Pt_{11}I_6$: (a) view perpendicular to the layers, emphasising the platinum-centred bismuth polyhedra; (b) network of platinum atoms; (c) view parallel to the layers; (d) coordination of platinum atoms; ellipsoids represent 99 % probability.

For comparison, in Bi_2Pt($hP9$) with octahedral coordination of platinum by bismuth atoms, the range is 274 pm to 284 pm.[174]

ELI-D real-space analysis shows different bonding patterns for the Pt−Bi interactions (Figure 5.3a and Appendix: Table A.42). Distinct two-centre bonds are found e.g. for Pt1− Bi1, Pt 1 −Bi 2, and Pt 3 −Bi 6. The corresponding localisation domains are disk-shaped for the latter two, but ring-shaped for the Pt 1 −Bi 1 bond. This could point to a possible multi-centre character of the Pt 1 −Bi 1 bond involving the Bi6 atoms. Bi−Bi distances start at 330 pm, i.e. are about 30 pm longer than expected for a covalent single bond. ELI-D may not reveal such weaker bonding interactions, as it does not in case of elemental bismuth.

Covalent Pt−Pt bonds penetrate the faces of the [$PtBi_n$] polyhedra forming a two-dimensional network. The enhanced connectivity matches the increased noble-metal content. The nodal connectivity in the network is three or four, such that the total coordination number of all platinum atoms is ten. The network consists of three, four, and five membered rings. Pt2, Pt3, and Pt4 lie in a plane parallel (0 0 1) with less than 2 pm deviation, but Pt1 is out of plane by 137 pm, alternately to both sides. Pt−Pt bond lengths (274 pm to 289 pm) resemble elemental platinum (277 pm),[175] except bonds involving Pt1, which are noticeably longer (311 pm).

The topological analysis of the ELI-D field reveals the two shortest Pt−Pt bonds as bonding basins, namely Pt 4 −Pt 4 and Pt 3 −Pt 4, which form the three-membered ring (Figure 5.3b and Appendix: Table A.42). The longer Pt−Pt bonds, which form the other rings of the network, do not appear as separate basins. However, this does not preclude the presence of weaker bonds between these atoms. It was observed, that in the ELI-D field certain (multi-centre) bonds do not show up, which can be identified otherwise.[177] On the other hand, ELI-D is very sensitive towards very small changes in the electronic structure, which might result from the variation of atomic positions or employing different basis sets or DFT functionals.[177, 178]

Whereas the iodide ion I1 is essentially non-coordinating ($Bi\cdots I \geq 345$ pm), I2 is coordinating the Bi1 atom (312 pm), which protrudes from the intermetallic layer. The thereby formed $[Bi^{II}I_4]^{2-}$ square is known from ${}^1_\infty[Bi^0Bi^{II}I_{4/2}]$ strands in Bi_4I_4[97] and comparatively halogen-rich clusters $[Bi_6MI_{12}]^{n-}$.[138, 143] $[BiI_4]^{2-}$ squares of adjacent layers are interlocked and thus prevent stacking disorder in $Bi_{16}Pt_{11}I_6$ crystals. Although Bi1 lies almost in the same height as the iodide ions, the nearest bismuth atom in the neighbouring layer is 380 pm apart.

Table 5.2.: Selected interatomic distances /pm in $Bi_{16}Pt_{11}I_6$ at 298(1) K. Standard deviations are 0.1 pm.

Atoms	Distance	Atoms	Distance	Atoms	Distance
Pt 1 –Bi 1	277.7	Pt 3 –Bi 2	305.7	Pt 4 –Bi 3	284.0
–Bi 2	266.6	–Bi 4	284.6	–Bi 3	285.3
–Bi 6	4 × 294.2	–Bi 4	288.2	–Bi 4	299.9
–Pt 3	4 × 310.7	–Bi 5	296.9	–Bi 4	300.1
		–Bi 5	300.9	–Bi 5	278.7
Pt 2 –Bi 4	2 × 298.7	–Bi 6	280.8	–Bi 6	289.7
–Bi 5	2 × 279.3	–Bi 6	281.4	–Pt 2	282.0
–Bi 6	2 × 292.1	–Pt 1	310.7	–Pt 3	285.2
–Pt 3	2 × 289.0	–Pt 2	289.0	–Pt 4	273.6
–Pt 4	2 × 282.0	–Pt 4	285.2	–Pt 4	283.8
Bi–Bi	≥ 330.3	Bi···I1	≥ 345.6	Bi 1 –I 2	4 × 312.3

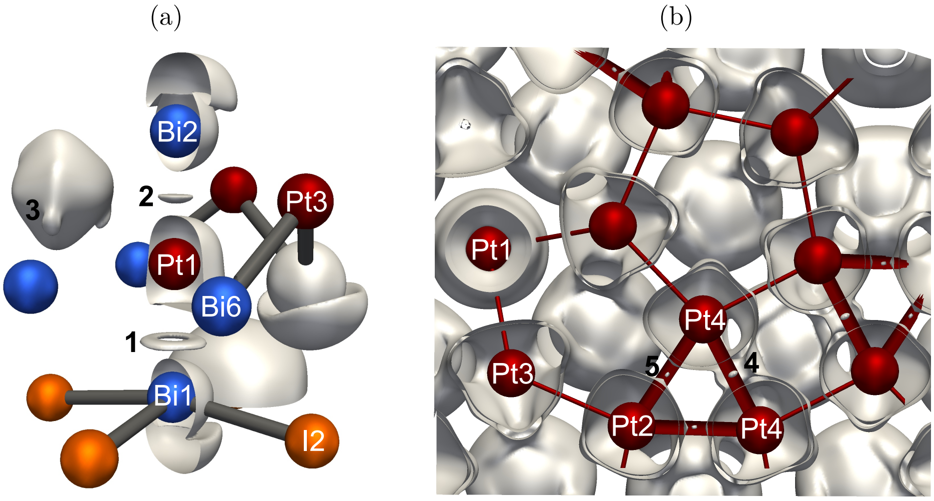

Figure 5.3.: (a) Selected isosurfaces of the ELI-D field in the surrounding of the Pt1 atom in $Bi_{16}Pt_{11}I_6$. Numbers **1**, **2**, and **3** indicate localisation domains, which belong to bonding basins. $\Upsilon_D^\sigma = 1.02$ for bismuth atoms and bonding basin **1**; $\Upsilon_D^\sigma = 0.97$ for all others. For Bi1, Bi2 and Pt1 the domains were cut for clarity.
(b) Isosurfaces of the ELI-D field in $Bi_{16}Pt_{11}I_6$ for $0.3 \leq z \leq 0.5$. The "inner" surfaces, closer to the Pt atoms and localisation domain **4**, are drawn at $\Upsilon_D^\sigma = 0.945$, the "outer" surfaces and domain **5** at $\Upsilon_D^\sigma = 0.926$.

5.1.2. Calculations and Physical Properties

The two compounds have rather similar densities of states (DOS) and are expected to be metallic (Figure 5.4a). The DOS at the Fermi level (E_F) has a relative minimum, yet no pseudo gap. The valence states between E_F and -7 eV have strong contributions of largely localised and thus almost filled platinum $5d$-orbitals ($9.9\,e^-$) and iodine $5p$-orbitals ($5.3\,e^-$, for QTAIM charges see Appendix: Tables A.35 and A.41). The contribution of iodine to states close to E_F as well as charges between -0.3 and -0.5 (Appendix: Tables A.35 and A.41) hint at partially covalent Bi-I interactions. Bismuth $6p$-states contribute to the whole valence region.

The electronic band structures of the two compounds are markedly different (Figure 5.4b). The unit cell of $Bi_{16}Pt_{11}I_6$ is about four times larger than the primitive cell of $Bi_8Pt_5I_3$, which produces four times the number of bands. Beyond this, a

(a) Densities of states

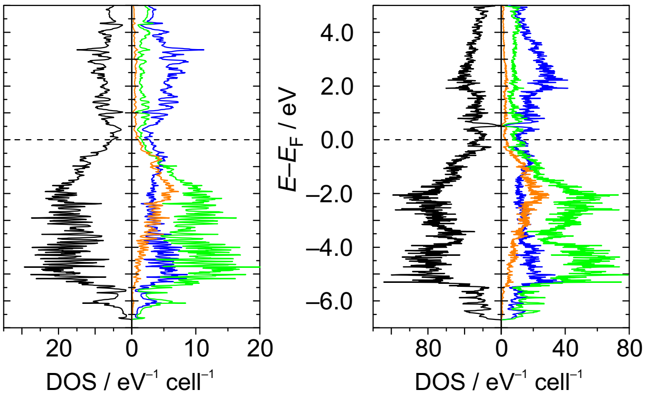

(b) Band structures

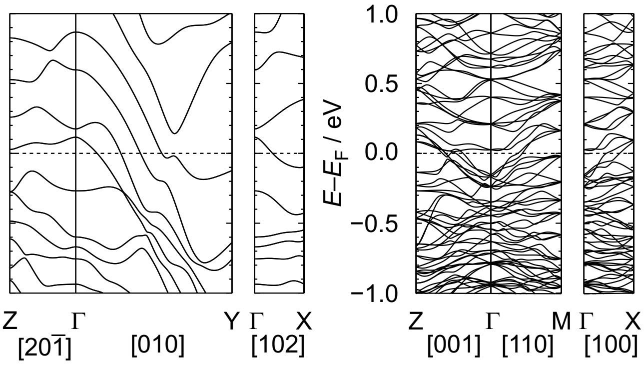

Figure 5.4.: (a) Total density of states (DOS; black) and projected DOS of bismuth (blue), platinum (green) and iodine (orange) in $Bi_8Pt_5I_3$ (left) and $Bi_{16}Pt_{11}I_6$ (rigth).
(b) Electronic band structures along selected directions in $Bi_8Pt_5I_3$ (left) and $Bi_{16}Pt_{11}I_6$ (right). The directions given in square brackets refer to the conventional (centred) crystal lattice.

pseudo two-dimensional character (gap in stacking direction $\overline{\Gamma Z}$) is only observed for $Bi_8Pt_5I_3$, whereas in the case of $Bi_{16}Pt_{11}I_6$ bands cross E_F along $\overline{\Gamma Z}$, i.e. in stacking direction. The latter interlayer interaction may be associated with those bismuth atoms that protrude from the intermetallic layer and form $[BiI_4]^{2-}$ squares. Perpendicular to the stacking direction, in [100] and [110], bands of moderate dispersion cross E_F. This matches with the fully two-dimensional connectivity in the intermetallic network. In contrast, the electronic structure of the intermetallic layer of $Bi_8Pt_5I_3$ is quite anisotropic. Along [010], i.e. parallel to the covalent platinum strands, all bands show strong dispersion, whereas the dispersion of the orthogonal bands, along [102], is surprisingly weak.

Measurements of the electrical resistivity $\rho(T)$ show that both compounds are metallic conductors (Figure 5.5a), albeit of different character. $Bi_{16}Pt_{11}I_6$ has a low resistivity of $8.5 \times 10^{-6}\,\Omega\text{m}$ at 20 °C, which is similar to that of graphite ($8 \times 10^{-6}\,\Omega\text{m}$[179]). Since the PXRD and magnetisation data indicate impurities of BiPt (Figure 5.5b), which has almost the same resistivity,[180] these values should be taken with care. However, the dependence of the electrical resistivity on temperature is qualitatively different in our study: $\rho(T)$ increases strongly up to about 150 K and then varies almost linear with temperature. The small residual-resistivity ratio (RRR) of 1.6 indicates a high number of defects in the structure. The resistivity of $Bi_8Pt_5I_3$

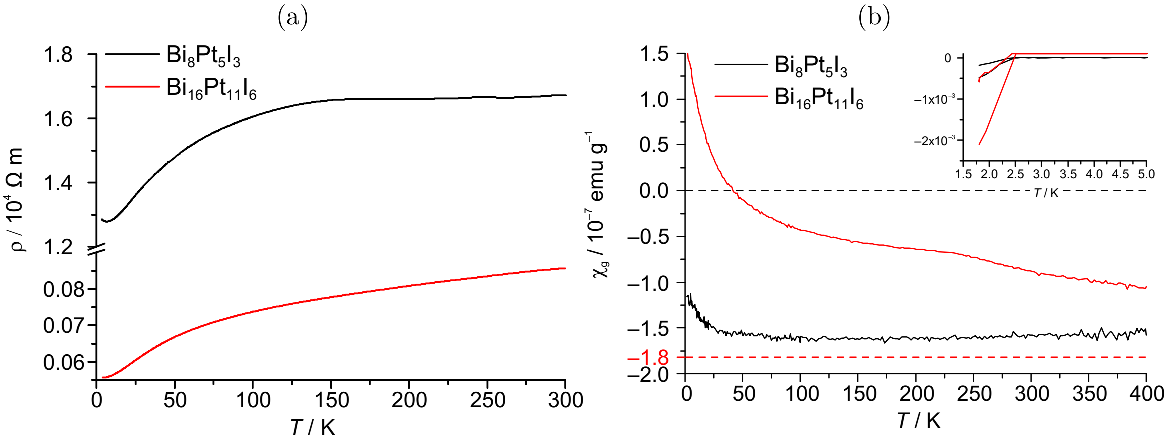

Figure 5.5.: (a) Temperature dependence of the electrical resistivity of $Bi_8Pt_5I_3$ and $Bi_{16}Pt_{11}I_6$.
(b) Magnetic susceptibility of $Bi_8Pt_5I_3$ (black) and $Bi_{16}Pt_{11}I_6$ (red) corrected for ferromagnetic impurities. $-1.8 \times 10^{-7}\,\text{emu}\,\text{g}^{-1}$ indicates the sum of diamagnetic increments, which is almost identical for both structures.[158]
Inset: Magnetisation at low temperatures in a field of 2 mT reveals BiPt impurities, which are superconducting below 2.4 K.[161]

is much higher than that of $\mathrm{Bi_{16}Pt_{11}I_6}$ and has a different temperature dependence: $\rho(T)$ increases up to about 150 K but then stays almost constant at $1.7 \times 10^{-4}\,\Omega\mathrm{m}$. Here, the low RRR of 1.3 may also be due to bad contacts between the grains. It can be expected that the layered character of the compounds additionally increases the resistance of the cold-compressed pellet.

Magnetisation measurements show temperature-independent diamagnetism for both compounds (Appendix: Figure 5.5b). The quite strong paramagnetic contribution in the case of the $\mathrm{Bi_{16}Pt_{11}I_6}$ sample are assigned to isolated impurities or to charged point defects. The anticipated Pauli paramagnetism of the conduction electrons is overcompensated by the diamagnetism caused by the large number of paired electrons in both compounds. From a fit to the corrected susceptibility with a constant χ_0 and a Curie term for the paramagnetic impurities one obtains $\chi_0 = -0.39 \times 10^{-3}\,\mathrm{emu\,mol^{-1}}$ for $\mathrm{Bi_{16}Pt_{11}I_6}$ (theo.: $-1.14 \times 10^{-3}\,\mathrm{emu\,mol^{-1}}$) and $\chi_0 = -0.52 \times 10^{-3}\,\mathrm{emu\,mol^{-1}}$ for $\mathrm{Bi_8Pt_5I_3}$ (theo.: $-0.55 \times 10^{-3}\,\mathrm{emu\,mol^{-1}}$), respectively.

5.2. A Strand Phase – Bi_4RhI_2

5.2.1. Structure

Bi_4RhI_2 is a compound with a structure composed of strands. It is very similar to Bi_4RuI_2[181] and crystallises in the space group $P2_1/n$ (No. 14) with $a = 6.3364(2)$, $b = 18.0156(5)$, $c = 16.2333(5)$ and $\beta = 93.0660(19)°$ at RT (Figure 5.6a; details see Appendix: Table A.43 to A.49).

Within the strands, the rhodium atoms are surrounded by eight bismuth atoms to form distorted tetragonal antiprisms, which share their faces (Figure 5.6b; $d(\mathrm{Rh{-}Bi}) =$ 273.9(1) pm to 304.1(1) pm, details in Appendix: Table A.46). The rhodium atoms form pairs ($d(\mathrm{Rh} - \mathrm{Rh}) = 286.5(2)\,\mathrm{pm}$) which are separated by a longer distance ($d(\mathrm{Rh} - \mathrm{Rh}) = 347.2(2)\,\mathrm{pm}$; Figure 5.6a and 5.6b). The Bi−Bi distance in the polyhedra range from 298.0(1) pm to 377.8(1) pm and are distributed broadly (Figure 5.7 and Appendix: Table A.46). The strands are surrounded by iodide ions, with most Bi−I distances in a range typical for ionic interactions ($d(\mathrm{Bi} \cdots \mathrm{I}) \geq 333.7(1)\,\mathrm{pm}$, Appendix: Table A.46), except for three, which are significantly shorter ($d(\mathrm{Bi\,3} - \mathrm{I\,4}) =$ 208.0(1) pm, $d(\mathrm{Bi\,1} - \mathrm{I\,2}) = 313.6(1)\,\mathrm{pm}$ and $d(\mathrm{Bi\,3} - \mathrm{I\,2}) = 325.9(1)\,\mathrm{pm}$), two of them similar to the Bi−I distances within BiI_3 (305.4 and 312.5 pm). These significantly shorter distances indicate partially covalent interactions between bismuth and iodine.

Two structures, Bi_4RuI_2 and $Bi_9Rh_2I_3$, with globally and locally very similar arrangements are considered for comparison. The one closest related is Bi_4RuI_2, which is almost isotypic (Figure 5.6c and 5.6d), but higher symmetric with a four-fold rotation axis running along the Ru−Bi strands (space group $I4/m$, No. 87). Nevertheless, the arrangement of the strands in Bi_4RuI_2 does not allow for a two-fold screw-rotation axis perpendicular to the strands, as it is found in Bi_4RhI_2. Therefore, no direct connection between both structures can be found within a family tree according to BÄRNIGHAUSEN.[182] But one can build a hypothetical aristotype Bi_4MI_2 in the spacegroup $I4/mcm$, from which both structures, Bi_4RuI_2 and Bi_4RhI_2, can be derived by a transformation of index 2 and 8, respectively (Appendix: Table A.50 to A.52). The cells of both structures can therefore be compared. With a monoclinic angle $\beta = 93.066°$ and a c/b ratio of 0.9 the cell of Bi_4RhI_2 is still close to a tetragonal cell. The axis along the strands in Bi_4RuI_2 (c-axis) and Bi_4RhI_2 (a-axis) have a length of 669.7 pm and 633.6 pm, respectively, which corresponds to a contraction of 15 %. Perpendicular to the strands, one direction is very similar with $\sqrt{2}\cdot 1183.9\,\mathrm{pm} = 1674.3\,\mathrm{pm}$ (Bi_4RuI_2) versus 1623.3 pm (Bi_4RhI_2), what yields a contraction of 3 %. The other direction perpendicular to the strands shows the strongest deviation with 1801.6 pm for

(a) Bi_4RhI_2 (b)

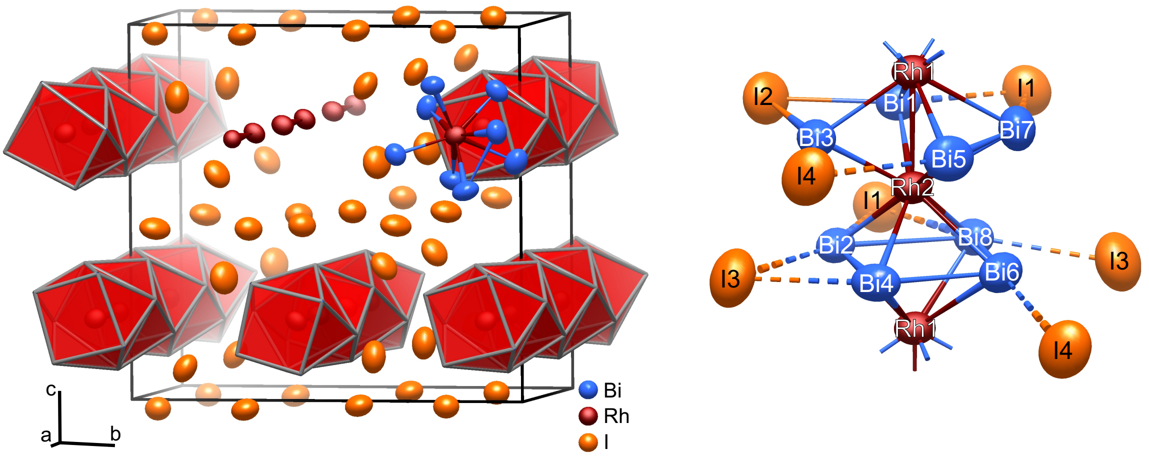

(c) Bi_4RuI_2 (d) (e) $Bi_9Rh_2I_3$ (f)

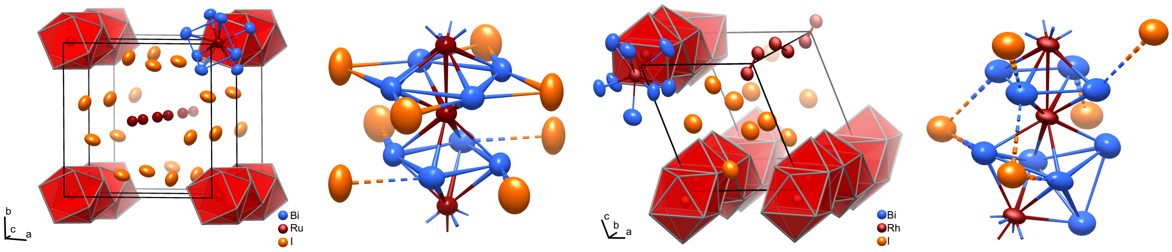

Figure 5.6.: (a) Crystal structure of Bi_4RhI_2: view along the strands. For one strand the bismuth atoms were removed to reveal the rhodium pairs. (b) One strand in detail. Bi−Bi bonds are drawn up to 338 pm, Bi−I bonds up to 330 pm, Bi···I connections up to 369 pm (details in Appendix: Table A.46); ellipsoids represent 99 % probability.
(c), (d) Crystal structure of Bi_4RuI_2 [181] similarly arranged as in (a), (b).
(e), (f) Crystal structure of $Bi_9Rh_2I_3$ [137] similarly arranged as in (a), (b).

the (monoclinic) *b*-axis of the rhodium compound, which corresponds to an expansion of 8 %. All in all, comparing Bi_4RuI_2 and Bi_4RhI_2 one observes an contraction of the cell volume by 1 %, while the number of valence electrons has increased by one. Although, this seems contradicting on a first glimpse, the lower symmetry and the therefore denser arrangement of the strands could be an explanation. Considering the individual atoms, the mean deviation of the atoms in Bi_4RuI_2 from the higher symmetrical positions is only 2 % (maximum of 2 % for I1), while even for Bi_4RhI_2 the mean deviation is only 2 %, but with I2 and I3 being off the higher symmetrical position by approximately 10 %.

The other very similar structure is the one of $Bi_9Rh_2I_3$, although with a slightly

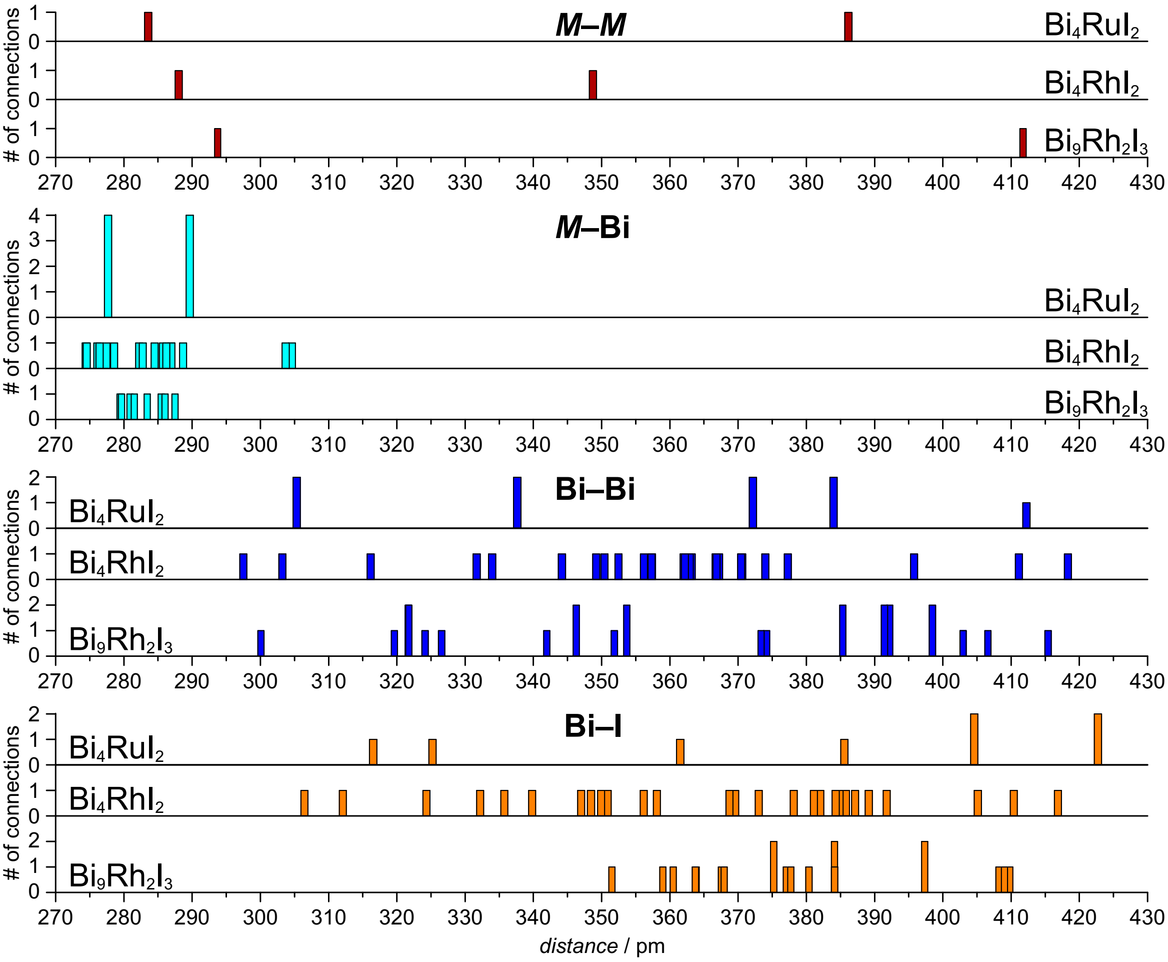

Figure 5.7.: Histogramm of $M-M$, $M-$Bi (M =Ru or Rh), Bi−Bi, and Bi−I distances in Bi_4RuI_2, Bi_4RhI_2 and $Bi_9Rh_2I_3$.

different composition ($Bi_{4.5}RhI_{1.5}$). Globally one also finds Rh−Bi strands embedded in an ionic matrix of iodide ions (Figure 5.6e and 5.6f). Furthermore, as in Bi_4RhI_2, every rhodium atom is surrounded by eight bismuth atoms and the thereby formed polyhedra share their faces to form the strands. Nevertheless, only every second shared face is a rectangle, while the other four bismuth atoms form a “butterfly” with two triangular faces of which only one is shared between two adjacent polyhedra (Figure 5.6f). Interestingly, the symmetry of the global arrangement of the strands in $Bi_9Rh_2I_3$ (space group $P2_1/m$, No. 11) is closer to the one of Bi_4RhI_2 then the one of Bi_4RuI_2.

A first idea of the chemical bonding can be derived from the different distances in Bi_4RhI_2, Bi_4RuI_2 and $Bi_9Rh_2I_3$, which are summarised as histograms in Figure 5.7. In all three compounds one finds alternating long and short $M-M$ distances (M = Ru/Rh), with the shorter one being 284 pm, 286 pm, and 292 pm for Bi_4RuI_2, Bi_4RhI_2,

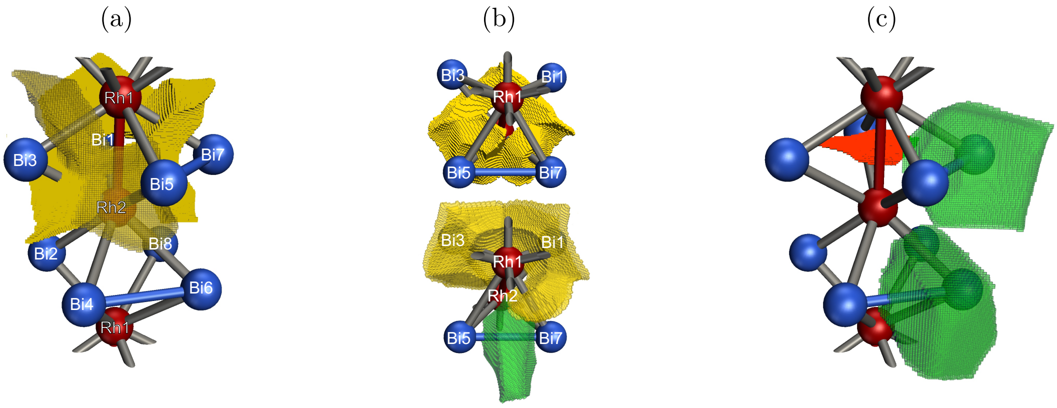

Figure 5.8.: ELI-D bonding basins in Bi_4RhI_2 from the topological analysis of the ELI-D field. (a) The same structural detail as in Figure 5.6b with the seven two-centre Rh–Bi bonds (yellow). (b) View on the Bi1-Bi3-Bi5-Bi7 square with the upper picture showing the four two-centre Rh–Bi bonds to Rh2 (yellow) and the lower picture showing the three two-centre Rh–Bi bonds to Rh1 (yellow) and the Bi 5 –Bi 7 bond (green). (c) The same structural detail as in (a) with the three-centre Rh–Bi–Rh bond (red) and the two Bi–Bi bonds (green). Quantitative evaluation see Appendix: Table A.54.

and $Bi_9Rh_2I_3$, respectively. This coincides with the fact, that the number of electrons available for the intermetallic substructure within these compounds rises in the same sequence, either as the transition element has more electrons (Ru to Rh), or as the relative bismuth content rises and the iodine content decreases. Most probably, the need of electrons of the transition element has to be fulfilled by $M-M$ bonds if the number of electrons is not high enough. In the case of Bi_4RuI_2 this is underlined by Ru–Ru bonds, which were found via a topological analysis of the ELI-D field in a closely related structural fragment in $[Ru_2Bi_{14}Br_4](AlCl_4)$, with the same Ru–Ru distance.[183] Consequently, as the Rh atom has more electrons available, for the longer $M-M$ distance in Bi_4RhI_2 only a Rh–Bi–Rh multi-centre basin was found (Figure 5.8c and Appendix: Table A.54). As no ELI-D analysis is available for $Bi_9Rh_2I_3$ one can only speculate, whether there is still a (weaker) multi-centre interaction for the even longer $M-M$ distance, or maybe no basin directly shared between two adjacent transition element atoms.

This trend for the $M-M$ bonds is not repeated for any of the other distances. The M–Bi and Bi–Bi distances in all compounds are distributed in a similar range, although rather broadly in the cases of the lower symmetric Bi_4RhI_2 and $Bi_9Rh_2I_3$ (Figure 5.7). Nevertheless, locally the arrangements are quite different, which becomes most obvious for the bismuth squares (Figure 5.9). While in Bi_4RuI_2 a $[Bi_4I_4]$ unit

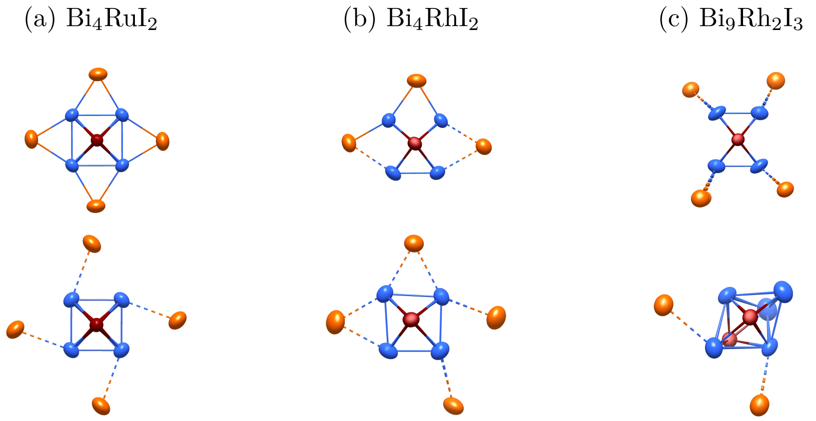
(a) Bi_4RuI_2 (b) Bi_4RhI_2 (c) $Bi_9Rh_2I_3$

Figure 5.9.: (a), (b), (c) Top view on the two different types of bismuth rectangles (double-butterfly) in the corresponding strands of Bi_4RuI_2, Bi_4RhI_2 and $Bi_9Rh_2I_3$, respectively. The upper rectangle is the one bridging the short and the lower rectangle/double-butterfly is the one bridging the long $M-M$ distance. Bi−Bi bonds are drawn up to 338 pm, Bi−I bonds up to 330 pm, Bi···I connections up to 369 pm (details in Appendix: Table A.46).

bridges the short Ru−Ru distance, the comparable fragment in Bi_4RhI_2 distorts and becomes a "[$(Bi_2)Bi_2I_3$]" unit (and an "isolated" iodide ion) and finally in case of $Bi_9Rh_2I_3$ a "[$(Bi_2)_2I_3$] unit where all iodide ions are only loosely attached. Although the change for the second square, bridging the longer $M-M$ distance is less pronounced between Bi_4RuI_2 and Bi_4RhI_2, in case of $Bi_9Rh_2I_3$ it becomes a "double-butterfly", due to the slightly different composition.

Therefore, a better understanding needs a quantum-mechanical analysis which has partially already been performed for Bi_4RuI_2 and is herein presented for Bi_4RhI_2. In Bi_4RhI_2 the bismuth atoms of the "[$(Bi_2)Bi_2I_3$]" unit (Bi1, Bi3, Bi5, Bi7) are almost exclusively involved in two-centre interactions with Rh1 and Rh2, respectively. Only Bi5 has just one two-centre bond to Rh2, but therefore another two-centre bond to Bi7 (Figure 5.8; Appendix: Table A.54). As mentioned, this square bridges the short Rh−Rh distance and additionally one finds comparatively short Bi−I distances (Table A.46), what makes this square the corresponding structural fragment to Bi_4I_4 in Bi_4RuI_2. The latter has been extensively discussed as an eight-electron donor in many further structures, such as $Bi_{39.67}Ru_2Br_{35}$, $[Ru_2Bi_{14}Br_4](AlCl_4)$ or $Bi_{24}Ru_3Br_{20}$ (for the latter as Bi_4Br_4).[181, 183–185] The eight two-centre bonds which were identified via ELI-D in these cases,[183] agree well with the seven two-centre bonds found in Bi_2RhI_2 for these four bismuth atoms, the eighth bond most probably being no longer necessary, as the number of electrons has increased and therefore the electrons being localised in the mentioned Bi 5 −Bi 7 bond. Simultaneously, in contrast to the other three Bi−Bi connections, this Bi–Bi bond is no longer bridged by an iodide anion, all in all justifying the description as $[(Bi_2)Bi_2I_3]$ fragment. Counting the electrons available for the Bi–Rh bonds, following the ELI-D analysis (similarly to reference 183), one gets: $4 \cdot 3(\mathrm{Bi}6p) - 3(3\mathrm{I}^-) - 2(\mathrm{Bi}\,5 - \mathrm{Bi}\,7\ \mathrm{bond}) = 7$.

As no ELI-D analysis is available in case of $Bi_9Rh_2I_3$, the corresponding bismuth rectangle which also bridges the shortest Rh–Rh distance, can only be evaluated based on the distances, which leads to a $[(Bi_2)_2I_3]$ fragment. A suggestion for the formal electronic situation, taking into account the known ELI-D patterns in Bi_4RuI_2 and Bi_4RhI_2, could be: $4 \cdot 3(\mathrm{Bi}6p) - 3(3\mathrm{I}^-) - 4(\mathrm{Bi{-}Bi\ bonds}) = 5$.

For the second square of bismuth atoms in Bi_4RhI_2 (Bi2, Bi4, Bi6, Bi8) one finds almost isolated Bi atoms (three lone pairs with approximately 5 electrons), except for one two-centre bond between Bi4 and Bi6 (Figure 5.8c, Appendix: Table A.54) and loosely attached iodide ions. As these bismuth atoms also have a less positive Bader charge compared to the other four Bi atoms (Appendix: Table A.53) it seems as if this fragment is much weaker coordinated to the adjacent Rh atoms. A possible scenario to evaluate the number of electrons within the square is: $4 \cdot 3(\mathrm{Bi}6p) - 2(\mathrm{Bi}\,4 - \mathrm{Bi}\,6\ \mathrm{bond}) - 1(\mathrm{I}^-) = 9$. Structurally, this square of bismuth atoms is related to a fragment from Bi_4RuI_2 which was originally discussed as ${Bi_4}^0$,[181] and later on as ${Bi_4}^{2-}$.[184] If one considers the latter interpretation, which involves six electrons in bonding molecular orbitals, but with the other $4 \cdot 3(\mathrm{Bi}6p) - 6(\mathrm{Bi{-}Bi\ bonds}) = 6$ Bi6p electrons being (formally) available to ruthenium, this yields a comparable situation to the herein presented ELI-D analysis for Bi_4RhI_2. Unfortunately, in this case no ELI-D analysis is available for the ruthenium case.

As this second type of bismuth square bridges the longer $M - M$ distance in Bi_4RhI_2 as well as in Bi_4RuI_2, it is related to the double-butterfly in $Bi_9Rh_2I_3$, which for its part does the same. As its bonding is difficult to interpret without an ELI-D analysis, one can only guess based on the atomic distances. A more or less consistent picture evolves if one considers 7 "covalent bonds" between the bismuth atoms corresponding to the shortest Bi–Bi distances, which would sum up as follows: $5 \cdot 3(\mathrm{Bi}6p) - 14(\mathrm{Bi{-}Bi\ bonds}) = 1$.

The double-butterfly is the consequent evolution of the distortion with an additional Bi atom being added. Interestingly, the increasing distortion of the bismuth-rings from Bi_4RuI_2 to Bi_4RhI_2 and finally to $Bi_9Rh_2I_3$ goes hand in hand with a decreasing distance of the bismuth atoms along the strands. While the shortest Bi–Bi distance along the intermetallic strands in Bi_4RuI_2 is 372 pm, it decreases to 345 pm in Bi_4RhI_2 and to 342 pm in $Bi_9Rh_2I_3$. This "compression" along the intermetallic strands with increasing electron count might be a sign of an increasing delocalisation of the chemical bonding and is reflected by the shortening of the axis along the strands from Bi_4RuI_2 to Bi_4RhI_2. It is supported by a decreasing band gap (Section 5.2.2). The very similar compound $Bi_9Ir_2I_3$, which is isotypic to $Bi_9Ir_2I_3$, even becomes metallic due to the more diffusive Ir 5*d*-orbitals.[137]

Nevertheless, following the above presented electron distribution, one can develop the following picture for the three compounds. In Bi_4RuI_2, $[Bi_4I_4]$ donates eight electrons and $[Bi_4]$ six electrons. Per ruthenium with its eight valence electrons this makes $8+{}^{(8+6)}/_2 = 15$ valence electrons. Forming a Ru−Ru bond, it achieves an advantageous 16-electron count.

In Bi_4RhI_2, $[(Bi_2)Bi_2I_3]$ donates five and $[(Bi_2)Bi_2I]$ donates nine electrons. For rhodium with its nine valence electrons this makes $9 + {}^{(7+9)}/_2 = 17$ valence electrons. Forming a multi-centre Rh−Bi−Rh bond, it achieves an advantageous 18-electron count.

Finally, in $Bi_9Rh_2I_3$, $[(Bi_2)_2I_3]$ could donate five electrons and $[Bi_5]$ one electron. Per rhodium atom with its nine valence electrons this makes $9 + {}^{(5+1)}/_2 = 12$ valence electrons, which is as well a favourable electron count. As no verification via ELI-D is available, the latter interpretation has to be handled with care.

Although this is a very formal electron distribution, as e.g. the case of the metal $Bi_9Ir_2I_3$ indicates, it makes a comparison to other similar structures possible, which are formed by elements of other groups. Examples are Te_4MoBr, Te_4MI and $(Se_2M)_2I$ with M = Nb or Ta, where the latter features a whole family of compounds.[186–190] In these cases, similar strands are formed with Nb, Ta or Mo in the centres, being separated by short and long distances (various patterns). In all these cases, bismuth is substituted by the electron-richer main group element tellurium or selenium, while ruthenium or rhodium within the strands is substituted by the electron-poorer transition elements molybdenum, niobium or tantalum. The introduced structures are inversely polarised, with the following charges having been assigned by the authors: $[(Te_2^{2-})_2Br]^{5-}[Mo^{5+}]$, $[(Te_2^{2-})_2I]^{5-}[M^{5+}]$ and $[(Se_2^{2-})_2]_3[I^-]_2[M^{5+}][M_2^{4+}]$ (M = Nb or Ta). All in all, this structure type seems to be very flexible with respect to the constituting elements and charge distribution. That is of interest, as the strands can host 1D-electrons, resulting in unique transport phenomena, such as charge density waves (e.g. in $(Se_4Ta)_2I$).[189]

5.2.2. Calculations and Physical Properties

The topological analysis of the ELI-D field of Bi_4RhI_2 already indicates, that the structure is dominated by the ionic interactions between the intermetallic part and the iodide ions on one hand, and by covalent interactions within the intermetallic

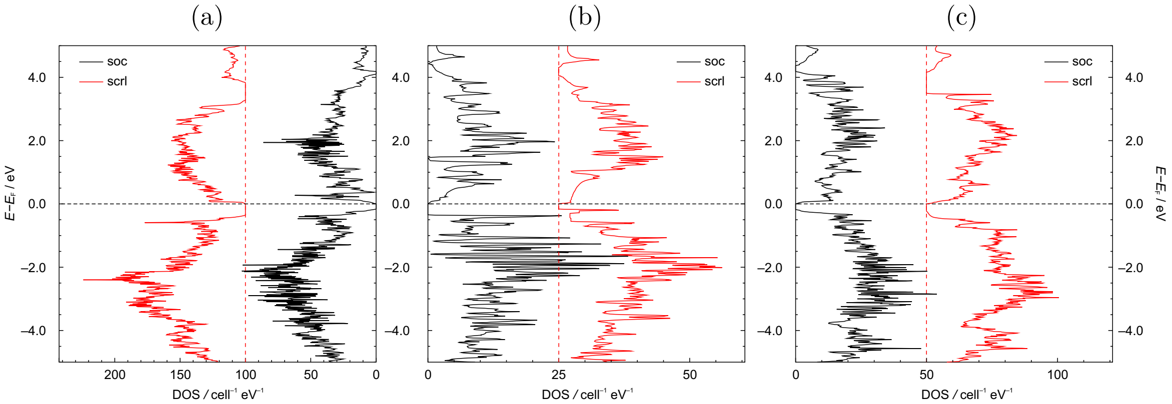

Figure 5.10.: Density of states (DOS) from scalar-relativistic (red) and full-relativistic (black) calculations for (a) Bi_4RhI_2 (b) Bi_4RuI_2 and (c) $Bi_9Rh_2I_3$. The DOS has be adapted to the number of atoms/formula units per cell $(Z_{\mathrm{Bi_4RhI_2}} = 4Z_{\mathrm{Bi_4RuI_2}} = 2Z_{\mathrm{Bi_9Rh_2I_3}})$.

strands on the other hand (Section 5.2.1). The bonding basins hint at a localisation of the electrons, even within the strands. This anticipates the fact, that Bi_4RhI_2 is a semiconductor with an indirect band gap of 157 meV according to the quantum chemical calculations (Figure 5.10a and 5.11). This result was confirmed by resistivity measurements, from which an intrinsic band gap was extracted (Figure 5.12a). This band gap is about 74 meV in case of a compressed powder[1] and ≈ 100 meV in case of a single crystal, or most probably a bunch of equally oriented single crystals. These results agree well with the calculated value, which is surprising on a first glimpse, as DFT generally underestimates band gaps.[172] Nevertheless, the size of the band gap changes from the scalar to the full-relativistic calculation (Figure 5.10a), which means, that the size of the gap is determined by the SOC. As in FPLO SOC is treated on the basis of the four component Dirac equation, which yields an exact description of the physical effect, the calculated band gap corresponds well with the experimentally observed one.

Furthermore, one can compare the gap sizes of Bi_4RhI_2 with the other two very similar structures which have been introduced, Bi_4RuI_2 and $Bi_9Rh_2I_3$. As briefly mentioned in the discussion of the bonding situation (Section 5.2.1), the degree of condensation *along* the intermetallic strands increases, going hand in hand with shorter Bi−Bi distances in this direction in the sequence Bi_4RuI_2, Bi_4RhI_2 and $Bi_9Rh_2I_3$. Simultaneously, the band gap decreases from 350 meV to 160 meV and 170 meV, respectively. While the latter two are almost the same within the error, the gap of the ruthenium compound is approximately twice as large. Additionally, the high symmetry of the

---

[1] For the powder additionally an extrinsic band gap of about 45 meV was derived.

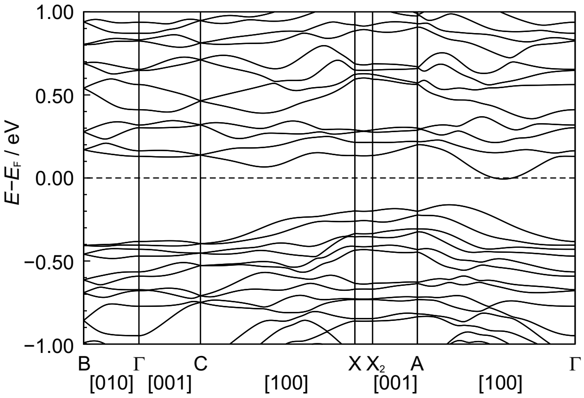

Figure 5.11.: Full-relativistic, electronic band structure of Bi_4RhI_2 along selected directions. The directions given in square brackets refer to the conventional crystal lattice. CX and $A\Gamma$ correspond to the direction along the Bi-Rh-strands at the edge and in the centre of the first Brillouin zone, respectively.

compound suggests that the electronic situation in the ruthenium structure is close to an optimum. Therefore, in the rhodium compounds unfavoured (anti-bonding) states would have to be occupied. Avoiding this, the system undergoes several distortions, which lead to the observed lowering of the symmetry for the rhodium structures. The new optima are still very similar to the original structure, although with partially different bonding patterns. This shortens the Bi−Bi bonds along the strands and reduces the band gap, nevertheless still yielding semiconducting phases. This trend seems to culminate in $Bi_9Ir_2I_3$, which has a similar structure compared to $Bi_9Rh_2I_3$, but is a metal due to the more diffusive *d*-orbitals of the iridium atom compared to rhodium.[137]

The band structure of Bi_4RhI_2 helps to further verify the picture of the bonding situation (Figure 5.11). Along two different, orthogonal directions, both perpendicular to the strands ($\overline{\mathrm{B}\Gamma}$ and $\overline{\Gamma\mathrm{C}}$), almost no dispersion of the bands close to the Fermi energy is observed, which can be interpreted as no overlap of the orbitals and only electrostatic (ionic) interactions along this direction. On the contrary, along the intermetallic strands ($\overline{\mathrm{A}\Gamma}$ and $\overline{\mathrm{CX}}$, with the latter being at the edge of the first Brillouin zone) dispersion is observed for the valence and the conduction band forming the mentioned indirect band gap and indicating overlap of the orbitals in this direction.

In the comparison of the band gaps and the stability of the three compounds one interesting detail shall be mentioned. While the spin-orbit coupling stabilises Bi_4RhI_2 and $Bi_9Rh_2I_3$, meaning it increases the band gap in both cases, it does the opposite for Bi_4RuI_2, where it decreases the band gap (Figure 5.10a). As bismuth has the strongest SOC, the atomic orbitals of bismuth which are involved in bonding

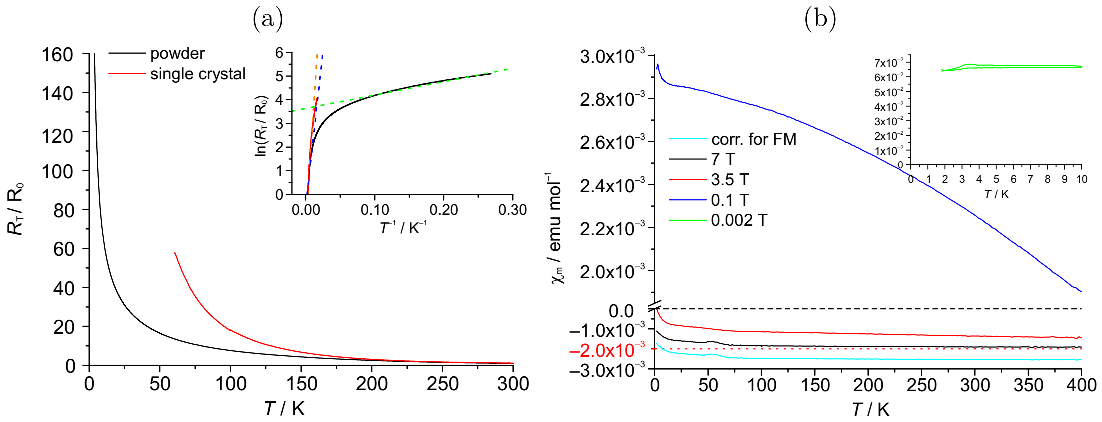
(a)
(b)

Figure 5.12.: (a) Resistivity vs. temperature for Bi_4RhI_2 measured on a powder pressed as pellet (black) and on a single crystal (red). The inset is an Arrhenius plot for the resistivity behavior with linear fits for the extrinsically (green) and intrinsically (orange, blue) dominated regimes.
(b) Magnetic susceptibility vs. temperature for Bi_4RhI_2 in different magnetic fields and corrected for ferromagnetic impurities (cyan). A χ_{mol} of -2.0×10^{-4} emu mol^{-1} indicates the sum of the diamagnetic increments.[168] At 2 mT no indication of superconductivity was found down to 2 K (inset).

should be considered for an explanation. Especially one peculiar difference between scalar- and full-relativistic orbitals is important. In the scalar relativistic case one has three degenerate p-orbitals, pointing in three orthogonal directions (p_x, p_y, p_z). Spin-orbit coupling transforms these in one spherical $p_{1/2}$-orbital with s-like character and two doughnut-shaped $p_{3/2}$-orbitals, both oriented in two orthogonal planes.[191] The scalar-relativistic situation is perfect for the formation of regular squares, with two equally close neighbours (found in Bi_4RuI_2) as two orbitals are available in the same plane. This changes with SOC, when only one orbital is left within the same plane. Therefore, the bonding situation in Bi_4RuI_2 is slightly destabilised by introducing SOC. The opposite is the case for Bi_4RhI_2 and $Bi_9Rh_2I_3$, where no regular squares are formed, but an interaction along the strands with the adjacent square is strengthened. In this case, the two $p_{3/2}$ orbitals in two perpendicularly oriented planes are perfect, one orbital overlapping with the neighbours within the square and the other orbital overlapping with the neighbours of the adjacent square. Consequently, SOC stabilises the bonding situation in Bi_4RhI_2 and $Bi_9Rh_2I_3$.

Finally, magnetic measurements yield a diamagnetic susceptibility which is in good agreement with the sum of the diamagnetic increments of the constituting atoms (Figure 5.12b). The data were corrected for small ferromagnetic impurities (most probably introduced during preparation) with an Honda-Owen type correction and for paramagnetic impurities with a respective Curie term for the fit. No significant superconducting volume fraction was observed in the magnetic susceptibility measurements.

6. Summary and Outlook

This thesis was inspired by the discovery of the first "weak" 3D-TI $\mathrm{Bi_{14}Rh_3I_9}$ and has been concerned with the topic of topological insulators in general. It followed two main approaches to gain a deeper understanding of this new state of matter. On one hand, it was aimed at expanding the material's basis, with the hope of finding compounds directly related to $\mathrm{Bi_{14}Rh_3I_9}$. On the other hand, by developing a simple model of the structure, the properties of the different structural fragments should be revealed. While the latter would give a theoretical background, the synthesis of new materials is indispensable if one wants to conduct physical experiments.

During the work it turned out that both approaches complemented each other in a very fruitful way. Theoretical predictions triggered new experiments and vice versa. Finally, due to an extensive research on the thermodynamic properties of the compounds, it was possible to characterise the discovered materials in various physical experiments and strong evidence was found for the unique properties of $\mathrm{Bi_{14}Rh_3I_9}$ related to the non-trivial topology of the electronic band structure.

New Structures in the Bismuth–Platinum-metal–Iodine Phase Systems

The chemical and crystallographic variety of the bismuth subiodides was enriched by six new phases in the course of the presented systematic investigation of the metal-rich parts of the bismuth–platinum-metal–iodine phase systems.

Besides $\mathrm{Bi_{13}Pt_3I_7}$[107] and $\mathrm{Bi_{14}Rh_3I_9}$, two new stable phases, $\mathrm{Bi_{13}Pd_3I_7}$ and $\mathrm{Bi_{38}Pt_9I_{14}}$, with the honeycomb network ${}^{2}_{\infty}[(\mathrm{Bi}_{8/2}\mathrm{M})_3\mathrm{I}]$ as structural motif were discovered. Together with the metastable compound $\mathrm{Bi_{12}Pt_3I_5}$,[142] these establish a family of layered materials, which is very promising in view of understanding their chemical bonding and physical properties. Furthermore, this family can be expanded to other known compounds. Considering only the local arrangement of the platinum-metal, surrounded by eight bismuth atoms (cubes or antiprisms) and the connection of these polyhedra forming a network, one can include the halide compounds $\mathrm{Bi_{12}Rh_3Br_2}$[192] and $\mathrm{Bi_{12}Rh_3Cl_2}$,[193] as well as the intermetallic compounds

Bi_4Rh[194–197], $Bi_{14}Rh_3$[193, 198] and Bi_4Ir[199]. Especially the latter could be a hint, that there are even more structures to be discovered, as no Bi−Ir−halide compound with a similar structural motif has been found up to date.

In addition, the careful thermal analysis coupled with PXRD yielded three further structures, $Bi_8Pt_5I_3$, $Bi_{16}Pt_{11}I_6$ and Bi_4RhI_2. The latter is a distorted variant of the known Bi_4RuI_2 structure,[181] which is also similarly adopted by the compounds $Bi_9Rh_2I_3$, $Bi_9Rh_2Br_3$ and $Bi_9Ir_2I_3$[137] or is echoed in a variety of phases with tellurium or selenium instead of bismuth, and niobium, tantalum or molybdenum instead of the platinum-metal, such as Te_4NbI, $(Se_2Ta)_2I$ and Te_4MoBr.[186–190] A first classification comparing the structure and bonding to the very close relatives Bi_4RuI_2 and $Bi_9Rh_2I_3$ has been conducted, but maybe all these strand phases together open the opportunity to establish a more general concept for the formation of this structure type. On the other hand, the layered metals $Bi_8Pt_5I_3$ and $Bi_{16}Pt_{11}I_6$ showed completely new structural arrangements within the class of bismuth subiodides. The formation of expanded 2D networks with transition-element bonds as in these examples has not been observed so far. The very similar composition, which leads to these two different, layered arrangements, makes it very probable that further unique structural solutions could be discovered within the bismuth subiodides.

Characterisation and Understanding of Physical Properties by Quantum-Chemical Calculations and Experiments

The different discovered materials were successfully characterised with respect to their physical properties by means of quantum-mechanical calculations and various physical experiments. The calculations yielded DOS and electronic band structures, which could be compared to transport experiments. Moreover, with respect to the introduced class of the topological insulators, the Chern numbers, more precisely the Z_2-invariants, of all materials were calculated. In case of an insulator (semiconductor) and a semimetal this allowed to classify them as either a normal, topologically trivial, or a topologically non-trivial “insulator”.

As this classification revealed, $Bi_{14}Rh_3I_9$ belongs to a so far relatively little investigated class of topologically non-trivial materials, the “weak” 3D-TIs. That triggered several experiments to confirm this calculated property as well as to understand its origin. The experiments included ARPES to verify the electronic band structure and STM/STS to reveal the 1D edge states present at a certain surface of this material class. Both methods yielded convincing arguments for (a) the accuracy of the calculations and (b) the presence of the expected, protected edge states. Therefore, forthcoming research on $Bi_{14}Rh_3I_9$ could start to explore suggested applications, ranging from spin-channels and spin-filters with extremely small footprints for spintronics, to Majorana fermions as qubits in quantum computers.[24–29,44,74,200]

To understand the observations, a simplified model, an isolated layer structure (ILS), of $Bi_{14}Rh_3I_9$ was developed. The dominant structural motif of $Bi_{14}Rh_3I_9$, the honeycomb layer ${}^{2}_{\infty}[(Bi_{8/2}M)_3I]$, was extracted and examined separately. The similarity of this ILS and the original compound with respect to their electronic structure confirmed that $Bi_{14}Rh_3I_9$ could actually be seen as a stack of 2D-TIs. Furthermore, an analogy to graphene beyond purely structural aspects was drawn and the term "heavy graphene analogue", meaning "graphene" with strong SOC, was justified. Finally, it made it possible to analyse the influence of the substitution of other platinum-metal elements for rhodium.

As mentioned, this theoretical study was related to experimentally realised materials, with palladium and platinum instead of rhodium, but the same honeycomb network as the dominant structural motif. As not only the platinum-metal varies between the different real materials, but also the *separation* of the honeycomb layers, this theoretical study made it possible to separately analyse the different influences on the properties. Especially the non-trivial topological properties confirmed for the ILS in case of iridium, platinum and palladium, besides for rhodium, were discovered to be heavily dependent on the separation of the 2D-TI layers. In case of the compounds $Bi_{13}Pt_3I_7$ and $Bi_{13}Pd_3I_7$ this meant that they are trivial semimetals, in contrast to the weak 3D-TI $Bi_{14}Rh_3I_9$. Again, STM/STS experiments gave strong evidence for the validity of the calculations.

One observation from ARPES and STS hampering the possibility to exploit the unique properties of $Bi_{14}Rh_3I_9$ is the n-doping. It yields metallic transport properties independently of the transport in the topologically protected states, as was found in transport experiments. This n-doping is in contradiction to the quantum-mechanical calculations, but despite the fact that it has not been possible to resolve this issue up to now, at least an explanation was found. After substitution experiments with ruthenium were unsuccessful and no indication of a phase width with respect to bismuth was found, the ionic character of the layers turned out to be the root of this problem. At a surface, any ionic layer is unstable and undergoes certain electronic or structural changes. This leads to the n-doping of the honeycomb layer, while the iodido-bismuthate layer can desorb iodine to adjust to the situation at the surface. Having understood this problem, it should be possible to facilitate a solution in a chemical or a physical way. Chemically the oxidation of the surface could be imagined, e.g. with iodine deposited from the gaseous phase or from a solution in organic solvents. A physical attempt could be made with a sufficiently powerful top-gate or by selectively contacting channels of honeycomb layers that are not at the surface.

Finally, transport and magnetic measurements on $Bi_{13}Pt_3I_7$ and $Bi_{13}Pd_3I_7$ revealed, besides the calculated semimetallic behaviour, superconductivity. Although only a small volume fraction of the measured samples became superconducting, this could be a hint at unusual superconductivity due to edge or surface states. Even if this is so far a vague hypothesis, in case of a verification this would open new possibilities for the application of the weak 3D-TI $Bi_{14}Rh_3I_9$ as a quantum computing material. Interfacing it with a superconductor should host Majorana fermions, thereby making advanced quantum circuitry directly accessible.[28, 201]

Understanding the Band Structure Topology in Terms of Chemical Bonding

This at last leads to the more fundamental questions raised in the beginning of this work. With an idea of the chemical bonding within the honeycomb network at hand, specifically in $Bi_{14}Rh_3I_9$, a chemical interpretation may be as follows. Within each of the different ionic stacks of the honeycomb layers and the separating layers, the honeycomb layers aim at having a favourable electronic state. As the calculations of the different ILSs indicate, this can be achieved for any of the experimentally observed electron counts on the honeycomb layer, because the electron counts realised in actual compounds correspond to energy gaps in the DOS. This favourable electronic state necessitates covalent bonding between the platinum-element and bismuth, as well as multi-centre bonding within the triangles of the triangular prisms of the honeycomb net. The Z_2-invariants for the calculated gaps only become non-trivial in cases, when the Bi−Bi bonding is present in the triangles. If one would cut through the honeycomb layer and thereby create an edge of the otherwise infinite 2D layer, these states would be present at such an edge as dangling bonds. Considering their partly delocalised (multi-centre) character, it seems valid to assume that these dangling bonds are actually the basis of the formed, metallic edge state.

Going further, a localisation as usually expected for a one-dimensional metallic state (Peierls-distortion[75, 93]) should be suppressed by the “bulk part” of the structure, as it dominates the structural arrangement and could hinder, e.g. by the strong bonds between platinum-metal and bismuth, the rearrangement at such an edge. This would be a structural analogy to the bulk-boundary correspondence in the electronic band structure.

That finally only $Bi_{14}Rh_3I_9$ is a (weak) 3D-TI, but the other compounds become topologically trivial, can be understood in terms of the varying strength of the interactions in stacking direction. The different spacers yield shorter or longer distances between adjacent honeycomb layers and therefore stronger or weaker interactions, respectively. For $Bi_{13}Pt_3I_7$ and $Bi_{13}Pd_3I_7$, the alternating short and long distances between the honeycomb layers yield a trivial (due to pairwise coupling) semimetal (due to stronger interactions over the short distance). In case of $Bi_{38}Pt_9I_{14}$, no final conclusions can be drawn. Possibly, a higher level of theory is necessary, or one would have to perform a, at that time, very expensive geometry optimisation. Complementary, experiments on this compound may give further inside on how the topological properties of the electronic band structure evolve in this case were the honeycomb layer is separated only by short distances.

Final Conclusion

All in all, this thesis might give an experimental and theoretical basis for a deeper understanding of the new state of matter, the topological insulators. It could therefore lay a foundation on which applications, maybe even based on $Bi_{14}Rh_3I_9$, can be developed. The 1D edge states on the surface of $Bi_{14}Rh_3I_9$ could be a chance to handle spins and therefore propel spintronic research. In combination with a superconductor, which might be already available within the same family of materials, Majorana fermions might become accessible. In a far future, a quantum computer might solve some of today's limitations connected to the usage of silicon. It is a long way, to overcome these limitations in one or the other way, as several attempts in the last years have shown. But maybe the solution comes again from a fundamentally new understanding of the solid-state as it was the case when the transistor was developed in the 20th century.

A. Appendix

A.1. Synthesis and Thermodynamic Properties

A.1.1. The Bi–Rh–I System

Table A.1.: DSC signals on heating of a mixture of Bi, Rh, BiI_3 (molar ratio: Bi : Rh : I = 14 : 3 : 9) from room temperature to 700 °C shown in Figure 3.2.

signal	ϑ_{onset} / °C	effect	assigned reaction
H1	260	endo- and exothermic	melting of Bi and formation of Bi_4Rh
H2	269	exo- and endothermic	formation of BiI and rt-Bi_2Rh and unknown effect
H3	305	endothermic	decomposition of BiI
H4	324	exothermic	formation of $Bi_{43}Rh_3I_{36}$
H5	355	exothermic	formation of $Bi_{14}Rh_3I_9$
A	441	endothermic	decomposition of $Bi_{14}Rh_3I_9$
B	475	endothermic	decomposition of Bi_4RhI_2

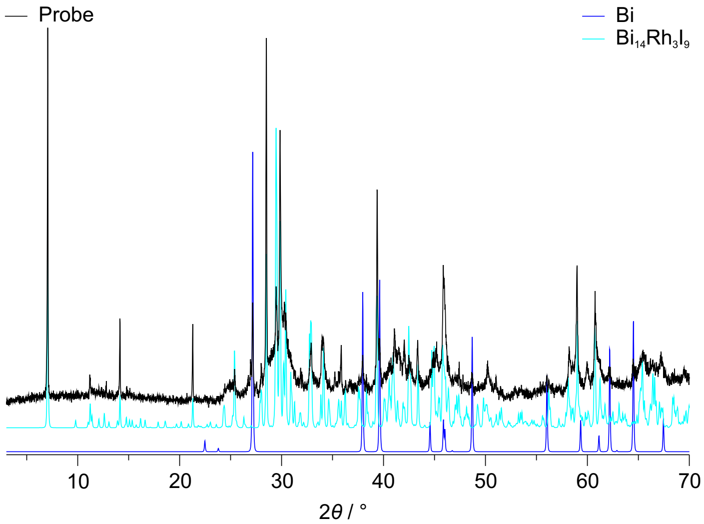

Figure A.1.: Powder X-ray diffraction pattern of a Bi-Rh-BiI_3-mixture (molar ratio Bi : Rh : I = 14 : 3 : 9) annealed for 1 h at 370 °C.

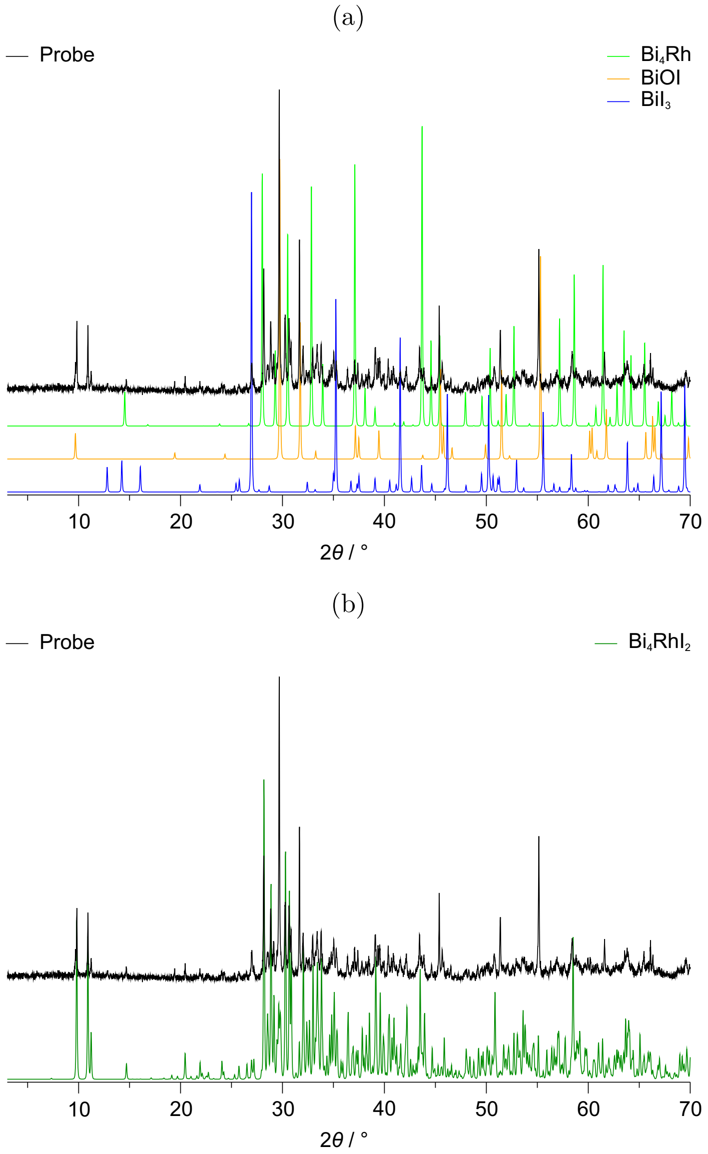

Figure A.2.: Powder X-ray diffraction pattern of a Bi-Rh-BiI_3-mixture (molar ratio Bi : Rh : I = 14 : 3 : 9) annealed for 1 h at 458 °C ((a) with binary references and (b) with ternary references).

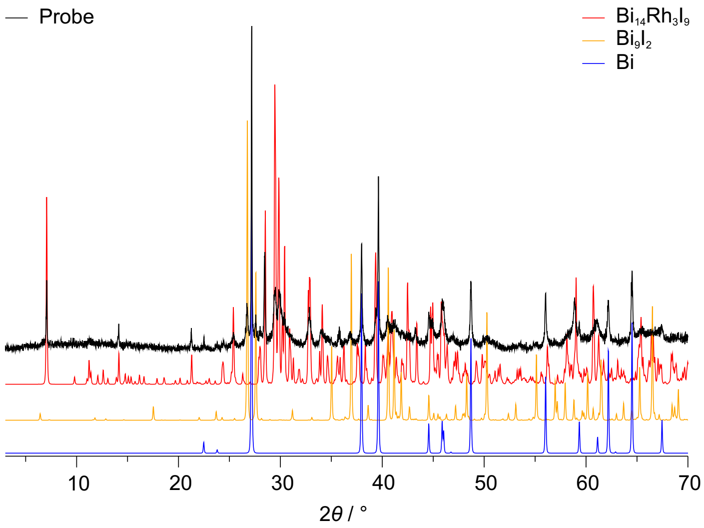

Figure A.3.: Powder X-ray diffraction pattern of a Bi-Rh-BiI_3-mixture (molar ratio Bi : Rh : I = 14 : 3 : 9) heated up to 600 °C, cooled with $-0.1\,K\,min^{-1}$ to 370 °C and annealed for 1 h.

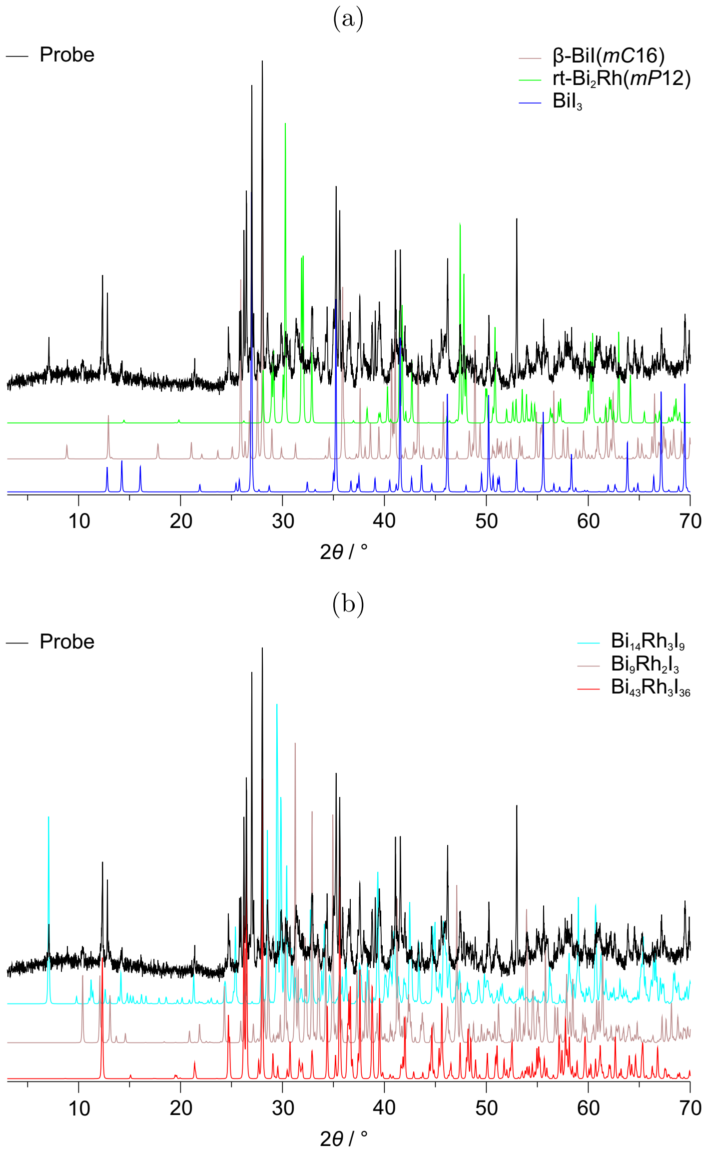

Figure A.4.: Powder X-ray diffraction pattern of a Bi-Rh-BiI_3-mixture (molar ratio Bi : Rh : I = 14 : 3 : 9) annealed for 1 h at 300 °C ((a) with binary references and (b) with ternary references).

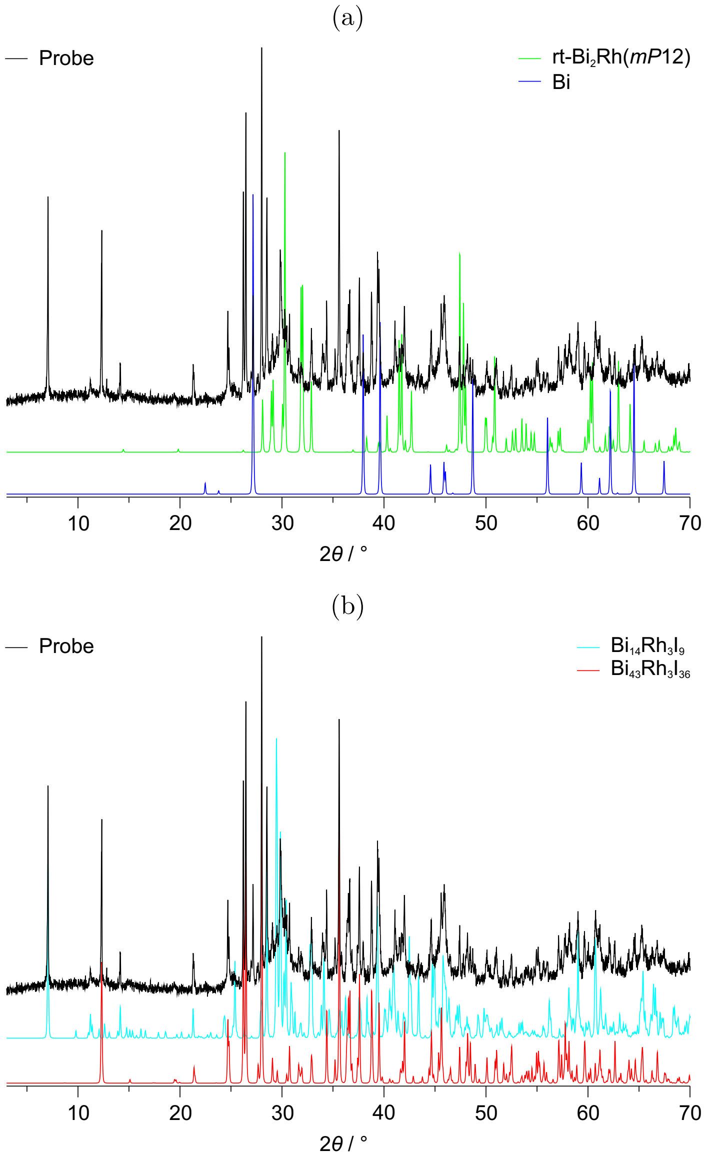

Figure A.5.: Powder X-ray diffraction pattern of a Bi-Rh-BiI_3-mixture (molar ratio Bi : Rh : I = 14 : 3 : 9) annealed for 1 h at 330 °C ((a) with binary references and (b) with ternary references).

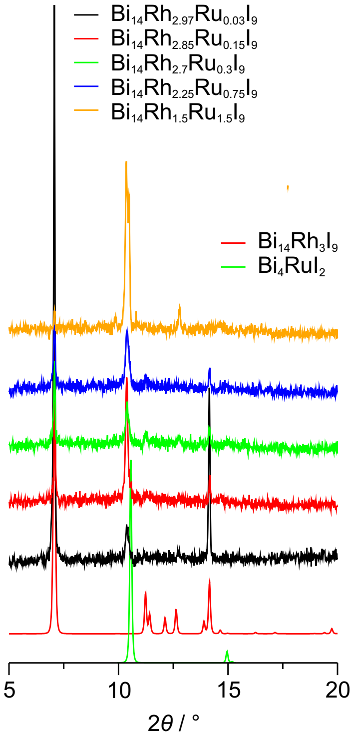

Figure A.6.: Powder X-ray diffraction pattern of the rhodium-rhuthenium substitution experiments, with reference patterns of $Bi_{14}Rh_3I_9$ and Bi_4RuI_2 zoomed into the range of $2\theta = 5°$ to $20°$. The shifted 2θ values in case of reflections belonging to the Bi_4RuI_2 structure indicate substitution of ruthenium by rhodium: $Bi_4Rh_{1-x}Ru_xI_2$. For the highest ruthenium content (nominal composition "$Bi_{14}Rh_{1.5}Ru_{1.5}I_9$") the reflection at approximately 11° is split, indicating either phase separation or formation of a lower symmetric phase (structurally most probably between Bi_4RuI_2 and Bi_4RhI_2).

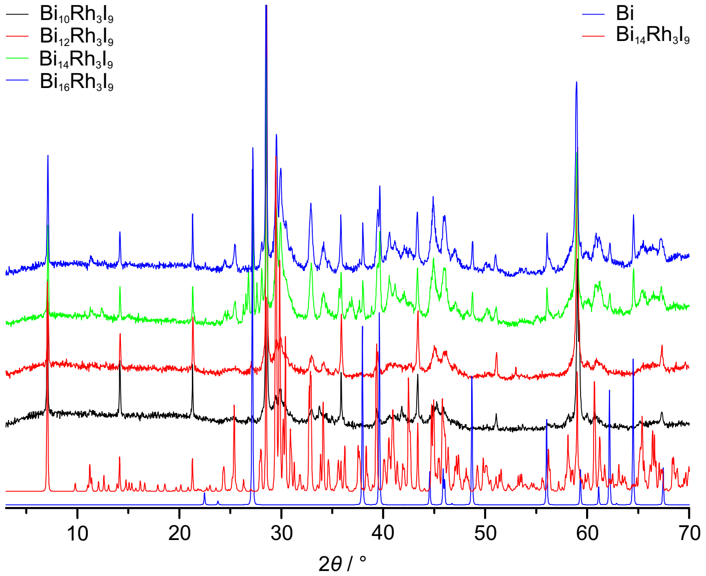

Figure A.7.: Powder X-ray diffraction pattern of the experiments on the phase width of $Bi_{14}Rh_3I_9$, with samples of the initial compositions $Bi_{10}Rh_3I_9$ (black), $Bi_{12}Rh_3I_9$ (red), $Bi_{14}Rh_3I_9$ (green) and $Bi_{16}Rh_3I_9$ (blue). $Bi_{14}Rh_3I_9$ (red) and Bi (blue) are given as references.

A.1.2. The Bi–Pt–I System

Table A.2.: (a) DSC signals upon heating of a mixture of Bi, PtI_2, and BiI_3 (Bi : Pt : I = 13 : 3 : 7) from RT to 800 °C (Figure 3.6a).
(b) DSC signals during heating of $Bi_{13}Pt_3I_7$ from RT to 800 °C and subsequent cooling (Figure 3.6b). Temperatures of pseudo binary reactions were taken from the binary phase diagram[136] and/or checked with a DSC measurement of a corresponding binary mixture.

(a) Heating of a mixture of Bi, PtI_2, and BiI_3

Signal	ϑ_{onset} / °C	effect	assigned process
H1	176	exothermic	formation of $Bi_{20}Pt_3I_{36}$
H2	261	endothermic	melting of bismuth (Bi-Pt eutectic)
H3	275	exothermic	formation of $Bi_2Pt(oP24)$
H4	283	endothermic	phase transition $Bi_2Pt(oP24) \rightarrow Bi_2Pt(cP12)$
H5	321	exothermic	formation of $Bi_{13}Pt_3I_7$; followed by melting of traces of BiI_3
H6	452	endothermic	peritectic decomposition of $Bi_{13}Pt_3I_7$
H7	540	endothermic	melting of $Bi_2Pt(hP9)$

(b) Heating of $Bi_{13}Pt_3I_7$

Signal	ϑ_{onset} / °C	effect	assigned process
H8	258	endothermic	melting of traces of bismuth
H9	459	endothermic	peritectic decomposition of $Bi_{13}Pt_3I_7$
H10	576	endothermic	melting of $Bi_2Pt(hP9)$
C1	534	exothermic	crystallisation of $Bi_2Pt(hP9)$
C2	420	exothermic	crystallisation of $Bi_{13}Pt_3I_7$

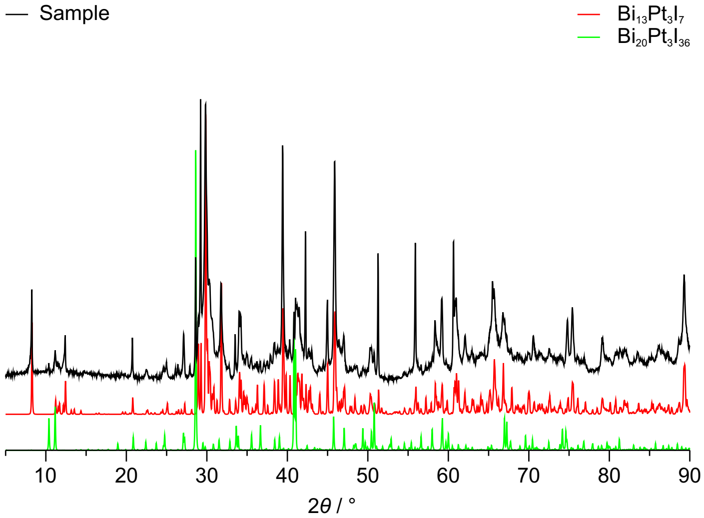

Figure A.8.: PXRD pattern of $Bi_{13}Pt_3I_7$ after peritectic decomposition and recrystallisation in a DSC experiment in a closed ampoule.

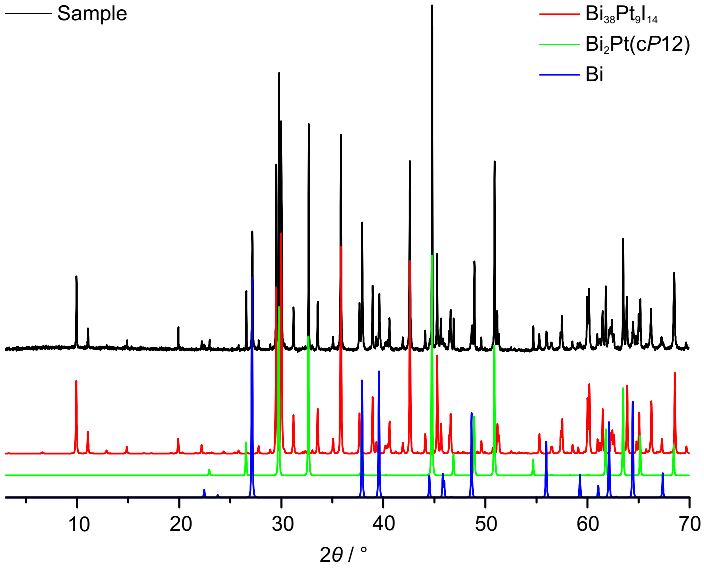

Figure A.9.: Powder X-ray diffraction pattern of a sample (Bi, BiI_3 and Pt in the molar ratio Bi : Pt : I = 38 : 9 : 14) annealed for one week at 290 °C and reference patterns of $Bi_{38}Pt_9I_{14}$, Bi and $Bi_2Pt(cP12)$.

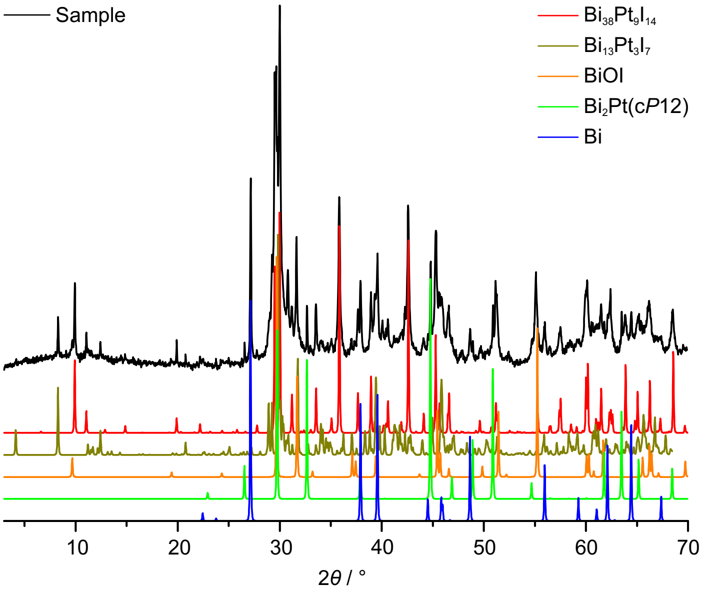

Figure A.10.: Powder X-ray diffraction pattern of a sample after a DSC-experiment (Figure 3.7b) with reference patterns of $Bi_{38}Pt_9I_{14}$, $Bi_{13}Pt_3I_7$, BiOI, Bi and Bi_2Pt(*cP*12). Most probably, BiOI was formed by reaction of BiI_3 with moisture from air during the preparation of the PXRD sample.

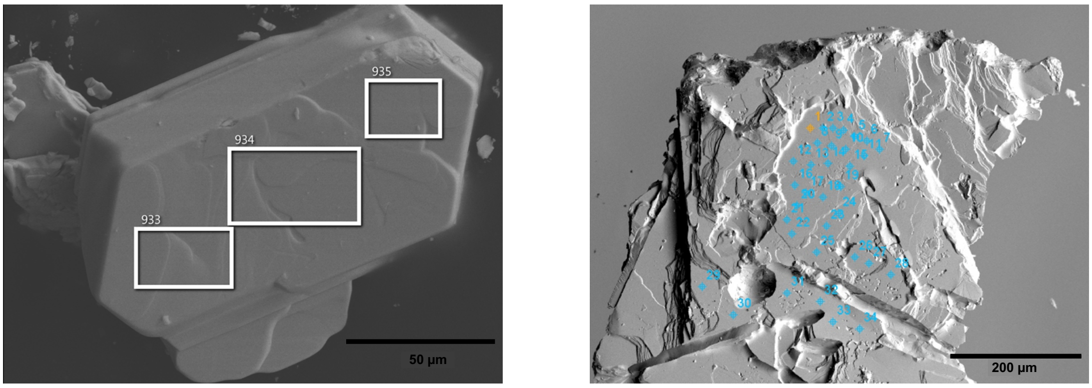
(a) (b)

(c)

	Bi / at%	Pt / at%	I / at%
	Experimental Data		
Figure A.11a	64.7(8)	14.6(1)	20.6(8)
Figure A.11b	64(1)	15(1)	21(1)
	Theoretical Data		
$Bi_{38}Pt_9I_{14}$	62.3	14.8	23.0
$Bi_{36}Pt_{11}I_{14}$	59.0	18.0	23.0
$Bi_{36}Pt_9I_{16}$	59.0	14.8	26.2

Figure A.11.: (a), (b) Scanning microscopy pictures of two different $Bi_{38}Pt_9I_{14}$ crystals with marked areas/spots where EDX spectra were taken. (c) The quantitative analysis and comparisson to possible theoretical compositions.

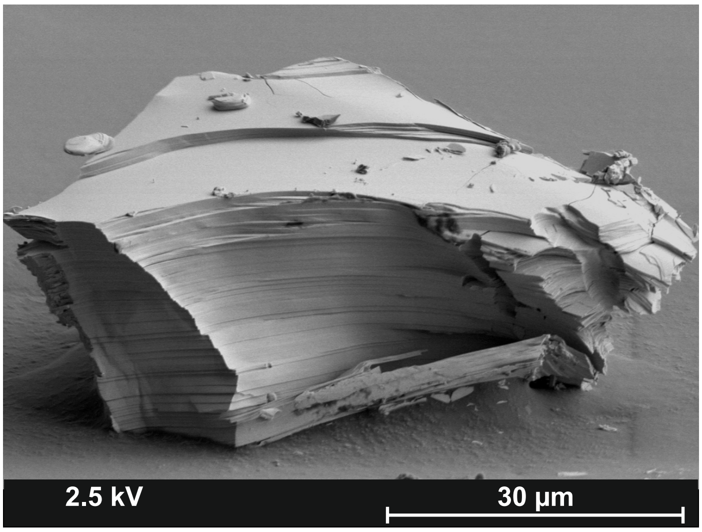

Figure A.12.: Scanning electron microscopy picture of a $Bi_{38}Pt_9I_{14}$ crystal.

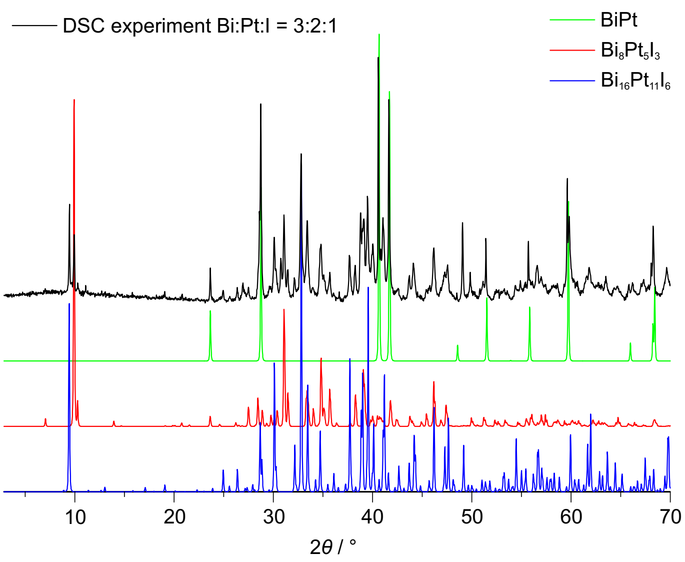

Figure A.13.: Powder X-ray diffraction pattern of the product (black) of a DSC measurement starting with a mixture of bismuth, platinum and BiI_3 in the molar ratio Bi : Pt : I = 3 : 2 : 1. Calculated reference patterns of the three majority phases in color.

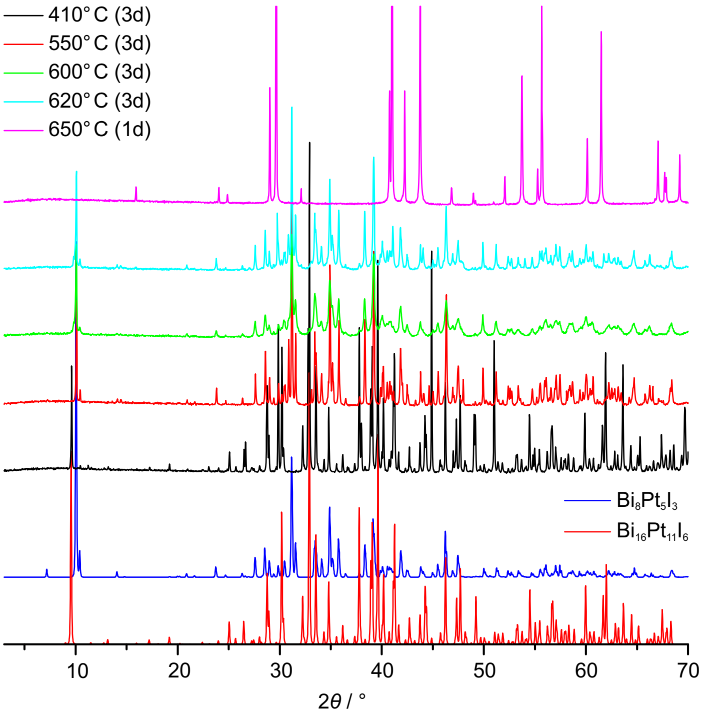

Figure A.14.: Powder X-ray diffraction pattern of the products after annealing mixtures of bismuth, platinum, and BiI_3 in the molar ratio Bi : Pt : I = 3 : 2 : 1 at 410 °C, 550 °C, 600 °C, 620 °C and 650 °C. Reference patterns are given for $Bi_8Pt_5I_3$ and $Bi_{16}Pt_{11}I_6$.

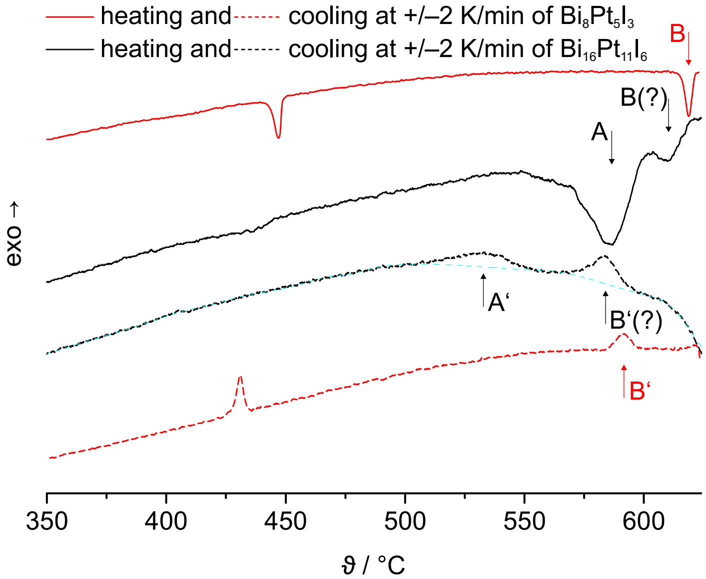

Figure A.15.: DSC measurements of $Bi_{16}Pt_{11}I_6$ and $Bi_8Pt_5I_3$, respectively. Signals in the course of heating indicate the decomposition of $Bi_{16}Pt_{11}I_6$ (A) and $Bi_8Pt_5I_3$ (B). In the cooling curve, the respective exothermic effects of the recrystallisation of the two compounds are A′ and B′, respectively. The additional endo- (heating) and exothermic (cooling) effect belongs to traces of $Bi_{20}Pt_3I_{36}$, which were identified via PXRD (Appendix: Figure A.16)

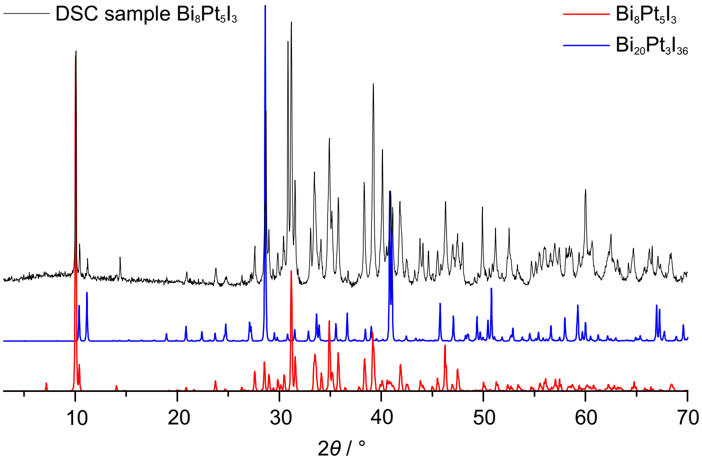

Figure A.16.: Powder X-ray diffraction pattern of the $Bi_8Pt_5I_3$ sample that was used for the DSC experiment shown in Figure A.15. Reference patterns are given for $Bi_8Pt_5I_3$ and $Bi_{20}Pt_3I_{36}$.

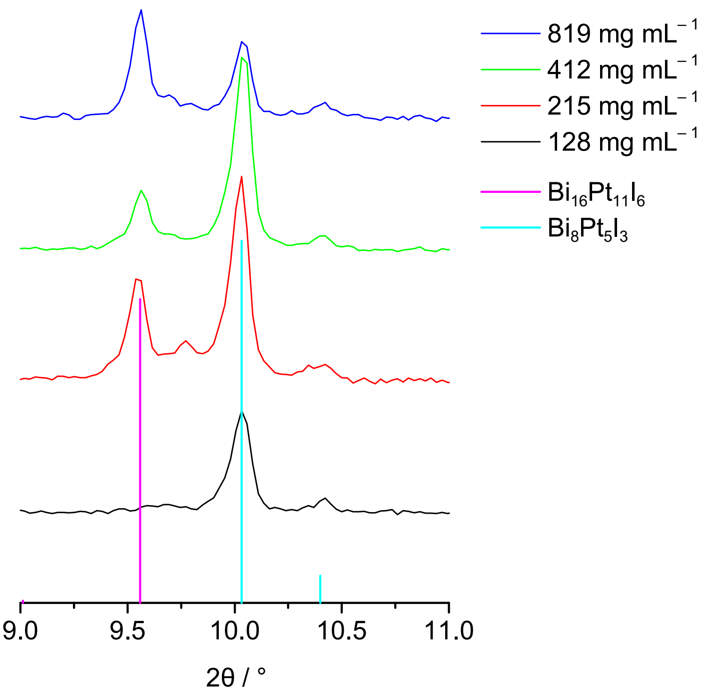

Figure A.17.: Powder X-ray diffraction pattern of the products after cooling (from 700 °C to RT with $-2\,\mathrm{K\,min^{-1}}$) mixtures of bismuth, platinum, and BiI_3 in the molar ratio Bi : Pt : I = 8 : 5 : 3 with different ampoule loads (see color code). To evaluate the approximate phase ratio between $Bi_8Pt_5I_3$ and $Bi_{16}Pt_{11}I_6$ a characteristic narrow angle interval was chosen.

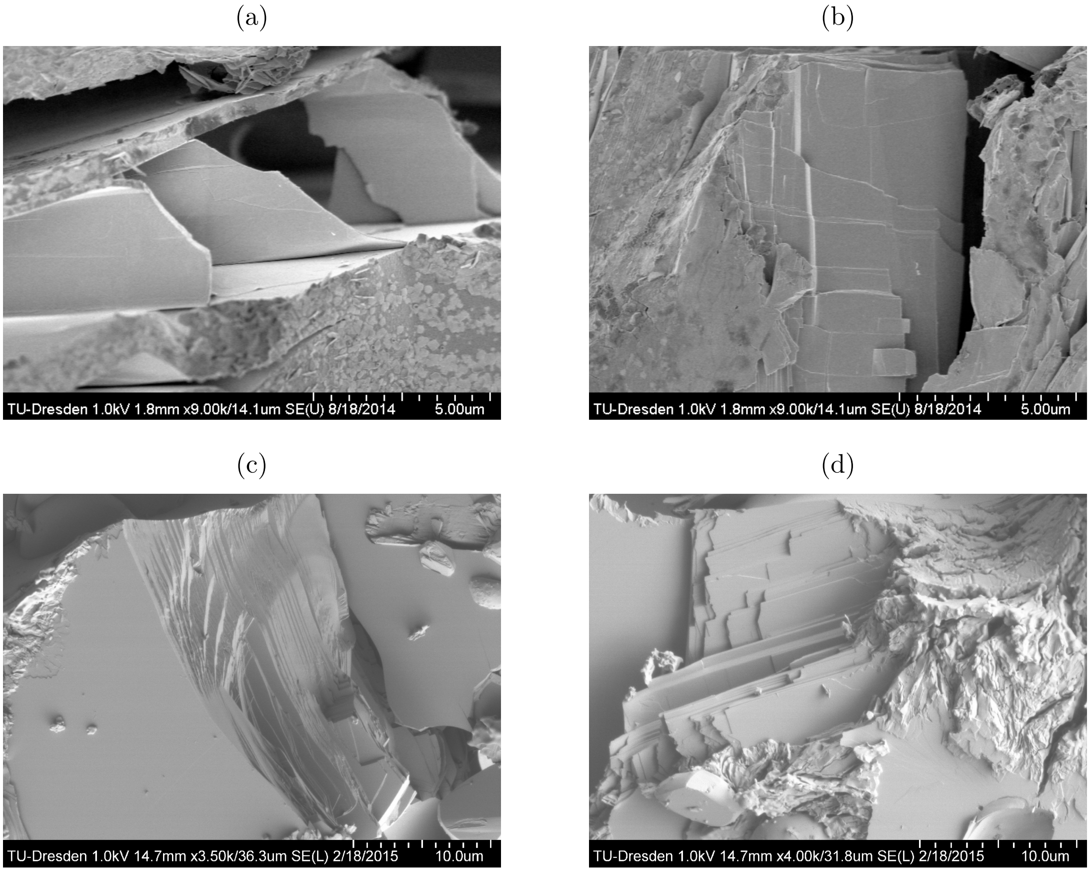

Figure A.18.: Scanning electron microscopy (SEM) images of (a), (b) $Bi_8Pt_5I_3$ and (c), (d) $Bi_{16}Pt_{11}I_9$ at 1 kV acceleration voltage.

Table A.3.: Peak temperatures and assigned reactions for effects in (a) the second heating cycle and (b) the second cooling cycle of a DSC experiment (Figure 3.8). Temperatures of pseudo binary reactions were taken from the binary phase diagram[136] and/or checked with a DSC measurement of a corresponding binary mixture.

(a) Heating

ϑ_{Peak} / °C	effect	assigned process
437	endothermic	$Bi_2Pt(cP12) \rightarrow Bi_2Pt(hP9)$, or peritectic decomposition of $Bi_{20}Pt_3I_{36}$
573	endothermic	peritectoid formation: $Bi_2Pt(cP12) + BiPt \rightarrow Bi_3Pt_2$
592	endothermic	peritectic decomposition of $Bi_{16}Pt_{11}I_6$
610	endothermic	peritectic decomposition of further unknown phase?
618	endothermic	peritectic decomposition of $Bi_8Pt_5I_3$
627	endothermic	peritectic decomposition: $Bi_2Pt(hP9) \rightarrow (Bi/Pt)_{(l)} + Bi_3Pt_2$
639	endothermic	traces of unreacted $Bi_2Pt(hP9)$?
673	endothermic	peritectic decomposition: $Bi_3Pt_2 \rightarrow (Bi/Pt)_{(l)} + BiPt$
712	endothermic	melting: $BiPt \rightarrow (Bi/Pt)(l)$

(b) Cooling

ϑ_{Peak} / °C	effect	assigned process
380	exothermic	crystallisation of BiI_3
422	exothermic	$Bi_2Pt(hP9) \rightarrow Bi_2Pt(cP12)$
496	exothermic	peritectoid decomposition: $Bi_3Pt_2 \rightarrow Bi_2Pt(hP9) + BiPt$
570	exothermic	peritectic formation of $Bi_{16}Pt_{11}I_6$ and/or $Bi_8Pt_5I_3$?
602	exothermic	peritectoid formation: $Bi_2Pt(hP9) + BiPt \rightarrow Bi_3Pt_2$
695	exothermic	crystallisation: $(Bi/Pt)_{(l)} \rightarrow BiPt$

A.1.3. Other Bi – *M* – I Systems

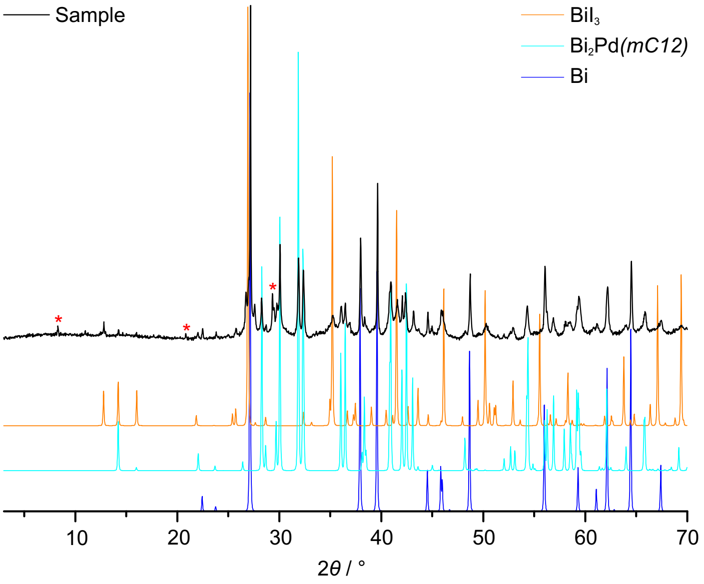

Figure A.19.: Powder X-ray diffraction pattern of the product of a DSC experiment of a mixture of bismuth, BiI_3 and palladium (molar ratio Bi : Pd : I = 13 : 3 : 7): twice heating from RT to 700 °C (2 K min^{-1}) and cooling down to RT (−2 K min^{-1}). References are given for bismuth, BiI_3 and $Bi_2Pd(mC12)$. Red marks indicate reflections which were assigned to the $Bi_{13}Pd_3I_7$ phase.

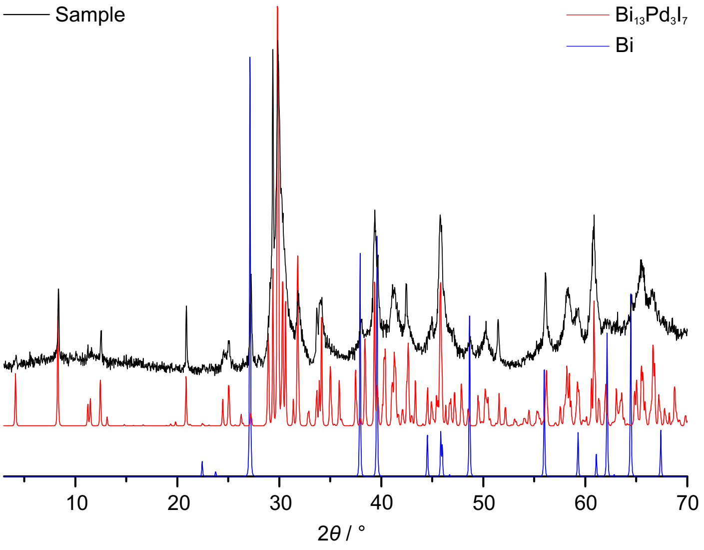

Figure A.20.: Powder X-ray diffraction pattern of the product after annealing a mixture of bismuth, BiI_3 and palladium (molar ratio Bi : Pd : I = 13 : 3 : 7) at 310 °C for 5 d. References are given for bismuth and $Bi_{13}Pd_3I_7$.

(a)

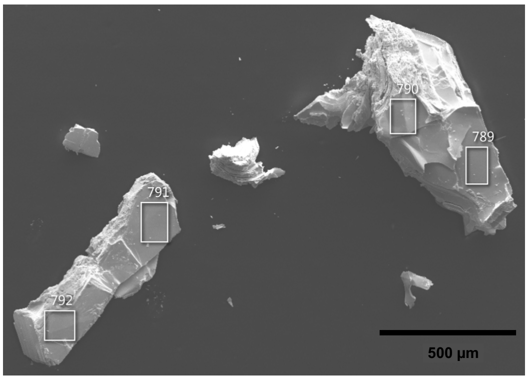

(b)

Bi / at%	Pd / at%	I / at%
Experimental Data		
57(2)	14(1)	29(1)
Theoretical Data		
56.5	13.0	30.4

Figure A.21.: (a) Scanning microscopy pictures of a $Bi_{13}Pd_3I_7$ crystal with marked areas where EDX spectra were taken.
(b) The quantitative results of the EDX measurements on the crystals in Figure A.21 and comparison to the theoretical composition.

A.2. Structures

A.2.1. $Bi_{14}Rh_3I_9$

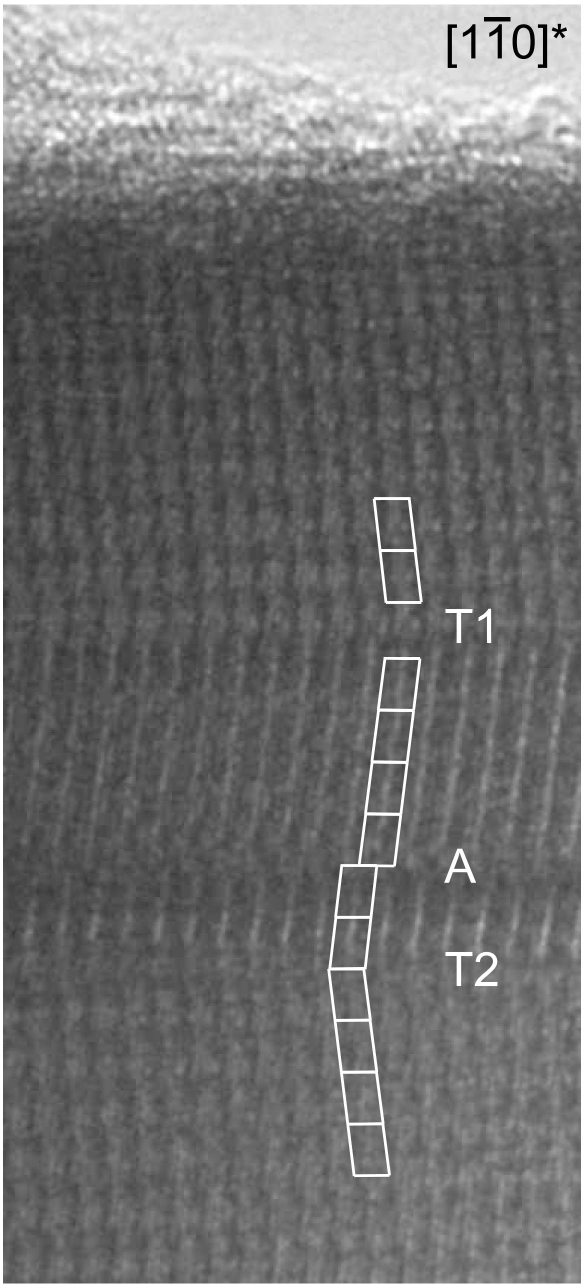

Figure A.22.: Experimentally observed twin domain boundaries at either an iodidobismuthate layer (T1) or an intermetallic layer (T2) as well as an antiphase shift (A) (scetch see Figure 4.6c. Imaging conditions are similar to those in Figure 4.5. The unit cell is outlined by a solid line.

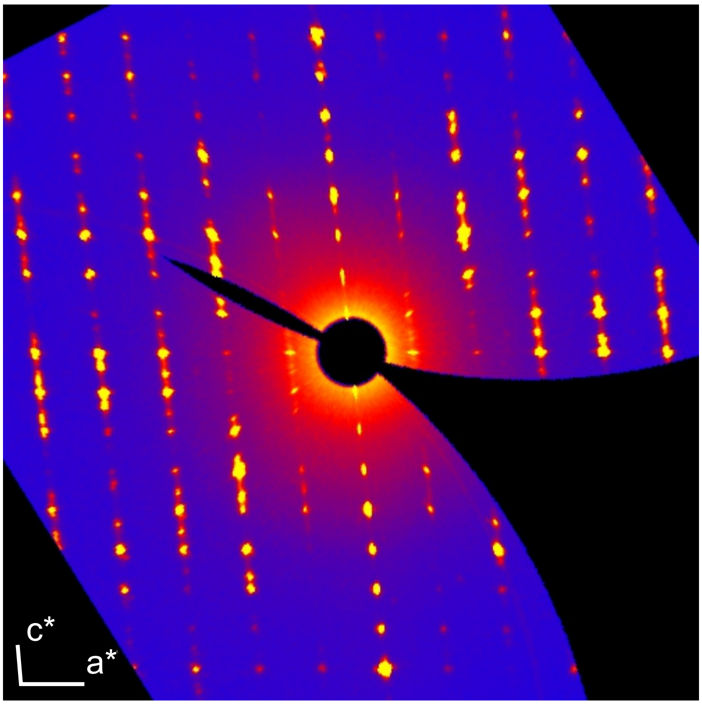

Figure A.23.: A $(h\,0\,l)$-cut of the reciprocal space of a crystal of $Bi_{14}Rh_3I_9$ with diffuse scattering in rows indicating severe stacking disorder.

Table A.4.: Crystal data and structure refinement for $Bi_{14}Rh_3I_9$ at 296 and 150 K.

Formula	$Bi_{14}Rh_3I_9$	
Formula weight	$4376.6\,\mathrm{g\,mol^{-1}}$	
Temperature	$T = 296\,\mathrm{K}$	$T = 150\,\mathrm{K}$
Crystal system	triclinic	
Space group	$P\bar{1}$ (no. 2)	
Cell parameters	$a = 914.10(4)\,\mathrm{pm}$, $b = 1578.72(7)\,\mathrm{pm}$, $c = 1426.35(7)\,\mathrm{pm}$, $\alpha = 62.7310(15)°$, $\beta = 80.9933(15)°$, $\gamma = 89.9431(15)°$.	$a = 908.97(6)\,\mathrm{pm}$, $b = 1570.23(10)\,\mathrm{pm}$, $c = 1416.97(9)\,\mathrm{pm}$, $\alpha = 62.694(2)°$, $\beta = 80.954(2)°$, $\gamma = 89.928(2)°$.
Volume	$V = 1801.2(2) \times 10^6\,\mathrm{pm}^3$	$V = 1768.9(2) \times 10^6\,\mathrm{pm}^3$
Formula units per cell	$Z = 2$	
Density (calculated)	$8.0697\,\mathrm{g\,cm^{-3}}$	$8.2168\,\mathrm{g\,cm^{-3}}$
Measurement device	Four-circle diffractometer Kappa APEX II (Bruker) with CCD detector, graphite-monochromated Mo-K_α radiation ($\lambda = 71.073\,\mathrm{pm}$)	
Absorption coefficient	$77.143\,\mathrm{mm^{-1}}$	$78.549\,\mathrm{mm^{-1}}$
Crystal size	$0.12 \times 0.07 \times 0.03\,\mathrm{mm}^3$	
Range of data collection	$2\theta_{max} = 56°$ $-12 \leq h \leq 12$ $-20 \leq k \leq 20$ $-18 \leq l \leq 18$	$2\theta_{max} = 56°$ $-12 \leq h \leq 12$ $-20 \leq k \leq 20$ $-18 \leq l \leq 18$
Number of measured / independent reflections	35327 / 8667	35455 / 8672
Absorption correction	numerical [110, 111]	
Max. and min. transmission	0.1795 and 0.0184	0.1619 and 0.0134
Data merging	$R_{int} = 0.0435$ $R_\sigma = 0.0550$	$R_{int} = 0.0739$ $R_\sigma = 0.0765$
Refinement method	Full matrix least squares on F^2 [114, 202]; anisotropic displacement parameters	
Data / restraints / parameters	8642 / 0 / 242	8503 / 0 / 242
Figures of merit	$R_1(\mathrm{all}F_o) = 0.0472$ $R_1(F_o > 4\sigma(F_o)) = 0.0242$ $wR_2(\mathrm{all}F_o) = 0.0582$ $GooF = 0.99$	$R_1(\mathrm{all}F_o) = 0.0581$ $R_1(Fo > 4\sigma(Fo)) = 0.0314$ $wR_2(\mathrm{all}F_o) = 0.0735$ $GooF = 1.1$
Residual electron density	3.86 to $-1.95e \times 10^{-6}\,\mathrm{pm}^{-3}$	4.07 to $-2.62e \times 10^{-6}\,\mathrm{pm}^{-3}$

Table A.5.: Atomic coordinates and equivalent isotropic displacement parameters (/pm^2) for $Bi_{14}Rh_3I_9$ at 296 K. U_{eq} is defined as one third of the trace of the orthogonalised U_{ij} tensor.

Atom	Wyckoff position	x	y	z	U_{eq}
Bi1	2i	0.04554(5)	0.30623(3)	0.12625(4)	159(2)
Bi2	2i	0.39341(5)	0.30601(3)	0.12704(4)	159(2)
Bi3	2i	0.39487(5)	0.08977(3)	0.12542(4)	160(2)
Bi4	2i	0.04546(5)	0.08774(3)	0.12856(4)	159(2)
Bi5	2i	0.10711(5)	0.41119(3)	−0.12755(4)	160(2)
Bi6	2i	0.45580(5)	0.41064(3)	−0.12698(4)	160(2)
Bi7	2i	0.45457(5)	0.19409(3)	−0.12886(4)	163(2)
Bi8	2i	0.10553(5)	0.19363(3)	−0.12553(4)	158(2)
Bi9	2i	0.21963(5)	0.48091(3)	0.12609(4)	156(2)
Bi10	2i	0.28127(5)	0.58549(3)	−0.12771(4)	156(2)
Bi11	2i	0.21962(5)	−0.08580(3)	0.12663(4)	165(2)
Bi12	2i	0.28047(5)	0.01929(3)	−0.12706(4)	163(2)
Bi13	2i	−0.15689(6)	0.12623(4)	0.49173(5)	283(2)
Bi14	2i	0.14452(6)	0.38071(4)	0.49921(4)	265(2)
Rh1	2i	0.25038(11)	0.24992(7)	−0.00028(9)	110(3)
Rh2	1c	0	1/2	0	112(6)
Rh3	1e	1/2	1/2	0	108(6)
Rh4	1d	1/2	0	0	113(6)
Rh5	1a	0	0	0	115(6)
I1	2i	−0.24928(10)	0.25051(7)	0.00188(9)	240(3)
I2	2i	−0.16978(11)	-0.09391(6)	0.62906(8)	305(4)
I3	2i	−0.31601(13)	0.12110(8)	0.33393(9)	469(5)
I4	2i	−0.41347(12)	0.14518(8)	0.62802(8)	407(5)
I5	2i	−0.09815(11)	0.34843(6)	0.36788(8)	293(4)
I6	2i	0.08636(11)	0.15784(7)	0.63303(8)	300(4)
I7	2i	0.39868(11)	0.34946(7)	0.36751(8)	336(4)
I8	2i	0.34234(11)	0.40439(7)	0.63041(8)	354(4)
I9	2i	0.15146(12)	0.59607(7)	0.34419(8)	369(4)

Table A.6.: Anisotropic displacement parameters (/pm^2) for $Bi_{14}Rh_3I_9$ at 296 K. The exponent of the anisotropic displacement factor takes the form: $-2\pi^2[h^2a^{*2}U_{11} + ... + 2hka^*b^*U_{12}]$.

Atom	U_{11}	U_{22}	U_{33}	U_{23}	U_{13}	U_{12}
Bi1	134(3)	126(2)	194(3)	−69(2)	12(2)	08(2)
Bi2	172(3)	126(2)	195(3)	−70(2)	−85(2)	16(2)
Bi3	168(3)	176(2)	196(3)	−122(2)	−84(2)	65(2)
Bi4	140(3)	176(2)	187(3)	−118(2)	12(2)	−19(2)
Bi5	175(3)	172(2)	195(3)	−118(2)	−91(2)	66(2)
Bi6	138(3)	177(2)	193(3)	−120(2)	07(2)	−21(2)
Bi7	140(3)	131(2)	196(3)	−70(2)	12(2)	12(2)
Bi8	172(3)	128(2)	188(3)	−70(2)	−84(2)	14(2)
Bi9	119(2)	222(2)	186(3)	−140(2)	−41(2)	27(2)
Bi10	118(2)	133(2)	188(3)	−43(2)	−44(2)	9(2)
Bi11	116(2)	141(2)	201(3)	−48(2)	−32(2)	9(2)
Bi12	118(2)	232(3)	201(3)	−150(2)	−35(2)	26(2)
Bi13	323(3)	289(3)	205(3)	−95(2)	−24(2)	18(2)
Bi14	310(3)	284(3)	196(3)	−105(2)	−50(2)	27(2)
Rh1	111(4)	98(4)	143(4)	−71(3)	−34(3)	15(3)
Rh2	97(7)	118(7)	139(8)	−71(6)	−32(6)	24(5)
Rh3	80(7)	116(7)	142(8)	−71(6)	−25(6)	0(5)
Rh4	91(7)	116(7)	147(8)	−70(6)	−30(6)	27(5)
Rh5	90(7)	114(7)	155(8)	−71(6)	−33(6)	9(5)
I1	168(4)	225(4)	395(5)	−195(4)	−74(3)	37(3)
I2	372(6)	264(5)	212(5)	−78(4)	30(4)	20(4)
I3	557(7)	553(7)	343(7)	−218(6)	−171(6)	11(5)
I4	401(6)	487(6)	220(6)	−95(5)	33(5)	124(5)
I5	385(6)	255(5)	202(5)	−59(4)	−106(4)	−20(4)
I6	393(6)	288(5)	178(5)	−69(4)	−68(4)	−2(4)
I7	379(6)	391(6)	198(5)	−113(5)	−15(5)	91(4)
I8	375(6)	473(6)	202(5)	−138(5)	−78(4)	−51(5)
I9	427(6)	304(5)	285(6)	−81(4)	3(5)	33(4)

Table A.7.: Atomic Distances /*pm* for $Bi_{14}Rh_3I_9$ at 296 K.

Rhodium–Bismuth		
Rh1	– Bi1	282.2(1)
	– Bi2	283.0(2)
	– Bi3	281.6(1)
	– Bi4	283.9(1)
	– Bi5	282.8(1)
	– Bi6	282.4(1)
	– Bi7	283.4(1)
	– Bi8	281.6(2)
Rh2	– Bi1	282.1(1)
	– Bi5	283.0(1)
	– Bi9	282.6(1)
	– Bi10	283.5(1)
Rh3	– Bi2	282.5(1)
	– Bi6	282.9(1)
	– Bi9	282.0(1)
	– Bi10	283.2(1)
Rh4	– Bi3	281.3(1)
	– Bi7	283.1(1)
	– Bi11	282.5(1)
	– Bi12	283.5(1)
Rh5	– Bi4	283.2(1)
	– Bi8	281.6(1)
	– Bi11	283.1(1)
	– Bi12	282.7(1)

Bismuth–Bismuth		
Bi1	– Bi2	318.2(1)
	– Bi4	343.4(1)
	– Bi5	316.8(1)
	– Bi9	318.4(1)
	– Bi10#1	344.2(1)
Bi2	– Bi3	342.4(1)
	– Bi6	317.1(1)
	– Bi9	318.0(1)
	– Bi10#2	343.7(1)
Bi3	– Bi4	318.7(1)
	– Bi7	317.4(1)
	– Bi11	319.5(1)
	– Bi12#3	342.7(1)
Bi4	– Bi8	317.1(1)
	– Bi11	317.6(1)
	– Bi12#4	343.4(1)
Bi5	– Bi6	318.9(1)
	– Bi8	342.2(1)
	– Bi9#1	343.9(1)
	– Bi10	317.9(1)
Bi6	– Bi7	343.1(1)
	– Bi9#2	343.2(1)
	– Bi10	318.4(1)
Bi7	– Bi8	318.4(1)
	– Bi11#3	343.0(1)
	– Bi12	317.5(1)
Bi8	– Bi11#4	343.2(1)
	– Bi12	318.9(1)
Bi9	– Bi10	316.8(1)
Bi11	– Bi12	316.7(1)

Bismuth–Iodine		
Bi13	– I2	310.1(1)
	– I2#5	336.7(1)
	– I3	289.5(2)
	– I4	291.1(1)
	– I5	312.1(1)
Bi14	– I5	329.7(1)
	– I6	313.6(1)
	– I7	294.1(1)
	– I8	293.5(2)
	– I9	308.6(1)
	– I9#6	336.2(1)

Symmetry transformations used to generate equivalent atoms:
#1 $x, y+1, z$ #2 $x+1, y+1, z$ #3 $x+1, y, z$ #4 $x-1, y-1, z-1$ #5 $x, y, z+1$
#6 $x, y+1, z+1$

Table A.8.: Atomic coordinates and equivalent isotropic displacement parameters (/pm^2) for $Bi_{14}Rh_3I_9$ at 150 K. U_{eq} is defined as one third of the trace of the orthogonalised U_{ij} tensor.

Atom	Wyckoff position	x	y	z	U_{eq}
Bi1	2*i*	0.04552(7)	0.30615(4)	0.12670(6)	122(3)
Bi2	2*i*	0.39341(7)	0.30588(5)	0.12734(6)	123(3)
Bi3	2*i*	0.39482(7)	0.08963(5)	0.12577(6)	121(3)
Bi4	2*i*	0.04529(7)	0.08768(5)	0.12887(6)	120(3)
Bi5	2*i*	0.10692(7)	0.41120(5)	−0.12771(6)	122(3)
Bi6	2*i*	0.45596(7)	0.41073(5)	−0.12730(6)	123(3)
Bi7	2*i*	0.45468(7)	0.19425(5)	−0.12920(6)	124(3)
Bi8	2*i*	0.10555(7)	0.19375(5)	−0.12577(6)	121(3)
Bi9	2*i*	0.21956(7)	0.48073(5)	0.12654(6)	121(3)
Bi10	2*i*	0.28125(7)	0.58566(4)	−0.12796(6)	120(3)
Bi11	2*i*	0.21941(7)	−0.08600(4)	0.12717(6)	122(3)
Bi12	2*i*	0.28069(7)	0.01929(5)	−0.12728(6)	124(3)
Bi13	2*i*	−0.15580(8)	0.12634(5)	0.49170(6)	200(3)
Bi14	2*i*	0.14363(8)	0.38070(5)	0.49942(6)	181(3)
Rh1	2*i*	0.25053(17)	0.24994(11)	−0.00024(14)	99(5)
Rh2	1*c*	0	½	0	96(8)
Rh3	1*e*	½	½	0	96(8)
Rh4	1*d*	½	0	0	101(8)
Rh5	1*a*	0	0	0	104(8)
I1	2*i*	−0.24927(15)	0.25064(9)	−0.00205(13)	160(4)
I2	2*i*	−0.17043(14)	−0.09414(9)	0.62911(11)	195(5)
I3	2*i*	−0.31588(16)	0.12108(10)	0.33340(11)	278(6)
I4	2*i*	−0.41383(15)	0.14544(10)	0.62796(11)	245(6)
I5	2*i*	−0.09890(14)	0.34907(9)	0.36785(11)	188(5)
I6	2*i*	0.08702(14)	0.15758(9)	0.63292(11)	188(5)
I7	2*i*	0.39889(15)	0.34925(9)	0.36764(11)	208(5)
I8	2*i*	0.34285(14)	0.40499(9)	0.63026(11)	213(5)
I9	2*i*	0.15118(15)	0.59641(9)	0.34367(11)	229(5)

Table A.9.: Anisotropic displacement parameters (/pm^2) for $Bi_{14}Rh_3I_9$ at 150 K. The exponent of the anisotropic displacement factor takes the form: $-2\pi^2[h^2a^{*2}U_{11} + ... + 2hka^*b^*U_{12}]$.

Atom	U_{11}	U_{22}	U_{33}	U_{23}	U_{13}	U_{12}
Bi1	111(4)	109(3)	140(4)	−62(3)	5(3)	6(2)
Bi2	130(4)	108(3)	143(4)	−60(3)	−48(3)	13(3)
Bi3	130(4)	132(3)	136(4)	−85(3)	−45(3)	35(3)
Bi4	113(3)	132(3)	133(4)	−85(3)	2(3)	−4(3)
Bi5	133(4)	134(3)	136(4)	−86(3)	−48(3)	37(3)
Bi6	114(3)	137(3)	134(4)	−85(3)	4(3)	−7(3)
Bi7	114(4)	111(3)	139(4)	−60(3)	3(3)	9(3)
Bi8	135(4)	112(3)	129(4)	−59(3)	−45(3)	12(3)
Bi9	103(3)	160(3)	133(4)	−97(3)	−21(3)	16(3)
Bi10	104(3)	111(3)	132(4)	−45(3)	−26(3)	08(2)
Bi11	102(3)	116(3)	137(4)	−50(3)	−19(3)	09(2)
Bi12	105(3)	162(3)	140(4)	−101(3)	−19(3)	15(3)
Bi13	224(4)	208(4)	155(4)	−79(3)	−15(3)	15(3)
Bi14	209(4)	194(4)	145(4)	−83(3)	−30(3)	19(3)
Rh1	100(6)	95(5)	113(6)	−58(5)	−19(5)	10(4)
Rh2	91(10)	97(10)	114(11)	−61(8)	−20(8)	16(7)
Rh3	87(10)	94(10)	121(11)	−60(9)	−20(8)	−1(7)
Rh4	94(10)	100(10)	121(11)	−61(9)	−18(8)	12(8)
Rh5	96(11)	110(10)	124(11)	−67(9)	−28(9)	12(8)
I1	133(5)	150(5)	230(6)	−113(5)	−37(4)	13(4)
I2	228(7)	179(6)	150(7)	−69(5)	21(5)	7(5)
I3	338(8)	320(8)	201(7)	−127(6)	−92(6)	14(6)
I4	245(7)	287(7)	146(7)	−67(6)	12(6)	66(6)
I5	236(7)	168(6)	139(7)	−47(5)	−54(6)	−8(5)
I6	234(7)	187(6)	127(7)	−59(5)	−33(6)	00(5)
I7	237(7)	234(7)	141(7)	−82(6)	−17(6)	52(5)
I8	224(7)	276(7)	138(7)	−91(6)	−43(5)	−23(5)
I9	269(7)	196(6)	180(7)	−64(5)	3(6)	22(5)

Table A.10.: Atomic Distances /*pm* for $Bi_{14}Rh_3I_9$ at 150 K.

Rhodium–Bismuth		
Rh1	–Bi1	280.8(2)
	–Bi2	281.5(2)
	–Bi3	280.2(2)
	–Bi4	282.5(2)
	–Bi5	281.3(2)
	–Bi6	280.8(2)
	–Bi7	281.8(2)
	–Bi8	280.3(2)
Rh2	–Bi1	280.6(1)
	–Bi5	281.5(1)
	–Bi9	281.3(1)
	–Bi10	281.9(1)
Rh3	–Bi2	281.0(1)
	–Bi6	281.6(1)
	–Bi9	280.6(1)
	–Bi10	281.8(1)
Rh4	–Bi3	279.9(1)
	–Bi7	281.7(1)
	–Bi11	281.2(1)
	–Bi12	281.9(1)
Rh5	–Bi4	281.9(1)
	–Bi8	280.1(1)
	–Bi11	281.8(1)
	–Bi12	281.2(1)

Bismuth–Bismuth		
Bi1	–Bi2	316.4(1)
	–Bi10#1	342.2(1)
	–Bi4	341.6(1)
	–Bi5	315.3(1)
	–Bi9	316.6(1)
Bi2	–Bi3	340.6(1)
	–Bi6	315.6(1)
	–Bi9	316.2(1)
	–Bi10#2	341.8(1)
Bi3	–Bi4	317.1(1)
	–Bi7	316.0(1)
	–Bi11	317.8(1)
	–Bi12#3	340.6(1)
Bi4	–Bi8	315.6(1)
	–Bi11	315.9(1)
	–Bi12#4	341.6(1)
Bi5	–Bi6	317.4(1)
	–Bi8	340.2(1)
	–Bi9#1	341.8(1)
	–Bi10	316.5(1)
Bi6	–Bi7	341.2(1)
	–Bi9#2	341.2(1)
	–Bi10	316.8(1)
Bi7	–Bi8	316.6(1)
	–Bi11#3	341.1(1)
	–Bi12	315.9(1)
Bi8	–Bi11#4	341.3(1)
	–Bi12	317.4(1)
Bi9	–Bi10	315.4(1)
Bi11	–Bi12	315.4(1)

Bismuth–Iodine		
Bi13	–I2	308.7(1)
	–I2#5	334.3(2)
	–I3	289.0(2)
	–I4	290.2(2)
	–I5	310.9(2)
	–I6	337.8(2)
Bi14	–I5	327.5(2)
	–I6	312.0(2)
	–I7	293.2(2)
	–I8	292.7(2)
	–I9	307.3(1)
	–I9#6	333.3(2)

Symmetry transformations used to generate equivalent atoms:
#1 $x, y+1, z$ #2 $x+1, y+1, z$ #3 $x+1, y, z$ #4 $x-1, y-1, z-1$ #5 $x, y, z+1$
#6 $x, y+1, z+1$

A.2.2. $Bi_{38}Pt_9I_{14}$

Table A.11.: Crystal data and structure refinement for $Bi_{38}Pt_9I_{14}$ at 296 and 120 K.

Formula	$Bi_{38}Pt_9I_{14}$	
Formula weight	$11\,473.65\,\mathrm{g\,mol^{-1}}$	
Temperature	$T = 296(1)\,\mathrm{K}$	$T = 120(2)\,\mathrm{K}$
Crystal system	hexagonal	
Space group	$P6/mmm$ (no. 191)	
Unit cell dimensions	$a = 922.50(2)\,\mathrm{pm}$, $c = 2671.09(7)\,\mathrm{pm}$.	$a = 919.15(3)\,\mathrm{pm}$, $c = 2661.79(9)\,\mathrm{pm}$.
Volume	$V = 1968.5(1) \times 10^6\,\mathrm{pm^3}$	$V = 1947.5(1) \times 10^6\,\mathrm{pm^3}$
Formula units per cell	$Z = 1$	
Density (calculated)	$9.678\,\mathrm{g\,cm^{-3}}$	$9.783\,\mathrm{g\,cm^{-3}}$
Measurement device	Four-circle diffractometer Kappa APEX II (Bruker) with CCD detector, graphite-monochromated Mo-K_α radiation ($\lambda = 71.073\,\mathrm{pm}$)	
Absorption coefficient	$105.956\,\mathrm{mm^{-1}}$	$107.103\,\mathrm{mm^{-1}}$
Crystal size	$0.14 \times 0.09 \times 0.01\,\mathrm{mm^3}$	
Range of data collection	$2\theta_{max} = 61°$ $-13 \leq h \leq 13$ $-13 \leq k \leq 13$ $-38 \leq l \leq 38$	$2\theta_{max} = 61°$ $-12 \leq h \leq 10$ $-10 \leq k \leq 12$ $-36 \leq l \leq 35$
Number of measured / independent reflections	42599 / 1244	26603 / 1180
Absorption correction	numerical[110, 111]	
Max. and min. transmission	0.3658 and 0.0072	0.3782 and 0.0081
Data merging	$R_{int} = 0.0492$ $R_\sigma = 0.0113$	$R_{int} = 0.0342$ $R_\sigma = 0.0093$
Refinement method	Full matrix least squares on F^2 [114, 202]; anisotropic displacement parameters	
Data / restraints / parameters	1244 / 0 / 45	1180 / 0 / 45
Figures of merit	$R_1(\mathrm{all}F_o) = 0.0313$ $R_1(F_o > 4\sigma(F_o)) = 0.0219$ $wR_2(\mathrm{all}F_o) = 0.0324$ $GooF = 1.129$	$R_1(\mathrm{all}F_o) = 0.0330$ $R_1(Fo > 4\sigma(Fo)) = 0.0273$ $wR_2(\mathrm{all}F_o) = 0.0695$ $GooF = 1.143$
Residual electron density	2.18 to $-2.15\ e \times 10^{-6}\,\mathrm{pm^{-3}}$	2.46 to $-2.89\ e \times 10^{-6}\,\mathrm{pm^{-3}}$

Table A.12.: Atomic coordinates and equivalent isotropic displacement parameters (/pm^2) for $Bi_{38}Pt_9I_{14}$ at 296 K. U_{eq} is defined as one third of the trace of the orthogonalised U_{ij} tensor.

Atom	Wyckoff position	x	y	z	U_{eq}
Pt1	$6i$	½	0	0.33212(2)	124(1)
Pt2	$3f$	½	0	0	120(1)
Bi1	$12o$	0.43904(4)	0.21952(2)	0.39459(2)	148(1)
Bi2	$12o$	0.43546(4)	0.21773(2)	0.06216(2)	180(1)
Bi3	$12o$	0.43175(4)	0.21587(2)	0.26988(2)	155(1)
Bi4	$2e$	0	0	0.26204(5)	277(2)
I1	$1a$	0	0	0	297(5)
I2	$2e$	0	0	0.38696(9)	348(5)
I3	$3g$	½	0	½	331(3)
I4	$6i$	½	0	0.16665(4)	279(2)
I5	$2e$	0	0	0.15233(9)	515(6)

Table A.13.: Anisotropic displacement parameters (/pm^2) for $Bi_{38}Pt_9I_{14}$ at 296 K. The exponent of the anisotropic displacement factor takes the form: $-2\pi^2[h^2a^{*2}U_{11} + ... + 2hka^*b^*U_{12}]$.

Atom	U_{11}	U_{22}	U_{33}	U_{23}	U_{13}	U_{12}
Pt1	128(2)	95(2)	138(2)	0	0	47(1)
Pt2	121(2)	94(3)	134(3)	0	0	47(1)
Bi1	140(2)	126(1)	183(2)	17(1)	35(1)	70(1)
Bi2	205(2)	152(1)	201(2)	32(1)	65(1)	103(1)
Bi3	158(2)	131(1)	185(2)	−15(1)	−29(1)	79(1)
Bi4	178(3)	178(3)	474(7)	0	0	89(1)
I1	209(7)	209(7)	472(16)	0	0	105(3)
I2	161(5)	161(5)	722(15)	0	0	80(2)
I3	484(7)	310(8)	142(6)	0	0	155(4)
I4	365(4)	302(5)	148(4)	0	0	151(2)
I5	536(9)	536(9)	473(13)	0	0	26.8(4)

Table A.14.: Atomic Distances $/pm$ for $Bi_{38}Pt_9I_{14}$ at 296 K.

Platinum–Bismuth		
Pt1	–Bi1	288.8(1)
	–Bi1#1	288.8(1)
	–Bi1#2	288.8(1)
	–Bi1#3	288.8(1)
	–Bi3#2	289.5(1)
	–Bi3#3	289.5(1)
	–Bi3#1	289.5(1)
	–Bi3	289.5(1)
Pt2	–Bi2#4	288.8(1)
	–Bi2#5	288.8(1)
	–Bi2#3	288.8(1)
	–Bi2	288.8(1)
	–Bi2#6	288.8(1)
	–Bi2#1	288.8(1)
	–Bi2#7	288.8(1)
	–Bi2#2	288.8(1)

Bismuth–Bismuth		
Bi1	–Bi1#8	315.0(1)
	–Bi1#1	315.0(1)
	–Bi3	333.2(1)
	–Bi1#2	350.8(1)
	–Bi1#9	350.8(1)
Bi2	–Bi2#8	319.9(1)
	–Bi2#1	319.9(1)
	–Bi2#5	332.0(1)
	–Bi2#2	347.9(1)
	–Bi2#9	347.9(1)
Bi3	–Bi3#8	325.1(1)
	–Bi3#1	325.1(1)
	–Bi3#9	344.9(1)
	–Bi3#2	344.9(1)
	–Bi4	345.6(1)
Bi4	–Bi3#9	345.6(1)
	–Bi3#10	345.6(1)
	–Bi3#11	345.6(1)
	–Bi3#2	345.6(1)
	–Bi3#12	345.6(1)

Bismuth–Iodine		
Bi4	–I5	293.1(3)
	–I2	333.7(3)

Symmetry transformations used to generate equivalent atoms:
#1 $-y+1, x-y, z$ #2 $y, -x+y, z$ #3 $-x+1, -y, z$ #4 $y, -x+y, -z$ #5 $-x+1, -y, -z$ #6 $-y+1, x-y, -z$ #7 $x, y, -z$ #8 $-x+y+1, -x+1, z$ #9 $x-y, x, z$ #10 $-x, -y, z$ #11 $-x+y, -x, z$ #12 $-y, x-y, z$

Table A.15.: Atomic coordinates and equivalent isotropic displacement parameters (/pm^2) for $Bi_{38}Pt_9I_{14}$ at 120 K. U_{eq} is defined as one third of the trace of the orthogonalised U_{ij} tensor.

Atom	Wyckoff position	x	y	z	U_{eq}
Pt1	6i	1/2	0	0.33219(2)	53(2)
Pt2	3f	1/2	0	0	51(2)
Bi1	12o	0.43895(5)	0.21947(3)	0.39480(2)	62(1)
Bi2	12o	0.43549(5)	0.21774(3)	0.06232(2)	76(1)
Bi3	12o	0.43194(5)	0.21597(3)	0.26978(2)	65(1)
Bi4	2e	0	0	0.26133(5)	111(2)
I1	1a	0	0	0	122(5)
I2	2e	0	0	0.38592(9)	130(4)
I3	3g	1/2	0	1/2	132(3)
I4	6i	1/2	0	0.16673(4)	115(2)
I5	2e	0	0	0.15146(9)	203(5)

Table A.16.: Anisotropic displacement parameters (/pm^2) for $Bi_{38}Pt_9I_{14}$ at 120 K. The exponent of the anisotropic displacement factor takes the form: $-2\pi^2[h^2a^{*2}U_{11} + ... + 2hka^*b^*U_{12}]$.

Atom	U_{11}	U_{22}	U_{33}	U_{23}	U_{13}	U_{12}
Pt1	52(2)	44(3)	61(3)	0	0	22(1)
Pt2	52(3)	45(4)	56(4)	0	0	23(2)
Bi1	60(2)	55(2)	73(2)	6(1)	13(1)	30(1)
Bi2	88(2)	67(2)	81(2)	13(1)	25(2)	44(1)
Bi3	63(2)	53(2)	81(2)	−5(1)	−11(1)	32(1)
Bi4	78(3)	78(3)	177(6)	0	0	39(2)
I1	98(8)	98(8)	170(14)	0	0	49(4)
I2	64(5)	64(5)	263(11)	0	0	32(3)
I3	189(6)	125(7)	61(6)	0	0	62(4)
I4	146(4)	122(5)	68(5)	0	0	61(3)
I5	211(7)	211(7)	187(10)	0	0	105(3)

Table A.17.: Atomic Distances $/pm$ for $Bi_{38}Pt_9I_{14}$ at 120 K.

Platinum–Bismuth			Bismuth–Bismuth			Bismuth–Iodine		
Pt1	–Bi1#1	288.0(1)	Bi1	–Bi1#8	314.0(1)	Bi4	–I5	292.4(3)
	–Bi1#2	288.0(1)		–Bi1#1	314.0(1)	Bi4	–I2	331.6(3)
	–Bi1#3	288.0(1)		–Bi3	332.8(1)			
	–Bi1	288.0(1)		–Bi1#9	349.4(1)			
	–Bi3	288.7(1)		–Bi1#2	349.4(1)			
	–Bi3#2	288.7(1)	Bi2	–Bi2#8	318.7(1)			
	–Bi3#1	288.7(1)		–Bi2#1	318.7(1)			
	–Bi3#3	288.7(1)		–Bi2#7	331.8(1)			
Pt2	–Bi2	288.0(1)		–Bi2#2	346.7(1)			
	–Bi2#4	288.0(1)		–Bi2#9	346.7(1)			
	–Bi2#1	288.0(1)	Bi3	–Bi3#1	323.6(1)			
	–Bi2#5	288.0(1)		–Bi3#8	323.6(1)			
	–Bi2#6	288.0(1)		–Bi3#9	343.8(1)			
	–Bi2#2	288.0(1)		–Bi3#2	343.8(1)			
	–Bi2#3	288.0(1)		–Bi4	344.6(1)			
	–Bi2#7	288.0(1)	Bi4	–Bi3#9	344.6(1)			
				–Bi3#10	344.6(1)			
				–Bi3#11	344.6(1)			
				–Bi3#12	344.6(1)			
				–Bi3#2	344.6(1)			

Symmetry transformations used to generate equivalent atoms:
#1 $-y+1, x-y, z$ #2 $y, -x+y, z$ #3 $-x+1, -y, z$ #4 $y, -x+y, -z$ #5 $-x+1, -y, -z$ #6 $-y+1, x-y, -z$ #7 $x, y, -z$ #8 $-x+y+1, -x+1, z$ #9 $x-y, x, z$ #10 $-x, -y, z$ #11 $-x+y, -x, z$ #12 $-y, x-y, z$

Table A.18.: Extrapolated principal mean square displacements ($/pm^2$) at 0 K together with the mean value and the standard deviation for all atoms in $Bi_{38}Pt_9I_{14}$. Bi4, I1, I2 and I5 are residing in the hexagonal the channels.

atom	principal mean square displacement at 0 K			mean value	standard deviation
Pt1	27	19	22	23	4
Pt2	22	21	24	23	1
Bi1	29	25	22	25	3
Bi2	42	25	27	31	9
Bi3	35	23	19	26	9
Bi4	49	35	35	40	8
I1	40	50	50	47	6
I2	65	22	22	36	25
I3	67	45	26	46	20
I4	55	44	34	44	11
I5	71	71	64	68	4

A.2.3. $Bi_{13}Pt_3I_7$

Table A.19.: Crystal data and structure refinement for $Bi_{13}Pt_3I_7$ at 150 K.

Formula	$Bi_{13}Pt_3I_7$
Formula weight	$4190.3\,g\,mol^{-1}$
Temperature	$T = 150\,K$
Crystal system	triclinic
Space group	$P\bar{1}$ (no. 2)
Cell parameters	$a = 908.15(5)\,pm$,
	$b = 1572.8(1)\,pm$,
	$c = 2235.4(1)\,pm$,
	$\alpha = 103.634(3)°$,
	$\beta = 101.681(3)°$,
	$\gamma = 90.113(3)°$.
Volume	$V = 3034.5(2) \times 10^6\,pm^3$
Formula units per cell	$Z = 4$
Density (calculated)	$9.172\,g\,cm^{-3}$
Measurement device	Four-circle diffractometer Kappa APEX II (Bruker) with CCD detector, graphite-monochromated Mo-K_α radiation ($\lambda = 71.073\,pm$)
Absorption coefficient	$95.952\,mm^{-1}$
Crystal size	$0.005 \times 0.047 \times 0.052\,mm^3$
Range of data collection	$2\theta_{max} = 55°$
	$-11 \leq h \leq 11$
	$-20 \leq k \leq 19$
	$-29 \leq l \leq 28$
Number of measured / independent reflections	48549 / 12104
Absorption correction	numerical[110, 111]
Max. and min. transmission	0.286 and 0.019
Data merging	$R_{int} = 0.0752$
	$R_\sigma = 0.0575$
Refinement method	Full matrix least squares on F^2[114, 202]; anisotropic displacement parameters
Data / restraints / parameters	12104 / 0 / 416
Figures of merit	$R_1(\text{all}F_o) = 0.0832$
	$R_1(F_o > 4\sigma(F_o)) = 0.0407$
	$wR_2(\text{all}F_o) = 0.0934$
	$GooF = 1.340$
Residual electron density	6.56 to $-6.66e \times 10^{-6}\,pm^{-3}$

Table A.20.: Atomic coordinates and equivalent isotropic displacement parameters ($/pm^2$) of $Bi_{13}Pt_3I_7$ at 150 K. U_{eq} is defined as one third of the trace of the orthogonalized U_{ij} tensor.

Atom	Wyckoff position	x	y	z	U_{eq}
Bi1	$2i$	0.50987(14)	0.02508(7)	0.12670(6)	76(4)
Bi2	$2i$	0.58968(14)	0.07832(7)	0.28274(6)	73(4)
Bi3	$2i$	0.76349(13)	0.25335(7)	0.28195(6)	76(4)
Bi4	$2i$	0.68621(14)	0.19948(7)	0.12378(6)	83(4)
Bi5	$2i$	0.18333(14)	0.13385(7)	0.12393(6)	84(4)
Bi6	$2i$	0.26281(13)	0.18606(7)	0.28203(6)	77(4)
Bi7	$2i$	0.43780(13)	0.36099(7)	0.28402(6)	74(4)
Bi8	$2i$	0.36395(14)	0.30988(7)	0.12699(6)	71(4)
Bi9	$2i$	0.01077(14)	0.30717(7)	0.12372(6)	80(4)
Bi10	$2i$	0.08745(14)	0.36158(7)	0.28141(6)	76(4)
Bi11	$2i$	0.09422(14)	0.57948(7)	0.28377(6)	75(4)
Bi12	$2i$	0.01175(14)	0.52551(7)	0.12707(6)	77(4)
Bi13	$2i$	0.36226(14)	0.52574(7)	0.12372(6)	80(4)
Bi14	$2i$	0.44091(14)	0.57759(7)	0.28148(6)	77(4)
Bi15	$2i$	0.26708(13)	0.75319(7)	0.28154(6)	76(4)
Bi16	$2i$	0.18960(13)	0.69933(7)	0.12381(6)	80(4)
Bi17	$2i$	0.68652(13)	0.63403(7)	0.12382(6)	79(4)
Bi18	$2i$	0.76706(13)	0.68658(7)	0.28199(6)	72(4)
Bi19	$2i$	0.59188(14)	0.86137(7)	0.28237(6)	75(4)
Bi20	$2i$	0.51328(14)	0.80720(7)	0.12409(6)	81(4)
Bi21	$2i$	0.86650(14)	0.81051(7)	0.12697(6)	73(4)
Bi22	$2i$	0.94108(13)	0.86229(7)	0.28357(6)	77(4)
Bi23	$2i$	0.86027(14)	0.02651(7)	0.12391(6)	80(4)
Bi24	$2i$	0.93862(14)	0.07948(7)	0.28268(6)	78(4)
Bi25	$2i$	0.64525(15)	0.11967(8)	0.50054(6)	132(4)
Bi26	$2i$	0.34209(15)	0.37784(8)	0.50358(6)	136(4)
Pt1	$2i$	0.47533(15)	0.19367(8)	0.20514(7)	44(5)
Pt2	$2i$	0.22667(16)	0.44378(9)	0.20492(7)	44(5)
Pt3	$2i$	0.47875(15)	0.69342(8)	0.20462(7)	44(5)
Pt4	$2i$	0.72751(16)	0.94401(8)	0.20499(7)	44(5)
Pt5	$2i$	0.97870(15)	0.69442(8)	0.20522(7)	41(5)
Pt6	$2i$	0.97489(15)	0.19383(8)	0.20458(7)	44(5)
I1	$2i$	0.7281(3)	0.44493(15)	0.20820(13)	93(8)
I2	$2i$	0.2285(3)	0.94517(14)	0.20910(13)	98(8)
I3	$2i$	0.6286(3)	0.37898(16)	0.01074(12)	174(9)
I4	$2i$	0.1238(3)	0.37523(15)	−0.00008(12)	98(8)
I5	$2i$	0.3733(3)	0.12546(15)	−0.00006(12)	97(8)
I6	$2i$	0.8681(3)	0.12133(16)	−0.01095(12)	174(9)
I7	$2i$	0.3412(3)	0.00247(15)	0.40990(12)	171(8)
I8	$2i$	0.8370(3)	0.01475(15)	0.42407(12)	161(9)
I9	$2i$	0.9084(3)	0.23032(16)	0.57695(13)	149(9)
I10	$2i$	0.4061(3)	0.23249(15)	0.57759(12)	134(9)
I11	$2i$	0.5815(3)	0.26182(16)	0.42240(12)	127(9)
I12	$2i$	0.0761(3)	0.27425(16)	0.42437(13)	189(9)
I13	$2i$	0.1892(3)	0.48069(16)	0.59520(12)	212(9)
I14	$2i$	0.6745(3)	0.48371(14)	0.57603(12)	135(8)

Table A.21.: Anisotropic displacement parameters (/pm^2) of $Bi_{13}Pt_3I_7$ at 150 K. The exponent of the anisotropic displacement factor takes the form: $-2\pi^2[h^2a^{*2}U_{11} + ... + 2hka^*b^*U_{12}]$.

Atom	U_{11}	U_{22}	U_{33}	U_{23}	U_{13}	U_{12}
Bi1	89(7)	76(6)	50(7)	6(5)	1(6)	16(5)
Bi2	108(7)	78(6)	46(6)	23(5)	34(6)	30(5)
Bi3	68(7)	90(6)	54(7)	−15(5)	13(6)	7(5)
Bi4	71(7)	127(6)	56(7)	41(5)	5(6)	9(5)
Bi5	84(7)	90(6)	57(7)	−22(5)	16(6)	3(5)
Bi6	76(7)	114(6)	54(7)	42(5)	18(6)	13(5)
Bi7	84(7)	71(6)	47(6)	−6(5)	−8(6)	15(5)
Bi8	94(7)	84(6)	49(6)	23(5)	33(6)	25(5)
Bi9	87(7)	100(6)	50(7)	31(5)	−10(6)	−4(5)
Bi10	108(7)	76(6)	43(6)	−3(5)	32(6)	−5(5)
Bi11	99(7)	85(6)	50(7)	20(5)	29(6)	30(5)
Bi12	89(7)	76(6)	51(7)	4(5)	−3(6)	13(5)
Bi13	106(7)	72(6)	56(7)	−10(5)	36(6)	−12(5)
Bi14	78(7)	82(6)	63(7)	28(5)	−15(6)	−11(5)
Bi15	65(7)	88(6)	56(7)	−14(5)	9(6)	5(5)
Bi16	72(7)	119(6)	60(7)	43(5)	17(6)	6(5)
Bi17	75(7)	85(6)	60(7)	−20(5)	21(6)	−2(5)
Bi18	71(7)	112(6)	48(6)	44(5)	22(6)	22(5)
Bi19	100(7)	74(6)	51(7)	2(5)	34(6)	−7(5)
Bi20	87(7)	101(6)	57(7)	39(5)	−9(6)	−11(5)
Bi21	94(7)	90(6)	48(6)	23(5)	37(6)	24(5)
Bi22	73(7)	83(6)	54(7)	−4(5)	−11(6)	13(5)
Bi23	107(7)	76(6)	52(7)	−10(5)	37(6)	−10(5)
Bi24	88(7)	79(6)	60(7)	30(5)	−15(6)	−13(5)
Bi25	166(7)	137(6)	90(6)	19(5)	30(5)	22(5)
Bi26	169(7)	147(6)	87(6)	34(5)	11(5)	13(5)
Pt1	43(8)	66(7)	20(8)	8(6)	3(6)	15(5)
Pt2	60(7)	51(6)	17(7)	3(6)	8(6)	5(5)
Pt3	54(8)	58(7)	13(8)	−4(6)	7(6)	1(5)
Pt4	63(8)	46(6)	22(7)	2(6)	11(6)	9(5)
Pt5	47(8)	54(6)	12(8)	−5(6)	2(6)	15(5)
Pt6	56(8)	55(7)	19(8)	1(6)	10(6)	4(5)
I1	68(13)	104(12)	106(14)	23(10)	15(11)	17(9)
I2	89(13)	82(11)	124(14)	27(10)	21(11)	14(9)
I3	226(15)	210(13)	73(14)	21(11)	19(12)	11(10)
I4	136(14)	125(12)	20(12)	5(9)	4(11)	3(9)
I5	130(14)	136(12)	10(12)	1(9)	2(10)	5(9)
I6	221(15)	208(13)	70(14)	10(11)	5(12)	5(10)
I7	194(14)	192(12)	122(13)	66(10)	−6(11)	−4(9)
I8	187(15)	201(13)	74(13)	−4(10)	27(11)	61(10)
I9	172(14)	187(12)	63(14)	0(11)	2(12)	−20(9)
I10	176(14)	153(12)	96(14)	48(10)	56(12)	50(9)
I11	170(14)	169(12)	52(13)	27(10)	42(11)	61(9)
I12	182(15)	256(14)	84(14)	17(11)	−44(12)	−82(10)
I13	280(15)	242(13)	105(13)	−9(10)	77(11)	60(10)
I14	183(14)	134(11)	66(12)	31(9)	−28(11)	−11(9)

Table A.22.: Atomic Distances /*pm* for $Bi_{13}Pt_3I_7$ at 150 K.

Platinum–Bismuth		
Pt1	– Bi1	287.0(2)
	– Bi2	285.3(2)
	– Bi3	284.4(2)
	– Bi4	291.1(2)
	– Bi5	290.7(2)
	– Bi6	285.2(2)
	– Bi7	286.5(2)
	– Bi8	286.6(2)
Pt2	– Bi7	286.7(2)
	– Bi8	286.1(2)
	– Bi9	290.8(2)
	– Bi10	284.7(2)
	– Bi11	286.4(2)
	– Bi12	286.0(2)
	– Bi13	291.1(2)
	– Bi14	284.3(2)
Pt3	– Bi13	288.3(2)
	– Bi14	284.6(2)
	– Bi15	284.9(2)
	– Bi16	288.6(2)
	– Bi17	287.9(2)
	– Bi18	284.8(2)
	– Bi19	285.6(2)
	– Bi20	287.9(2)
Pt4	– Bi1	287.3(2)
	– Bi2	286.5(2)
	– Bi19	284.9(2)
	– Bi20	290.0(2)
	– Bi21	286.7(2)
	– Bi22	286.2(2)
	– Bi23	290.0(2)
	– Bi24	285.0(2)
Pt5	– Bi11#2	286.5(2)
	– Bi12#2	286.8(2)
	– Bi15#2	283.9(2)
	– Bi16#2	290.9(2)
	– Bi17	291.1(2)
	– Bi18	284.4(2)
	– Bi21	286.7(2)
	– Bi22	286.7(2)
Pt6	– Bi3	285.3(2)
	– Bi4	288.1(2)
	– Bi5#2	288.3(2)
	– Bi6#2	284.9(2)
	– Bi9#2	288.2(2)
	– Bi10#2	284.6(2)
	– Bi23	287.3(2)
	– Bi24	284.6(2)
Bismuth–Bismuth		
Bi1	– Bi2	331.5(2)
	– Bi4	319.4(2)
	– Bi5	342.3(2)
	– Bi20#1	341.4(2)
	– Bi23	319.5(2)
Bi2	– Bi3	317.6(2)
	– Bi6	342.0(2)
	– Bi19#1	341.0(2)
	– Bi24	316.9(2)
Bi3	– Bi4	336.0(2)
	– Bi7	341.4(2)
	– Bi10#2	340.0(2)
	– Bi24	316.8(2)
Bi4	– Bi8	341.0(2)
	– Bi9#2	339.7(2)
	– Bi23	314.9(2)
Bi5	– Bi6	335.9(2)
	– Bi8	319.5(2)
	– Bi9	314.7(2)
	– Bi23#3	338.2(2)
Bi6	– Bi7	316.1(2)
	– Bi10	319.1(2)
	– Bi24#3	338.9(2)
Bi7	– Bi8	333.6(2)
	– Bi10	317.0(2)
	– Bi14	342.1(2)
Bi8	– Bi9	319.3(2)
	– Bi13	341.3(2)
Bi9	– Bi10	335.0(2)
	– Bi12	341.7(2)
Bi10	– Bi11	341.5(2)
Bi11	– Bi12	332.9(2)
	– Bi14	315.9(2)
	– Bi15	316.4(2)
	– Bi18#3	341.6(2)
Bi12	– Bi13	319.9(2)
	– Bi16	319.5(2)
	– Bi17#3	341.1(2)
Bi13	– Bi14	335.2(2)
	– Bi16	315.1(2)
	– Bi17	339.8(2)
Bi14	– Bi15	318.4(2)
	– Bi18	341.6(2)
Bi15	– Bi16	335.1(2)
	– Bi19	339.7(2)
	– Bi22#3	342.8(2)
Bi16	– Bi20	338.9(2)
	– Bi21#3	342.3(2)
Bi17	– Bi18	336.0(2)
	– Bi20	314.8(2)
	– Bi21	319.8(2)
Bi18	– Bi19	317.8(2)
	– Bi22	317.0(2)
Bi19	– Bi20	336.3(2)
	– Bi22	316.6(2)
Bi20	– Bi21	319.5(2)
Bi21	– Bi22	332.7(2)
	– Bi23#4	341.4(2)
Bi22	– Bi24#4	342.1(2)
Bi23	– Bi24	337.3(2)
Bismuth–Iodine		
Bi25	– I7	332.9(2)
	– I7#5	307.1(3)
	– I8	292.6(3)
	– I9	293.0(3)
	– I10	330.5(3)
	– I11	313.4(3)
Bi26	– I10	311.5(3)
	– I11	337.7(3)
	– I12	291.8(3)
	– I13	288.7(3)
	– I14	335.2(3)
	– I14#6	310.7(3)

Symmetry transformations used to generate equivalent atoms:
#1 $x, y-1, z$ #2 $x+1, y, z$ #3 $x-1, y, z$ #4 $x, y+1, z$ #5 $x+1, y, z+1$ #6 $x+1, y+1, z+1$

A.2.4. $Bi_{13}Pd_3I_7$

Table A.23.: Crystal data and structure refinement for $Bi_{13}Pd_3I_7$ at 296 and 120 K. The low quality of the data at 296 K necessitated the refinement in a smaller unit cell, although the respective superstructure reflections are still visible.

Formula	$Bi_{13}Pd_3I_7$	
Formula weight	$3924.24\,g\,mol^{-1}$	
Temperature	$T = 296\,K$	$T = 120\,K$
Crystal system	triclinic	
Space group	$P\bar{1}$ (no. 2)	
Cell parameters	$a = 914.68(6)$ pm, $b = 914.54(5)$ pm, $c = 2187.81(16)$ pm, $\alpha = 78.067(5)°$, $\beta = 78.141(5)°$, $\gamma = 60.080(5)°$.	$a = 910.73(8)$ pm, $b = 1577.50(13)$ pm, $c = 2182.61(18)$ pm, $\alpha = 76.035(5)°$, $\beta = 89.909(5)°$, $\gamma = 90.105(5)°$.
Volume	$V = 1540.6(2) \times 10^6\,pm^3$	$V = 3043.0(4) \times 10^6\,pm^3$
Formula units per cell	$Z = 2$	$Z = 4$
Density (calculated)	$8.460\,g\,cm^{-3}$	$8.566\,g\,cm^{-3}$
Measurement device	Four-circle diffractometer Kappa APEX II (Bruker) with CCD detector, graphite-monochromated Mo-K_α radiation ($\lambda = 71.073$ pm)	
Absorption coefficient	$82.643\,mm^{-1}$	$83.679\,mm^{-1}$
Crystal size	$0.005 \times 0.047 \times 0.052\,mm^3$	
Range of data collection	$2\theta_{max} = 55°$ $-11 \leq h \leq 11$ $-11 \leq k \leq 11$ $-28 \leq l \leq 28$	$2\theta_{max} = 52°$ $-11 \leq h \leq 11$ $-18 \leq k \leq 19$ $-26 \leq l \leq 26$
Number of measured / independent reflections	28686 / 6999	39818 / 12174
Absorption correction	numerical [110, 111]	
Max. and min. transmission	0.738 and 0.106	0.734 and 0.121
Data merging	$R_{int} = 0.0774$ $R_\sigma = 0.0893$	$R_{int} = 0.0884$ $R_\sigma = 0.1044$
Refinement method	Full matrix least squares on F^2 [114, 202]; anisotropic displacement parameters	
Data / restraints / parameters	6999 / 0 / 228	12174 / 0 / 423
Figures of merit	$R_1(\text{all}F_o) = 0.0828$ $R_1(F_o > 4\sigma(F_o)) = 0.0358$ $wR_2(\text{all}F_o) = 0.0619$ $GooF = 0.846$	$R_1(\text{all}F_o) = 0.1219$ $R_1(Fo > 4\sigma(Fo)) = 0.0333$ $wR_2(\text{all}F_o) = 0.0770$ $GooF = 0.82$
Residual electron density	2.75 to $-2.17e \times 10^{-6}\,pm^{-3}$	3.96 to $-3.97e \times 10^{-6}\,pm^{-3}$

Table A.24.: Atomic coordinates and equivalent isotropic displacement parameters ($/pm^2$) of $Bi_{13}Pd_3I_7$ at 296 K. U_{eq} is defined as one third of the trace of the orthogonalized U_{ij} tensor.

Atom	Wyckoff position	x	y	z	occupancy	U_{eq}
Bi1	$2i$	0.12621(8)	0.77440(9)	0.21965(4)	1	169(2)
Bi2	$2i$	0.07216(9)	0.72498(9)	0.37557(4)	1	188(2)
Bi3	$2i$	0.07754(8)	0.07704(9)	0.37174(4)	1	177(2)
Bi4	$2i$	0.12532(8)	0.12484(8)	0.21747(4)	1	167(2)
Bi5	$2i$	0.56037(8)	0.55954(8)	0.21773(4)	1	167(2)
Bi6	$2i$	0.50730(8)	0.50685(9)	0.37210(4)	1	177(2)
Bi7	$2i$	0.50988(8)	0.85679(9)	0.37526(4)	1	189(2)
Bi8	$2i$	0.55950(8)	0.90896(9)	0.21919(4)	1	169(2)
Bi9	$2i$	0.85710(9)	0.50940(9)	0.37531(4)	1	189(2)
Bi10	$2i$	0.90933(8)	0.55900(8)	0.21893(4)	1	172(2)
Bi11	$2i$	0.77536(9)	0.12533(8)	0.21955(4)	1	169(2)
Bi12	$2i$	0.72516(9)	0.07190(9)	0.37553(4)	1	186(2)
Bi13	$2i$	0.2756(2)	0.2591(2)	0.00404(8)	0.496(2)	283(5)
Bi14	$2i$	0.2407(2)	0.7441(2)	0.00025(9)	0.504(2)	361(5)
Pd1	$2i$	0.31788(17)	0.81726(17)	0.29537(7)	1	114(3)
Pd2	$2i$	0.81769(17)	0.31714(17)	0.29530(7)	1	115(3)
Pd3	$2i$	0.81737(17)	0.81678(17)	0.29573(7)	1	114(3)
I1	$2i$	0.31877(16)	0.31811(16)	0.29157(7)	1	229(3)
I2	$2i$	0.2538(2)	0.2538(2)	0.48893(8)	1	417(4)
I3	$2i$	0.24940(17)	0.75033(17)	0.50005(6)	1	235(3)
I4A	$2i$	0.3737(15)	0.3664(13)	0.0971(5)	0.496(2)	409(16)
I4B	$2i$	0.3923(14)	0.4037(12)	0.0884(5)	0.504(2)	369(16)
I5	$2i$	0.39525(18)	0.88167(18)	0.07631(7)	1	353(4)
I6	$2i$	0.89098(18)	0.89177(18)	0.07815(7)	1	345(4)
I7	$2i$	0.88322(18)	0.39347(18)	0.07630(7)	1	331(4)

Table A.25.: Anisotropic displacement parameters (/pm^2) of $Bi_{13}Pd_3I_7$ at 296 K. The exponent of the anisotropic displacement factor takes the form: $-2\pi^2[h^2a^{*2}U_{11} + ... + 2hka^*b^*U_{12}]$.

Atom	U_{11}	U_{22}	U_{33}	U_{23}	U_{13}	U_{12}
Bi1	134(3)	210(4)	189(4)	−81(3)	14(3)	−93(3)
Bi2	178(4)	205(4)	205(5)	34(4)	−66(3)	−114(3)
Bi3	158(4)	161(4)	190(5)	−48(3)	−50(3)	−41(3)
Bi4	130(3)	135(4)	184(4)	9(3)	4(3)	−44(3)
Bi5	143(4)	160(4)	176(4)	−50(3)	−40(3)	−39(3)
Bi6	150(4)	153(4)	178(5)	1(3)	6(3)	−53(3)
Bi7	150(4)	236(4)	209(5)	−93(4)	25(3)	−106(3)
Bi8	151(4)	182(4)	185(5)	25(3)	−41(3)	−97(3)
Bi9	230(4)	164(4)	209(5)	21(3)	−83(3)	−116(3)
Bi10	179(4)	158(4)	196(5)	−52(3)	28(3)	−100(3)
Bi11	203(4)	133(4)	195(5)	2(3)	−78(3)	−86(3)
Bi12	202(4)	182(4)	201(5)	−77(3)	46(3)	−118(3)
Bi13	352(9)	346(10)	193(10)	−32(7)	−22(7)	−202(8)
Bi14	372(10)	360(10)	202(10)	−42(8)	−22(8)	−66(8)
Pd1	102(6)	116(6)	113(7)	−9(5)	−21(5)	−42(5)
Pd2	118(6)	109(6)	113(7)	−17(5)	−8(5)	−51(5)
Pd3	115(6)	112(6)	123(7)	−8(5)	−18(5)	−60(5)
I1	169(5)	178(6)	345(8)	−53(6)	−26(5)	−81(5)
I2	502(9)	505(10)	208(9)	−30(8)	−6(8)	−231(8)
I3	315(7)	315(7)	90(7)	−19(6)	−9(5)	−169(6)
I4A	590(30)	510(40)	240(40)	−50(30)	−70(30)	−330(30)
I4B	410(30)	360(30)	260(30)	80(20)	30(20)	−200(20)
I5	385(8)	430(9)	185(8)	−4(7)	−22(7)	−167(7)
I6	431(9)	424(9)	194(9)	−33(7)	−27(7)	−219(7)
I7	408(8)	372(8)	187(8)	−30(7)	6(7)	−183(7)

Table A.26.: Atomic Distances /*pm* for $Bi_{13}Pd_9I_7$ at 296 K.

Palladium–Bismuth		
Pd1	– Bi1	284.9(2)
	– Bi2	291.6(2)
	– Bi3	286.2(2)
	– Bi4	286.9(2)
	– Bi5	287.3(2)
	– Bi6	286.3(2)
	– Bi7	290.3(2)
	– Bi8	285.0(2)
Pd2	– Bi5	286.6(2)
	– Bi6	286.8(2)
	– Bi9	290.7(2)
	– Bi10	285.2(2)
	– Bi11	284.9(2)
	– Bi12	291.2(2)
	– Bi3#	285.9(2)
	– Bi4#	287.1(2)
Pd3	– Bi1#	285.4(2)
	– Bi2#	288.1(2)
	– Bi7	288.0(2)
	– Bi8	285.2(2)
	– Bi9	287.8(2)
	– Bi10	285.8(2)
	– Bi11#	285.0(2)
	– Bi12#	288.4(2)

Bismuth–Bismuth		
Bi1	– Bi2	331.3(1)
	– Bi4	319.1(1)
	– Bi5	343.7(1)
	– Bi10#1	342.6(1)
	– Bi11#2	321.3(1)
Bi2	– Bi3	322.8(1)
	– Bi6	344.2(1)
	– Bi9#1	341.1(1)
	– Bi12#2	317.7(1)
Bi3	– Bi4	327.8(1)
	– Bi7	343.8(1)
	– Bi9#2	343.8(1)
	– Bi12#2	323.1(1)
Bi4	– Bi8	344.7(1)
	– Bi10#2	344.5(1)
	– Bi11#2	319.0(1)
Bi5	– Bi6	328.0(1)
	– Bi8	319.8(1)
	– Bi10	319.5(1)
	– Bi11	343.7(1)
Bi6	– Bi7	322.7(1)
	– Bi9	322.6(1)
	– Bi12	344.0(1)
Bi7	– Bi8	331.6(1)
	– Bi9	318.0(1)
	– Bi12#3	340.9(1)
Bi8	– Bi10	320.4(1)
	– Bi11#3	342.4(1)
Bi9	– Bi10	332.3(1)
Bi11	– Bi12	331.4(1)

Bismuth–Iodine		
Bi13	– I4B	308.6(15)
	– I5#6	320.9(2)
	– I5#7	295.1(2)
	– I6#7	342.1(2)
	– I7#1	331.1(2)
	– I7#7	307.1(2)
Bi14	– I4A	342.7(9)
	– I4B#7	327.7(10)
	– I5	315.5(3)
	– I6#1	306.0(2)
	– I6#8	315.7(2)
	– I7#7	295.8(3)

Symmetry transformations used to generate equivalent atoms:
#1 $x-1, y, z$ #2 $x-1, y+1, z$ #3 $x, y+1, z$ #4 $x+1, y, z$ #5 $x+1, y-1, z$ #6 $x, y-1, z$ #7 $-x+1, -y+1, -z$ #8 $-x+1, -y+2, -z$

Table A.27.: Atomic coordinates and equivalent isotropic displacement parameters ($/pm^2$) of $\mathrm{Bi_{13}Pd_3I_7}$ at 120 K. U_{eq} is defined as one third of the trace of the orthogonalized U_{ij} tensor.

Atom	Wyckoff position	x	y	z	occupancy	U_{eq}
Bi1	$2i$	0.12852(15)	0.18580(9)	0.21872(8)	1	67(5)
Bi2	$2i$	0.30281(15)	0.36159(9)	0.21785(8)	1	65(5)
Bi3	$2i$	0.80226(15)	0.02591(9)	0.37569(8)	1	77(6)
Bi4	$2i$	0.30477(15)	0.31054(9)	0.37251(8)	1	74(5)
Bi5	$2i$	0.62920(15)	0.19983(9)	0.37569(8)	1	72(5)
Bi6	$2i$	0.95158(15)	0.30739(9)	0.37548(8)	1	78(6)
Bi7	$2i$	0.94671(15)	0.52497(9)	0.37225(8)	1	70(5)
Bi8	$2i$	0.95342(15)	0.36077(9)	0.21831(8)	1	67(5)
Bi9	$2i$	0.12477(15)	0.75295(9)	0.21937(8)	1	66(5)
Bi10	$2i$	0.12569(15)	0.13373(9)	0.37559(8)	1	71(5)
Bi11	$2i$	0.30065(15)	0.57819(9)	0.21883(8)	1	66(5)
Bi12	$2i$	0.45477(15)	0.07993(9)	0.21646(8)	1	65(5)
Bi13	$2i$	0.44965(15)	0.86196(9)	0.21871(8)	1	65(5)
Bi14	$2i$	0.44904(15)	0.02577(9)	0.37182(8)	1	66(5)
Bi15	$2i$	0.95218(15)	0.57827(9)	0.21773(8)	1	67(5)
Bi16	$2i$	0.62257(15)	0.63390(10)	0.37534(8)	1	79(6)
Bi17	$2i$	0.12601(15)	0.69979(9)	0.37557(8)	1	74(5)
Bi18	$2i$	0.79925(15)	0.86155(9)	0.21687(8)	1	71(5)
Bi19	$2i$	0.62873(15)	0.25343(9)	0.21892(8)	1	69(5)
Bi20	$2i$	0.80413(15)	0.07710(9)	0.21951(8)	1	67(5)
Bi21	$2i$	0.30027(15)	0.52656(9)	0.37538(8)	1	78(6)
Bi22	$2i$	0.44887(15)	0.80804(9)	0.37537(8)	1	75(6)
Bi23	$2i$	0.62441(15)	0.68632(9)	0.21854(8)	1	67(5)
Bi24	$2i$	0.80190(15)	0.81050(9)	0.37203(8)	1	68(5)
Bi25	$2i$	0.84256(16)	0.62005(10)	0.00380(9)	0.906(2)	99(5)
Bi26	$2i$	0.14061(17)	0.87936(10)	0.00007(8)	0.912(2)	150(5)
Bi27	$2i$	0.4044(15)	0.6353(9)	0.0000(8)	0.094(2)	99(5)
Bi28	$2i$	0.638(2)	0.9005(11)	−0.0047(10)	0.088(2)	150(5)
Pd1	$2i$	0.6259(3)	0.9440(2)	0.2949(2)	1	43(13)
Pd2	$2i$	0.3781(3)	0.1943(2)	0.2950(2)	1	35(13)
Pd3	$2i$	0.3748(3)	0.6941(2)	0.2957(2)	1	44(13)
Pd4	$2i$	0.8779(3)	0.1937(2)	0.2955(2)	1	46(13)
Pd5	$2i$	0.8739(3)	0.6932(2)	0.2954(2)	1	41(13)
Pd6	$2i$	0.1264(4)	0.4437(2)	0.2951(2)	1	42(13)
I1	$2i$	0.6265(3)	0.4447(2)	0.29240(18)	1	85(11)
I2	$2i$	0.1261(3)	0.9453(2)	0.29116(18)	1	87(11)
I3	$2i$	0.3775(3)	0.1245(2)	0.50017(17)	1	86(11)
I4	$2i$	0.6256(3)	0.3786(2)	0.48969(19)	1	165(12)
I5	$2i$	0.8768(3)	0.1221(2)	0.51084(19)	1	166(12)
I6	$2i$	0.1270(3)	0.3756(2)	0.50000(17)	1	88(11)
I7	$2i$	0.6417(3)	0.5182(2)	0.09601(17)	1	213(10)
I8	$2i$	0.3839(3)	0.2752(2)	0.07503(18)	1	162(11)
I9	$2i$	0.3684(3)	0.7689(2)	0.07784(18)	1	148(11)
I10	$2i$	0.6266(3)	0.0147(2)	0.07657(17)	1	131(10)
I11	$2i$	0.1370(3)	0.5158(2)	0.07588(17)	1	132(11)
I12	$2i$	0.8795(3)	0.2617(2)	0.07835(18)	1	118(11)
I13	$2i$	0.8690(3)	0.7679(2)	0.07705(18)	1	119(10)
I14	$2i$	0.1148(3)	0.0038(2)	0.09022(16)	1	170(10)

Table A.28.: Anisotropic displacement parameters (/pm^2) of $Bi_{13}Pd_3I_7$ at 120 K. The exponent of the anisotropic displacement factor takes the form: $-2\pi^2[h^2a^{*2}U_{11} + ... + 2hka^*b^*U_{12}]$.

Atom	U_{11}	U_{22}	U_{33}	U_{23}	U_{13}	U_{12}
Bi1	44(7)	88(8)	76(11)	−33(8)	1(6)	−13(6)
Bi2	66(7)	70(8)	52(10)	−4(7)	12(6)	−12(6)
Bi3	67(7)	65(8)	89(11)	−1(8)	−25(7)	−19(6)
Bi4	67(7)	89(8)	73(11)	−34(8)	−17(7)	6(6)
Bi5	51(7)	109(8)	69(11)	−45(8)	−1(6)	−16(6)
Bi6	62(7)	84(8)	98(11)	−46(8)	15(7)	−26(6)
Bi7	70(7)	67(8)	66(11)	−2(7)	13(7)	−5(6)
Bi8	54(7)	67(8)	75(11)	−9(7)	−20(6)	−9(6)
Bi9	49(7)	80(8)	61(10)	−2(7)	6(6)	−16(6)
Bi10	51(7)	74(8)	77(11)	3(8)	−20(6)	−1(6)
Bi11	70(7)	67(8)	64(10)	−23(7)	15(6)	−23(6)
Bi12	60(7)	70(8)	72(11)	−32(7)	−13(7)	11(6)
Bi13	61(7)	69(8)	64(10)	−12(7)	−15(6)	−18(6)
Bi14	66(7)	62(8)	66(11)	−9(7)	18(7)	2(6)
Bi15	67(7)	71(8)	70(11)	−31(7)	−33(7)	6(6)
Bi16	45(7)	91(8)	90(11)	3(8)	−2(7)	−19(6)
Bi17	54(7)	100(8)	83(11)	−53(8)	3(6)	−8(6)
Bi18	58(7)	71(8)	79(11)	−11(7)	15(6)	8(6)
Bi19	38(7)	74(8)	87(11)	−6(8)	−10(6)	−1(6)
Bi20	59(7)	69(8)	84(11)	−41(8)	24(7)	−22(6)
Bi21	77(7)	68(8)	85(11)	−7(8)	−22(7)	−18(6)
Bi22	69(7)	96(8)	68(11)	−39(8)	11(7)	−29(6)
Bi23	43(7)	93(8)	73(11)	−38(8)	−6(6)	−9(6)
Bi24	74(7)	74(8)	59(10)	−20(7)	−22(7)	8(6)
Bi25	96(7)	115(8)	78(9)	−12(7)	−8(6)	−12(6)
Bi26	219(8)	146(8)	83(9)	−24(7)	4(7)	40(6)
Bi27	96(7)	115(8)	78(9)	−12(7)	−8(6)	−12(6)
Bi28	219(8)	146(8)	83(9)	−24(7)	4(7)	40(6)
Pd1	38(15)	38(19)	50(30)	−8(18)	−6(14)	−5(13)
Pd2	34(15)	50(20)	20(20)	−10(18)	−4(15)	0(13)
Pd3	37(15)	50(20)	40(30)	−11(19)	6(15)	−21(14)
Pd4	16(15)	60(20)	60(30)	−21(19)	−11(15)	−5(14)
Pd5	24(15)	43(19)	40(20)	15(18)	−2(15)	5(13)
Pd6	58(15)	40(20)	30(20)	−11(18)	0(14)	1(13)
I1	47(13)	103(18)	110(20)	−38(17)	−8(12)	−15(11)
I2	68(13)	62(17)	140(20)	−34(16)	−9(13)	−2(11)
I3	122(14)	106(17)	20(20)	−2(15)	−1(13)	−14(12)
I4	175(16)	225(19)	90(20)	−33(17)	−7(14)	−10(14)
I5	230(17)	181(18)	80(20)	−18(17)	−2(14)	−5(14)
I6	99(13)	127(17)	40(20)	−18(15)	−3(12)	−19(12)
I7	264(15)	201(15)	160(20)	−15(13)	74(13)	−21(12)
I8	171(14)	217(18)	90(20)	−27(15)	−34(13)	69(12)
I9	163(14)	194(17)	70(20)	0(15)	−11(13)	35(12)
I10	171(14)	162(16)	49(19)	−1(14)	4(12)	−52(12)
I11	150(14)	150(16)	110(20)	−51(14)	−26(13)	49(12)
I12	137(14)	149(16)	70(20)	−40(15)	18(13)	−19(11)
I13	133(13)	135(15)	90(20)	−23(14)	35(12)	−49(11)
I14	250(14)	189(15)	77(16)	−46(13)	−19(12)	37(11)

Table A.29.: Atomic Distances /*pm* for $Bi_{13}Pd_9I_7$ at 120 K.

Palladium–Bismuth		
Pd1	– Bi18	285.7(5)
	– Bi24	285.4(4)
	– Bi13#1	284.0(5)
	– Bi22#1	290.6(4)
	– Bi3#3	290.8(5)
	– Bi20#3	283.9(4)
	– Bi12#4	286.4(4)
	– Bi14#4	285.0(5)
Pd2	– Bi1	284.2(4)
	– Bi2	285.1(4)
	– Bi4	285.9(5)
	– Bi10	290.9(4)
	– Bi12	286.0(5)
	– Bi14	285.5(4)
	– Bi5#2	290.2(4)
	– Bi19#2	284.1(4)
Pd3	– Bi9	284.5(4)
	– Bi11	284.6(5)
	– Bi13	285.3(4)
	– Bi17	287.1(4)
	– Bi21	286.9(4)
	– Bi22	286.7(5)
	– Bi16#2	287.0(4)
	– Bi23#2	284.9(4)
Pd4	– Bi1	285.0(4)
	– Bi3	288.0(4)
	– Bi5	287.7(4)
	– Bi6	286.9(5)
	– Bi8	284.5(4)
	– Bi10	287.5(4)
	– Bi19	284.4(4)
	– Bi20	283.8(5)
Pd5	– Bi7	285.5(4)
	– Bi9	284.4(4)
	– Bi15	285.7(5)
	– Bi16	288.9(4)
	– Bi17	290.6(4)
	– Bi18	287.4(4)
	– Bi23	284.4(4)
	– Bi24	285.5(5)
Pd6	– Bi2	285.6(5)
	– Bi4	286.5(4)
	– Bi6	289.7(4)
	– Bi7	286.4(5)
	– Bi8	284.0(5)
	– Bi11	284.0(4)
	– Bi15	285.7(4)
	– Bi21	289.8(5)

Bismuth–Bismuth		
Bi1	– Bi2	318.9(2)
	– Bi10	332.3(2)
	– Bi12	341.7(2)
	– Bi20	341.1(2)
	– Bi8	318.8(2)
Bi2	– Bi4	327.6(2)
	– Bi8	318.2(2)
	– Bi11	342.2(2)
	– Bi19#1	342.4(2)
Bi3	– Bi5	316.7(2)
	– Bi10	339.9(2)
	– Bi14#2	321.9(2)
	– Bi20	330.8(2)
	– Bi24#3	341.8(2)
Bi4	– Bi5#1	342.8(2)
	– Bi6	321.8(2)
	– Bi10	321.5(2)
	– Bi21	342.4(2)
Bi5	– Bi6	338.8(2)
	– Bi14#2	321.5(2)
	– Bi19	332.0(2)
Bi6	– Bi7	341.6(2)
	– Bi8	332.9(2)
	– Bi10	316.7(2)
Bi7	– Bi15	327.3(2)
	– Bi16	342.8(2)
	– Bi17	321.8(2)
	– Bi21	322.1(2)
Bi8	– Bi15	342.8(2)
	– Bi19	340.4(2)
Bi9	– Bi11	319.3(2)
	– Bi13	341.8(2)
	– Bi15	317.8(2)
	– Bi17	330.8(2)
	– Bi18	342.1(2)
Bi10	– Bi14	341.6(2)
Bi11	– Bi15	317.4(2)
	– Bi21	331.6(2)
	– Bi23#1	340.3(2)
Bi12	– Bi13#3	342.7(2)
	– Bi14	329.1(2)
	– Bi19#1	317.2(2)
	– Bi20#1	318.3(2)
Bi13	– Bi18#1	318.5(2)
	– Bi22	331.8(2)
	– Bi23#1	319.9(2)
Bi14	– Bi22#3	341.7(2)
Bi15	– Bi23	344.3(2)
Bi16	– Bi21#2	338.6(2)
	– Bi22#2	317.3(2)
	– Bi23	332.1(2)
	– Bi24	321.3(2)
Bi17	– Bi21	316.4(2)
	– Bi22	339.7(2)
	– Bi24	342.4(2)
Bi18	– Bi20#5	341.5(2)
	– Bi23	318.0(2)
	– Bi24	328.6(2)
Bi19	– Bi20	320.8(2)
Bi22	– Bi24#1	321.6(2)

Bismuth–Iodine		
Bi25	– I7	289.7(3)
	– I8#6	293.1(3)
	– I11	333.9(3)
	– I11#6	307.5(4)
	– I12#6	338.5(3)
	– I13	313.9(4)
Bi26	– I9#6	296.9(4)
	– I10	295.1(3)
	– I12	312.3(4)
	– I13#6	325.3(3)
	– I14	331.1(3)
	– I14#7	310.6(4)
Bi27	– I7#8	326.0(14)
	– I8#2	269.4(14)
	– I9#6	302.8(18)
	– I11#6	327.0(14)
	– I12	330.8(14)
Bi28	– I10#5	282.0(22)
	– I10#8	300.9(18)
	– I13	319.7(18)
	– I14#6	307.5(18)

Symmetry transformations used to generate equivalent atoms:
#1 $x+1, y, z$ #2 $x-1, y, z$ #3 $x, y-1, z$ #4 $x+1, y-1, z$ #5 $x, y+1, z$ #6 $-x+1, -y+1, -z$
#7 $-x, -y+1, -z$ #8 $-x, -y+1, -z$

A.2.5. $Bi_8Pt_5I_3$

Table A.30.: Crystal data and structure refinement for $Bi_8Pt_5I_3$ at 298 and 150 K.

Formula	$Bi_8Pt_5I_3$	
Formula weight	$3027.9\,g\,mol^{-1}$	
Temperature	298(2) K	150(2) K
Crystal system	monoclinic	
Space group	$C2/m$ (no. 12)	
Cell parameters	$a = 1850.7(2)\,pm$, $b = 391.46(3)\,pm$, $c = 1340.5(1)\,pm$, $\beta = 113.28(1)°$	$a = 1843.4(1)\,pm$, $b = 390.96(2)\,pm$, $c = 1337.5(1)\,pm$, $\beta = 113.19(1)°$
Volume	$V = 892.1(2) \times 10^6\,pm^3$	$V = 886.1(1) \times 10^6\,nm^3$
Formula units per cell	$Z = 2$	
Density (calculated)	$\rho = 11.27\,mg\,cm^{-3}$	$\rho = 11.35\,mg\,cm^{-3}$
Measurement device	Four-circle diffractometer Kappa APEX II (Bruker) with CCD detector, graphite-monochromated Mo-K_α radiation ($\lambda = 71.073\,pm$)	
Absorption coefficient	$122.8\,mm^{-1}$	$123.6\,mm^{-1}$
Crystal size	$0.01 \times 0.02 \times 0.05\,mm^3$	
Range of data collection	$2\theta_{max} = 55°$ $-24 \leq h \leq 24$ $-5 \leq k \leq 5$ $-17 \leq l \leq 17$	$2\theta_{max} = 55°$ $-23 \leq h \leq 23$ $-5 \leq k \leq 5$ $-17 \leq l \leq 17$
Number of measured / independent reflections	5573 / 1170	5388 / 1152
Absorption correction	numerical [110, 111]	
Max. and min. transmission	0.4509 and 0.0557	0.4410 and 0.0527
Data merging	$R_{int} = 0.072$ $R_\sigma = 0.064$	$R_{int} = 0.067$ $R_\sigma = 0.058$
Refinement method	Full matrix least squares on F^2 [114, 202]; anisotropic displacement parameters	
Data / restraints / parameters	1170/0/51	
Figures of merit	$R_1(\text{all}F_o) = 0.050$ $R_1(F_o > 4\sigma(F_o)) = 0.029$ $wR_2(\text{all}F_o) = 0.039$ $GooF = 0.883$	$R_1(\text{all}F_o) = 0.042$ $R_1(Fo > 4\sigma(Fo)) = 0.025$ $wR_2(\text{all}F_o) = 0.034$ $GooF = 0.863$
Residual electron density	2.5 to $-3.0e \times 10^{-6}\,pm^{-3}$	2.5 to $-2.6e \times 10^{-6}\,pm^{-3}$

Table A.31.: Atomic coordinates and equivalent isotropic displacement parameters (/pm^2) for $Bi_8Pt_5I_3$ at 298 K. U_{eq} is defined as one third of the trace of the orthogonalised U_{ij} tensor.

Atom	Wyckoff position	x	y	z	U_{eq}
Pt1	$2d$	$1/2$	0	$1/2$	210(3)
Pt2	$4i$	0.44699(5)	$1/2$	0.34250(5)	143(2)
Pt3	$4i$	0.34682(5)	$1/2$	0.12677(6)	190(2)
Bi1	$4i$	0.39546(5)	$1/2$	0.52106(6)	182(2)
Bi2	$4i$	0.32346(5)	0	0.27044(6)	183(2)
Bi3	$4i$	0.48406(5)	0	0.21857(6)	177(2)
Bi4	$4i$	0.18270(5)	$1/2$	0.03018(5)	179(2)
I1	$2a$	0	0	0	473(7)
I2	$4i$	0.18443(9)	$1/2$	0.3265(1)	313(4)

Table A.32.: Anisotropic displacement parameters (/pm^2) for $Bi_8Pt_5I_3$ at 298 K. The exponent of the anisotropic displacement factor takes the form: $-2\pi^2[h^2a^{*2}U_{11} + ... + 2hka^*b^*U_{12}]$.

Atom	U_{11}	U_{22}	U_{33}	U_{23}	U_{13}	U_{12}
Pt1	368(8)	118(5)	92(5)	0	36(5)	0
Pt2	169(5)	141(3)	69(3)	0	−4(3)	0
Pt3	193(5)	212(4)	91(3)	0	−23(3)	0
Bi1	149(4)	251(4)	122(3)	0	26(3)	0
Bi2	172(5)	154(4)	207(4)	0	58(3)	0
Bi3	207(5)	171(4)	157(3)	0	76(3)	0
Bi4	189(5)	194(4)	117(3)	0	20(3)	0
I1	730(20)	270(10)	630(20)	0	490(20)	0
I2	290(10)	228(7)	481(9)	0	219(8)	0

Table A.33.: Atomic coordinates and equivalent isotropic displacement parameters (/pm^2) for $Bi_8Pt_5I_3$ at 150 K. U_{eq} is defined as one third of the trace of the orthogonalised U_{ij} tensor.

Atom	Wyckoff position	x	y	z	U_{eq}
Pt1	$2d$	$1/2$	0	$1/2$	126(2)
Pt2	$4i$	0.44674(4)	$1/2$	0.34230(5)	88(2)
Pt3	$4i$	0.34690(4)	$1/2$	0.12647(5)	112(2)
Bi1	$4i$	0.39533(4)	$1/2$	0.52103(5)	110(2)
Bi2	$4i$	0.32319(4)	0	0.27000(5)	109(2)
Bi3	$4i$	0.48403(4)	0	0.21825(5)	108(2)
Bi4	$4i$	0.18256(4)	$1/2$	0.03030(5)	107(2)
I1	$2a$	0	0	0	263(5)
I2	$4i$	0.18463(8)	$1/2$	0.3270(1)	177(3)

Table A.34.: Anisotropic displacement parameters (/pm^2) for $Bi_8Pt_5I_3$ at 150 K. The exponent of the anisotropic displacement factor takes the form: $-2\pi^2[h^2a^{*2}U_{11} + ... + 2hka^*b^*U_{12}]$.

Atom	U_{11}	U_{22}	U_{33}	U_{23}	U_{13}	U_{12}
Pt1	213(6)	77(4)	47(4)	0	8(4)	0
Pt2	105(4)	94(3)	31(3)	0	−10(3)	0
Pt3	122(4)	119(3)	46(3)	0	−17(3)	0
Bi1	100(4)	143(3)	59(3)	0	3(3)	0
Bi2	106(4)	94(3)	105(3)	0	18(3)	0
Bi3	127(4)	107(3)	75(3)	0	24(3)	0
Bi4	121(4)	112(3)	58(3)	0	2(3)	0
I1	400(10)	161(9)	350(10)	0	280(10)	0
I2	186(8)	138(6)	226(6)	0	104(6)	0

Table A.35.: Bader charges according to QTAIM[128] for $Bi_8Pt_5I_3$.

Bader charges					
Pt1	1.2	Bi1	0.8	I1	0.3
Pt2	1.0	Bi2	0.6	I2	0.4
Pt3	1.1	Bi3	0.7		
		Bi4	0.5		

A.2.6. $Bi_{16}Pt_{11}I_6$

Table A.36.: Crystal data and structure refinement for $Bi_{16}Pt_{11}I_6$ at 298 and 100 K.

Formula	$Bi_{16}Pt_{11}I_6$	
Formula weight	$6251.07\,\mathrm{g\,mol^{-1}}$	
Temperature	$T = 298(2)\,\mathrm{K}$	$T = 100(2)\,\mathrm{K}$
Crystal system	tetragonal	
Space group	$P42_12$ (no. 90)	
Cell parameters	$a = 1386.6(1)\,\mathrm{pm}$, $c = 924.5(1)\,\mathrm{pm}$.	$a = 1384.29(3)\,\mathrm{pm}$, $c = 921.55(2)\,\mathrm{pm}$.
Volume	$V = 1777.5(3) \times 10^6\,\mathrm{pm^3}$	$V = 1765.9(1) \times 10^6\,\mathrm{pm^3}$
Formula units per cell	$Z = 2$	
Density (calculated)	$\rho = 11.68\,\mathrm{mg\,cm^{-3}}$	$\rho = 11.756\,\mathrm{mg\,cm^{-3}}$
Measurement device	Four-circle diffractometer Kappa APEX II (Bruker) with CCD detector, graphite-monochromated Mo-K_α radiation ($\lambda = 71.073\,\mathrm{pm}$)	
Absorption coefficient	$127.1\,\mathrm{mm^{-1}}$	$127.976\,\mathrm{mm^{-1}}$
Crystal size	$0.02 \times 0.04 \times 0.05\,\mathrm{mm^3}$	
Absorption correction	numerical [110, 111]	
Max. and min. transmission	0.3528 and 0.0474	0.3785 and 0.0580
Range of data collection	$2\theta_{max} = 60°$	$2\theta_{max} = 60°$
	$-19 \leq h \leq 19$, $-19 \leq k \leq 19$, $-12 \leq l \leq 13$.	
Number of measured / independent reflections	40522 / 2569	57353 / 2597
Data merging	$R_{int} = 0.069$ $R_\sigma = 0.035$	$R_{int} = 0.0619$ $R_\sigma = 0.0243$
Refinement method	Full matrix least squares on F^2 [114, 202]; anisotropic displacement parameters	
Data / restraints / parameters	2569 / 0 / 80	2597 / 0 / 80
Flack parameter	$x = -0.04$	$x = -0.04$
Figures of merit	$R_1(\mathrm{all}F_o) = 0.022$ $R_1(F_o > 4\sigma(F_o)) = 0.018$ $wR_2(\mathrm{all}F_o) = 0.021$ $GooF = 0.803$	$R_1(\mathrm{all}F_o) = 0.0181$ $R_1(Fo > 4\sigma(Fo)) = 0.0165$ $wR_2(\mathrm{all}F_o) = 0.0289$ $GooF = 1.043$
Residual electron density	1.44 to $-1.20e \times 10^{-6}\,\mathrm{pm^{-3}}$	2.95 to $-2.10e \times 10^{-6}\,\mathrm{pm^{-3}}$

Table A.37.: Atomic coordinates and equivalent isotropic displacement parameters (/pm^2) for $Bi_{16}Pt_{11}I_6$ at 298 K. U_{eq} is defined as one third of the trace of the orthogonalised U_{ij} tensor.

Atom	Wyckoff position	x	y	z	U_{eq}
Bi1	$2c$	½	0	0.05386(9)	150(2)
Bi2	$2c$	½	0	0.6426(1)	187(2)
Bi3	$4d$	½	½	0.72213(6)	158(1)
Bi4	$8g$	0.32457(3)	0.32538(3)	0.67863(4)	131(1)
Bi5	$8g$	0.27495(3)	0.07036(3)	0.70314(6)	153(1)
Bi6	$8g$	0.29870(3)	0.06124(3)	0.31311(6)	127(1)
Pt1	$2c$	½	0	0.3543(1)	151(2)
Pt2	$4f$	0.19808(2)	0.19808(2)	½	135(1)
Pt3	$8g$	0.40540(2)	0.17664(2)	0.50461(8)	128(1)
Pt4	$8g$	0.50259(3)	0.35789(2)	0.50097(8)	141(1)
I1	$4e$	0.11789(5)	0.11789(5)	0	262(2)
I2	$8g$	0.69747(4)	0.10357(4)	0.0062(1)	190(2)

Table A.38.: Anisotropic displacement parameters (/pm^2) for $Bi_{16}Pt_{11}I_6$ at 298 K. The exponent of the anisotropic displacement factor takes the form: $-2\pi^2[h^2a^{*2}U_{11} + ... + 2hka^*b^*U_{12}]$.

Atom	U_{11}	U_{22}	U_{33}	U_{23}	U_{13}	U_{12}
Bi1	162(2)	162(2)	126(5)	0	0	0
Bi2	207(3)	207(3)	147(6)	0	0	0
Bi3	170(3)	166(3)	137(3)	−12(2)	0	0
Bi4	131(2)	137(2)	124(2)	1(1)	−2(2)	3(2)
Bi5	173(2)	141(2)	147(3)	−24(2)	−25(2)	10(2)
Bi6	139(2)	108(2)	134(3)	−11(2)	8(2)	−3(2)
Pt1	149(3)	149(3)	154(6)	0	0	0
Pt2	91(1)	91(1)	223(3)	2(2)	−4(3)	4(3)
Pt3	100(2)	112(2)	172(2)	−10(1)	4(3)	−4(3)
Pt4	108(2)	81(2)	233(2)	0(1)	−17(3)	2(3)
I1	267(3)	267(3)	252(6)	−17(4)	4(6)	−4(6)
I2	201(3)	210(3)	159(4)	−33(2)	14(5)	10(5)

Table A.39.: Atomic coordinates and equivalent isotropic displacement parameters (/pm^2) for $Bi_{16}Pt_{11}I_6$ at 100 K. U_{eq} is defined as one third of the trace of the orthogonalised U_{ij} tensor.

Atom	Wyckoff position	x	y	z	U_{eq}
Bi1	$2c$	½	0	0.05335(11)	56(2)
Bi2	$2c$	½	0	0.64350(12)	68(2)
Bi3	$4d$	½	½	0.72285(6)	57(1)
Bi4	$8g$	0.32476(3)	0.32550(3)	0.67828(5)	48(1)
Bi5	$8g$	0.27514(3)	0.07053(3)	0.70380(6)	58(1)
Bi6	$8g$	0.29876(3)	0.06141(3)	0.31253(6)	46(1)
Pt1	$2c$	½	0	0.35422(12)	58(2)
Pt2	$4f$	0.19823(3)	0.19823(3)	½	49(1)
Pt3	$8g$	0.40577(2)	0.17636(2)	0.50437(8)	46(1)
Pt4	$8g$	0.50283(3)	0.35796(2)	0.50110(8)	53(1)
I1	$4e$	0.11897(4)	0.11897(4)	0	91(2)
I2	$8g$	0.69780(4)	0.10330(4)	0.00646(12)	68(1)

Table A.40.: Anisotropic displacement parameters (/pm^2) for $Bi_{16}Pt_{11}I_6$ at 100 K. The exponent of the anisotropic displacement factor takes the form: $-2\pi^2[h^2a^{*2}U_{11} + ... + 2hka^*b^*U_{12}]$.

Atom	U_{11}	U_{22}	U_{33}	U_{23}	U_{13}	U_{12}
Bi1	57(2)	57(2)	53(5)	0	0	0
Bi2	70(2)	70(2)	62(6)	0	0	0
Bi3	60(3)	56(3)	54(3)	0	0	−1(2)
Bi4	48(2)	48(2)	49(2)	3(2)	−3(2)	1(1)
Bi5	64(2)	51(2)	58(3)	6(2)	−9(2)	−9(1)
Bi6	46(2)	39(2)	52(2)	−1(2)	3(2)	−3(1)
Pt1	56(2)	56(2)	62(6)	0	0	0
Pt2	34(1)	34(1)	80(3)	1(2)	−1(2)	1(2)
Pt3	39(2)	41(2)	60(2)	−2(2)	−1(2)	−2(1)
Pt4	43(2)	31(2)	84(2)	−2(2)	−7(3)	−2(1)
I1	92(2)	92(2)	90(5)	−2(4)	2(4)	−3(3)
I2	72(3)	70(3)	62(4)	1(4)	3(4)	−9(2)

Table A.41.: Bader charges according to QTAIM [128] for $Bi_{16}Pt_{11}I_6$.

Bader charges					
Pt1	−0.7	Bi1	0.4	I1	−0.5
Pt2	−0.7	Bi2	0.1	I2	−0.4
Pt3	−0.8	Bi3	0.4		
Pt4	−0.8	Bi4	0.5		
		Bi5	0.5		
		Bi6	0.5		

Table A.42.: Bonding basins from the topological analysis of the ELI-D field in $Bi_{16}Pt_{11}I_6$.

Contributing atoms	number of electrons	maximum within the basin
Pt 2 – Pt 4	0.06	0.93
Pt 4 – Pt 4	0.20	0.95
Pt 4 – Bi 5	0.10	0.96
Pt 3 – Bi 6	0.22	0.98
Pt 1 – Bi 1	0.76	1.02
Pt 1 – Bi 2	1.01	0.98

A.2.7. Bi_4RhI_2

Table A.43.: Crystal data and structure refinement for Bi_4RhI_2 at 296 K and 150 K.

Formula	Bi_4RhI_2	
Formula weight	$1192.63\,g\,mol^{-1}$	
Temperature	$T = 296(2)\,K$	$T = 150\,K$
Crystal system	monoclinic	
Space group	$P2_1/n$ (no. 14)	
Cell parameters	$a = 633.64(2)\,pm$, $b = 1801.56(5)\,pm$, $c = 1623.33(5)\,pm$, $\beta = 93.066(1)°$.	$a = 633.27(4)\,pm$, $b = 1792.93(11)\,pm$, $c = 1612.94(10)\,pm$, $\beta = 93.218(3)°$.
Volume	$V = 1850.4(1) \times 10^6\,pm^3$	$V = 1828.5(2) \times 10^6\,pm^3$
Formula units per cell	$Z = 8$	
Density (calculated)	$\rho = 8.562\,mg\,cm^{-3}$	$\rho = 8.665\,mg\,cm^{-3}$
Measurement device	Four-circle diffractometer Kappa APEX II (Bruker) with CCD detector, graphite-monochromated Mo-K_α radiation ($\lambda = 71.073\,pm$)	
Absorption coefficient	$84.153\,mm^{-1}$	$85.165\,mm^{-1}$
Crystal size	$0.13 \times 0.01 \times 0.01\,mm^3$	
Absorption correction	numerical [110, 111]	
Max. and min. transmission	0.3528 and 0.0474	0.2717 and 0.1109
Range of data collection	$2\theta_{max} = 55°$	$2\theta_{max} = 55°$
	$-8 \leq h \leq 8$, $-23 \leq k \leq 23$, $-21 \leq l \leq 21$.	
Number of measured / independent reflections	30149 / 4252	26525 / 4177
Data merging	$R_{int} = 0.0730$ $R_\sigma = 0.0617$	$R_{int} = 0.0884$ $R_\sigma = 0.0736$
Refinement method	Full matrix least squares on F^2 [114, 202]; anisotropic displacement parameters	
Data / restraints / parameters	4252 / 0 / 128	4177 / 0 / 128
Figures of merit	$R_1(\text{all}F_o) = 0.0566$ $R_1(F_o > 4\sigma(F_o)) = 0.0327$ $wR_2(\text{all}Fo) = 0.0550$ $GooF = 0.971$	$R_1(\text{all}F_o) = 0.0597$ $R_1(Fo > 4\sigma(Fo)) = 0.0303$ $wR_2(\text{all}F_o) = 0.0628$ $GooF = 0.98$
Residual electron density	1.95 to $-1.89e \times 10^{-6}\,pm^{-3}$	2.46 to $-2.60e \times 10^{-6}\,pm^{-3}$

Table A.44.: Atomic coordinates and equivalent isotropic displacement parameters (/pm^2) for Bi_4RhI_2 at 296 K. U_{eq} is defined as one third of the trace of the orthogonalised U_{ij} tensor.

Atom	Wyckoff position	x	y	z	U_{eq}
Bi1	4e	0.72015(9)	0.56560(3)	0.38858(4)	195(1)
Bi2	4e	0.20932(8)	0.64634(3)	0.31016(4)	201(1)
Bi3	4e	0.69566(9)	0.66565(3)	0.20283(4)	198(1)
Bi4	4e	0.18056(9)	0.58522(3)	0.11533(4)	227(1)
Bi5	4e	0.68789(9)	0.48762(3)	0.10651(4)	252(2)
Bi6	4e	0.18463(9)	0.42303(3)	0.16652(4)	245(2)
Bi7	4e	0.71033(9)	0.40414(3)	0.26523(4)	237(2)
Bi8	4e	0.21520(8)	0.46657(3)	0.35578(4)	205(1)
Rh1	4e	0.47419(17)	0.54031(7)	0.24616(7)	175(3)
Rh2	4e	0.92640(17)	0.54187(7)	0.24691(7)	176(3)
I1	4e	0.24106(17)	0.59971(6)	0.51426(7)	293(3)
I2	4e	0.70443(17)	0.73959(6)	0.38619(7)	310(3)
I3	4e	0.20761(19)	0.77591(6)	0.16319(8)	384(3)
I4	4e	0.67685(18)	0.66859(6)	0.01288(7)	340(3)

Table A.45.: Anisotropic displacement parameters (/pm^2) for Bi_4RhI_2 at 296 K. The exponent of the anisotropic displacement factor takes the form: $-2\pi^2[h^2a^{*2}U_{11} + ... + 2hka^*b^*U_{12}]$.

Atom	U_{11}	U_{22}	U_{33}	U_{23}	U_{13}	U_{12}
Bi1	179(3)	25.1(3)	156(3)	−11(3)	22(2)	3(2)
Bi2	153(3)	190(3)	262(3)	−35(3)	18(2)	−2(2)
Bi3	184(3)	195(3)	216(3)	19(3)	24(2)	0(2)
Bi4	196(3)	310(4)	178(3)	37(3)	31(2)	8(3)
Bi5	275(3)	312(4)	169(3)	−52(3)	11(3)	−6(3)
Bi6	217(3)	233(3)	288(4)	−57(3)	36(3)	10(3)
Bi7	270(3)	175(3)	267(4)	3(3)	31(3)	−8(3)
Bi8	189(3)	211(3)	218(3)	42(3)	39(2)	9(2)
Rh1	137(6)	215(7)	174(7)	−16(5)	9(5)	−2(5)
Rh2	148(6)	199(7)	182(7)	−24(5)	33(5)	−1(5)
I1	347(6)	298(6)	237(6)	−8(5)	35(5)	−28(5)
I2	347(6)	258(6)	323(7)	−88(5)	11(5)	−30(5)
I3	430(7)	268(7)	453(8)	21(6)	15(6)	69(5)
I4	456(7)	357(7)	209(6)	40(5)	29(5)	61(5)

Table A.46.: Atomic Distances /pm for Bi_4RhI_2 at 296 K.

Rhodium–Rhodium		
Rh1	– Rh2	286.5(2)

Rhodium–Bismuth		
Rh1	– Bi1	275.6(1)
	– Bi2	278.1(1)
	– Bi3	276.9(1)
	– Bi4	286.4(1)
	– Bi5	286.4(1)
	– Bi6	304.1(1)
	– Bi7	288.1(1)
	– Bi8	281.7(1)
Rh2	– Bi1	273.9(1)
	– Bi3	274.1(1)
	– Bi2#3	275.9(1)
	– Bi4#3	285.2(1)
	– Bi5	284.0(1)
	– Bi6#3	303.2(1)
	– Bi7	285.7(1)
	– Bi8#3	282.2(1)

Bismuth–Bismuth		
Bi1	– Bi3	350.9(1)
	– Bi7	353.0(1)
	– Bi8	367.7(1)
	– Bi8#2	367.2(1)
Bi2	– Bi3	363.7(1)
	– Bi3#3	362.5(1)
	– Bi4	334.5(1)
	– Bi8	332.2(1)
Bi3	– Bi2#2	362.5(1)
	– Bi5	356.7(1)
Bi4	– Bi5	367.4(1)
	– Bi5#3	357.9(1)
	– Bi6	303.8(1)
Bi5	– Bi4#2	357.9(1)
	– Bi6	357.8(1)
	– Bi6#2	344.7(1)
	– Bi7	298.0(1)
Bi6	– Bi5#3	344.7(1)
	– Bi7	363.4(1)
	– Bi7#3	349.7(1)
	– Bi8	316.7(1)
Bi7	– Bi6#2	349.7(1)
	– Bi8#2	362.7(1)
Bi8	– Bi1#3	367.2(1)
	– Bi7#3	362.7(1)

Bismuth–Iodine		
Bi1	– I1#1	337.3(1)
	– I2	313.6(1)
Bi2	– I1	341.4(1)
	– I3	333.7(1)
Bi3	– I2	325.9(1)
	– I4	308.0(1)

Symmetry transformations used to generate equivalent atoms:
#1 $-x+1, -y+1, -z+1$ #2 $x+1, y, z$ #3 $x-1, y, z$

Table A.47.: Atomic coordinates and equivalent isotropic displacement parameters (/pm^2) for Bi_4RhI_2 at 150 K. U_{eq} is defined as one third of the trace of the orthogonalised U_{ij} tensor.

Atom	Wyckoff position	x	y	z	U_{eq}
Bi1	4e	0.71736(10)	0.56552(4)	0.38932(4)	113(2)
Bi2	4e	0.20635(10)	0.64631(4)	0.31011(4)	116(2)
Bi3	4e	0.69209(10)	0.66620(4)	0.20272(4)	116(2)
Bi4	4e	0.17627(10)	0.58508(4)	0.11503(4)	128(2)
Bi5	4e	0.68416(11)	0.48767(4)	0.10608(4)	139(2)
Bi6	4e	0.18081(10)	0.42283(4)	0.16664(4)	137(2)
Bi7	4e	0.70756(10)	0.40393(4)	0.26506(4)	134(2)
Bi8	4e	0.21216(10)	0.46643(4)	0.35539(4)	118(2)
Rh1	4e	0.4716(2)	0.54033(8)	0.24590(8)	109(4)
Rh2	4e	0.9222(2)	0.54202(8)	0.24682(8)	101(4)
I1	4e	0.23973(18)	0.60013(7)	0.51423(7)	161(4)
I2	4e	0.70034(18)	0.73927(7)	0.38722(7)	170(4)
I3	4e	0.20386(19)	0.77510(7)	0.16262(8)	204(4)
I4	4e	0.67300(19)	0.66889(7)	0.01248(7)	182(4)

Table A.48.: Anisotropic displacement parameters (/pm^2) for Bi_4RhI_2 at 150 K. The exponent of the anisotropic displacement factor takes the form: $-2\pi^2[h^2a^{*2}U_{11} + ... + 2hka^*b^*U_{12}]$.

Atom	U_{11}	U_{22}	U_{33}	U_{23}	U_{13}	U_{12}
Bi1	110(3)	133(4)	96(3)	−6(3)	15(3)	0(3)
Bi2	99(3)	111(4)	140(4)	−20(3)	16(3)	−3(3)
Bi3	110(3)	115(4)	126(4)	10(3)	17(3)	1(3)
Bi4	113(3)	172(4)	99(4)	16(3)	20(3)	6(3)
Bi5	149(3)	165(4)	102(4)	−26(3)	15(3)	−2(3)
Bi6	127(3)	129(4)	159(4)	−26(3)	27(3)	7(3)
Bi7	149(3)	102(4)	152(4)	2(3)	23(3)	0(3)
Bi8	115(3)	121(4)	119(4)	14(3)	29(3)	0(3)
Rh1	89(6)	125(8)	112(7)	−3(6)	7(5)	0(6)
Rh2	102(7)	103(8)	100(7)	−9(6)	16(5)	−1(6)
I1	201(6)	156(7)	127(6)	3(5)	24(5)	−20(5)
I2	182(6)	145(7)	183(7)	−41(5)	22(5)	−19(5)
I3	223(7)	149(7)	243(7)	11(6)	25(6)	33(5)
I4	248(7)	174(7)	125(6)	18(5)	23(5)	22(5)

Table A.49.: Atomic Distances /pm for Bi_4RhI_2 at 150 K.

Rhodium–Rhodium		
Rh1	– Rh2	285.3(2)

Rhodium–Bismuth		
Rh1	– Bi1	275.2(2)
	– Bi2	277.5(2)
	– Bi3	276.4(2)
	– Bi4	285.5(2)
	– Bi5	285.1(2)
	– Bi6	303.3(2)
	– Bi7	287.4(2)
	– Bi8	281.0(2)
Rh2	– Bi1	273.4(2)
	– Bi3	273.3(2)
	– Bi5	282.7(2)
	– Bi7	284.8(2)
	– Bi2#3	275.1(2)
	– Bi4#3	284.4(2)
	– Bi6#3	302.6(2)
	– Bi8#3	281.3(2)

Bismuth–Bismuth		
Bi1	– Bi2	370.7(1)
	– Bi2#1	371.0(1)
	– Bi3	350.5(1)
	– Bi7	352.1(1)
	– Bi8	367.4(1)
	– Bi8#1	367.0(1)
Bi2	– Bi3	363.1(1)
	– Bi3#3	361.9(1)
	– Bi4	332.8(1)
	– Bi8	330.6(1)
Bi3	– Bi4	377.7(1)
	– Bi4#1	374.2(1)
	– Bi5	355.9(1)
Bi4	– Bi5	367.0(1)
	– Bi5#3	356.8(1)
	– Bi6	302.6(1)
Bi5	– Bi6	358.0(1)
	– Bi6#1	344.3(1)
	– Bi7	296.8(1)
Bi6	– Bi7	362.9(1)
	– Bi7#3	348.6(1)
	– Bi8	313.9(1)
Bi7	– Bi8	370.6(1)
	– Bi8#1	361.5(1)

Bismuth–Iodine		
Bi1	– I1#2	335.7(1)
	– I2	311.7(1)
Bi2	– I3	331.5(1)
Bi3	– I2	324.9(1)
	– I4	306.4(1)

Symmetry transformations used to generate equivalent atoms:
#1 $x+1, y, z$ #2 $-x+1, -y+1, -z+1$ #3 $x-1, y, z$

Table A.50.: Family tree according to Bärnighausen relating Bi_4RuI_2 to a hypothetical aristotype "Bi_4MI_2" in the spacegroup $I4/mcm$ from which Bi_4RuI_2 and Bi_4RhI_2 can be derived. Positions of Bi_4MI_2 were calculated as mean values of the respective atoms in Bi_4RuI_2 and are given up to the last significant value.

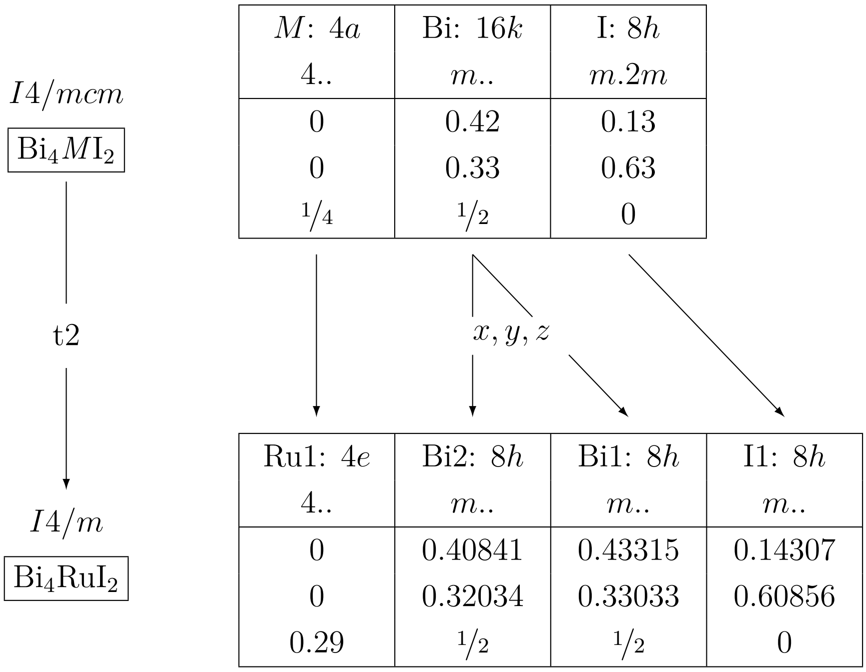

M: 4a	Bi: 16k	I: 8h
4..	m..	m.2m
0	0.42	0.13
0	0.33	0.63
1/4	1/2	0

Ru1: 4e	Bi2: 8h	Bi1: 8h	I1: 8h
4..	m..	m..	m..
0	0.40841	0.43315	0.14307
0	0.32034	0.33033	0.60856
0.29	1/2	1/2	0

Table A.51.: Part one (part two below) of the family tree according to Bärnighausen relating Bi_4RhI_2 to a hypothetical aristotype “Bi_4MI_2” in the spacegroup $I4/mcm$ from which Bi_4RuI_2 and Bi_4RhI_2 can be derived. Positions of Bi_4MI_2 were calculated as mean values of the respective atoms in Bi_4RuI_2 and are given up to the last significant value.

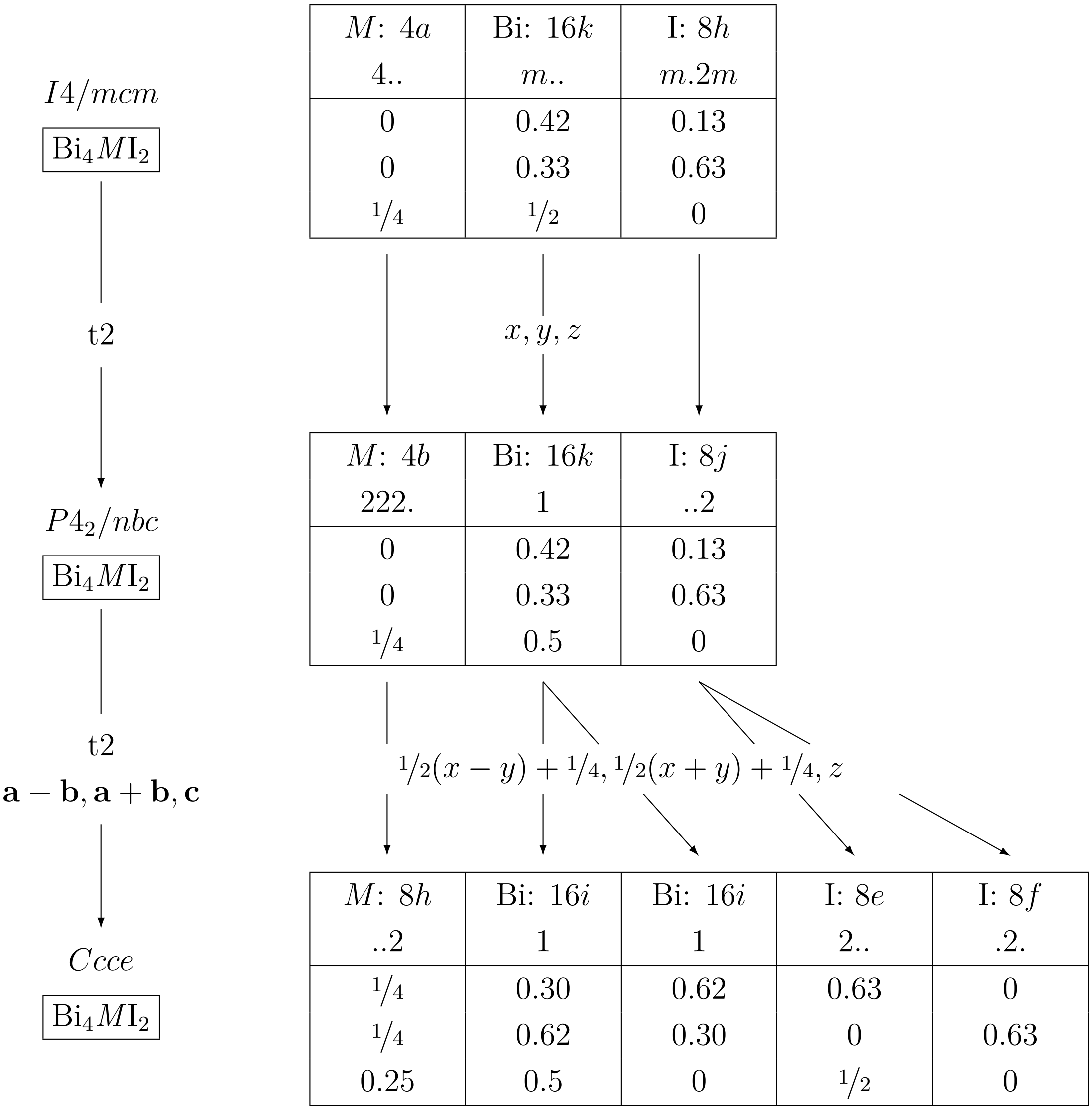

$I4/mcm$

$\boxed{Bi_4MI_2}$

M: 4a	Bi: 16k	I: 8h
4..	m..	m.2m
0	0.42	0.13
0	0.33	0.63
1/4	1/2	0

t2

x, y, z

$P4_2/nbc$

$\boxed{Bi_4MI_2}$

M: 4b	Bi: 16k	I: 8j
222.	1	..2
0	0.42	0.13
0	0.33	0.63
1/4	0.5	0

t2

$\mathbf{a} - \mathbf{b}, \mathbf{a} + \mathbf{b}, \mathbf{c}$

$1/2(x - y) + 1/4, 1/2(x + y) + 1/4, z$

$Ccce$

$\boxed{Bi_4MI_2}$

M: 8h	Bi: 16i	Bi: 16i	I: 8e	I: 8f
..2	1	1	2..	.2.
1/4	0.30	0.62	0.63	0
1/4	0.62	0.30	0	0.63
0.25	0.5	0	1/2	0

Table A.52.: Part two (part one above) of the family tree according to BÄRNIGHAUSEN relating Bi_4RhI_2 to a hypothetical aristotype "Bi_4MI_2" in the spacegroup $I4/mcm$ from which Bi_4RuI_2 and Bi_4RhI_2 can be derived. Positions of Bi_4MI_2 were calculated as mean values of the respective atoms in Bi_4RuI_2 and are given up to the last significant value.

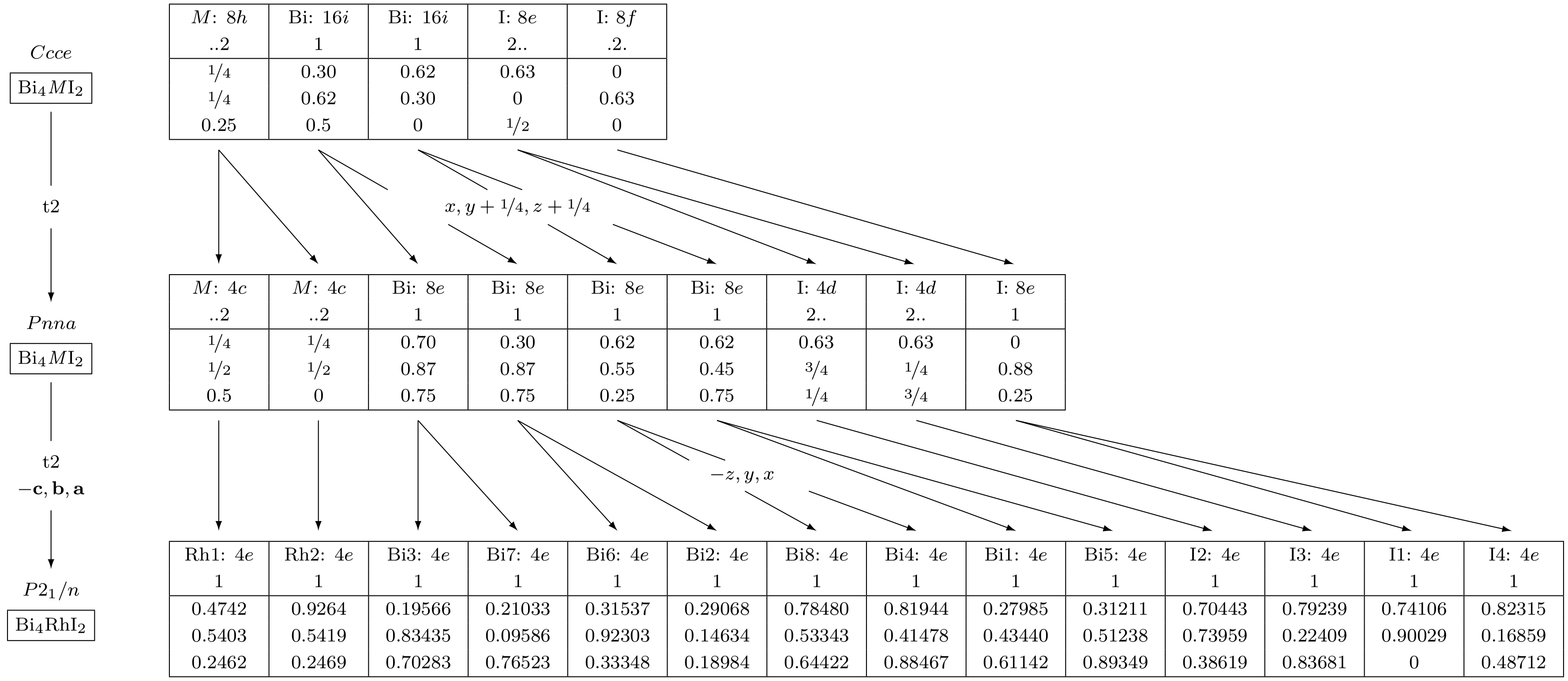

$Ccce$, Bi_4MI_2

M: 8h	Bi: 16i	Bi: 16i	I: 8e	I: 8f
..2	1	1	2..	.2.
1/4	0.30	0.62	0.63	0
1/4	0.62	0.30	0	0.63
0.25	0.5	0	1/2	0

$Pnna$, Bi_4MI_2

M: 4c	M: 4c	Bi: 8e	Bi: 8e	Bi: 8e	Bi: 8e	I: 4d	I: 4d	I: 8e
..2	..2	1	1	1	1	2..	2..	1
1/4	1/4	0.70	0.30	0.62	0.62	0.63	0.63	0
1/2	1/2	0.87	0.87	0.55	0.45	3/4	1/4	0.88
0.5	0	0.75	0.75	0.25	0.75	1/4	3/4	0.25

$P2_1/n$, Bi_4RhI_2

Rh1: 4e	Rh2: 4e	Bi3: 4e	Bi7: 4e	Bi6: 4e	Bi2: 4e	Bi8: 4e	Bi4: 4e	Bi1: 4e	Bi5: 4e	I2: 4e	I3: 4e	I1: 4e	I4: 4e
1	1	1	1	1	1	1	1	1	1	1	1	1	1
0.4742	0.9264	0.19566	0.21033	0.31537	0.29068	0.78480	0.81944	0.27985	0.31211	0.70443	0.79239	0.74106	0.82315
0.5403	0.5419	0.83435	0.09586	0.92303	0.14634	0.53343	0.41478	0.43440	0.51238	0.73959	0.22409	0.90029	0.16859
0.2462	0.2469	0.70283	0.76523	0.33348	0.18984	0.64422	0.88467	0.61142	0.89349	0.38619	0.83681	0	0.48712

Table A.53.: Bader charges according to QTAIM[128] for Bi_4RhI_2. Due to the standard deviation they do not sum up to 0.

Bader charges					
Rh1	−0.7	Bi1	0.4	I1	−0.4
Rh2	−0.7	Bi2	0.3	I2	−0.4
		Bi3	0.4	I3	−0.4
		Bi4	0.1	I4	−0.4
		Bi5	0.1		
		Bi6	0.1		
		Bi7	0.1		
		Bi8	0.2		

Table A.54.: ELI-D bonding basins (as in Figure 5.8) with contributing atoms ($\geq 5\,\%$) and the respective integrated electron density for Bi_4RhI_2.

Contributing Atoms		Electron count
Two-centre bonds		
Rh1	−Bi 1	0.8
	−Bi 3	1.1
	−Bi 7	0.6
Rh2	−Bi 1	0.8
	−Bi 3	0.7
	−Bi 5	0.7
	−Bi 7	0.5
Bi4	−Bi 6	1.9
Bi5	−Bi 7	1.4
Three-centre bonds		
Rh 1	−Bi 1 −Rh 2	0.2

Contributing Atoms		Electron count
Bismuth lone pairs		
Bi1	Square 1	2.7
Bi3		2.6
Bi5		4.0
Bi7		3.4
Bi2	Square 2	4.7
Bi4		4.9
Bi6		3.5
Bi8		5.0

A.3. Theoretical Modelling and Physical Properties

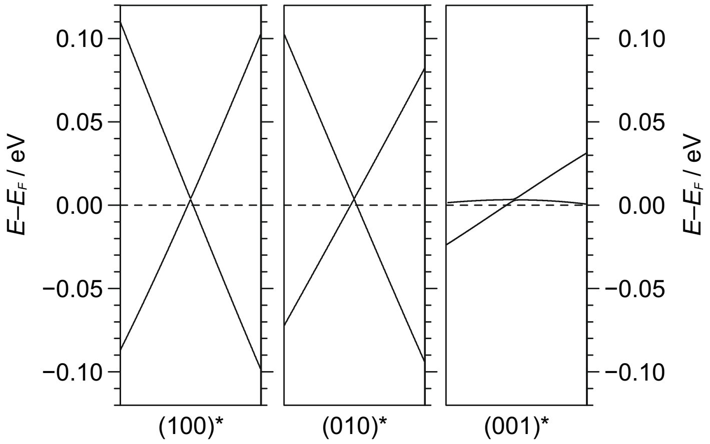

Figure A.24.: Zoom-in on the Dirac cone in the scalar-relativistic band structure of $Bi_{14}Rh_3I_9$. The dispersion of the bands forming the Dirac cone is shown along the reciprocal axes ($(1\,0\,0)^*$, $(0\,1\,0)^*$ and $(0\,0\,1)^*$) on a length of $0.1 \cdot {}^{2\pi}/_{a}$, where the first two more or less correspond to directions in the plane of the honeycomb layer (not precisely, as $\alpha = 62.7°$ and $\beta = 81.0°$) and the latter corresponds to the stacking direction perpendicular to the honeycomb layer.

A.3.1. The Isolated Layer Model

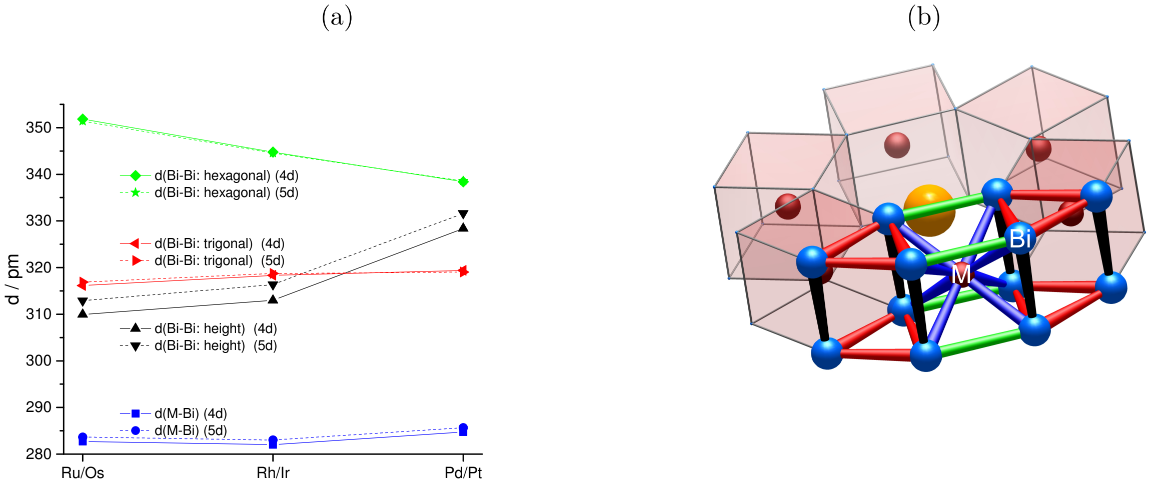
(a)

(b)

Figure A.25.: (a) Bond lengths for the M−Bi bonds and all Bi−Bi bonds in the ILSs coloured according to the scetch in (b).

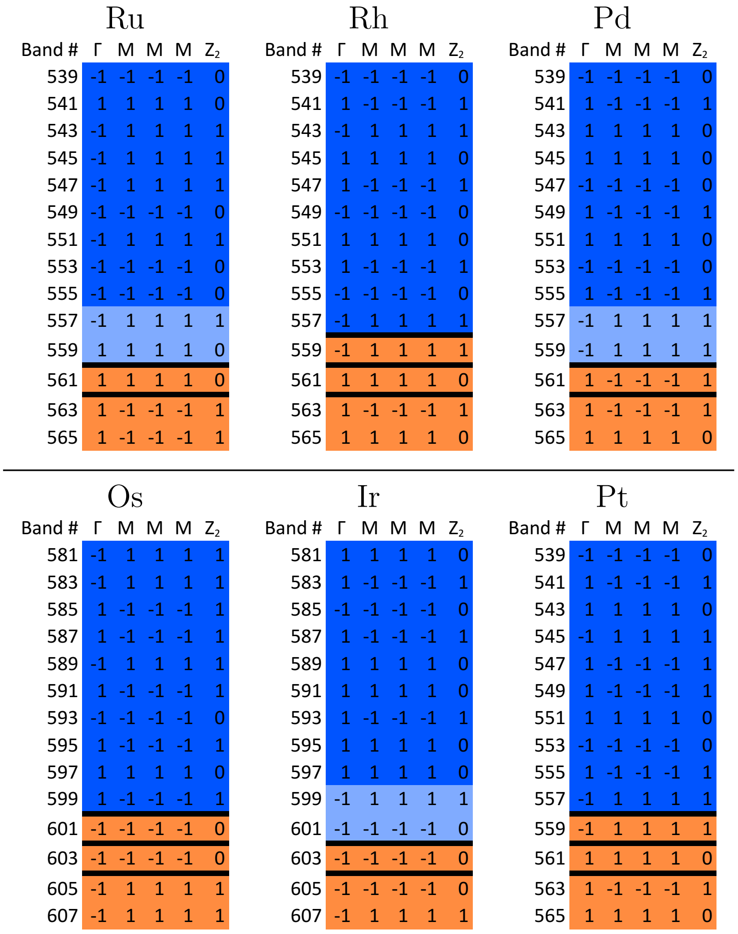

Ru

Band #	Γ	M	M	M	Z_2
539	-1	-1	-1	-1	0
541	1	1	1	1	0
543	-1	1	1	1	1
545	-1	1	1	1	1
547	-1	1	1	1	1
549	-1	-1	-1	-1	0
551	-1	1	1	1	1
553	-1	-1	-1	-1	0
555	-1	-1	-1	-1	0
557	-1	1	1	1	1
559	1	1	1	1	0
561	1	1	1	1	0
563	1	-1	-1	-1	1
565	1	-1	-1	-1	1

Rh

Band #	Γ	M	M	M	Z_2
539	-1	-1	-1	-1	0
541	1	-1	-1	-1	1
543	-1	1	1	1	1
545	1	1	1	1	0
547	1	-1	-1	-1	1
549	-1	-1	-1	-1	0
551	1	1	1	1	0
553	1	-1	-1	-1	1
555	-1	-1	-1	-1	0
557	-1	1	1	1	1
559	-1	1	1	1	1
561	1	1	1	1	0
563	1	-1	-1	-1	1
565	1	1	1	1	0

Pd

Band #	Γ	M	M	M	Z_2
539	-1	-1	-1	-1	0
541	1	-1	-1	-1	1
543	1	1	1	1	0
545	1	1	1	1	0
547	-1	-1	-1	-1	0
549	1	-1	-1	-1	1
551	1	1	1	1	0
553	-1	-1	-1	-1	0
555	1	-1	-1	-1	1
557	-1	1	1	1	1
559	-1	1	1	1	1
561	1	-1	-1	-1	1
563	1	-1	-1	-1	1
565	1	1	1	1	0

Os

Band #	Γ	M	M	M	Z_2
581	-1	1	1	1	1
583	-1	1	1	1	1
585	1	-1	-1	-1	1
587	1	-1	-1	-1	1
589	-1	1	1	1	1
591	1	-1	-1	-1	1
593	-1	-1	-1	-1	0
595	1	-1	-1	-1	1
597	1	1	1	1	0
599	1	-1	-1	-1	1
601	-1	-1	-1	-1	0
603	-1	-1	-1	-1	0
605	-1	1	1	1	1
607	-1	1	1	1	1

Ir

Band #	Γ	M	M	M	Z_2
581	1	1	1	1	0
583	1	-1	-1	-1	1
585	-1	-1	-1	-1	0
587	1	-1	-1	-1	1
589	1	1	1	1	0
591	1	1	1	1	0
593	1	-1	-1	-1	1
595	1	1	1	1	0
597	1	1	1	1	0
599	-1	1	1	1	1
601	-1	-1	-1	-1	0
603	-1	-1	-1	-1	0
605	-1	-1	-1	-1	0
607	-1	1	1	1	1

Pt

Band #	Γ	M	M	M	Z_2
539	-1	-1	-1	-1	0
541	1	-1	-1	-1	1
543	1	1	1	1	0
545	-1	1	1	1	1
547	1	-1	-1	-1	1
549	1	-1	-1	-1	1
551	1	1	1	1	0
553	-1	-1	-1	-1	0
555	1	-1	-1	-1	1
557	-1	1	1	1	1
559	-1	1	1	1	1
561	1	1	1	1	0
563	1	-1	-1	-1	1
565	1	1	1	1	0

Table A.55.: Calculated Z_2 invariants at the four time-reversal invariant k-points (in two dimensions) for all ILSs with a valence-electron count equal to the one in the original QSH-layer $[(\mathrm{Bi}_{8/2}\mathrm{Rh})_3\mathrm{I}]^{2+}$ (blue: filled band; light blue: partially filled band; orange: empty band). Energy gaps are marked with a black line.

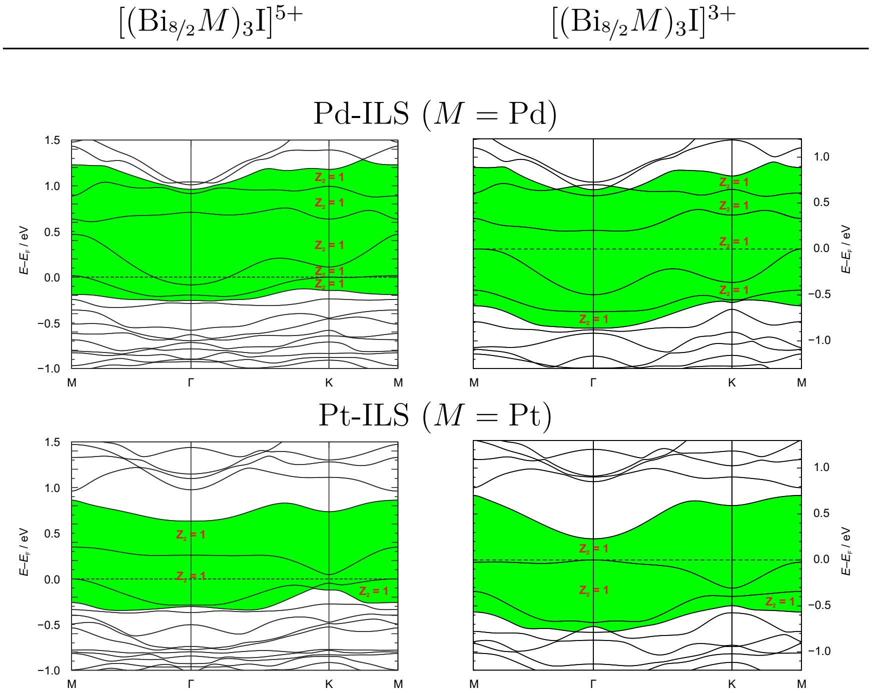

Figure A.26.: Full-relativistic band structures for the M-ILSs with M = Pd and Pt for different valence electron counts in the intermetallic layer with the calculated 2D-Z_2 invariants for gaps close to the Fermi energy. Thereby, $[(\mathrm{Bi}_{8/2}M)_3\mathrm{I}]^{5+}$ corresponds to the situation as found in the original Rh-ILS $[(\mathrm{Bi}_{8/2}\mathrm{Rh})_3\mathrm{I}]^{2+}$ and $[(\mathrm{Bi}_{8/2}M)_3\mathrm{I}]^{3+}$ corresponds to the situation as found in the compounds $\mathrm{Bi}_{13}\mathrm{Pt}_3\mathrm{I}_7$ and $\mathrm{Bi}_{13}\mathrm{Pd}_3\mathrm{I}_7$.

A.3.2. $Bi_{13}Pt_3I_7$ and $Bi_{13}Pd_3I_7$

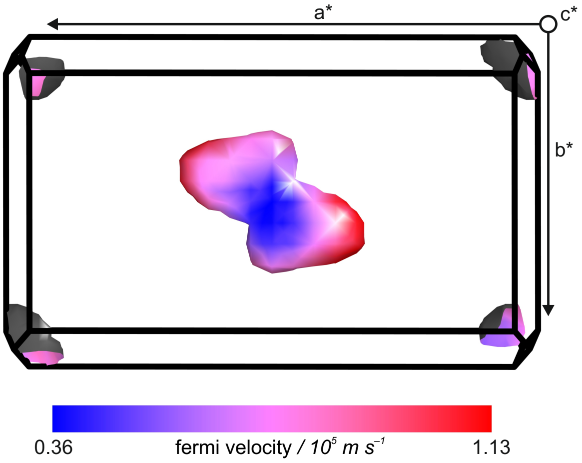

Figure A.27.: Fermi surface with Fermi velocities for $Bi_{13}Pt_3I_7$ from a full-relativistic calculation shown in the first Brillouin zone. $\vec{a}^*$ and $\vec{b}^*$ have a length of $0.1121\,\text{Å}^{-1}$ and $0.0653\,\text{Å}^{-1}$, respectively, which yields as area of the $\vec{a}^*$-$\vec{b}^*$ plane in the first Brillouin zone about $7.32 \times 10^{13}\,\text{cm}^{-2}$.

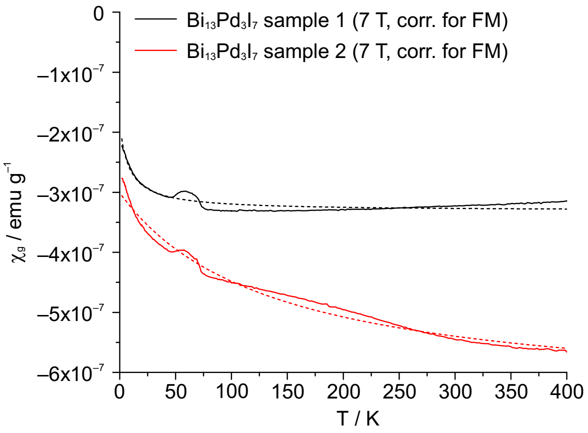

Figure A.28.: Magnetic susceptibility corrected for ferromagnetic impurities via Honda-Owen type correction vs. temperature for two samples of $Bi_{13}Pd_3I_7$ at 7 T with Curie-Weiss fits. The feature in magnetisation near 50 K is very likely due to traces of molecular oxygen in the magnetometer.

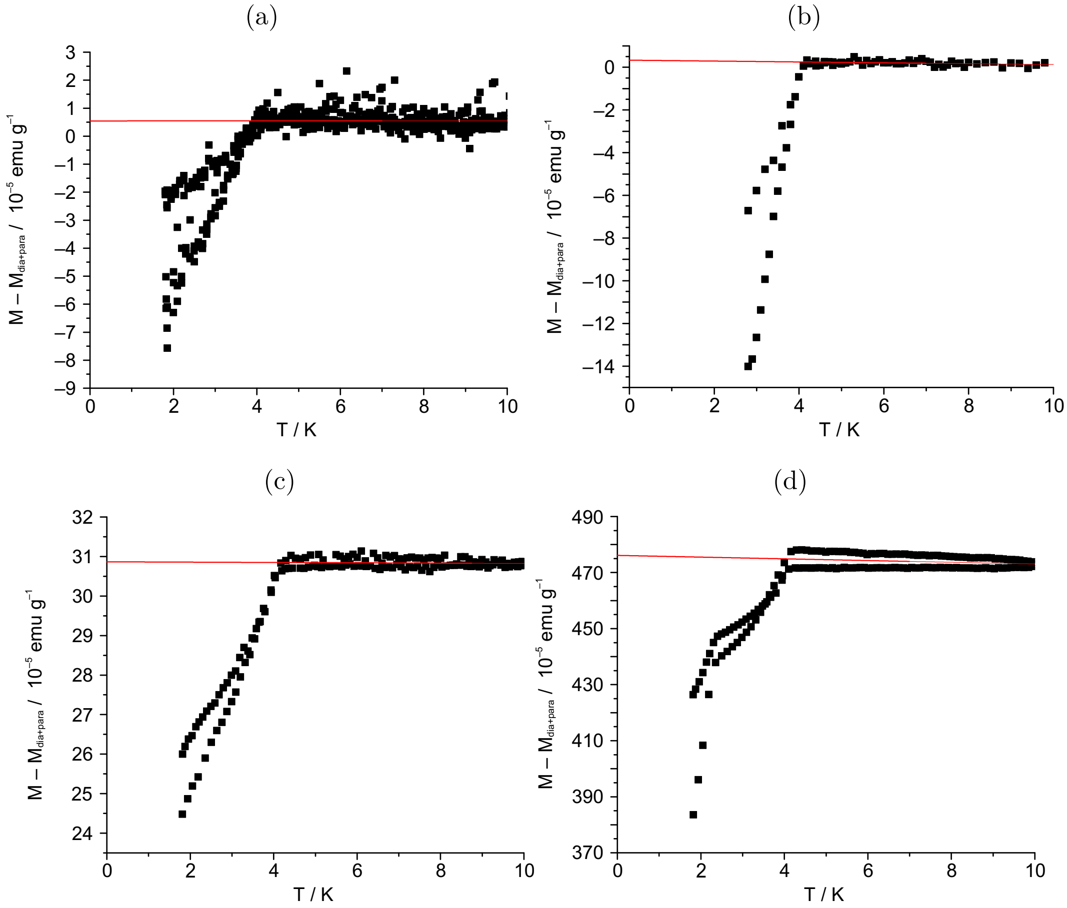

Figure A.29.: Magnetisation versus temperature zero field cooled and field cooled (lower and upper data points, respectively) corrected for the dia- and paramagnetic part at high fields (Figure 4.27b) to fit the ferromagnetic part at small fields (red line) for $Bi_{13}Pt_3I_7$ ((a) sample 1 and (b) sample 2 at 50 mT) as well as for $Bi_{13}Pd_3I_7$ ((c) sample 1 and (d) sample 2 at 20 mT). For sample 2, two different phases become superconducting, therefore it was not considered for the discussion. Results are summarised in Table 4.1.

A.3.3. $Bi_{38}Pt_9I_{14}$

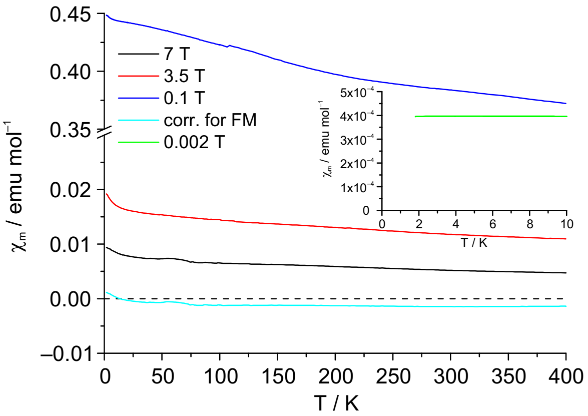

Figure A.30.: Magnetic susceptibility vs. temperature of $Bi_{38}Pt_9I_{14}$ in different magnetic fields and corrected for ferromagnetic impurities (cyan). The inset shows the behaviour in very low fields to check for superconductivity down to 2 K.

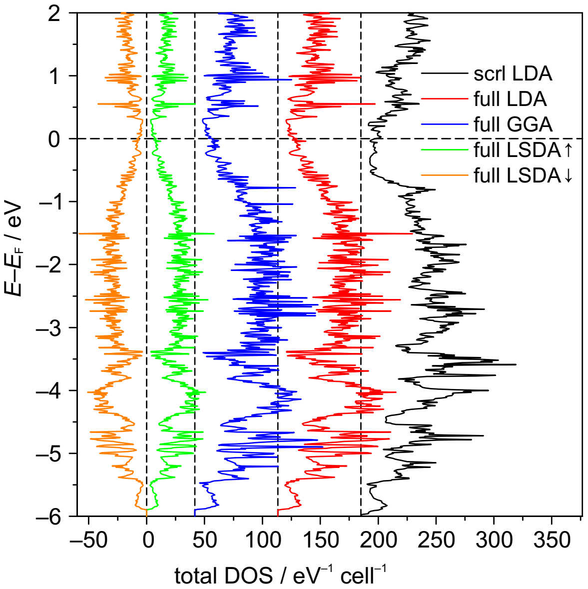

Figure A.31.: Total density of states (DOS) for $Bi_{38}Pt_9I_{14}$ from scalar-relativistic (scrl) and full-relativistic (full) DFT calculations, with different exchange correlation potentials (local density approximation: LDA; generalised gradient approximation: GGA; local spin density approximation: LSDA). Vertical dashed lines mark the respective zero value.

Table A.56.: Strong and weak topological invariants, as well as the δ_i values calculated from the parity eigenvalues at the time-reversal invariant momenta (TRIM) for bands close to the Fermi level. The latter is indicated by the fat line.

$E_B - E_F$ at Γ / eV	occupation	topological invariants		δ_i values at all eight TRIM							
				Γ	M		K	A	L		H
		strong	weak	[000]	[100]	[010]	[110]	[001]	[101]	[011]	[111]
$-0.554\,77$	full	1	(001)	1	1	1	1	1	-1	-1	-1
$-0.412\,29$	full	1	(000)	-1	1	1	1	-1	-1	-1	-1
$-0.267\,56$	partial	0	(001)	1	-1	-1	-1	-1	1	1	1
$-0.056\,24$	partial	1	(000)	1	-1	-1	-1	1	1	1	1
$0.054\,04$	partial	1	(000)	-1	1	1	1	1	1	1	1
$0.085\,52$	empty	1	(000)	-1	1	1	1	-1	-1	-1	-1
$0.268\,62$	empty	1	(000)	-1	1	1	1	-1	-1	-1	-1

B. Bibliography

[1] J. C. Maxwell, *Phil. Trans. R. Soc. Lond.* **1865**, *155*, 459–512.

[2] H. Hertz, *Ann. Phys.* **1888**, *270*, 155–170.

[3] M. Guarnieri, *IEEE Industrial Electronics Magazine* **2012**, *6*, 41–43.

[4] G. L. Pearson, W. H. Brattain, *P. IRE* **1955**, *43*, 1794–1806.

[5] W. F. Brinkman, D. E. Haggan, W. W. Troutman, *IEEE J. Solid-St. Circ.* **1997**, *32*, 1858–1865.

[6] M. Riordan, *IEEE Spectrum: Technology, Engineering, and Science News* **2005**, 46–51.

[7] J. C. Bose, *Detector for electrical disturbances*, **1904**, Cooperative Classification H01L29/00. http://www.google.de/patents/US755840.

[8] F. Braun, *Ann. Phys.* **1875**, *229*, 556–563.

[9] A. Van Dormael in *Proceedings of the 2004 IEEE Conference on the History of Electronics*. http://www.cdvandt.org/VanDormael.pdf.

[10] *The New York Times* **1948**, 46.

[11] K. Rupp, *40 Years of Microprocessor Trend Data | Karl Rupp*, **2015**. https://www.karlrupp.net/2015/06/40-years-of-microprocessor-trend-data/.

[12] *Creative Commons — Attribution-ShareAlike 4.0 International — CC BY-SA 4.0*, **2016**. http://creativecommons.org/licenses/by-sa/4.0/.

[13] G. E. Moore, *Electronics* **1965**, 114–117.

[14] G. E. Moore, others, *IEDM Tech. Digest* **1975**, 11–13.

[15] M. M. Waldrop, *Nature News* **2016**, *530*, 144.

[16] M. Hopkinson, *With silicon pushed to its limits, what will power the next electronics revolution?*, **2015**. http://theconversation.com/with-silicon-pushed-to-its-limits-what-will-power-the-next-electronics-revolution-46287.

[17] *Intel® 14-nm-Technik*, **2015**. http://www.intel.com/content/www/de/de/silicon-innovations/intel-14nm-technology.html.

[18] M. H. Devoret, R. J. Schoelkopf, *Nature* **2000**, *406*, 1039–1046.

[19] D. Terdiman, *Fast Company* **2015**.

[20] Q. Cao, S.-j. Han, *Nanoscale* **2013**, *5*, 8852–8863.

[21] F. Schwierz, *Nat. Nano.* **2010**, *5*, 487–496.

[22] P. Avouris, Z. Chen, V. Perebeinos, *Nat. Nano.* **2007**, *2*, 605–615.

[23] K. K. Likharev, *P. IEEE* **1999**, *87*, 606–632.

[24] S. D. Bader, S. S. P. Parkin, *Annu. Rev. Condens. Matter Phys.* **2010**, *1*, 71–88.

[25] T. D. Ladd, F. Jelezko, R. Laflamme, Y. Nakamura, C. Monroe, J. L. O'Brien, *Nature* **2010**, *464*, 45–53.

[26] J. Moore, *Nature* **2010**, *464*, 194–198.

[27] M. Z. Hasan, C. L. Kane, *Rev. Mod. Phys.* **2010**, *82*, 3045–3067.

[28] J. Alicea, *Rep. Prog. Phys.* **2012**, *75*, 076501.

[29] J. Q. You, Z. D. Wang, W. Zhang, F. Nori, *Sci. Rep.* **2014**, *4*.

[30] L. Fu, C. Kane, *Phys. Rev. B* **2007**, *76*, 045302.

[31] D. Hsieh, Y. Xia, D. Qian, L. Wray, F. Meier, J. H. Dil, J. Osterwalder, L. Patthey, A. V. Fedorov, H. Lin, A. Bansil, D. Grauer, Y. S. Hor, R. J. Cava, M. Z. Hasan, *Phys. Rev. Lett.* **2009**, *103*, 146401.

[32] Y. Ando, *J. Phys. Soc. Jpn.* **2013**, *82*, 102001.

[33] X.-L. Qi, S.-C. Zhang, *Rev. Mod. Phys.* **2011**, *83*, 1057–1110.

[34] S.-s. Chern, *Ann. Math.* **1946**, *47*, 85.

[35] D. Thouless, M. Kohmoto, M. P. Nightingale, M. den Nijs, *Phys. Rev. Lett.* **1982**, *49*, 405–408.

[36] K. v. Klitzing, G. Dorda, M. Pepper, *Phys. Rev. Lett.* **1980**, *45*, 494–497.

[37] J. E. Avron, D. Osadchy, R. Seiler, *Physics Today* **2003**, *56*, 38–42.

[38] C. L. Kane, E. J. Mele, *Phys. Rev. Lett.* **2005**, *95*, 146802.

[39] C. L. Kane, E. J. Mele, *Phys. Rev. Lett.* **2005**, *95*, 226801.

[40] B. A. Bernevig, S.-C. Zhang, *Phys. Rev. Lett.* **2006**, *96*, 106802.

[41] J. E. Moore, L. Balents, *Phys. Rev. B* **2007**, *75*, 121306.

[42] R. Roy, *Phys. Rev. B* **2009**, *79*, 195322.

[43] L. Fu, *Phys. Rev. Lett.* **2011**, *106*, 106802.

[44] Y. Ando, L. Fu, *Annu. Rev. Condens. Matter Phys.* **2015**, *6*, 361–381.

[45] T. Senthil, *Annu. Rev. Condens. Matter Phys.* **2015**, *6*, 299–324.

[46] V. Peano, C. Brendel, M. Schmidt, F. Marquardt, *Phys. Rev. X* **2015**, *5*, 031011.

[47] L. V. Levitin, R. G. Bennett, A. Casey, B. Cowan, J. Saunders, D. Drung, T. Schurig, J. M. Parpia, *Science* **2013**, *340*, 841–844.

[48] X.-L. Qi, *Science* **2012**, *338*, 1550–1551.

[49] R. B. Laughlin, *Phys. Rev. B* **1981**, *23*, 5632–5633.

[50] F. D. M. Haldane, *Phys. Rev. Lett.* **1988**, *61*, 2015–2018.

[51] S. Murakami, N. Nagaosa, S.-C. Zhang, *Phys. Rev. Lett.* **2004**, *93*, 156804.

[52] M. Dyakonov, V. Perel, *JETP Letters* **1971**, *13*, 467–469.

[53] J. E. Hirsch, *Phys. Rev. Lett.* **1999**, *83*, 1834–1837.

[54] M. Onoda, N. Nagaosa, *Phys. Rev. Lett.* **2005**, *95*, 106601.

[55] R. S. K. Mong, J. H. Bardarson, J. E. Moore, *Phys. Rev. Lett.* **2012**, *108*, 076804.

[56] Z. Ringel, Y. E. Kraus, A. Stern, *Phys. Rev. B* **2012**, *86*, 045102.

[57] L. Fu, C. L. Kane, *Phys. Rev. Lett.* **2012**, *109*, 246605.

[58] K. Kobayashi, T. Ohtsuki, K.-I. Imura, *Phys. Rev. Lett.* **2013**, *110*, 236803.

[59] H. Obuse, S. Ryu, A. Furusaki, C. Mudry, *Phys. Rev. B* **2014**, *89*, 155315.

[60] Y. Yoshimura, A. Matsumoto, Y. Takane, K.-I. Imura, *Phys. Rev. B* **2013**, *88*.

[61] J. H. Bardarson, J. E. Moore, *Rep. Prog. Phys.* **2013**, *76*, 056501.

[62] M. König, S. Wiedmann, C. Brüne, A. Roth, H. Buhmann, L. W. Molenkamp, X.-L. Qi, S.-C. Zhang, *Science* **2007**, *318*, 766 –770.

[63] D. Hsieh, D. Qian, L. Wray, Y. Xia, Y. S. Hor, R. J. Cava, M. Z. Hasan, *Nature* **2008**, *452*, 970–974.

[64] D. Hsieh, Y. Xia, L. Wray, D. Qian, A. Pal, J. H. Dil, J. Osterwalder, F. Meier, G. Bihlmayer, C. L. Kane, Y. S. Hor, R. J. Cava, M. Z. Hasan, *Science* **2009**, *323*, 919–922.

[65] H. Zhang, C.-X. Liu, X.-L. Qi, X. Dai, Z. Fang, S.-C. Zhang, *Nat. Phys.* **2009**, *5*, 438–442.

[66] Y. Xia, D. Qian, D. Hsieh, L. Wray, A. Pal, H. Lin, A. Bansil, D. Grauer, Y. S. Hor, R. J. Cava, M. Z. Hasan, *Nat. Phys.* **2009**, *5*, 398–402.

[67] Y. L. Chen, J. G. Analytis, J.-H. Chu, Z. K. Liu, S.-K. Mo, X. L. Qi, H. J. Zhang, D. H. Lu, X. Dai, Z. Fang, S. C. Zhang, I. R. Fisher, Z. Hussain, Z.-X. Shen, *Science* **2009**, *325*, 178–181.

[68] S. Barua, K. P. Rajeev, *AIP Advances* **2014**, *4*, 017135.

[69] J. Sánchez-Barriga, A. Varykhalov, J. Braun, S.-Y. Xu, N. Alidoust, O. Kornilov, J. Minár, K. Hummer, G. Springholz, G. Bauer, R. Schumann, L. V. Yashina, H. Ebert, M. Z. Hasan, O. Rader, *Phys. Rev. X* **2014**, *4*, 011046.

[70] P. Roushan, J. Seo, C. V. Parker, Y. S. Hor, D. Hsieh, D. Qian, A. Richardella, M. Z. Hasan, R. J. Cava, A. Yazdani, *Nature* **2009**, *460*, 1106–1109.

[71] J. Seo, P. Roushan, H. Beidenkopf, Y. S. Hor, R. J. Cava, A. Yazdani, *Nature* **2010**, *466*, 343–346.

[72] I. K. Drozdov, A. Alexandradinata, S. Jeon, S. Nadj-Perge, H. Ji, R. J. Cava, B. Andrei Bernevig, A. Yazdani, *Nat. Phys.* **2014**, *10*, 664–669.

[73] E. Majorana, *Nuovo Cim.* **1937**, *14*, 171–184.

[74] C. W. J. Beenakker, *Annu. Rev. Condens. Matter Phys.* **2013**, *4*, 113–136.

[75] C. Kittel, *Einführung in die Festkörperphysik 14th ed.*, Oldenbourg Wissenschaftsverlag, München u.a., **2005**.

[76] S. Hunklinger, *Festkörperphysik 4th ed.*, De Gruyter Oldenbourg, Berlin, Boston, **2014**.

[77] M. Ruck, *Z. Kristallogr.* **2010**, *225*, 167–172.

[78] L. M. Liz-Marzán, M. Giersig, *Low-Dimensional Systems: Theory, Preparation, and Some Applications 1st ed.*, Springer Netherlands, Dordrecht, **2003**.

[79] M. R. Geller, *Physics* **2001**, *2451*, 13.

[80] G. A. Ozin, A. C. Arsenault, *Nanochemistry: a chemical approach to nanomaterials*, Royal Society of Chemistry (Great Britain), Cambridge, **2005**.

[81] R. J. Busch, *Nano(bio)technologie im öffentlichen Diskurs 1st ed.*, Herbert Utz Verlag, München, **2008**.

[82] D. V. Talapin, J.-S. Lee, M. V. Kovalenko, E. V. Shevchenko, *Chem. Rev.* **2010**, *110*, 389–458.

[83] F. Kreupl, *Nature* **2012**, *484*, 321–322.

[84] G. Fiori, F. Bonaccorso, G. Iannaccone, T. Palacios, D. Neumaier, A. Seabaugh, S. K. Banerjee, L. Colombo, *Nat. Nano.* **2014**, *9*, 768–779.

[85] M. Osada, T. Sasaki, *Adv. Mater.* **2012**, *24*, 210–228.

[86] J. Reinhold, *Quantentheorie der Moleküle - Eine Einführung*, Teubner, Wiesbaden, **2006**.

[87] R. J. D. Tilley, *Understanding Solids: The Science of Materials*, John Wiley & Sons, Chichester, **2013**.

[88] T. L. Meek, L. D. Garner, *J. Chem. Educ.* **2005**, *82*, 325.

[89] A. E. van Arkel, *Molecules and crystals in inorganic chemistry*, Butterworth, London, **1949**.

[90] J. A. A. Ketelaar, *Chemical constitution – an introduction to the theory of the chemical bond*, Elsevier, Amsterdam [u.a.], **1958**.

[91] J. Zhao, J. Corbett, *Inorg. Chem.* **1995**, *34*, 378–383.

[92] S. M. Kauzlarich, *Chemistry, structure, and bonding of Zintl phases and ions*, VCH, New York, **1996**.

[93] U. Müller, *Anorganische Strukturchemie 6th ed.*, B.G. Teubner Verlag, Wiesbaden, **2008**.

[94] P. de Marcillac, N. Coron, G. Dambier, J. Leblanc, J.-P. Moalic, *Nature* **2003**, *422*, 876–878.

[95] *NIST Physical Reference Data*, **2016**. http://www.nist.gov/pml/data/.

[96] B. Predel, D. Rothacker, *Thermochimica Acta* **1970**, *1*, 477–487.

[97] H. von Schnering, H. von Benda, C. Kalveram, *Z. Anorg. Allg. Chem.* **1978**, *438*, 37–52.

[98] E. V. Dikarev, V. A. Trifonov, B. A. Popovkin, *Zhur. Neorg. Khim.* **1987**, *32*, 430–432; E. V. Dikarev, V. A. Trifonov, B. A. Popovkin, *Russ. J. Inorg. Chem.* **1987**, *32*, 238–240.

[99] E. V. Dikarev, B. A. Popovkin, *Dokl. Akad. Nauk SSSR* **1990**, *310*, 117–120.

[100] E. Dikarev, B. Popovkin, A. Shevelkov, *Z. Anorg. Allg. Chem.* **1992**, *612*, 118–122.

[101] M. Lindsjö, L. Kloo, A. Kuznetzov, B. Popovkin, *Eur. J. Inorg. Chem.* **2008**, *2008*, 5196–5202.

[102] M. Lê Anh, *Lösungsmittelbasierte Synthese von bismutreichen Subhalogeniden und die Untersuchung der physikalischen Eigenschaften von* $Bi_{14}I_4$ *und* $Bi_{18}I_4$, Bachelorarbeit, Technische Universität Dresden, **2014**.

[103] G. Autès, A. Isaeva, L. Moreschini, J. C. Johannsen, A. Pisoni, R. Mori, W. Zhang, T. G. Filatova, A. N. Kuznetsov, L. Forró, W. Van den Broek, Y. Kim, K. S. Kim, A. Lanzara, J. D. Denlinger, E. Rotenberg, A. Bostwick, M. Grioni, O. V. Yazyev, *Nat. Mater.* **2016**, *15*, 154–158.

[104] M. Ruck, *Angew. Chem. Int. Ed.* **2001**, *40*, 1182–1193; *Angew. Chem.* **2001**, *113*, 1222–1234.

[105] M. Ruck in *Reference Module in Chemistry, Molecular Sciences and Chemical Engineering*, Elsevier, **2015**.

[106] T. Herrmannsdörfer, R. Skrotzki, J. Wosnitza, D. Köhler, R. Boldt, M. Ruck, *Phys. Rev. B* **2011**, *83*, 140501.

[107] M. Ruck, *Z. Anorg. Allg. Chem.* **1997**, *623*, 1535–1541.

[108] M. Ruck, *Z. Kristallogr.* **1995**, *210*, 650–655.

[109] *AZtec*, **2013**.

[110] *X-Red32*, **2009**.

[111] *X-Shape, Program for Crystal Optimisation for Numerical Absorption Correction*, **1999**.

[112] *Jana2006, The crystallographic computing system*, **2015**.

[113] V. Petricek, M. Dusek, L. Palatinus, *Z. Kristallogr.* **2014**, *229*, 345–352.

[114] G. Sheldrick, *SHELX2014, Program for crystal structure determination*, **2014**.

[115] K. Brandenburg, *DIAMOND 3.2k, Crystal and Molecular Structure Visualization*, **2014**.

[116] P. Stadelmann, *JEMS software*, **2012**. http://cimewww.epfl.ch/people/stadelmann/jemsWebSite/jems.htlm.

[117] T. Mashoff, M. Pratzer, M. Morgenstern, *Review of Scientific Instruments* **2009**, *80*, 053702.

[118] M. Morgenstern, *Surf. Rev. Lett.* **2003**, *10*, 933–962.

[119] S. V. Borisenko, *Synchrotron Radiation News* **2012**, *25*, 6–11.

[120] S. V. Borisenko, V. Zabolotnyy, A. A. Kordyuk, D. V. Evtushinsky, T. K. Kim, E. Carleschi, B. P. Doyle, R. Fittipaldi, M. Cuoco, A. Vecchione, H. Berger, *J. Vis. Exp.* **2012**, e50129.

[121] K. Honda, *Ann. Phys.* **1910**, *337*, 1003–1026.

[122] M. Owen, *Ann. Phys.* **1912**, *342*, 657–699.

[123] K. Koepernik, H. Eschrig, *Phys. Rev. B* **1999**, *59*, 1743–1757.

[124] J. Perdew, Y. Wang, *Phys. Rev. B* **1992**, *45*, 13244.

[125] J. P. Perdew, K. Burke, M. Ernzerhof, *Phys. Rev. Lett.* **1996**, *77*, 3865–3868.

[126] B. Rasche, A. Isaeva, M. Ruck, S. Borisenko, V. Zabolotnyy, B. Büchner, K. Koepernik, C. Ortix, M. Richter, J. van den Brink, *Nat. Mater.* **2013**, *12*, 422–425.

[127] R. S. Mulliken, *J. Chem. Phys.* **1955**, *23*, 1833–1840.

[128] R. F. Bader, *Atoms in Molecules: A Quantum Theory*, Oxford University Press, Oxford, **1990**.

[129] M. Kohout, *DGrid*, **2013**.

[130] A. Ormeci, H. Rosner, F. R. Wagner, M. Kohout, Y. Grin, *J. Phys. Chem. A* **2006**, *110*, 1100–1105.

[131] M. Kohout, *Int. J. Quantum Chem.* **2004**, *97*, 651–658.

[132] M. Kohout, *Faraday Discuss.* **2007**, *135*, 43.

[133] *Paraview: Parallel visualization application*, **2008**. http://paraview.org.

[134] B. Rasche, A. Isaeva, A. Gerisch, M. Kaiser, W. Van den Broek, C. T. Koch, U. Kaiser, M. Ruck, *Chem. Mater.* **2013**, *25*, 2359–2364.

[135] M. Ruck, *Acta Crystallogr., Sect. B: Struct. Sci.* **1996**, *52*, 605–609.

[136] T. B. Massalski, *Binary Alloy Phase Diagrams 2nd ed.*, T. B. Massalski, H. Okamoto (Eds.), ASM, New York, **1990**.

[137] M. Ruck, R. M. Heich, *Z. Anorg. Allg. Chem.* **2000**, *626*, 2449–2456.

[138] M. Ruck, *Z. Anorg. Allg. Chem.* **2000**, *626*, 14–22.

[139] E. Ahrens, *Röntgenographischer Nachweis der Koexistenz von* $Bi_8{}^{2+}$*- und* $Bi_9{}^{5+}$*-Polykationen in Bismutsubhalogeniden*, Bachelorarbeit, Technische Universität Dresden, **2009**.

[140] G. Koch, *Synthese und Charakterisierung von* $Bi(SCN)_3$ *& Substitution im System* Bi_4RuI_2, Diplomarbeit, Technische Universität Dresden, **2009**.

[141] B. Rasche, *Quasi-Zweidimensionale Systeme – Die Bismutsubiodide* $Bi_{13}Pt_3I_7$ *und* $Bi_{14}Rh_3I_9$, Masterarbeit, Technische Universität Dresden, **2012**.

[142] M. Kaiser, B. Rasche, A. Isaeva, M. Ruck, *Chem. Eur. J.* **2014**, *20*, 17152–17160.

[143] A. Günther, F. Steden, M. Ruck, *Z. Anorg. Allg. Chem.* **2008**, *634*, 423–430.

[144] B. Rasche, W. Van den Broek, M. Ruck, *Chem. Mater.* **2016**, *28*, 665–672.

[145] B. Rasche, W. Schnelle, M. Ruck, *Z. Anorg. Allg. Chem.* **2015**, *641*, 1444–1452.

[146] H. Oppermann, K. Witte, K. Zacher, H. Brückner, *Z. Anorg. Allg. Chem.* **1991**, *601*, 83–92.

[147] C. Pauly, B. Rasche, K. Koepernik, M. Richter, S. Borisenko, M. Liebmann, M. Ruck, J. van den Brink, M. Morgenstern, *ACS Nano* **2016**, *10*, 3995–4003.

[148] H. C. Hsueh, R. K. Chen, H. Vass, S. J. Clark, G. J. Ackland, W. C.-K. Poon, J. Crain, *Phys. Rev. B* **1998**, *58*, 14812–14822.

[149] B. Robertson, W. McPherson, E. Meyers, *J. Phys. Chem.* **1967**, *71*, 3531–3535.

[150] V. I. Sidey, Y. V. Voroshilov, S. V. Kun, E. Y. Peresh, *J. Alloy. Compd.* **2000**, *296*, 53–58.

[151] H. Min, J. E. Hill, N. A. Sinitsyn, B. R. Sahu, L. Kleinman, A. H. MacDonald, *Phys. Rev. B* **2006**, *74*, 165310.

[152] L. Fu, C. L. Kane, E. J. Mele, *Phys. Rev. Lett.* **2007**, *98*, 106803.

[153] A. Altland, M. R. Zirnbauer, *Phys. Rev. B* **1997**, *55*, 1142–1161.

[154] L. Cano-Cortés, C. Ortix, J. van den Brink, *Phys. Rev. Lett.* **2013**, *111*, 146801.

[155] P. Wei, J. Yang, L. Guo, S. Wang, L. Wu, X. Xu, W. Zhao, Q. Zhang, W. Zhang, M. S. Dresselhaus, J. Yang, *Adv. Funct. Mater.* **2016**, *26*, 5360–5367.

[156] P. S. Galbraith, *g3data*, **2001**. https://github.com/pn2200/g3data.

[157] B. Rasche, A. Isaeva, M. Ruck, K. Koepernik, M. Richter, J. van den Brink, *Sci. Rep.* **2016**, *6*, 20645.

[158] H. Lueken, *Magnetochemie: Eine Einführung in Theorie und Anwendung*, Springer, Berlin, Heidelberg, **1999**.

[159] N. Zhuravlev, *Soviet Phys. JETP* **1957**, *5*, 1064.

[160] N. Zhuravlev, *Soviet Phys. JETP* **1957**, *5*, 1073.

[161] N. Zhuravlev, A. Stepanova, N. Zyuzin, *J. Exptl. Theoret. Phys.* **1959**, *37*, 880–881.

[162] in *Ac - Na*, of *Landolt-Börnstein - Group III Condensed Matter*, Springer, Berlin, Heidelberg, **1990**, DOI: 10.1007/b31114.

[163] D. N. Zheng, A. M. Campbell, J. D. Johnson, J. R. Cooper, F. J. Blunt, A. Porch, P. A. Freeman, *Phys. Rev. B* **1994**, *49*, 1417–1426.

[164] C. Pauly, B. Rasche, K. Koepernik, M. Liebmann, M. Pratzer, M. Richter, J. Kellner, M. Eschbach, B. Kaufmann, L. Plucinski, C. M. Schneider, M. Ruck, J. van den Brink, M. Morgenstern, *Nat. Phys.* **2015**, *11*, 338–343.

[165] A. L. Efros, B. I. Shklovskii, *J. Phys. C: Solid State Phys.* **1975**, *8*, L49.

[166] J. Tersoff, D. R. Hamann, *Phys. Rev. B* **1985**, *31*, 805–813.

[167] B. Zhou, H.-Z. Lu, R.-L. Chu, S.-Q. Shen, Q. Niu, *Phys. Rev. Lett.* **2008**, *101*, 246807.

[168] C. Meyer, J. Klijn, M. Morgenstern, R. Wiesendanger, *Phys. Rev. Lett.* **2003**, *91*, 076803.

[169] B. Yan, L. Müchler, C. Felser, *Phys. Rev. Lett.* **2012**, *109*, 116406.

[170] Y. Kim, C. L. Kane, E. J. Mele, A. M. Rappe, *Phys. Rev. Lett.* **2015**, *115*, 086802.

[171] A. Lau, C. Ortix, J. van den Brink, *Phys. Rev. B* **2015**, *91*, 085106.

[172] R. M. Martin, *Electronic Structure: Basic Theory and Practical Methods*, Cambridge University Press, Cambridge, **2004**.

[173] B. Nowak, D. Kaczorowski, *J. Phys. Chem. C* **2014**, *118*, 18021–18026.

[174] M. Kaiser, A. I. Baranov, M. Ruck, *Z. Anorg. Allg. Chem.* **2014**, *640*, 2742–2746.

[175] R. H. Schröder, N. Schmitz-Pranghe, R. Kohlhaas, *Z. Metallkde.* **1972**, *63*, 12–16.

[176] *ICSD-Datenbank*, Fachinformationszentrum (FIZ), Karlsruhe, **2015**.

[177] A. Günther, M. Heise, F. R. Wagner, M. Ruck, *Angew. Chem. Int. Ed.* **2011**, *50*, 9987–9990; *Angew. Chem.* **2011**, *123*, 10163–10167.

[178] A. I. Baranov, M. Kohout, *J. Phys. Chem. Solids* **2010**, *71*, 1350–1356.

[179] W. M. Haynes, *CRC Handbook of Chemistry and Physics, 95th Edition*, CRC Press, Boca Raton, **2014**.

[180] X. Li, P. Kharel, V. Shah, D. Sellmyer, *Philos. Mag.* **2011**, *91*, 3406–3415.

[181] M. Ruck, *Z. Anorg. Allg. Chem.* **1997**, *623*, 1583–1590.

[182] H. Bärnighausen, *MATCH* **1980**, *9*, 139–175.

[183] M. F. Groh, A. Isaeva, M. Ruck, *Chem. Eur. J.* **2012**, *18*, 10886–10891.

[184] M. F. Groh, A. Isaeva, C. Frey, M. Ruck, *Z. Anorg. Allg. Chem.* **2013**, *639*, 2401–2405.

[185] M. Ruck, *Z. Anorg. Allg. Chem.* **1997**, *623*, 1591–1598.

[186] J. Beck, *J. Solid State Chem.* **1996**, *125*, 165–170.

[187] W. Tremel, *Chem. Ber.* **1992**, *125*, 2165–2170.

[188] W. Tremel, *Chem. Ber.* **1994**, *127*, 11–14.

[189] P. Gressier, L. Guemas, A. Meerschaut, *Acta. Crystallogr. Sec. B* **1982**, *38*, 2877–2879.

[190] P. Gressier, A. Meerschaut, L. Guemas, J. Rouxel, P. Monceau, *J. Solid State Chem.* **1984**, *51*, 141–151.

[191] N. C. Norman, *Chemistry of arsenic, antimony, and bismuth*, Thomson Science, London, **1998**.

[192] M. Ruck, *Solid State Sci.* **2001**, *3*, 369–375.

[193] M. Kaiser, B. Rasche, M. Ruck, *Angew. Chem. Int. Ed.* **2014**, *53*, 3254–3258; *Angew. Chem.* **2014**, *126*, 3319–3323.

[194] E. J. Rode, *Communications of the Platinum Institute* **1929**, *7*, 21.

[195] N. E. Alekseevskii, G. S. Zhdanov, N. N. Zhuravlev, *Soviet Phys. JETP* **1955**, *1*, 99–102.

[196] R. G. Ross, W. Hume-Rothery, *J. Less-Common Met.* **1959**, *1*, 304–308.

[197] R. Ross, W. Hume-Rothery, *J. Less-Common Met.* **1962**, *4*, 454–459.

[198] Q. F. Gu, G. Krauss, Y. Grin, W. Steurer, *J. Solid State Chem.* **2007**, *180*, 940–948.

[199] A. Isaeva, M. Ruck, K. Schäfer, U. C. Rodewald, R. Pöttgen, *Inorg. Chem.* **2015**, *54*, 885–889.

[200] C. Brüne, A. Roth, H. Buhmann, E. M. Hankiewicz, L. W. Molenkamp, J. Maciejko, X.-L. Qi, S.-C. Zhang, *Nat. Phys.* **2012**, *8*, 485–490.

[201] J. Alicea, Y. Oreg, G. Refael, F. von Oppen, M. P. A. Fisher, *Nat. Phys.* **2011**, *7*, 412–417.

[202] G. M. Sheldrick, *Acta Crystallogr., Sect. A* **2008**, *64*, 112–122.

C. Acknowledgement

During the past years I experienced great professional and private support, for which I would like to thank.

First of all, I would like to thank Prof. Ruck for supervising me during the last years and giving me the opportunity to do research in his group. Through his great lectures he was also one of the reasons that brought me to solid-state chemistry. In many discussions I was able to profit from his comprehensive knowledge and only the manifold resources of the group enabled me to explore the chemistry in these many different ways.

Part of these "manifold resources" were many great people, with whom I had the chance to work together. Especially Dr. Anna Isaeva accompanied my research from the beginning and inspired many experiments. As we worked together on the DFG project SPP 1666 "Topological Insulators" we had many discussions on the topic and together forged our way through this research field dominated by physicists. She was also a great company at the different conferences.

I would also like to thank Dr. Martin Kaiser, who supported me especially in the beginning of my PhD studies and with whom I had very intense discussions. He and Alexander Weiz were amongst the many great colleges in my office, which made me want to go to work every day, even if the research was not going so well. Actually, the whole group contributed to this great working atmosphere, any door was open at any time for any question and during breakfast or the coffee breaks the set-backs of the day could be forgotten. I would also like to mention Dr. Alexey Baranov explicitly, who I asked for advice in all questions concerning quantum chemistry and calculations. For the technical support within our group I would like to thank Gudrun Kadner, Andrea Brünner, Michaela Münch, Kerstin Zechel and Dr. Ilka Kunert. For the provided computational facilities I would like to thank the ZIH TU Dresden.

But this work would not have been possible without the very fruitful collaborations, especially with the IFW Dresden, the Helmholtz Centre Dresden-Rossendorf (HZDR), the MPI CPFS and the RWTH Aachen and the University of Ulm. At the IFW Dresden I would like to thank the whole group of Prof. van den Brink, especially Dr. Manuel Richter and Dr. Klaus Koepernik, with whom we developed a lot of understanding of the "TI problem" during long hours of discussions and who did lots of work within the SPP 1666 concerning the theory and the quantum-chemical calculations. Furthermore, Dr. Sergey Borisenko shall be mentioned, who performed the ARPES measurements and also the group of Dr. Christian Hess, who performed many of the transport experiments.

Other transport experiments and many magnetic measurements were performed at the HZDR by Dr. Richard Skrotzki, Marcel Naumann, Rico Schönemann and Dr. Erik Kampert, for which I would like to thank them.

Finally, Dr. Walter Schnelle and Ralf Koban from the MPI CPFS also measured magnetic and transport properties of several samples, for which I am very thankful. One other person working at the MPI CPFS has to be mentioned: Dr. Yuri Prots. Already before I started working on my PhD, he was one of the reasons for my exaltation concerning solid-state chemistry.

At the RWTH Aachen we collaborated with Prof. Morgenstern and his group. Only his belief in the theoretical predictions and first experiments concerning $Bi_{14}Rh_3I_9$ made the great physical experiments via STM and STS possible. Dr. Christian Pauly and partly Dr. Marcus Liebmann performed these great experiments and with all three of them we had fruitful discussions on the TI topic. I would also like to thank for the great time at the different conferences and the invitation to Aachen.

At the University of Ulm, Dr. Anna Isaeva and Dr. Wouter Van den Broek had the chance to measure HRTEM for my samples in the group of Prof. Kaiser and Prof. Koch, and I am very thankful for that.

Last but not least I have been experiencing lots of private support. One important part has been my family, especially my Mother, my Father and my Sister who were always there for me and encouraged me to go my way and follow my interests. But life is nothing without friends and therefore I am very lucky to have some very good ones and would like to say thank you to all of them. Most of my private time during these years of my PhD studies I have shared with my girlfriend Christine Roßberg and therefore she had to suffer most from my tics, for what I am very sorry. I would like to thank her for all the great moments we have been sharing.

There are many other people, especially teachers at my high school in Weimar and Erfurt, who were part of my way on becoming what I am today and who sparked my exaltation for chemistry, physics and science in general and I would like to thank them all.

D. List of Publications

Results presented within this work have already been published within the following articles. If longer parts have been used, this is explicitly indicated by a citation in the heading.

- B. Rasche, A. Isaeva, M. Ruck, S. Borisenko, V. Zabolotnyy, B. Büchner, K. Koepernik, C. Ortix, M. Richter, J. van den Brink, "Stacked topological insulator built from bismuth-based graphene sheet analogues", *Nat. Mater.* **2013**, *12*, 422–425.
- B. Rasche, A. Isaeva, A. Gerisch, M. Kaiser, W. Van den Broek, C. T. Koch, U. Kaiser, M. Ruck, "Crystal Growth and Real Structure Effects of the First Weak 3D Stacked Topological Insulator $Bi_{14}Rh_3I_9$", *Chem. Mater.* **2013**, *25*, 2359–2364.
- M. Kaiser, B. Rasche, A. Isaeva, M. Ruck, "Low-Temperature Topochemical Transformation of $Bi_{13}Pt_3I_7$ into the New Layered Honeycomb Metal $Bi_{12}Pt_3I_5$" *Chem. Eur. J.* **2014**, *20*, 17152–17160.
- B. Rasche, W. Schnelle, M. Ruck, "The Bismuth Subiodides $Bi_8Pt_5I_3$ and $Bi_{16}Pt_{11}I_6$ – Layered Metals with Covalent Platinum Networks", *Z. Anorg. Allg. Chem.* **2015**, *641*, 1444–1452.
- C. Pauly, B. Rasche, K. Koepernik, M. Liebmann, M. Pratzer, M. Richter, J. Kellner, M. Eschbach, B. Kaufmann, L. Plucinski, C. M. Schneider, M. Ruck, J. van den Brink, M. Morgenstern, "Subnanometre-wide electron channels protected by topology", *Nat. Phys.* **2015**, *11*, 338–343.
- B. Rasche, A. Isaeva, M. Ruck, K. Koepernik, M. Richter, J. v. d. Brink, "Correlation between topological band character and chemical bonding in a $Bi_{14}Rh_3I_9$-based family of insulators", *Sci. Rep.* **2016**, *6*, 20645.
- B. Rasche, W. Van den Broek, M. Ruck, "New Environment for a Two-Dimensional Topological Insulator with Hexagonal Channels Hosting Diiodidobismuthate(I) Anions in a Singlet State", *Chem. Mater.* **2016**, *28*, 665–672.
- C. Pauly, B. Rasche, K. Koepernik, M. Richter, S. Borisenko, M. Liebmann, M. Ruck, J. van den Brink, M. Morgenstern, "Electronic Structure of the Dark

Surface of the Weak Topological Insulator $Bi_{14}Rh_3I_9$", *ACS Nano* **2016**, *10*, 3995–4003.

The following articles have also been published, but are not or only loosely connected to the results presented within this work.

- B. Rasche, G. Seifert, A. Enyashin, "Stability and Electronic Properties of Bismuth Nanotubes"*J. Phys. Chem. C* **2010**, *114*, 22092–22097.
- A. Isaeva, B. Rasche, M. Ruck, "Bismuth-based candidates for topological insulators: Chemistry beyond Bi_2Te_3", *physica status solidi (RRL) – Rapid Research Letters* **2013**, *7*, 39–49.
- B. Mendoza-Sánchez, B. Rasche, V. Nicolosi, P. S. Grant, "Scaleable ultra-thin and high power density graphene electrochemical capacitor electrodes manufactured by aqueous exfoliation and spray deposition", *Carbon* **2013**, *52*, 337–346.
- M. Heise, B. Rasche, A. Isaeva, A. I. Baranov, M. Ruck, K. Schäfer, R. Pöttgen, J.-P. Eufinger, J. Janek, "A Metallic Room-Temperature Oxide Ion Conductor", *Angew. Chem. Int. Ed.* **2014**, *53*, 7344–7348; *Angew. Chem.* **2014**, *126*, 7472–7476.
- M. Kaiser, B. Rasche, M. Ruck, "The Topochemical Pseudomorphosis of a Chloride into a Bismuthide", *Angew. Chem. Int. Ed.* **2014**, *53*, 3254–3258; *Angew. Chem.* **2014**, *126*, 3319–3323.
- K. Stolze, B. Rasche, M. Ruck, "Mixed-Valent Selenium Ligands in the Uncharged Iridium Complexes $[Ir_4Se_{10}Br_{16}]$ and $[Ir_6Se_8Cl_{30}]$", *Eur. J. Inorg. Chem.* **2015**, *2015*, 4343–4347.

E. List of Collaborations

Following the good scientific practise all collaborations with other persons and/or groups which are part of this thesis are listed below:

- TEM measurements and data analysis as well as preparation of the figures were performed by Dr. Isaeva (TU Dresden). The facilities were provided by Prof. Koch and Prof. Kaiser at the University of Ulm. (Section 4.1.1)
- STEM measurements and data analysis were performed by Dr. Van den Broek (HU Berlin). The facilities were provided by Prof. Koch and Prof. Kaiser at the University of Ulm. (Section 4.1.2)
- STM and STS measurements and data analysis as well as preparation of most of the figures were performed by Dr. Pauly under supervision of Prof. Morgenstern at the RWTH Aachen. (Section 4.1.1 and 4.2.4)
- ARPES measurements have been carried out at the 1^3-ARPES facility[119, 120] at Helmholtz centre Berlin using the synchrotron radiation from the BESSY storage ring and were supervised by Dr. Borisenko from the IFW Dresden. He also performed the data analysis and preparation of the figures. (Section 4.2.1)
- Electrical resistivity measurements on powders were performed by Mr. Koban and Dr. Schnelle at the Max Planck Institute for Chemical Physics of Solids Dresden (Section 4.2.5, 4.2.3, 5.1.2 and 5.2.2). Measurements on single crystals were conducted by Dr. Skrotzki, M.Sc. Naumann, Dr. Schönemann and Dr. Kampert at the Helmholtz Centre Dresden Rossendorf (Section 4.2.1). Measurements on single crystals of $Bi_{14}Rh_3I_9$ were also performed by Dr. Vakaliuk under the supervision of Dr. Heß at the IFW Dresden (Section 4.2.1). Most of the results were discussed and analysed together with the experimentalists.
- Most magnetisation measurements were performed by Mr. Koban and Dr. Schnelle at the Max Planck Institute for Chemical Physics of Solids Dresden (Section 4.2.5, 4.2.3, 5.1.2 and 5.2.2). Measurements on $Bi_{13}Pt_3I_7$ were conducted by Dr. Skrotzki, M.Sc. Naumann, Dr. Schönemann and Dr. Kampert at the Helmholtz Centre Dresden Rossendorf (Section4.2.3).
- Dr. Koepernik (IFW Dresden) developed the tight-binding model for the isolated layer model (Section 4.2.2) and calculated the unfolded electronic band structure

of $Bi_{14}Rh_3I_9$ (Section 4.2.1 and 4.2.2). Dr. Richter calculated finite slabs of $Bi_{14}Rh_3I_9$ and the dispersion of the Dirac cone (Section 4.1.1 and 4.2.1). Many results were discussed and interpreted together with Dr. Koeprnik, Dr. Richter, Dr. Isaeva and Prof. van den Brink. Results of the real space analysis were discussed with Dr. Baranov and Dr. Isaeva. Facilities were provided by Prof. van den Brink at the IFW Dresden and the ZIH of the TU Dresden.

F. Versicherung und Erklärung

Hiermit versichere ich, dass ich die vorliegende Arbeit ohne unzulässige Hilfe Dritter und ohne Benutzung anderer als der angegebenen Hilfsmittel angefertigt habe; die aus fremden Quellen direkt oder indirekt übernommenen Gedanken sind als solche kenntlich gemacht. Die Arbeit wurde bisher weder im Inland noch im Ausland in gleicher oder ähnlicher Form einer anderen Prüfungsbehörde vorgelegt.

Die vorliegende Arbeit wurde an der Professur für Anorganische Chemie II der Technischen Universität Dresden unter wissenschaftlicher Betreuung von Herrn Prof. Dr. rer. nat. habil. Michael Ruck im Zeitraum von Mai 2012 bis September 2016 angefertigt.

Es haben keine früheren erfolglosen Promotionsverfahren stattgefunden.

Hiermit erkenne ich die Promotionsordnung der Fakultät Mathematik und Naturwissenschaften der Technischen Universität Dresden in der Fassung vom 23. Februar 2011, zuletzt geändert am 15. Juni 2011 und 18. Juni 2014, an.

Dresden, September 2016 Bertold Rasche